

SCIENTIFIC & TECHNICAL REPORT 2022

IMPRINT

Full report title CSEM Scientific and Technical Report 2022

Editor and publisher CSEM SA
info@csem.ch
T +41 32 720 5111

Publication Yearly frequency
Printed and digital editions



Cover page design Contreforme
www.contreforme.ch

Printing Imprimerie Baillod SA, Bevaix (Switzerland)

PREFACE

Dear Reader,

The year 2022 proved to be rich in unexpected changes. Tensions in the energy markets have forced nations to rethink their sourcing and production strategies, giving a boost to renewable energies. A shortage of semiconductor chips has highlighted our dependence on their production. Change can be an engine of progress. As shown in this year's list of scientific achievements fostered by CSEM, every sector is trying out change.

One unstoppable change is the world's progression into the digital age. For many companies and SMEs in Switzerland, fully taking the leap into the digital realm is still a daunting prospect. However, when matched with the right innovations, solutions and technologies, digitalization is worth pursuing as it is the key to increasing competitiveness and making businesses more efficient and profitable. At CSEM, we make it our business to connect our customers with the right technical solution to their particular problem.

In an effort to offset the effect of rising energy prices, many companies have been looking for better ways to implement renewable energy resources into their businesses and become more sustainable. Our smart data-driven solutions are helping companies adapt and thrive by optimizing their approaches to integrating, storing, monitoring, controlling, and maintaining renewables.

As healthcare costs rise as well, we are working on changing how healthcare is administered, using the latest IoT, wearables, and edge computing solutions to help create personalized health treatments with safer production processes. Besides, we are helping manufacturers throughout Europe embrace precision manufacturing by using 3D printing to develop never imagined products to help them augment their production facilities.

We may not know what the future holds, but we like to treat change as an opportunity. As the Swiss technology innovation center, we are convinced it is possible to build a better world and face our time's challenges.

Alexandre Pauchard

CEO, CSEM SA

CONTENTS

PREFACE

MULTIDISCIPLINARY INTEGRATED PROJECTS—MIPS

| | |
|---|----|
| DEMON – End-to-End Secure Multi-actor Data Sharing for Industry 4.0 Smart Systems | 10 |
| MIRA – Miniaturized Multi-sensing Arrays | 11 |
| LINIO-PIC – Towards a Packaged Lithium-Niobate-on-Insulator (LNOI) based Carrier-envelope Offset Frequency Detector for Femtosecond Laser Stabilization | 12 |
| COSIMA – Cooperative Sensors for Electrographic Imaging | 13 |
| SILOSCAPE – a Novel Escapement for FlexMEMS-based Watch Oscillators | 14 |

DIGITAL TECHNOLOGIES

| | |
|--|----|
| Ultra-low Power High Dynamic Range Image Sensor for IoT Applications | 17 |
| Lattice-based Crypto using Convolutional Neuronal Network Accelerator | 18 |
| Designing Lightweight SCA-resistant Cryptography Implementations for IoT | 19 |
| User-centric Key Management for End-to-End IoT Security and Privacy | 20 |
| Hardening μ111 RTOS with ARM Trustzone-M Technology | 21 |
| Towards Low-power AI-based Embedded Person Detection using Early Exiting | 22 |
| LoRaWAN-based IoT Solution for Real-time Monitoring of Natural Resources in Silos | 23 |
| AI-based Localization: Learning from Synthetic Data from a Genetically Guided Digital Twin | 24 |
| Pilot Demonstration of RF-based Localization and Monitoring in Offshore Platforms | 25 |
| IEEE 1588 Synchronization for Embedded Devices | 26 |
| 3D Printing for a New Efficient Production Method of mm-Wave Waveguide-based Antennas and Components | 27 |
| Embedded Wear Monitoring of Mechanical Parts | 28 |
| Deep Neural Networks vs. Random Features: a Performance Comparison on an Industrial Dataset | 29 |
| Safely Applying Auto-tuning to Industrial Controllers | 30 |
| Spot the Difference – Anomaly Detection using Neural Image Comparison | 31 |
| My Chemical Romance – an AI-Chemist assisting Thermal Analysis | 32 |
| LeafEye – Robust Plant Pests' Identification and Classification | 33 |
| Industry Guard | 34 |
| Smartphone-based Blood Pressure Measurement during Induction of General Anesthesia | 35 |

| | |
|---|-----------|
| Introduction of Artificial Intelligence in Cardiotocography Interpretation for the Clinical Use | 36 |
| Limitation of Calibration-free PPG-based Blood Pressure Estimation | 37 |
| Optical Heart Rate Monitoring – Continuous Improvement Strategies | 38 |
| Compact Long-term 8-channel Electroencephalography with High Functional Sensitivity using Cooperative-sensor Technology with Dry Electrodes | 39 |
| ICARUS – a Wearable Platform for Voice-as-a-Digital-Biomarker Applications | 40 |
| Lung-monitoring Wearable with Low-power Sensors Seamlessly Integrated in a Garment | 41 |
| A Benchmarking Solution for Edge Devices | 42 |
| Deep Learning Based Detection of Intrauterine Growth Restrictions in Piglets | 43 |
| SCA-resistant Implementations of Elliptic Curve Cryptography in Embedded Secure Software | 44 |
| Applications of Artificial Intelligence in Side-channel Security | 45 |
| Arbitrary-scale Image Generation | 46 |
| Improving the Classification of an Unbalanced Spheroids Dataset by Oversampling with Synthetic Images from Generative Adversarial Network | 47 |
| FETA – a Flexible Low-power AI/ML Accelerator for Time Series Signals | 48 |
| EdgeML Deployment Flow for CSEM's End-to-End Machine Learning Solution | 49 |
| RISC-V Core Extension for Efficient Vector Processing using the X-Interface | 50 |
| Implementation of a Cryptographic Function for Hashing and Message Encryption | 51 |
| ULP 57-66 GHz MIMO FMCW RADAR in 22-nm FDSOI CMOS | 52 |
| Bluetooth® Dual Mode Transceiver Performances in 22 nm Bulk and FD-SOI CMOS Technologies | 53 |
| ASIC-driven Miniature Atomic Clock | 54 |
| PRECISION MANUFACTURING | 55 |
| Direct Laser Writing Maskless Photolithography Equipment | 57 |
| First Measurements of High-temperature Silicon Carbide-based Sensors | 58 |
| PMUT-based Acoustofluidic Devices using Highly Piezoelectric AlScN Layers | 59 |
| Coolers for RF and LF Power Modules | 60 |
| Laser Assisted Wafer Level Encapsulation / Benchmarking with State-of-art Technologies | 61 |
| High Aspect Ratio 3D Pyramidal Probes on CMOS MEA's for in vitro Tissue Model Study: Fabrication and Biological Validation | 62 |
| Elaboration of the Reliability Assessment Methodology for RF Electromechanical Relays in Space Applications: Bi-parameter Thermal – Mechanical Stress Testing | 63 |

| | | | |
|--|----|---|------------|
| Ultra-sensitive Photonics Accelerometers for Next-generation Seismic Sensor Networks | 64 | Automated Microfluidic System for High-throughput Genomics | 95 |
| Packaging of PICs for Fluidic Applications | 65 | Digital Lateral and Vertical Flow Assays | 96 |
| Additive Manufacturing of Metal Matrix Composites for Space Applications | 66 | Urine – Non-invasive Matrix in Human Biomonitoring | 97 |
| MADAM – Damped Flexures Based on Additive Manufacturing | 67 | Functional Printing | 98 |
| Post-processing Development for High-performance mm-Wave Antennas Manufactured by LPBF Process | 68 | Machine Learning-powered Digital Support to Avoid Mistakes in the Lab | 99 |
| Precise Controlling of Transformation Temperature in Nitinol | 69 | SLOTT – Straylight Lidar OGSE Verification Tool | 100 |
| MANUELA – Additive Manufacturing using Metal Pilot Line | 70 | AUDACITY – a Novel Actuator for Aeronautics Applications | 101 |
| New Approach to the Generation of Compliant Mechanisms Designs for the Space Industry | 71 | LUPINE – High-resolution Position Sensor for Space Applications | 102 |
| Full Chain Process Development for 4D Printing of Two-way Shape Memory Alloy for Space Applications | 72 | Configurable Slit Mask Unit for the MIRMOS instrument | 103 |
| Additively Manufactured Flexure Pivots for Space Cryo Application | 73 | Fast Steering Mirror for Line-of-Sight Stabilization | 104 |
| Protective Coatings on Anodized Aluminum Oxide for Watch and Medical Components | 74 | Applications of Coherent FMCW Lidar on Surface Metrology | 105 |
| UV-patterning of Phosphonic Acid Monolayers for Copper Electroplating on Solar Cells | 75 | | |
| Mechanically Resistant Antibacterial Coatings for Medical Tools | 76 | | |
| Optical Oxygen Sensor for Monitoring Water Quality | 77 | | |
| Protective, Passivating, and Selective Transport Layers in Perovskite/c-Si Tandem Solar Cells | 78 | | |
| Nanoimprint Lithography of Polyimide for Very Thin and Flexible Medical Technologies | 79 | | |
| Manufacturing of LIGA Parts with Functional Sidewalls | 80 | | |
| Broadband Atmospheric Gas Sensing with State-of-the-Art Supercontinuum Light Source and Machine Learning Spectral Analysis | 81 | | |
| Ultrastable Low-noise Optical Frequency Ruler | 82 | | |
| High-power fs Pulse Amplification with an Yb:YScO Crystal | 83 | | |
| Wafer-scale in-plane Micro-optical Interconnects for Fiber arrays | 84 | | |
| Wafer-scale Fabrication of Low-loss Waveguides in Lithium Niobate on Insulator (LNOI) Integrated Photonics Platform | 85 | | |
| Toward an Open Access Integrated Photonics Foundry for Lithium Niobate on Insulator (LNOI) | 86 | | |
| Increasing the Quantum Efficiencies of Quantum Devices with Microlens Arrays | 87 | | |
| Manufacturing Acceleration of Free-form Micro-optical Arrays | 88 | | |
| Nanoimprinted Metasurfaces for Foldable and Rollable Displays | 89 | | |
| Contactless Water Quality Monitoring for Sewers | 90 | | |
| Tools for Controlled Positioning of Organoids | 91 | | |
| High-precision Membranes for Cell Isolation | 92 | | |
| Microfluidic SMART LIDS for Safe and Standardized Processes in Multi-well Plates | 93 | | |
| Perfusion Platform for Bioengineered Tissues | 94 | | |
| | | SUSTAINABLE ENERGY | 107 |
| Toward Sustainable PV: Activities at the Sustainable Energy Center | | | 109 |
| Recent Developments of the Plastics Compounding Platform | | | 110 |
| The SIRIUS Project – Swiss Pilot Line for Aesthetic and Ultimate Power PV Modules | | | 111 |
| Dynamic Photovoltaic Modules for Dual-land Usage | | | 112 |
| High-performance Large-area Organic Perovskite Devices for Lighting, Energy, and Pervasive Communications | | | 113 |
| High-efficiency 3-Terminal Perovskite/Silicon Tandems Based on Tunnel Junction IBC | | | 114 |
| Platform for Highly Efficient Industrial c-Si-based Solar Cells | | | 115 |
| Lightweight Photovoltaic Modules for Vehicle Integration at CSEM | | | 116 |
| Solar-powered Smart Freight Container for Medicine Transportation | | | 117 |
| Reliable PV Solution for Stratospheric Applications | | | 118 |
| Graph-based Multi-site PV Forecasting Models | | | 119 |
| Data-driven Flexibility Estimation of Buildings with Uncertainty Quantification | | | 120 |
| Automatic Quality Inspection of PV Modules Based on Minimal Set of Labelled Training Data | | | 121 |
| Battery SoX Balancing Based on zBMS Platform | | | 122 |
| SoXery – an Online Tool to Evaluate Battery Ageing | | | 123 |
| Results on Dendrite Detection for Li-metal Batteries | | | 124 |
| Assessment of Hydrogen and Electric Buses for Public Transport in Switzerland | | | 125 |

ANNEXES

127

| | |
|---|-----|
| Publications | 127 |
| Proceedings | 129 |
| Conferences and Workshops | 131 |
| Research Projects | 133 |
| Innosuisse – Swiss Innovation Agency | 135 |
| European Commission Projects | 139 |
| Space Projects | 142 |
| Industrial Property | 144 |
| Collaboration with Research Institutes and Universities | 144 |
| Teaching | 150 |
| Theses | 151 |
| Commissions and Committees | 153 |
| Prizes and Awards | 156 |

CSEM SA

CSEM is a Swiss public-private, non-profit technology innovation center. We innovate, develop, and transfer world-class technologies to the industrial sector to stimulate competition in the Swiss economy and beyond. We address societal and industrial challenges with disruptive technologies to increase sustainability, to improve people's quality of life, and to grow the economy.

We build **precision manufacturing, digital, and sustainable energy technologies** that are crucial for our future environmental, economic, and social sustainability:

Digital Technologies—We help build end-to-end digital solutions by providing state-of-the-art IoT, wearables, edge computing, artificial intelligence, and industry 4.0 solutions – while covering and tackling the critical issues of secure and private data handling and processing. Our research contributes to more personalized health treatment, smarter energy systems, safer production processes, and quantum technologies that achieve unprecedented levels of sensitivity and accuracy.

Precision Manufacturing—Our research focuses on sensor and advanced microfabrication technologies and processes, bringing innovative ideas to life. By finding ways to scale up these solutions, we can push precision engineering to new heights while minimizing cost and waste and mitigating risks. Our engineering expertise encompasses additive manufacturing, MEMS technology, surface coatings, and more.

Sustainable Energy—Our research is at the forefront of technological and digital energy developments in the renewables and energy management sectors. Our solutions are helping businesses adapt and thrive by optimizing their approaches to integrating, storing, monitoring, controlling, and producing renewable energy for a sustainable society.

MULTIDISCIPLINARY INTEGRATED PROJECTS—MIPs

Harry Heinzelmann

CSEM's multidisciplinary integrated projects (MIPs) are an integral part of our research program. With the MIP program, we can exploit the synergies of the technologies developed in our three research priorities **Precision Manufacturing**, **Digital Technologies**, and **Sustainable Energy**. Every year, CSEM dedicates considerable resources to multidisciplinary projects, with a view to increasing our potential to create innovative solutions.

New proposals for MIP projects are evaluated regularly to ensure a constant renewal of the projects pipeline. This also helps us to quickly respond to newly emerging market needs. Each project aims at developing technology demonstrators with a high maturity level (i.e., a high technology readiness level) for novel applications with high market potential in relatively short development times.

An overview of 2022 MIPs can be found below. The projects are presented in more detail in the following pages of this report.

DEMON – End-to-End Secure Remote Connectivity for Industry 4.0

Industry 4.0 is introducing new ways to collect, transmit, and valorize valuable data through an ecosystem of specialized machinery with advanced features. However, data sharing involves considerable risk, which could expose industrial secrets or know-how. CSEM has integrated its technologies into a secure, end-to-end framework with efficient data distribution and private computing to encourage data sharing in this complex trust landscape. DEMON enables secure and confidential multi-actor data sharing and high real-time data accessibility.

MIRA – Miniaturized Multi-sensing Array

Several significant trends are driving innovation in biosensors, chemical sensors, point-of-care kits, personalized medicine, food, water, and air quality monitoring. MIRA addresses the miniaturization of electrochemical sensors and their integration onto CMOS, to address applications in complex media and buffers. Incorporating electrochemical sensors on a CMOS chip helps industry develop miniaturized health monitoring solutions (with electronics and sensing parts embedded on a small surface area). The MIRA concept has been demonstrated based on several assay technologies such as molecular imprinted polymers, enzymatic sensing layers, and ionophore-based sensors. Additionally, machine learning is implemented to help refine measurements, while taking into account matrix effects and interferences from other compounds present in the sample.

LINIO-PIC – Lithium Niobate on Insulator (LNOI) PIC Platform

One of the most promising new materials for photonic integrated circuits (PICs) is lithium niobate on insulator (LNOI), thanks to its excellent properties: high electro-optic coefficient, high intrinsic 2nd and 3rd order nonlinearities and a large transparency window. The LINIO-PIC project leverages CSEM's expertise in PIC design and fabrication, packaging, system engineering, laser stabilization and metrology to build a carrier-envelope offset frequency (f_{CEO}) detection unit demonstrator. Such a unit is key for the stabilization of femtosecond lasers used in most precise

measurements and metrology applications. It will provide considerable advantages over the standard fiber approach, in terms of size, cost and minimum pulse energy. The demonstrator, based on LNOI waveguides produced by etching techniques, will encompass a low-loss optical fiber to waveguide coupling and a photodetector providing the f_{CEO} signal, mounted in a butterfly package.

COSIMA – Cooperative Sensors for Electrographic Imaging

The medical market increasingly relies on electrographic imagery to support assisted surgery and improve preventive diagnostics. Acquiring biological signals with miniature electrodes in array arrangements with light and flexible interconnections has high potential in numerous medical and sports applications. COSIMA addresses the optimization of dense electrode arrays (imaging wearables) while preserving high signal quality thanks to dry electrodes. An ASIC prototype has been developed and tested during electrocardiograms (ECG) and electromyograms (EMG) measurements, under laboratory conditions.

SIOSCAPE – A novel Constant-Force Escapement

CSEM is a pioneer in the design and production of centimeter-scale silicon parts featuring fine mechanical functions comprised of flexures (FlexMEMS). These technologies are very promising for designing and producing novel watch mechanisms. Through SIOSCAPE, CSEM has designed and produced multiple novel high-performance watch oscillators and escapements. In 2022, CSEM presented to the mechanical watch market a novel SIOSCAPE escapement that specifically exploits the potential and specificities of FlexMEMS-based oscillators.

DEMON – End-to-End Secure Multi-actor Data Sharing for Industry 4.0 Smart Systems

D. Vizár, C. Kassapoglou-Faist, I. Kastanis, M. Russi, E. Muntané-Calvo, R. Berguerand

The Industry 4.0 introduces capabilities to collect, transmit and valorize useful data into the ecosystem of specialized machinery, enabling a number of advanced features. However, data sharing is perceived as a potential risk to expose know-how. CSEM integrates its technologies into an end-to-end secure framework including efficient data distribution and private computing expected to encourage data sharing in this complex trust landscape.

The Industry 4.0 sees manufacturers of specialized machinery integrating real-time data acquisition and visualization capabilities, intelligence, and communication to enhance their products. This unlocks new opportunities for the machine users, such as predictive maintenance, remote monitoring, remote (re)configuration or advanced quality control. Smart systems are often based on Artificial Intelligence methods requiring the collection of large amounts of data to train the algorithms. Yet, data sharing among the multiple actors on the industrial floor creates a complex trust landscape and granting access is often perceived as a potential risk. In addition, data sharing poses security and logistical challenges. Numerous recent cyberattacks have highlighted the need to secure production systems. In addition to data confidentiality and authenticity, it is important to ensure appropriate access control to data and remote functionalities by various actors, internal and external to the enterprise, without impairing the efficiency or the functioning of the machinery and minimizing down-time. In its mission to support innovation in the Industry, CSEM focuses on vertically integrated production lines. A production line is a heterogeneous conglomeration of hardware devices and software components, often integrated in an ecosystem that includes data storage, advanced visualization, Decision Support Systems and Enterprise Resource Planning systems, requiring up-to-date data feed (e.g., CSEM's VISARD [1] system). Integrated in such a complex system, the data collected by a machine's components have a potential to create substantially higher value for all involved parties, including the component manufacturer, the production line integrator as well as the machine owner. However, the machine owners tend to be extremely hesitant to share any data from production, fearing a leakage of know-how, IP, or other information, e.g., through a cloud infrastructure.

CSEM has designed a solution for secure and private multi-actor data sharing along with high real time data accessibility (see Figure 1). At the heart of the proposed system lies CSEM's secure data distribution technology (XEMWAY) developed initially in the medical and IoT fields. It ensures a timely delivery of the right data to the right entity, be it data store, integrator's remote administration console, machine owner's own remote monitoring interface, or infrastructure of other parties. An access control mechanism allows the data owner to manage permissions in a fine-grained manner, ensuring that data travels only among authenticated and authorized entities (users, devices etc.). A cutting-edge end-to-end security framework [2] (originally developed for medical application) further lets the data to be distributed across the ecosystem in encrypted form, without a priori sharing any decryption keys, and provides a mechanism for the data consumer to request them, fully electronically, at any granularity and subject to the data owner's consent. Key sharing

is designed to be efficient at any request granularity. Sensitive data can thus be safely disseminated in encrypted form to many parties (e.g., a data analysts), since it remains virtually unusable, unless a request to get the encryption key(s) is explicitly issued and approved. A CSEM technology based on Trusted Execution Environments allows a data analyst to decrypt, analyze and destroy such sensitive data inside a protected environment, which only yields the results of the analysis, but keeps the raw data unavailable to anyone, including the analyst and the cloud service provider. The overall emerging solution scales up and may use well-established commercial cloud services.

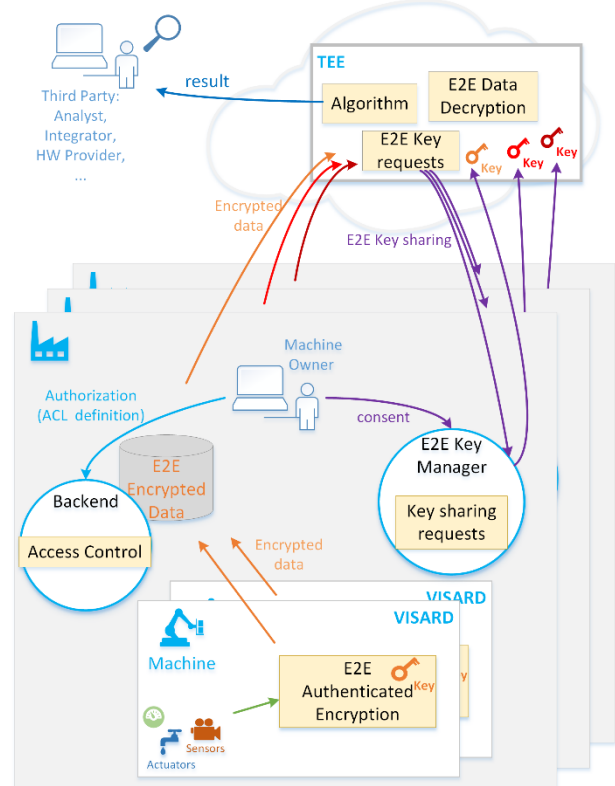


Figure 1: End-to-end secure and private, multi-actor data sharing.

The usefulness of the solution in unlocking new value and overcoming the issues of trust in the ecosystem is best illustrated by the use case of support and predictive maintenance. An integrator can process bigger volumes of data, from multiple installations and possibly contact the hardware providers, passing them specific (encrypted) data sets for examination. The hardware provider will get the decryption keys on his turn, based on his intent of use, and get valuable feedback. Another hot topic is algorithm training: a developer trains an algorithm for her client based on data from various actors, without any data cross-leak. Note, the algorithm may remain secret to all actors as well.

[1] "CSEM VISARD" www.visard.ch

[2] M. de Ree, D. Vizár, G. Mantas, J. Bastos, C. Kassapoglou-Faist, J. Rodriguez "A Key Management Framework to Secure IoMT-enabled Healthcare Systems", CAMAD52502.2021.9617796.

MIRA – Miniaturized Multi-sensing Arrays

X. Lefèvre, M. Crenna, A. Finelli, N. Glaser, B. Petkus, P.-F. Rüedi, M. Dia

The MIRA project targets miniaturization of electrochemical sensors as well as their integration on CMOS to address applications in complex media and buffers. Two use cases are investigated (1) the detection of dysfunction markers in body fluids such as urine, e.g., albumin, creatinine, glucose, ions, and (2) the monitoring of harmful compounds in complex media e.g., nicotine in smoke-bubbled solutions. Electrochemical sensors have been miniaturized on printed electrodes for existing and new CSEM sensors (glucose, Na⁺, K⁺, nicotine and creatinine) and a first CMOS design of the multi-sensor array has been developed. with combinations of several assay technologies based on molecular imprinted polymers, enzymatic sensing layers, and ionophore-based sensors.

Biosensors and chemical sensors receive significant traction from several megatrends: the COVID-19 pandemic accelerated the adoption of point-of-care diagnostic kits, organoids and organs-on-chips boom with shift to personalized medicine, and food quality and water quality awareness are quickly following the trend of air quality monitoring. Incorporating electrochemical sensors on a CMOS chip is promising for developing miniaturized health monitoring sensors as electronic and sensing parts are embedded in a small area. A CMOS chip consisting of an electrode array was developed (Figure 1) and was functionalized with electrochemical sensors to evaluate process compatibility.

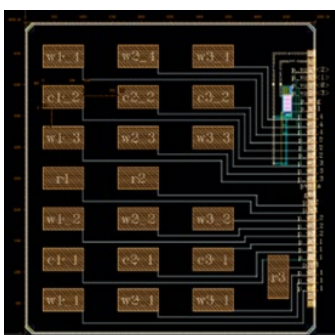


Figure 1: CMOS chip developed for the multi-sensing platform. Chip is 5 × 5 mm.

In parallel, printed electrodes have been miniaturized across all respective biochemical assays from CSEM's standard size of 2.0 mm to 0.8 mm, and even for some sensors to 0.4 mm electrodes. This is a significant achievement for satisfying a small device footprint. The first miniaturized sensor array has been printed and will be integrated in a flow-device for semi-automated data generation (Figure 2). A "large experiment" is scheduled to test 6 sensors in parallel across 30 urine samples to generate data for machine learning.

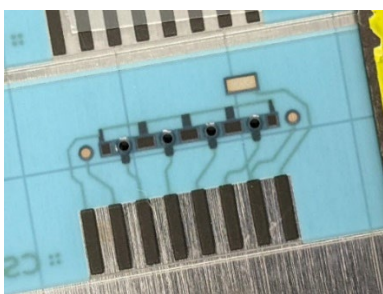


Figure 2: Miniaturized sensor array on flexible substrate. Electrodes are 0.8 mm diameter.

Regarding sensors, a new MIP-based sensor for creatinine has been developed and characterized in KCl buffer. Its response (seen on Figure 3) is suitable for monitoring creatine in urine. The MIP was electrodeposited on screen-printed electrodes including miniaturized ones with no significant loss in performances. Enzymatic (glucose) and ionophore-based (Na, K, and pH) sensors were also successfully miniaturized opening the path for

the functionalization of the CMOS platform. The creatinine sensor will be tested in urine to determine its robustness and participate to the aforementioned "large experiment". In parallel, first sets of data were generated using nicotine MIP-based sensor along with two nicotine analogues' sensors developed for this purpose (namely nornicotine and cotinine). These data will be used for the development of machine learning to improve the accuracy.

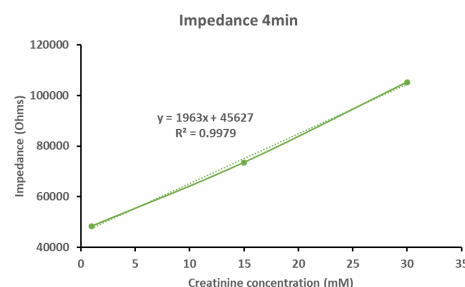


Figure 3: Electrochemical response of the creatinine MIP-based sensor.

For the advanced data processing and machine learning (ML), an automated pipeline for data loading and wrangling has been developed to create a database from different sensors. The process includes data integration, transformation, and handling of errors. Exploratory data analysis has been conducted on the first data set (nicotine use-case) to quantify the sensor variabilities, detect outliers, and spot patterns or interactions between sensors. Furthermore, a first ML predictive model, using linear and non-linear ML algorithms, has been trained to predict the type of mixtures based on multi-sensor responses. The results depicted in Figure 4 show promising directions where the random forest ML model learnt different interactions between three sensors and classifies two mixtures with high accuracy. Future work will extend this analysis to larger datasets that cover the entire input space under different physical conditions.

| | | Recall | | | |
|-----------------|------------|-----------|----------------|-----------------|------------|
| | | Nico+coti | Nico+norni | Nico+norni+coti | Norni+coti |
| True | Nico+coti | 23.61% | 15.28% | 56.94% | 4.17% |
| | Nico+norni | 30.56% | 65.28% | 0.00% | 4.17% |
| Norni+coti | 0.00% | 0.00% | 100.00% | 0.00% | |
| Nico+norni+coti | 0.00% | 0.00% | 0.00% | 100.00% | |

Figure 4: Confusion matrix of 4-class classification on test data.

LINIO-PIC – Towards a Packaged Lithium-Niobate-on-Insulator (LNOI) based Carrier-envelope Offset Frequency Detector for Femtosecond Laser Stabilization

M. Renggli, I. Bundalo, H. Sattari, A. Ghadimi, E. Obrzud, J. Holzer, D. Grassani, S. Lecomte

One of the most promising new materials for photonic integrated circuits (PICs) is lithium niobate on insulator (LNOI). This platform offers a variety of unique optical characteristics, including a high electro-optic (EO) coefficient, high intrinsic 2nd and 3rd order nonlinearities, and a large transparency window (350 to 5500 nm). The objective of this project is to increase CSEM's knowledge and competence in various value chain stages, including PIC design, simulation, fabrication, photonics packaging, testing, and finally building an experimental demonstrator. The maturity of the technology allows integration of a detector for carrier-envelope frequency offset, which is used for stabilization of a femtosecond laser. Implementing such a demonstrator will highlight CSEM capabilities of a fully packaged competitive PIC-based solution covering the phases from the design to the final product.

In this project CSEM is leveraging the capabilities among several field of competencies (PIC design and fabrication, packaging, system engineering, laser stabilization and metrology), which are required to build a full demonstrator of a carrier-envelope offset frequency (f_{CEO}) detection unit. Based on LNOI waveguide technology [1], the f_{CEO} detection requires reduced optical pulse energy and becomes compacter and cheaper than the standard approach based on highly nonlinear fiber and frequency doubling crystal. Such characteristics are key to contribute to the more widespread use of optical frequency combs in industrial applications as well as in space technology. Indeed, it will notably bring down cost, size and power consumption.

The demonstrator is based on low-loss etching of LNOI waveguide (< 0.2 dB/cm), that has demonstrated the necessary reliability under femtosecond pulses illumination [1] as well as two-level waveguides etching for the realization of a double-inverse taper required for efficient light coupling between the optical fiber and the LNOI waveguide (target of < 1 dB / facet, current result is 4 dB / facet). In addition to the fiber and the LNOI waveguide, the demonstrator comprises a photodiode located at the waveguide output to simply detect the f_{CEO} signal.

In Figure 1, the CAD design of the demonstrator is presented where all the different components are located in a standard butterfly 14-pin package. The components are glued on-top of a Peltier element that serves as a micro-bench. Hermetic sealing is foreseen as well.

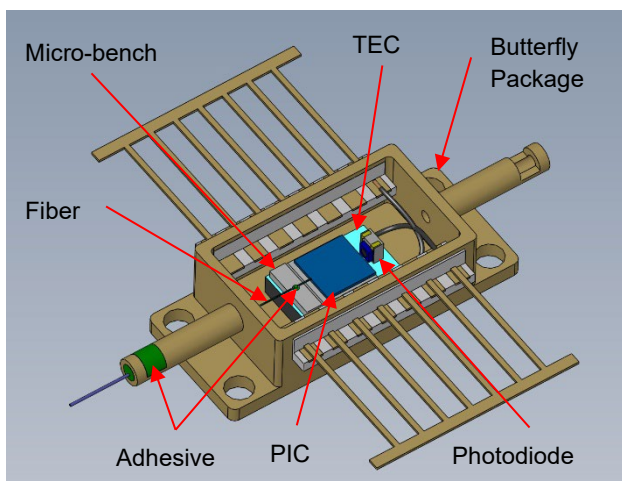


Figure 1: CAD design for the demonstrator.

On the packaging side, one important challenge is related to the precise gluing of the optical fiber in front of the waveguide. As the mode field diameter is small (around 3 μm), the tolerances on the position of the fiber in front of the waveguide are very tight. The fiber fixation process has to be controlled well enough to ensure alignment even after permanent fixation. To do so, a 6 degrees of freedom (6 DOF) assembly machine from Aixemtec was delivered in February 2022 to establish the two-side sub-micron optical fiber alignment and fixation by adhesives (see Figure 2). Efforts were made to assess in a deterministic way the shrinkage behavior of the adhesive during curing, which is crucial in overcoming the drift of optical fiber coupling, respectively the resulting misalignment. The so-called "first light" detection scheme to facilitate the automated fiber alignment has been developed in collaboration with Aixemtec, which should greatly speed up the packaging in research environment, as well as in industrial settings.

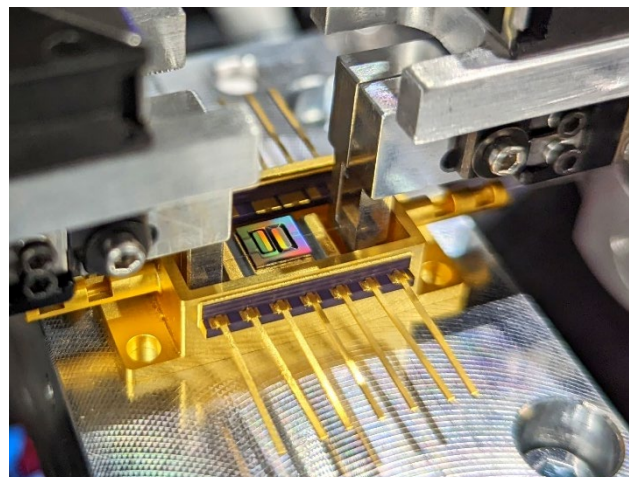


Figure 2: Butterfly package with PIC in 6 DOF alignment station.

This project is a first step towards CSEM's objective to becoming a key strategic partner in PIC device developments covering the full value chain from design and fabrication to system integration and packaging. CSEM is seeking further partnerships in particular for the industrial grade packaging implementations. The LNOI PIC platform, with its unique capabilities, offers a tremendous potential to impact many fields of applications like laser technology, telecommunication, sensing, and quantum.

[1] E. Obrzud, et al., "Stable and compact RF-to-optical link using lithium niobate on insulator waveguides", APL Photonics 6, 121303 (2021).

COSIMA – Cooperative Sensors for Electrographic Imaging

A. Fivaz, O. Chételat, B. Sporrer, M. Pons

Electrographic imagery is increasingly demanded in the medical market to support assisted surgery and to improve preventive diagnostics. Images are obtained from high density electrodes and the developed concept of dot size Cooperative Sensors provides high resolution in a highly integrated form factor. Besides, the use of body sensors is increasingly common in the day-to-day life, in sports, and in other areas as, for example, in immersive gaming where the sensors are meant to detect the activation of the fingers or the eyelids. One common denominator is usability which implies many challenges, such as miniaturization, signal quality, and wiring for the integration of sensors into wearables. A demonstration electronics dedicated to these many miniature sensors applications has been developed and tested in laboratory conditions with respect to the measurement of the electrocardiogram.

Biopotentials measurement has long been used in medical practices to obtain a patient's electrocardiogram (ECG) or electroencephalogram (EEG). Those who have experienced the conventional setup remember for sure the cumbersome cabling arrangement and the irritations provoked by the gel used to apply the electrodes on the skin. In contrast, the technology developed at CSEM—the so-called Cooperative Sensors—offers medical-quality signals using non-irritating dry electrodes and reduces the wiring to merely a two-wire bus connection between the sensors. In addition, electrical impedance tomography (EIT) and electromyogram (EMG) are provided with the same architecture.

The current development, named COSIMA (COoperative Sensors for electrographic IMAGING), was built for testing and pre-validation, and has already demonstrated the potential of the concept. A first miniaturization step has been reached with the electronics fitting a 7×7 mm board.

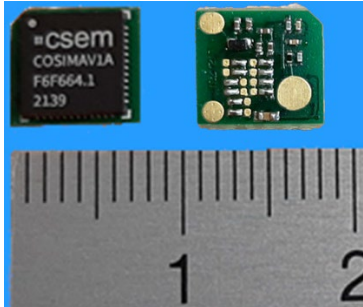


Figure 1: ASIC packaged and mounted on top of a PCB with, on bottom, a few external components and address configuration strips.

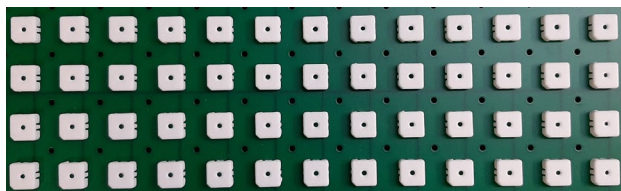


Figure 2: Test board with array of cooperative sensors.

A key measure to reduce the size of the sensor is the integration of all required functionality into a single integrated circuit. That means powering, synchronization and communication to from an external unit electrode signal acquisition, are all integrated in the same die. The ExG receiver chain is programmable to use different sampling rates from 2 kHz up to 25 kHz (traded off against the maximum number of sensors that can be connected to a single bus). The gain can also be adapted to fit the different input-signal voltage ranges demanded by the EEG, ECG, and EMG applications. The additional functionalities for EIT stimulation and acquisition are provided by a parallel set of circuits. The whole functionality is performed with a power budget of $400 \mu\text{A}$ a.c. harvested from the square-wave voltage provided by the two-wire bus. The ASIC prototype has been produced in a 180 nm mixed-signal node suited for the targeted frequency range and a design that is dominated in area by analog circuitry.

The size of the board is mainly dictated on the top by the selected 48-pin package which offers the desired test pins and on the bottom by the many configuration pads which have been implemented. The ASIC die is 2.1×1.8 mm and all the sensor electronics, in a final implementation, could almost fit in that surface.

While the system is sized to accommodate up to 250 sensors, the tests have been performed so far with an assembly of 15 sensors on a test bench (see Figure 2) and with two sensors applied on a patient (see Figure 3).

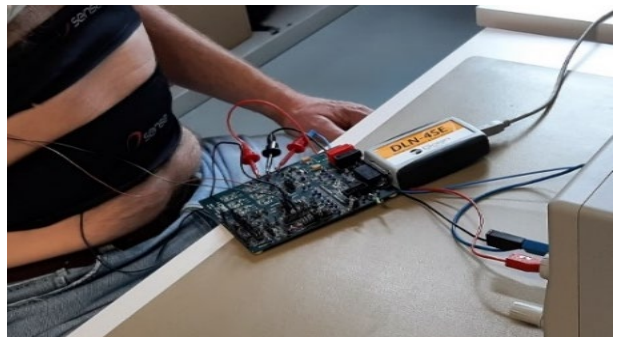


Figure 3: Experimental test setup on body with two sensors connected on the 2-wire bus.

The first measurements on the bench showed a noise performance in the range of the IEC-60601 standards ($< 30 \mu\text{V}$ pp for a bandwidth 0.05–150 Hz). On the body, the ECG signal is clearly visible but remains noisy with a noticeable contribution from the 50 Hz mains collected from the laboratory instruments.

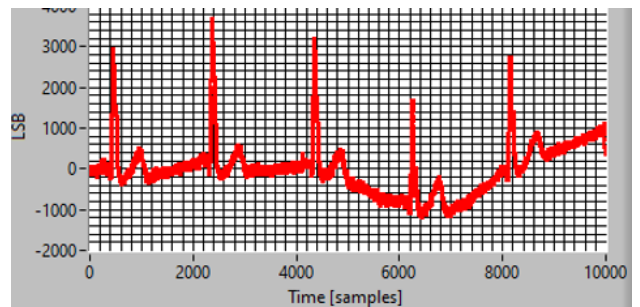


Figure 4: Example of recorded ECG from the setup of Figure 3.

The activity performed so far proved the concept and allowed identifying shortcomings and ways of improvements to realize a second iteration with an updated ASIC foreseen in the coming year.

SIOSCAPE – a Novel Escapement for FlexMEMS-based Watch Oscillators

F. Barrot, G. Musy, O. Laesser*, Y. Petremand, R. Winiger*, L. Giriens, E. Dominé

CSEM, with its combined expertise in micro-manufacturing techniques and precision mechanisms, has been a pioneer in the design and production of centimeter scale silicon parts featuring fine mechanical functions comprising flexures (FlexMEMS), opening up new opportunities for both the design and production of novel watch mechanisms. In the frame of SIOSCAPE MIPs, CSEM is focusing on the design and production of novel high-performance watch oscillators and escapements. This year, CSEM is presenting a novel escapement specifically targeted to exploit the potential and specificities of FlexMEMS based oscillators.

With the invention of the thermally compensated Silicon hairsprings, CSEM paved the way to a new trend in the watch industry: the use of silicon as a base material for the design and production of mechanical watch parts^[1]. For the past 20 years, CSEM has relentlessly kept on working to push forward the technological boundaries of the micromechanical structuration of silicon at the watch scale^[2], proposing new watch mechanisms that can only be addressed with this approach^[3]. Leveraging its expertise in the design of precision mechanisms guided by flexure blades in lieu of classical bearings, a frictionless guiding approach requiring no lubrication, CSEM has proposed the so-called "FlexMEMS approach", which combines the advantages provided by the precise micromechanical structuration of silicon to those of flexure bearings, for the design and production of novel high-end oscillators and escapements^[4]. In the past years, with the "Siloscope"^[5, 6] and the "Double Hammer"^[7] escapements, CSEM has addressed two complementary market segments: high power reserve and chronometric performances.

The so called "frog escapement" is the latest escapement designed and produced by CSEM (Figures 1 and 2). This innovative escapement is designed to be paired with FlexMEMS oscillators and is targeting a very precise time keeping (typically $\pm 2 \text{ s/d}$) together with a regular power reserve and a simple design.

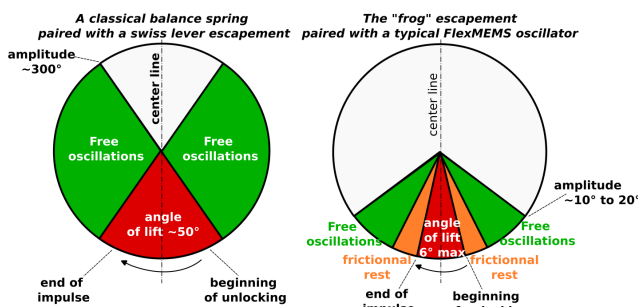


Figure 1: Comparison of the oscillation characteristics of a classical balance spring paired with a Swiss lever escapement and a FlexMEMS oscillator paired with the "frog" escapements.

A classical balance spring has an amplitude of about 300° and is characterized by a large free swing portion followed by a swing portion of about 50° corresponding to the angle of lift, i.e., the angle where the release of the escape wheel and the impulse of

the escapement to the inertial element take place. Compared to a balance spring, FlexMEMS oscillators are characterized by a higher rigidity of the return spring, lower oscillation amplitudes ($< 20^\circ$) and lower angles of lift ($< 6^\circ$) which make them difficult to be auto-starting with a Swiss lever escapement unless the angle of lift is lowered further. However, it is impossible to resize the fork of a traditional Swiss lever escapement to make it compatible with an angle of lift of 6° or less. Indeed, the clearances and securities between the fork and the impulse pin would be unachievable. Furthermore, due to the higher stiffness of the return spring of a FlexMEMS oscillator compared to a classical balance spring, it would be very difficult to ensure the self-starting of the FlexMEMS oscillators while keeping the typically low driving torque of the escape wheel.

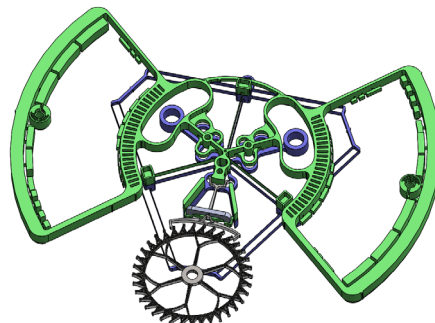


Figure 2: The Frog escapement (paired with a CR3 oscillator).

To design a self-starting lever escapement compatible with the specificities of FlexMEMS oscillators, CSEM has added a frictional resting phase to lower the angle of lift and make it possible to build a fork-and-pin mechanism with a very low angle of lift and reasonable clearances and securities. The unlocking phase is preceded by a first frictional resting phase, which is itself preceded by a first free oscillation phase. The impulse phase is followed by a second frictional resting phase, which is itself followed by a second free oscillation phase. The frog escapement is therefore at rest during a portion of the oscillation but is free outside this portion of oscillation. In that sense, the frog escapement is a semi-detached escapement. A first prototype featuring for the first time a CR3 oscillator^[8] in a watch movement, was assembled and first functional tests confirmed the validity and potential of the concept.

* External key contributors: "Olivier Laesser" and "Winiger Horloger"

^[1] A. Perret, "Le silicium comme matériau dans la fabrication de pièces mécaniques", SSC, 2001.

^[2] O. Dubochet, et al., "L'hybridation du silicium", SSC, 2015.

^[3] M. Despont, et al., "Tic-Tac" made in Silicon", SSC, 2019.

^[4] F. Barrot, et al., "Un nouveau régulateur mécanique pour une réserve de marche exceptionnelle", SSC, 2014.

^[5] F. Barrot, et al., "A Novel Silicon-based Flextech Watch Escapement", CSEM Scientific and Technical Report (2019) 20.

^[6] G. Musy, et al., "Les technologies de micro-fabrication et de l'aérospatiale au service de l'innovation horlogère", SSC 2021.

^[7] F. Barrot, et al., "A novel Constant Force Escapement", CSEM Scientific and Technical Report (2021) 14.

^[8] F. Barrot, et al., "Flexure based oscillators for mechanical watches", CSEM Scientific and Technical Report (2018) 19.

DIGITAL TECHNOLOGIES

Alain-Serge Porret

Digitalization affects all CSEM activities to a certain extent. As a result, we structure this activity along two – applied and technological – axes, each of which divided into three areas.

Application axis

IoT and Vision covers markets such as consumer devices, smartwatches, and a wide range of applications where distributed sensors can be used, from agriculture to infrastructure monitoring. Our goal is to create tools capable of locally sensing and processing anything, anywhere, in hidden ways, including images, sound, vibrations, vital signs, and environmental data.

Industry 4.0 concerns digitalization's impact on manufacturing across various industries, including machines, transportation, robots, pharmaceuticals, chemicals, and food. Our competencies include condition monitoring, predictive maintenance, self-diagnosis, and smart robotics.

Digital Health encompasses medical, wellness and sports applications, as well as various devices, from wearables to medical implants. We also focus on handling and exploiting the data they generate.

We aim to deliver end-to-end sensing and analytic cloud solutions, customized to the needs of vertical markets. Our work is grounded in decades of experience in building specialized hardware and software. AI for Life Sciences (in the Precision Manufacturing chapter) and Energy monitoring and planning (in the Sustainable Energy chapter) are further important applications. Combined, these application areas cover essential digitalization needs of Swiss industries dealing with physical goods.

Technological axis

Data & AI deals with the information processing bottlenecks common to many applications: (1) Security and privacy: How to guarantee that data are kept safe from unauthorized access, from the sensor to the cloud, down to the end user. (2) Efficient and assisted data annotation: How to reduce the effort of labeling data, one of the main deterrents against AI implementations. (3) Distributed and hierarchical computing: How to partition information processing from the end node to the cloud to minimize data traffic, promote privacy, and preserve edge resources.

ASICs for the Edge provide hardware integrated circuit solutions (ASIC) to acquire, pre-process and send information wirelessly from an end node. The effort focuses on ultra-efficient accelerators for embedded inferences, analog sensing interfaces, imagers, and radios, which constitute system-on-chips (SoC) core building blocks for autonomous smart sensors.

Quantum Technology is the next revolution in exploiting the laws of physics in computation, communication, and sensing. In this sector, we are developing miniaturized devices to accurately measure time, magnetic fields, angular accelerations, gas concentrations and even to build novel mm wave and THz imagers.

IoT & Vision

CSEM creates key sustainable IoT technologies and AI-enabled vision sensors for digitalization on any scale, for actors in Industry 4.0, medical, aerospace, building automation, agriculture, and energy, to name but a few. We are helping to develop a resilient IoT by extending device lifetime and autonomy while reducing latency. We are also increasing the service availability as well as the secure and privacy-preserving operations of our solutions' lifecycle, by reducing their environmental footprints even after decommissioning. This is achieved through our ultra-low power (ULP) and embedded hardware and software solutions (including the μ111 ULP secure real-time operating system – RTOS), wireless communication, localization, flexible and ULP AI and machine learning solutions for detection, recognition and decision features, in-sensor and at the edge, in resource-limited autonomous nodes. This includes the design of special antennas and sustainable electronics. All these elements converge to help us build smart, low latency, dependable and scalable systems toward sustainable solutions.

Industry 4.0

Industry 4.0 is an amalgamation of several different technologies that form the basis of the interconnected web of smart systems that lie at the heart of modern manufacturing techniques. All these components make industrial production efficient, adaptive, optimized and robust, by estimating the state of the machines and their products, controlling production processes, and enabling the use of robots that allow fully automated production.

We develop advanced Industry 4.0 technologies for agile and efficient manufacturing. This would not be possible without our multidisciplinary expertise in Data & AI and IoT & Vision. Successful implementation of Industry 4.0 relies heavily on data acquisition, smart algorithms, and adaptive concepts to deliver smart and highly flexible processes, machines and equipment. Aligning with the Swiss market's needs, CSEM is active in three main areas: (1) Industrial quality and process control, often based on machine vision algorithms and predictive quality concepts. (2) Predictive maintenance – the state of industrial equipment – is addressed by monitoring and predicting its status for optimum operating efficiency. (3) Cognitive robotics drive human-centric automation strategies that avoid demotivating and deskilling humans.

Digital Health

Through our Digital Health activities, we design innovative sensing and processing concepts for vital human signs non-invasive monitoring. Medical wearables are valuable tools for gathering patient data in real-time and allowing big data analysis, using artificial intelligence. These devices are also the answer to limiting Switzerland's increasing healthcare costs, fueled by the nation's aging population. It has also been noted that at-home monitoring with medical wearables fosters patient empowerment, enables disease self-management and provides valuable data for developing new treatments and drugs.

We develop innovative platforms for high-performance medical wearables, in different form factors, for multiple body locations

that can simultaneously acquire physiological signals. Given that significant challenges remain regarding data ownership and privacy as well as new platforms' integration into the current health systems and regulatory boundaries, CSEM is focusing on reducing these pinch points. We develop medical wearables that are easy to integrate, can work with limited resources and are miniaturized. We ensure these solutions are accurate, reliable, usable, and cost-effective. Three key technologies we develop are (1) Standalone sensors, e.g., sensors placed on a single body location that can monitor multiple physiological signals that can be generated in different form factors, including wrist bands, arm-pods, patches, or headbands. (2) Cooperative sensors, e.g., sensors worn on different points of the body, which work in together to measure biopotentials and/or bioimpedance in form factors addressing the constraints of imaging wearables. (3) Medical digitalization, e.g., we address the constraints of medical developments in compliance with our ISO13485-certified quality management systems.

Data & AI

The rapidly increasing quantity of data collected by the world's sensors requires intelligent digital data processing. Prospects are exciting, from extensive automation of mundane or repetitive tasks to supplementing human intervention to surpassing human experts. Yet, the question remains: how do we concretely harness this potential? CSEM Data & AI is working to tackle the challenges currently preventing the uptake of the latest data-driven techniques by the Swiss Industry by (1) Harnessing the potential of artificial intelligence to conduct data processing and labeling. By leveraging our privileged position in the data landscape as a trusted partner with access to premium data, we can provide our customers with bespoke, highly efficient methods for processing, generating and labeling data. (2) We are also actively testing and developing efficient hierarchical machine learning algorithms and system architectures to enable more sustainable machine learning solutions and improve machine learning systems' end-to-end efficiency. (3) Security and privacy are paramount in business and personal contexts, so we build innovative security architectures, from HW security foundations for constrained devices to embedded security features. We also supply end-to-end data security and privacy and advanced security architectures for secure processing in the cloud.

ASICs for the Edge

CSEM's ASICs for the Edge build compact systems that can extract higher level relevant information locally, wherever data are generated. This means we perform decision-making and feedback in real-time, with minimum latency and preserve customer privacy by minimizing the amount of data shared with third parties. Moreover, our systems' overall energy efficiencies are drastically improved by limiting wireless transfer to information-rich data.

We develop (1) Sophisticated systems-on-chip (SoC) combining sensor interfaces, imagers, ADC, MCU, ML-derived hardware accelerators, wireless communication, as well as ranging and localization circuits. (2) By co-integrating our power management and energy harvesting solutions, we are paving the way towards always-on, energy-autonomous smart sensing systems. (3) We develop custom hardware that does not exist as off-the-shelf components, often achieving a 10x power reduction, due to architectural innovation enabled by carefully selected trade-offs.

Quantum Technology

Quantum Technologies are the next revolution in exploiting the laws of physics for better devices and ground-breaking improvements in computation, communication and sensing. Taking advantage of non-classical light and atomic properties, coupled with new technologies related to photonics and miniaturization, we aim to unleash quantum technologies' potential for future products with unprecedented performance.

Quantum technologies will impact everyday life by offering fully secure communication, quantum computing capabilities and sensors with distinctive characteristics. CSEM provides (1) chip-scale atomic sensor developments by transferring miniaturized low-cost atomic clocks to industry and bringing other sensors like magnetometers closer to prototype stage. (2) Our novel optical hot vapor clocks are the next generation of high-performance clocks for ground and space applications. (3) To achieve this, we provide offers services in system integration, physics, application-specific integrated circuits (ASICs), photonics and photonic integrated circuits (PICs), as well as a long-standing experience in the development of all kinds of atomic clocks.

Ultra-low Power High Dynamic Range Image Sensor for IoT Applications

P.-F. Rüedi, R. Quaglia, H.-R. Graf

A high-dynamic range ultra-low power VGA (640×480) image sensor has been developed in a stacked CMOS process, achieving a power consumption of $930 \mu\text{W}$ at 10 frames per second (fps). Its on-chip frame memory and ease of integration makes it perfectly suited for resources constrained systems.

There is an increasing need for robust and reliable autonomous vision systems performing visual scene analysis (e.g., face detection, intrusion detection, object detection, ...) in uncontrolled environmental conditions. To maximize their autonomy the power consumption of such systems is an important factor to take into consideration. To achieve this, a high dynamic range is desirable to cope with changing environmental conditions so that the image sensor have a data representation as independent as possible from the illumination level to facilitate visual scene analysis. This would also minimize the associated processing power consumption, which is a key factor for extending the system autonomy.

The ERGO image sensor fulfills these requirements. Figure 1 shows a block diagram of the chip. It contains a VGA array of pixels with in-pixel A/D conversion and data storage to enable a high dynamic range. Based on a time to saturation approach, it offers a logarithmic data representation which enables to encode more than 6 decades of illumination on 10 bits, with 150 steps per decade and simplifies data processing. The rather complex pixel needed to implement this scheme takes advantage of an advanced stacked CMOS process enabling to stack the photodiode on top of the pixel circuitry with a connection between the 2 wafers in each pixel to minimize pixel size while maximizing the fill factor.

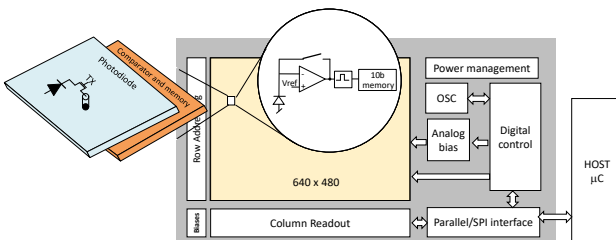


Figure 1: Block diagram of the Ergo chip.

With an intra-scene dynamic range of 120 dB, while consuming on average only $930 \mu\text{W}$ at 10 fps and $90 \mu\text{W}$ at 1 fps, it enables to realize ultra-low power always-on vision systems working in uncontrolled environments. Table 1 summarizes the characteristics of the ERGO image sensor.

Table 1: ERGO characteristics.

| Characteristics | Value |
|--|--|
| Pixel pitch | $6.3 \mu\text{m}$ |
| Resolution | 640×480 |
| Active area | $4 \text{ mm} \times 3 \text{ mm}$ |
| Fill factor | 86% |
| Sensitivity | 6.4 V/lux/s |
| Minimum illumination at 10 fps with F# 2.1 objective | 0.2 lux |
| Dynamic range | 120 dB |
| Frame rate (maximum, at full resolution) | 50 fps |
| Shutter type | Global |
| Data representation | logarithmic on 10 bit |
| On-chip frame memory | 1 |
| Sub-sampling modes | 1/2/4/8 |
| Interface | SPI + parallel |
| Average power consumption at 10 fps | 0.9 mW |
| Average power consumption at 1 fps | 90 μW |
| Power supply | 1.8 V and 3.3 V |
| Dimensions | $4.42 \text{ mm} \times 4.87 \text{ mm}$ |

Figure 2 shows a microphotograph of the chip.

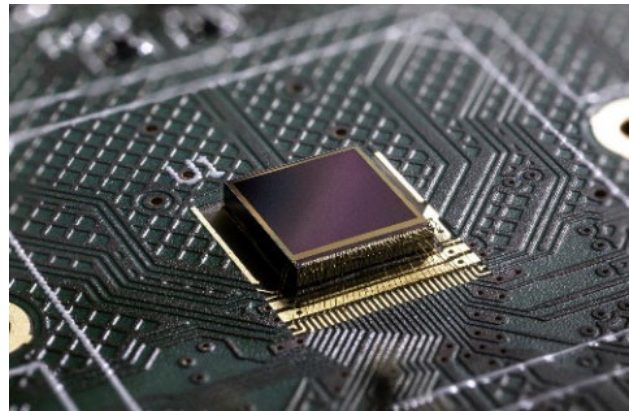


Figure 2: Microphotograph of the chip.

Figure 3 illustrates the high dynamic range of the ERGO chip. All parts of the image are correctly exposed and usable, while on the color inset, obtained with a smartphone, dark areas are underexposed and therefore not suitable for vision tasks.

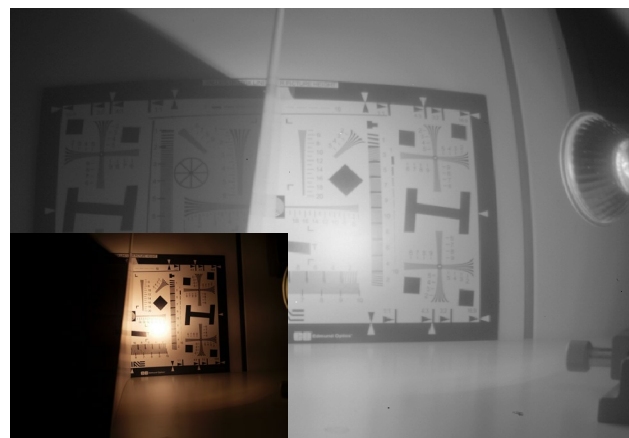


Figure 3: High dynamic range image.

The ERGO image sensor incorporates versatile communication interfaces, combining an OCTO-SPI/SPI interface and a parallel DCMI interface, making it easily interfaceable to a large range of microcontrollers. For example, the on-chip frame memory combined with the possibility to read the image on-demand via SPI enables to interface it with very resource limited microcontrollers. In addition, it requires a very low bill of material restricted to only a few capacitors.

The ERGO image sensor offers the possibility to develop low power vision systems operating in uncontrolled environments. Some application examples are activity tracking, surveillance, biometry, smart toys.

This project received the support of Innosuisse under grant 34950_1_IP-ENG_190823. We thank them for their support.

Lattice-based Crypto using Convolutional Neuronal Network Accelerator

F. Valencia, P. Jokic

With the development of quantum computer, classical public key cryptography is becoming obsolete. Several candidates compete for a standard post-quantum solution for public key cryptography, one of them being Lattice-based. NIST selected Kyber as key exchange algorithm, extensively using polynomial multiplication, which are efficiently executed by CSEM convolutional neural network accelerators.

Cryptography algorithms based on lattice problems are becoming increasingly popular because to date, no quantum algorithm is able to break them. Kyber is a key exchange mechanism based on such lattices, selected by the National Institute of Standards and Technology (NIST) contest for post-quantum cryptography [1]. It consists of 3 operations: key generation, encoding and decoding. The main functions of Kyber are hash functions and ring operations, which are based on polynomial operations. From polynomial operations, the multiplication is the most time consuming. From a computational point of view, polynomial multiplications are similar to convolutions. In the past years, CSEM has developed neuronal network accelerators that efficiently compute convolution operations for convolutional neural networks (CNNs) [2]. This study evaluated how to use such CNN accelerators to also accelerate Kyber and if potential improvements can be identified.

Polynomials in Kyber can be represented in time domain or in Number Theoretic Transform (NTT) domain. NTT is the discrete Fourier transform defined in a ring. Additionally, all arithmetic operations are modular operations. The Montgomery reduction is thus used to facilitate modular multiplications but requires to transform to, or back, Montgomery representations. Finally, the Barret reduction is used to facilitate modular reductions.

To use the CNN accelerator for polynomial multiplications, they need to be transformed to time domain, where the multiplication becomes a convolution, along with auxiliary operations (e.g., adding zero-padding to the vectors before convolution). Figures 1 and 2 illustrate the convolution operations required for CNNs (as implemented in the accelerator) and for Kyber, respectively. Moving to time domain for potential computation efficiency improvements adds additional overhead that reduces the improvement potential. Assessing the balance of improvements versus overheads is the goal of this analysis.

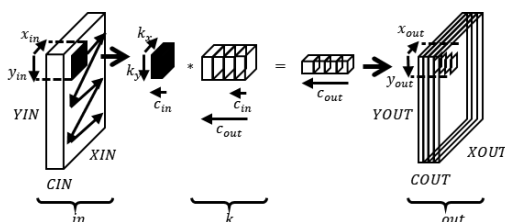


Figure 1: Illustration of 2D convolution within a CNN accelerator.

This work evaluated the execution of Kyber ($N=256$) on a CNN accelerator system-on-chip to assess the speed-up with respect to standard software-based execution. In a first step Kyber must be defined using a matrix of random polynomials "A". The experiments have been performed with two options, a) generating "A" in NTT domain and moving it to time domain, and b) generating "A" directly in time domain. The algorithms are

executed on a RISC-V microcontroller and compared to the baseline of running the same algorithm with a fully softwarebased implementation on the same platform.

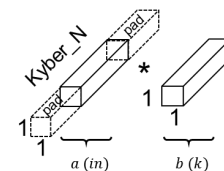


Figure 2: Illustration of convolution within Kyber.

Figure 3 summarizes the experimental results, showing execution speed-up/overheads for option a) and b). For algorithm option a), an overhead of 4% (keypair gen.) - 503% (decoding) has been measured, while for option b), the best-case CNN-accelerated execution was 23% faster than the baseline (keypair gen.), but up to 476% longer in the other execution phases (decoding).

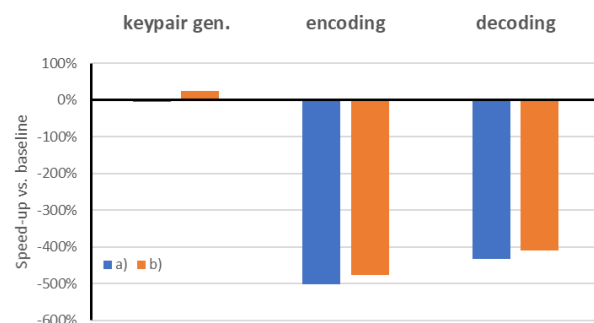


Figure 3: Summary of speed-up vs baseline.

This analysis showed that a naive mapping of the convolutions within Kyber only speed-up operations in the optimal case during the keypair generation, while adding significant overhead of up to 5x execution time in the encoding and decoding phases due to domain conversions. This also exhibits the inappropriateness of the traditional NN accelerators, optimized for 2D convolutions, making it less efficient for generic 1D operations with (unsupported) auxiliary functions.

CSEM has identified the necessary improvements to be brought in the future algorithm developments and to the accelerator architecture. The next generation of CSEM CNN accelerators and crypto-algorithms will support these new specifications.

[1] <https://csrc.nist.gov/Projects/post-quantum-cryptography/selected-algorithms-2022>

[2] P. Jokic, et al., "A ULP 22 nm System-on-Chip with Dual-engine Hardware Acceleration for Edge ML Inference", CSEM Scientific and Technical Report (2020) 106.

Designing Lightweight SCA-resistant Cryptography Implementations for IoT

D. Vizár, F. Valencia, H.-R. Graf

Side-channel attacks (SCA) allow the extraction of secret material (e.g., keys), due to information leaked by cryptographic implementations through power consumption and other physical characteristics. Embedded devices need to integrate cryptography implementations that resist to SCAs, while minimizing the overhead. To cater to the needs of IoT applications, lightweight implementations with varying security-overhead trade-offs have been developed. A reusable leakage simulation toolchain has been developed to shorten the development cycles of protected implementations.

The number of connected embedded devices is skyrocketing and they all need cryptography, be it to protect sensitive data or for secure communication. Internet of things (IoT) systems are often deployed in an environment, where potential attackers can physically access the devices. Therefore, systems need to be protected against side-channel attacks (SCA), which extract secret keys using the dependency of a side channel, such as the power consumption of the implementation on the device and key being used. The number of power consumption traces needed for an attack to succeed depends on, i.a., noise, equipment, attack algorithm. Symmetric cryptography, notably AES [1], are widely deployed in constrained devices given the low footprint and fast execution, however, AES is also known to be vulnerable to SCAs. Thus, a SCA protected implementation of AES is necessary to keep up with the IoT security requirements and ensure interoperability. Many SCA countermeasures have been studied.^[2] *Shuffling* consists in randomizing the execution order of independent blocks. *Masking* uses functionally equivalent transformations of sensitive operations that use randomized data.

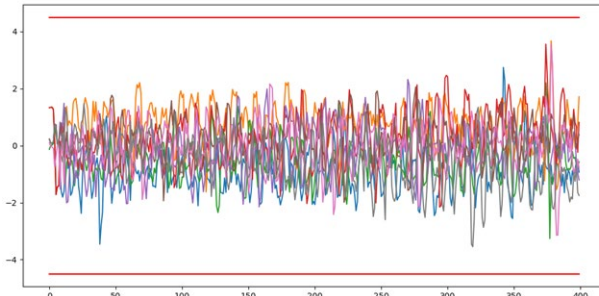


Figure 1: Side-channel evaluation of shuffled AES. X-axis is discrete time and Y-axis is t-statistic, the red lines indicating leakage. Each curve corresponds to evaluation of one of the 16 key bytes of AES-128.

An AES hardware (HW) acceleration module protected against SCA using shuffling technique has been developed. An AES execution consists of 11 iterated rounds. The AES round was divided into 4 independent blocks, which were shuffled based on a random input. Sampling from the 24 possible permutations of 4 blocks needs care, as a direct modular reduction of a 5-bit variable introduces a statistical bias favoring some permutations in a straightforward implementation. To avoid this bias, which could be used to defeat the countermeasure, a fair permutation generator was implemented at the cost of using more random bits (from 5 to 16). T-test method was used to evaluate SCA security of the implementation. It measures if the statistical distributions of two sets of power traces are distinguishable; if the t-statistic is outside of the interval [-4.5, 4.5], there is a possible leakage. The first set corresponds to AES execution with fixed plaintext and key. The second set corresponds to fix key and

[1] Mark Randolph and William Diehl. Power side-channel attack analysis: A review of 20 years of study for the layman. *Cryptography*, 4(2), (2020).

random plaintext. Figure 1 shows the results of this analysis of the shuffled implementation, indicating no leakage in the full AES run.

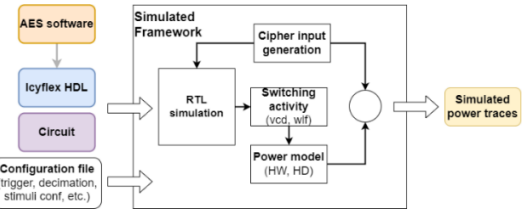


Figure 2: Power simulator diagram.

Development of HW SCA countermeasures is iterative and can become prohibitively long for ASICs, as the final assessment needs to be performed on the final implementation. Testing the circuit in FPGA does not always yield reliable results due to different characteristic to an ASIC. To streamline the development process, a power simulation framework was developed (Figure 2). A circuit description or an Icyflex-V (RISC-V processor) description with the embedded software is used to simulate the execution of an implementation with suitably generated plaintext and key, obtaining the switching activity. The power is obtained calculating either the Hamming Weight (HW) or Hamming Distance (HD) of the switching activity (Figure 3). The power simulator has been validated by performing SCA with simulated traces, against AES software on Icyflex-V and custom AES HW module and compared to attacks on FPGA. Both have shown leakage in the same, vulnerable points and indicated no leakage in the shuffled implementation.

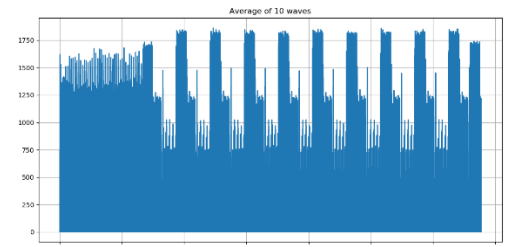


Figure 3: Example simulated power trace. Power vs discrete time.

A protected AES hardware module has been implemented and the bias in the AES quarter-round shuffling have been removed. This block is essential for to deploying secure, yet resource-constrained embedded systems. Additionally, a platform for early assessment of the security was implemented, which speeds up iterations in the design of secure hardware, with a potential for integration into CI/CD pipelines. The two technologies reinforce CSEM's portfolio and competences for securing IoT platforms.

[2] M. J. Dworkin, E. B. Barker, J. R. Nechvatal, J. Foti, L. E. Bassham, E. Roback, J. F. Dray Jr. Advanced encryption standard (AES). FIPS 197.

User-centric Key Management for End-to-End IoT Security and Privacy

D. Vizár, C. Kassapoglou-Faist, R. Berguerand

The extensive sensing of the human beings in internet of things (IoT) applications generates large volumes of personal data. The large attack surface of IoT systems made of constrained, (inter)connected embedded devices systems, calls for end to end-to-end (E2E) encryption, but the difficult key management -hampers adoption. CSEM designed a unique solution that integrates E2E encryption and electronic data sharing in the spirit of GDPR.

The internet of things (IoT) technologies enable new features or even new applications in numerous markets. However, the IoT architecture also exposes a large attack surface, spanning the cloud and the heterogeneous connected devices and connection technologies (often with inadequate security), with attacks on devices already on the rise [1]. A user has no choice but to trust an ever-growing number of applications with handling their data securely and to accept data processing requests, where fine granularity and user control is often at odds with flexibility and data reusability. The so-far presented results [2] do not fully address the security requirements and IoT constraints and end-to-end (E2E) authenticated encryption (from device to the cloud application), a robust security solution, seldom sees deployment in practice because of the difficulty of distributing encryption keys.

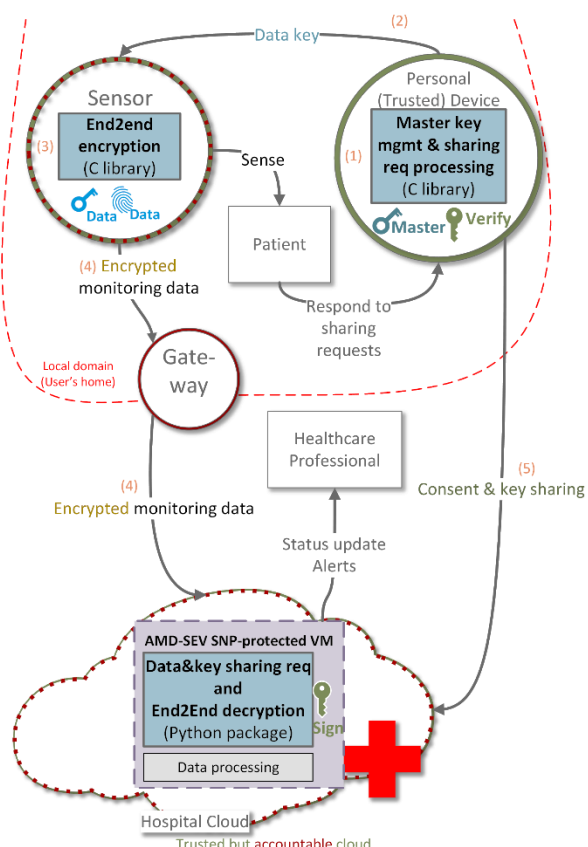


Figure 1: Remote patient monitoring with end-to-end security and privacy.

An E2E framework [3] has been designed at CSEM in the scope of the EU project Moore4Medical [4], primarily for continuous patient monitoring applications (Figure 1, orange numbers link to the description). It proposes a *trusted personal device* (1), a dedicated wearable or a virtual device in the smartphone, which

acts as a personal key manager, securely storing a long-term master key. Mid-term *data protection keys* derived from the master key are provisioned to the IoT devices (2), which run a lightweight, configurable multi-stage key-schedule to derive encryption keys deterministically (3). E.g., encryption keys may be rotated once per day, derived through two intermediate secrets rotated each week and month, respectively. The encrypted data is sent to the cloud *with no keys* (4), enhanced with metadata that fully determine the derivation of the encryption key. A cloud application then issues a non-repudiable *digitally signed sharing request*, detailing both the desired secrets (by the key metadata) and the intent of the processing. The structure of the key schedule enables both fine-grained and bulk access, by requesting encryption keys, the appropriate intermediate secrets or even data protection keys. Subject to user's consent, the key manager can then provision the requested secrets to the requesting processing application (5). In the example above, two months-worth of data would correspond to two, short binary metadata strings for both the request and response.

The design is scalable (in amount of data. Nr. of sensors and nr. of patients), with only a small footprint on both the devices and the key manager, ensuring a perfect fit with the constraints of IoT. Apart from the robustness afforded by E2E encryption, the framework also provides privacy well beyond the state of the art, empowering the user with a direct, technical control over the data they own, in a fashion that is along the principles of GDPR. This increase of personal control may, paradoxically, increase the likelihood that users would agree to (re)share reasonable subsets of their data, unlocking even more value form the data being collected. For example, a patient may agree for encrypted, key-less data to be stored long-term and then electronically agree to use data from a month for the development of a new, life improving drug. The framework has been implemented (Figure 1) and successfully demonstrated using CSEM's ultra-low-power platform Wisenode and μ111 operating system. Further extensions of the technology are identified, such as using User-Managed Access (UMA) tools to alleviate the need of the users' personal trusted device to be online whenever a sharing request is sent, or the integration of the processing application and the data processor module in a Trusted Execution Environment to ensure that data is decrypted within an isolated, secure environment and never needs to leave it.

In conclusion, the novel E2E security and privacy solution designed and implemented at CSEM is an ideal mean of affording robust, E2E security and privacy to data in any IoT-like application. An adaptation to industry 4.0 is already in progress. Provable security of the solution is currently being investigated.

[1] C. Cimpanu, "New HEH botnet can wipe routers and IoT devices", ZDNet, 2020.

[2] S. Sridhar and S. Smys, "Intelligent security framework for iot devices cryptography based end-to-end security architecture," ICISC 2017.

[3] M. de Ree, D. Vizár, G. Mantas, J. Bastos, C. Kassapoglou-Faist, Corinne, J. Rodriguez "A Key Management Framework to Secure IoMT-enabled Healthcare Systems" CAMAD52502.2021.9617796.

[4] EU project Moore4Medical. (2020) <https://moore4medical.eu/>

Hardening μ111 RTOS with ARM Trustzone-M Technology

D. Vizár, I. Ben Salah, M. Fumeaux

To protect embedded applications against software exploits, CSEM proposes TrustZone-hardened architectures for the μ111 real-time operating system and an implementation of a virtual secure element to secure connected embedded devices, in the form of a proof of concept.

Due to form-factor, autonomy or cost requirements, embedded devices are typically constrained in terms of power consumption and other resources, exhibiting a lack of security features. This creates a tension, as the connectivity exposes the devices to remote attacks. Addressing this, ARM proposed the TrustZone (TZ) technology, allowing to isolate the trusted ("secure") part of the firmware from the rest. This work explores the possibility of hardening CSEM's in-house real-time operating system (RTOS) μ111 using TZ. The proposed solution generalizes to most RTOS architectures. A validation implementation has been done on the STM32L552 system on chip. TrustZone-M [1] provides means for securing a firmware running on ARM Cortex-M processor by mapping all resources, i.e., code, data, RAM, and peripherals (all mapped to a single address space) into two "worlds": Secure (S) & Non-Secure (NS). TZ provides silicon-enforced restrictions on how the two worlds interact, preventing any leakage of information from the Secure world.

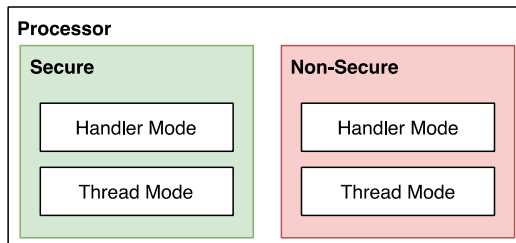


Figure 1: TrustZone separation of processor in two worlds.

TZ mitigates software exploits, such as *code injection* (write a memory location adjacent to a buffer to tamper with the code), *code reuse*: (abuse standard libraries' functions to perform return address manipulation) or *format string attack* (inject arbitrary code as part of a format specifier in variable argument functions such as printf), allowing attackers to jump to malicious code, which can leak sensitive information, abuse a peripheral, or usurp control over the device. By moving the most sensitive parts of the firmware, RAM and peripherals into the Secure world, the restrictions of the interactions between worlds through designated *non-secure callable* (NSC) functions (Figure 2) can help contain a breach within the NS world. If the NSC functions are vulnerable, it may be possible to penetrate the S world, however.

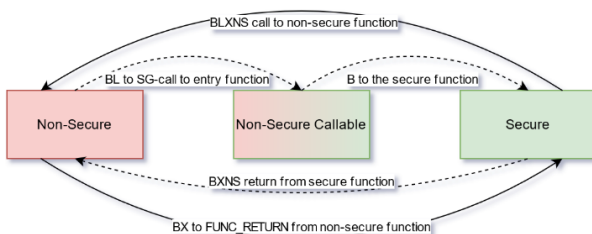


Figure 2: Instructions implemented on TrustZone-M for Security state switch & call functions from between Secure and Non-secure worlds.

Several architectures introducing TZ into an RTOS have been proposed, to serve scenarios with different requirements. (1) *NS RTOS with a S library* is suitable when protecting critical assets and/or logic is top priority, e.g., protecting cryptographic credentials of the device and their manipulation. (2) *S RTOS and NS library* architecture can isolate one or more 3rd party libraries in NS world to mitigate supply chain attacks. (3) *S process scheduler* protects the RTOS itself and enables primitives such as per-process separated buffers. (4) *S scheduler and a process* allows to have distinct execution environment for more involved tasks, such as IP-protected AI models. The last two designs require a context switch between S and NS processes.

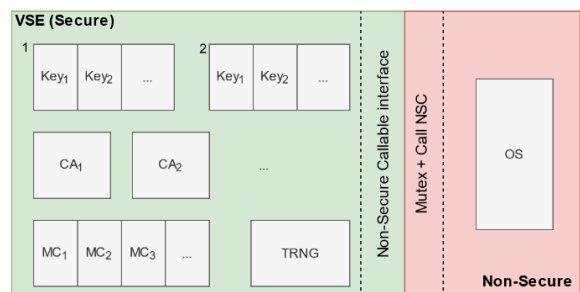


Figure 3: Virtual Secure Element architecture.

A Virtual Secure Element (VSE) protecting cryptographic code and keys has been designed to exemplify the architecture "Secure library". The VSE places cryptographic algorithms, the onboard true random number generator, and a part of flash for R/W non-volatile storage of keys in the S world. The VSE then exposes API to generate keys, store them in slots and use them with the correct cryptographic algorithm using handles, ensuring the keys are never exposed to the NS world. Monotonic counters have also been added. A simple but extensible PoC of the VSE supporting AES [2] has been implemented and integrated in μ111. The VSE requires each world to have its own firmware built separately, the Secure using the GNU Cortex-M Security (CMSE) attributes to handle the security state switching. Additional toolchain is required to both build and correctly link these separate firmwares. As such tools were not readily available, a tool has been developed to provide the needed definitions for each firmware and link the firmware.

TZ can harden embedded applications against software exploits, however the effectiveness heavily depends on how firmware is split to S and NS worlds. Multiple architectures solving this problem for RTOS have been proposed, and a VSE element has been implemented as PoC, with possibility to extend it easily for any TZ-enabled application needing to protect critical credentials.

[1] ARM Limited "TrustZone for Cortex-M", <https://www.arm.com/technologies/trustzone-for-cortex-m>

[2] M. J. Dworkin, E. B. Barker, J. R. Nechvatal, J. Foti, L. E. Bassham, E. Roback, J.F. Dray Jr. Advanced encryption standard (AES). FIPS 197.

Towards Low-power AI-based Embedded Person Detection using Early Exiting

J. Beysens, M. Sénéclauze, P. Dallemagne

Introducing AI processing on low-power IoT devices poses challenges as these devices are typically resource-limited. CSEM exploits the early exit mechanism to split a neural network for hierarchically optimizing the execution path to reduce latency and energy consumption, and to increase robustness and privacy. We demonstrate and evaluate the approach on a person detection application showing its potential for low-power embedded AI.

Traditional AI applications run centralized machine learning (ML) computations, which result in high latency, high sensitivity to connectivity failures and high energy consumption spent on communication, for sending all the data over the network. Moreover, privacy is at risk in cloud-based solutions. CSEM develops a framework for IoT applications that efficiently distributes the neural network inference in a hierarchical manner, to reduce latency and energy consumption, as well as to increase the application robustness. To achieve this, CSEM investigates the early exit mechanism. This technique allows to stop inference calculations already in one of the middle layers of the neural network, instead of proceeding until the final layer [1].

To evaluate the potential of this technique, we consider a person detection application scenario, aiming at deciding whether a person is in the image or not. Figure 1 presents an overview of the architecture.

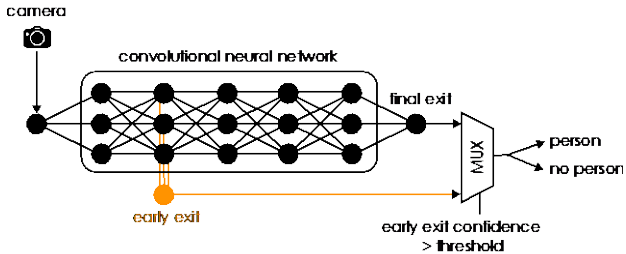


Figure 1: Hierarchical ML inference architecture for person detection.

The camera captures images and feeds them to a convolutional neural network (CNN). This ML model is extended with an *early exit*, attached to a specific layer in the model. This exit enables to acquire an early classification output with its associated confidence level (how certain the model is about this classification). If this level is higher than a predefined threshold, the inference of the next layers is not executed, avoiding wasting resources on the second part of the ML model. If the required confidence threshold is not reached, inference continues until the final exit, and the final classification output is obtained.

The lightweight CNN MobileNetV2 exhibits good performance on resource-constrained devices and uses depth-wise separable convolutions to reduce the computational burden [2]. Similar as the well-known ResNet architecture, this model also uses residual connections to overcome the vanishing gradient problem. We train this model on the Visual Wake Words dataset, which filters the labels of the publicly available COCO dataset to provide a dataset of 115k training and test images with labels of "person" and "no person". Next, the resolution of the images is reduced to 96x96 pixels, to limit the size of the input layer.

First, we train the baseline model without any early exit using the Adam optimizer during 300 epochs. Then, we add a single early exit at a predefined layer in the model and continue training the

[1] J. Beysens, et al., "Hierarchical Machine Learning for Low-Power IoT: let's exit early!", CSEM Scientific and Technical Report (2021) 49.

model with the early exit during 10 epochs. We repeat this process for different layers in the model. Figure 2 shows the test top-1 accuracy of the trained models.

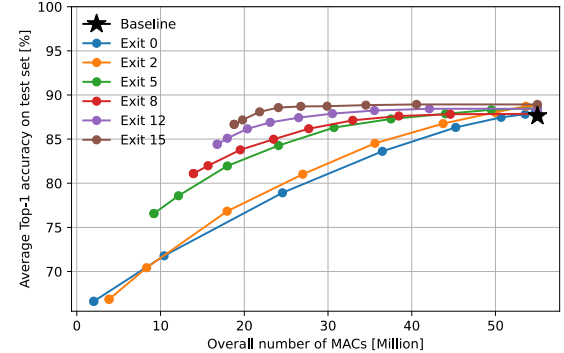


Figure 2: Test set accuracy vs. processing power for MobileNetV2 on the Visual Wake Words dataset.

The legend represents the layer to which the early exit is attached, while the horizontal axis shows the processing power in terms of multiply-accumulate (MAC) operations, which is a measure for the computational load of the model. The dots represent the result for different confidence thresholds between 0 and 1; the lower the threshold, the smaller the number of MACs, at the cost of a reduced accuracy. We conclude that early exits allow to trade-off processing power with accuracy. Moreover, for the same accuracy, they can reduce the processing power significantly. For example, exit 15 achieves the same accuracy as the baseline, with 3x reduction in number of MACs.

This configuration with exit 15 is implemented in a demonstrator classifying images from the webcam of a laptop in real-time. (Figure 3). Taking the early exit (in blue) allows to process images at a rate of 18.5 frames per seconds (FPS), 7x faster than the 2.6 FPS when taking the final exit (in red), at the cost of a lower, yet acceptable, confidence (0.7 vs. 1, approximately).



Figure 3: Performance (FPS, confidence) of person detection running on a laptop, early exit (blue, left) and final exit (red, right).

Future work will implement this technique on embedded devices, as well as investigate its appropriateness for ML models specialised for time-series data.

[2] M. Sandler, et al., "MobileNetV2: Inverted Residuals and Linear Bottlenecks", IEEE CVPR, (2018).

LoRaWAN-based IoT Solution for Real-time Monitoring of Natural Resources in Silos

J. Beysens, L. Bergamini, Y. Liechti, E. Franz, J.-M. Koller, L. André

A low-power IoT bridge using LoRa as LPWAN technology enables remote monitoring of silos in industrial environments, with a focus on agricultural commodities such as grain. The bridge collects data from various sensors (e.g., silo filling level, temperature, humidity) and connects them to a cloud service for remote management and monitoring.

In the trading of natural resources, there is a growing demand to remotely monitor the storage of commodities in real-time, used as collateral. Parameters of interest include and are not limited to 1) environmental conditions to ensure the correct conservation of goods, and 2) the filling level of silos (e.g., fraud detection). The goal of this project, realized by CSEM and its partner Argos Inspection and Technologies SA, consists of the design and development of an IoT system that allows for remote monitoring of commodities in silos. Figure 1 shows the system architecture of the developed solution.

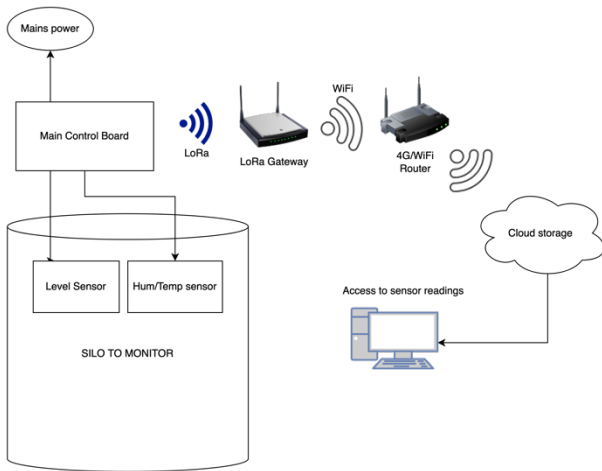


Figure 1: System architecture of the developed solution.

The main board hosts a low-power system-on-chip (SoC) interfaced with temperature, humidity, and distance sensor (up to 60 meters). It also accommodates an accelerometer to detect any movement of the board. The central processor is responsible for periodically reading the sensors and transmitting the recorded data towards a cloud service, using the onboard LoRa modem. To guarantee uninterrupted functioning and include the possibility of working in harsh and remote environments, the board can be powered both by a mains supply and with a set of AA batteries. The optimal power source is automatically chosen by the hardware; battery power is only used when the main supply is not available (not connected or because of a power outage). Hardware and software are optimized to minimize the energy consumption. Even with the galvanic isolation needed to protect the processor operation in industrial environments, the developed solution is expected to achieve a battery life of approximately 1 year based on laboratory measurements.

To monitor the data from sensors remotely and be informed of alarm events in case of problems, LoRaWAN is selected as a low-power wide access network (LPWAN) because of its 1) low energy consumption, 2) wide communication range, 3) possibility to create a private network and 4) security through 128 AES encryption [1].

A LoRaWAN network is typically comprised of end devices, gateways, and a network server. The developed board in this project acts as an end device; it gathers, encrypts, and transmits sensor data to the gateways in its range. The board is capable of detecting failures remotely, after which it sends a high-priority alert. The LoRa gateway, which is installed outside the silo, receives and forwards this data to the network server via a 4G backhaul, which decrypts and sends the messages to the application server (e.g., an IoT visualization web service). Together, these components form a wide-area private network.

Although the communication is mainly uplink from the end device to the network server, downlink messages are supported as well. These messages allow remote management by updating important parameters remotely, such as the wake-up interval or the sensor measurement interval.



Figure 2: Developed components: main board (left), level sensor (top right), and humidity & temperature sensor (bottom right).

The system was successfully deployed in a real environment in May 2022 on the premises of a major player in the milling industry in Switzerland. To test the functionality and robustness of the designed solution, sensors were installed in a cell of a concrete silo, continuously tracking the environmental conditions and grain levels. The main board was mounted outside the silo, but still indoors, and connected to a nearby LoRa gateway. The system has been running for more than two months without any interruption or anomaly.

The next steps include validating the system in additional real sites in different areas of the world, as well as the industrial development of the system. Since the main board is designed with the possibility of extensions in mind, extra sensors may be added to the system, as well as new software features.

[1] "Migrating an Internet of Things (IoT) Sensor Design to LoRaWAN", Semtech White Paper (2018).

AI-based Localization: Learning from Synthetic Data from a Genetically Guided Digital Twin

J. Beysens, S. Narduzzi, L. Bergamini

Synthetic datasets for training a machine learning model is a promising approach to reduce the need for real data. However, the simulated data should be representative of the real data. As a consequence, the tuning of the simulation parameters is critical to reproduce the real environment in the most accurate way. At CSEM we design and evaluate a genetic algorithm (GA) that proposes the optimal parameters for the network simulator.

Indoor localization is a complex problem, for which many approaches and solutions are proposed. Although new technologies like Angle of Arrival or Time of Flight promise improved precision in location estimation, the received signal strength indicator (RSSI) remains a competitive alternative that is easier to deploy at lower cost. In a previous work [1], we studied how using machine learning (ML) can improve the estimation accuracy of an emitter using RSSI. However, ML requires a large amount of labeled data to properly train it, making it unfeasible for large-scale realistic scenarios. We demonstrated that it is possible to generate usable synthetic datasets by representing the deployment area in a simulator, which are sufficient to train the ML model and in this work we show the benefits from applying GA for the optimization of the simulation parameters.

Training an ML model to localize objects in the deployment environment necessitates an accurate virtual representation of it, as any mismatch between the real and virtual environments introduces a bias and has a strong impact on the performance of the ML model. The network simulator we used (OmNET++ with the INET framework) offers a wide range of parameters that can be tuned to accurately reproduce the reality. Further, it offers the possibility of introducing obstacles like walls, closets and so on. For each wall, it is possible to specify its material, and its dimensions (length, height, and thickness), and when the simulated signal passes through a wall, its RSSI is attenuated depending on the type of walls it crossed.

Our initial analysis shows that the parameters having the most critical impact on the RSSI value of each transmitted packet are 1) the wall thickness, 2) the path loss exponent and 3) the radio transmission power. We design a genetic algorithm (GA) that proposes a new set of those parameters at each iteration. A graphical representation of the GA loop is depicted in Figure 1. In each iteration of the genetic loop (generation), the GA proposes a set of populations (set of parameter values) to the simulator, which then generates a new simulated RSSI dataset for each set. A Multi-Layer Perceptron (MLP) with 9 layers is then trained using this simulated dataset. Each trained model is then tested on a small portion of data recorded from the real environment (real test set) to provide a fitness score. The fitness scores associated with each set of parameters guide the GA for the next generation, improving the virtual representation of the environment and reducing the mismatch over time. To reduce the execution time, we distribute the simulator and fitness score calculation on 8 different docker machines, each running on 24 cores in parallel. Ideally, the loop is repeated until convergence is reached, but given the high number of parameters we decided to stop the loop manually (a future improvement on which we are currently working concerns the modification of the GA to reduce the number of parameters to

optimize). At the end of the loop, the GA obtains a set of parameters that represents the configuration of the simulator that better represents the real environment (having the best fitness score).

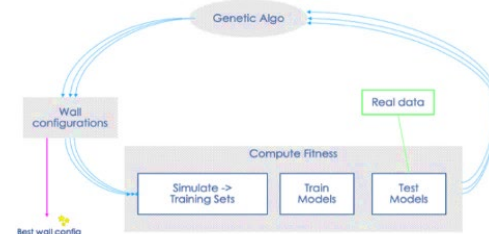


Figure 1: the genetic algorithm loop.

At this point, we train the MLP with a simulated dataset generated using this best configuration, and we use real data to evaluate the accuracy of the localization estimated by the MLP. We aim at realizing a system capable of localizing objects at a room level, which is more than enough for many applications that do not require the exact location. An estimation is considered correct if the estimated room corresponds to the room where the real emitter is placed. Table 1 compares the balanced accuracy on the real test set 1) obtained by the MLP when trained using a synthetic dataset generated using standard parameters ("Standard" column) to 2) those obtained by the same MLP but trained using a dataset obtained with the best configuration ("Best config") as suggested by the GA. We evaluate the performance using 5 different initialization seeds ("Seed"). Although we trained the model using synthetic data for the whole area to monitor, we only evaluate its accuracy for the rooms containing an emitter used in the fitness score calculation. Generalizing this to the whole area is part of future activities.

Table 1: Comparison of balanced accuracy on test set.

| Seed | Standard | Best config |
|-----------|------------------|-----------------|
| 0 | 76.53 % | 84.53 % |
| 42 | 72.43 % | 87.05 % |
| 276 | 72.45 % | 95.19 % |
| 1024 | 72.10 % | 83.78 % |
| 12345 | 79.44 % | 80.26 % |
| Avg (std) | 74.59 % (+- 2.9) | 86.23% (+- 4.9) |

We observe that the localization accuracy is increased by more than 10% on average, confirming the positive impact of the GA in the improvement of the representation of the reality in the simulated dataset. These results are extremely encouraging, and once we will reduce the GA convergence time and we generalize the MLP to work in rooms not part of the initial training data set, we will be able to obtain a reliable room-level localization solver that can be quickly deployed in any indoor environment and trained using only a small real dataset as reference.

[1] L. Bergamini, et al., "Mantis: an Indoor Localization and Navigation Framework with Machine Learning Support", CSEM Scientific and Technical Report (2021) 24.

Pilot Demonstration of RF-based Localization and Monitoring in Offshore Platforms

C. Kassapoglou-Faist, R. Berguerand, A. Restrepo Zea, M. Sénéclauze, P. Dallemande

The OffshoreMuster technology enables localisation of personnel in high-risk environments, such as offshore platforms or oil-rigs. CSEM's ultra-low power communication and localisation system was successfully tested in real scale and target environment, showing commercialisation maturity.

Oil & Gas offshore platforms are industrial towns, ranked among the world's most hazardous work environments. Personnel safety may be endangered by fire, explosion, suffocation from toxic gases, fatigue, failure of structures or extreme weather conditions. Emergency situations are unpredictable, in the midst of time pressure, high risk, ambiguous information on incident escalation, lack of real-time people location information or rapidly changing conditions. With EU Horizon 2020 FTI project OffshoreMuster [1] (OSM), CSEM and its partners propose an innovative decision support system capable of real-time personnel localisation, situational awareness and advanced incident escalation monitoring in emergency response [2].

OSM adapts and extends the person localisation technology developed for safe evacuation of passengers and crew on large cruise ships (Lynceus2Market EU project). Connected, low-cost, ultra-low power mobile devices are worn by the personnel, periodically transmitting short radio-frequency signals that are captured by dedicated base stations (gateways). A data collection infrastructure (using the Publish/Subscribe paradigm and capitalizing on Apache Kafka), processing components and an interactive, rich-featured Graphic User Interface provide a holistic view of the situation on the platform in real time (Figure 1), showing people location, movement and alerts, instant headcount etc. Localisation is based on Received Signal Strength Intensity (RSSI) and uses two algorithms (particle filtering and a simple, proximity-based one as a backup).



Figure 1: Monitoring display showing personnel in a meeting room.

Zakher Marine International offered to conduct pilot tests and a demonstration of the system in one of the company operations barge, the QMS PRIDE, at the port of Abu Dhabi (UAE). A total of 82 gateways were deployed in several areas on the barge, covering various space types (cabins, corridors, indoor and outdoor open spaces, engine room, galley, etc.). Their placement was based on know-how acquired from test deployments at CSEM premises and on RSSI signal measurement campaigns conducted beforehand. In addition, the deployment on QMS PRIDE was validated using localisation data obtained by placing mobile devices in various known positions, as shown in Figure 2.

Up to 21 OSM mobile devices participated in these pilots, a limit set by the constrained timeframe and the available personnel to run the test scenarios (the Lynceus pilots had involved over 500 crew members). The latter scenario covered manifest reporting and personnel localisation over normal, non-emergency conditions, mobile device re-assignment, mustering, missing people localisation (including overboard localisation), alerting (using alert buttons on the mobile devices) and manifest reporting over emergency conditions. In addition, a few experimental features were tested, such as presence detection in a restricted area (e.g., in the engine room) or overboard fall detection (using gateways with directional antennas).



Figure 1: Gateways (in blue) and mobiles (in orange) on a few decks.

The system showed extremely good stability throughout testing and demonstration (for over a week). Mobile device connectivity (coverage by the gateways) was very stable overall, which is key to good performance, only experiencing slight perturbations in spaces with many metallic elements (e.g., engine room) or on outer outdoor spaces. The device positions were computed at the expected rate (every 5 seconds) with only occasional position misses. Localization has performed very well in indoor areas such as cabins, offices, recreation areas, corridors and isolated outdoor areas, with a precision below 5m. In the "known position" tests, the average precision per device varied from 1.8m to 13.9m. The larger errors occurred when the mobile device signals were detected by gateways on more than one deck, or when connectivity was at times deficient (device detected by less than three gateways, i.e., when the proximity algorithm was used). Latency (measured as time from beacon emission to position calculation output) was consistently around 10 seconds (with maximum values below 20s for most devices).

OffshoreMuster marks a step-change in worker safety offshore with a good perspective for commercialization.

[1] <https://offshoremuster.com/>

[2] I. Panaretou, et al., "OffshoreMuster: An Integrated Real Time Localisation, Mustering And Evacuation Management System For

IEEE 1588 Synchronization for Embedded Devices

R. Berguerand, D. Piguet

IEEE 1588 Precision timing protocol (PTP) is a protocol used to synchronize multiple devices, typically using Ethernet frames, with high accuracy in a variety of application such as industrial automation or communication systems. CSEM implemented it on the μ 111 embedded real-time OS for distributed sensor monitoring data fusion and correlation. This new implementation allows a synchronization with a precision below the μ s when dedicated hardware is used.

PTP was defined by the IEEE1588 in 2001 and revised in 2008 [1]. PTP is regarded as an evolution of the Network Time Protocol (NTP), which has a maximum precision of 200 μ s. While GPS clocks synchronization provides better accuracy, the GPS receivers are more expensive and requires GPS signal, which is not always available. Both NTP and PTP, on other hands can be implemented relying on the available networking elements.

The precision of the protocol is determined by the clock's precision of the nodes in the network. The PTP grandmaster clock synchronizes the network and maintains the reference clock. Other nodes (sink) synchronize their clocks to the Grandmaster using the protocol. In the case of multi-hop networks, nodes can serve as intermediate master clocks, synchronized with the grandmaster clock and providing the clock to their neighboring nodes.

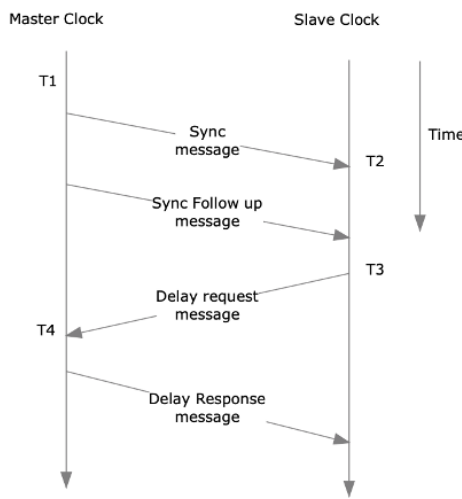


Figure 1: PTP Synchronization mechanism [2].

Sink clocks can compute and correct their offset with the master clock using a sequence of sync frames (detailed in [2]). This procedure is repeated periodically (typically each second) to correct hardware clock shift between the sink and the master. To improve the accuracy of the protocol, dedicated Ethernet transceivers use hardware timestamping, which allows the precise recording of the instant when the frame is transmitted or received. Hardware timestamping avoids irregular delays caused by frame processing or CPU usage by other parallel applications.

PTP was ported on the Cortex-M7-based STM32H743 chip running the CSEM μ 111 embedded real time OS, which runs the LwIP open-source TCP/IP stack. This processor includes an Ethernet transceiver with hardware timestamping. The PTP clock is running at 250 MHz.

[1] NIST, Introduction to IEEE 1588,
<https://www.nist.gov/el/intelligent-systems-division-73500/introduction-ieee-1588>

As a starting point, an open-source implementation PTP daemon (PTPd) [3] was ported on μ 111 and specific hardware. μ 111 and its LwIP TCP/IP stack send and receive the different PTP sync frames.

Two configurations were used to evaluate the protocol accuracy:

- One using a Raspberry Pi running a Linux operating system with a PTPd implementation serves as the clock master, and a NucleoH743 as the clock sink. The Raspberry Pi's PTP clock is a standard clock with a maximum precision of 1 μ s (1 MHz) and does not provide hardware timestamping.
- The other using two NucleoH743 (a master and a sink).

In both tests, the master and sink were connected directly through Ethernet. The master was configured to send one sync messages every second. The accuracy was measured by recording the offset between the sink and the master clock at each synchronization.

The Raspberry Pi exhibited a maximum offset of $\pm 25 \mu$ s, implying that two sinks could have a clock difference of up to 50 μ s. This offset can be explained by the drift due to the clocks of both the sink and the master. Another reason is that the Raspberry Pi does not implement hardware timestamping which introduces variable timing during the synchronization protocol.

The hardware timestamping of the two NucleoH743 allows for a maximum offset of $\pm 0.5 \mu$ s. This performance is also due to more precise clock in both devices.

In the future, the protocol will be tested on multi-hop networks to assess the impact of this topology on the protocol accuracy. Furthermore, the impact on the power consumption and the memory should also be measured on the OS.

The protocol was ported on embedded device in the scope of the SMARTWISE project that has the goal to develop a smart, miniaturized and energy autonomous wireless sensor platform dedicated to data collection for the Structural Health Monitoring System (SHMS) of future multi mission regional aircrafts. The protocol is used to timestamp data from sensor devices located throughout the aircraft, allowing for precise structural health temporal analysis and monitoring.

The SMARTWISE project has received funding from the Clean Sky 2 Join Undertaking (JU) under grant agreement No 886605. The JU receives support from the European Union's Horizon 2020 research and innovation programme and the Clean Sky 2 JU members other than the Union.

[2] EndRun Technologies, PTP-Protocol,
<https://endruntechnologies.com/pdf/PTP-1588.pdf>

[3] PTPd source code, <https://github.com/ptpd/ptpd>

3D Printing for a New Efficient Production Method of mm-Wave Waveguide-based Antennas and Components

A. Vorobyov, S. Unterhofer, O. Sereda

An efficient and affordable production method for high-precision mm-wave waveguide antennas and RF components has been developed. It is based on Additive Manufacturing (AM) and on selected post-processes such as thermal treatment, surface polishing and surface plating.

The 3D printing combined with specific post-process treatments enables the manufacturing of functional parts by an innovative approach, which has been successfully used for prototyping complex mm-wave and RF components within the Clean Sky 2 "3DGUIDE" project.

Laser Powder Bed Fusion (L-PBF) 3D printing is an Additive Manufacturing process for metal materials, building parts layer by layer, by depositing material according to the digital 3D design data. This process allows for the fabrication of parts that are difficult or impossible to be produced with traditional machining, such as high-precision mm-wave components. The selected Aluminum alloy exhibits low RF losses and allows for thin features fabrication ($160 \mu\text{m} \pm 15$) with a surface roughness of ~ 7 to $10 \mu\text{m}$ after printing (As-Built) and below 4 to $6 \mu\text{m}$ after surface treatment (chemical polishing ad metal plating). The resulting AM part's physical properties (mechanical and electrical) are approaching those of bulk material.

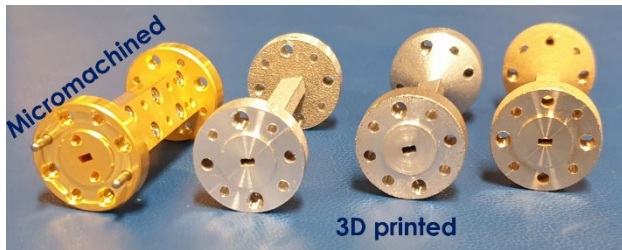


Figure 1: mm-wave (75-110 GHz) waveguide sections.

The waveguide (WG) sections have been prototyped and characterized (Figure 1) in the W-band (75 GHz-110 GHz). A printed and post-processed Al-12-Si sample performance is compared with the standard high-quality micromachined section (Figure 2).

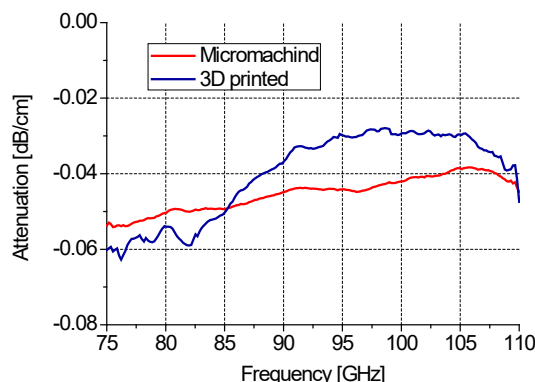


Figure 2: Measured losses in the mm-wave waveguides.

The measurement result shows that the 3D-printed WG section performs similar to or better than the micromachined one WG losses (4-6 dB/m).

The process also applies for producing complex 2D antenna arrays, such as the antenna shown in Figure 3, comprising 8 interconnected linear arrays.

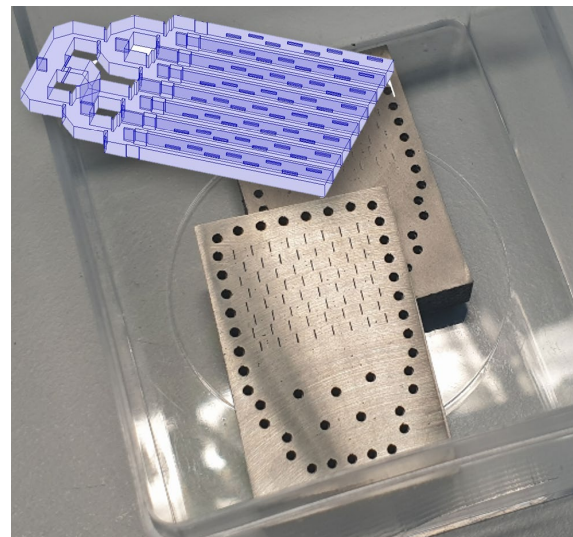


Figure 3: 3D printed 2D antenna array (central freq. 94 GHz).

The prototype of a 3D-printed phase-shifter based on waveguides is presented in Figure 4. The phase-shifter iris elements were printed directly in the WR-10 ($1.27 \times 2.54 \text{ mm}$) WG aperture. Measurement of the equivalent phase bit resolution is equal to 1.93 bit, which is close to theoretical estimation (1.96 bit).

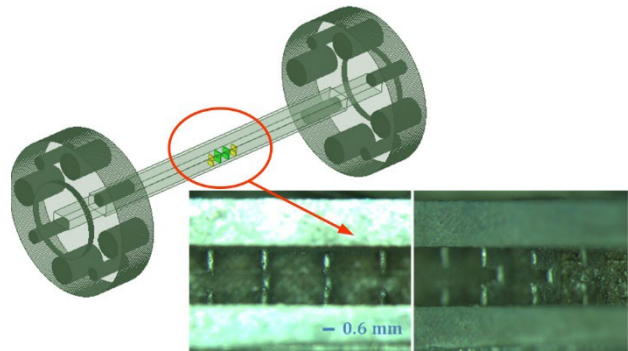


Figure 4: Phase shifter.

The design freedom provided by L-PBF technology presents many advantages in the manufacturing of micro-wave components, such as weight reduction, assembly simplification and cooling channels integration. The obtained results show 3D printing potential in manufacturing antennas with complex 3D shapes (e.g., waveguide) with reduced assembly steps and lower costs. It is particularly well suited for prototyping and high-quality small series.

This research has received funding from the Clean Sky Program under grant agreement no. 886696 and was carried out in the frame of the 3DGUIDE project (Feasibility demonstration of 3D printing for a new efficient production method of mm-wave waveguide antenna).

Embedded Wear Monitoring of Mechanical Parts

C. Hennemann, L. André, Y. Liechti, P. Nussbaum, A. Restrepo Zea, L. Bergamini, R. Berguerand

Springs are common yet critical components of mechanical devices. Failure of such mechanical parts can lead to considerable damages, costs and casualties. Their health status is however difficult to assess. CSEM has developed an extremely miniature and long lifetime IoT solution to estimate the wear of mechanical parts.

The traditional approach to handle wear of mechanical parts is to include security margins in the design and perform inspections on site to monitor aging clues. The former doesn't prevent failures from unexpected stress and the later is only economically viable for the most critical applications.

The present work proposes to retrofit mechanical parts (Figure 1) with a strain monitoring system that will provide an estimation of wear from the integral, life-long stress of the part. The solution value is to bring preventive maintenance of low-cost yet critical parts and ultimately to improve the design of parts (cost, lifetime, ...) based on the data collected during operations. The device is designed to be tightly attached to a key location of the mechanical part (here a spring) and to ensure 10 years of autonomy.



Figure 1: Concept: monitoring device (in red) attached to a mechanical part (blue spring) stressed on a test bench.

A first embodiment of the concept, based on a flat spring and only reporting strain, has been used as a demonstration platform (Figure 2) to prove the concept and test interest from end customers. It comprises a strain gauge aligned with principal stress direction. At this stage, the electronics (green PCB in transparent case) was not yet integrated. The strain gauge has been attached to the mechanical part using standard gauge adhesives. Since the adhesive is a critical factor influencing the product lifetime, a custom and more durable solution is under development by our industrial partner.

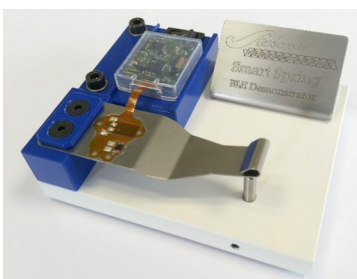


Figure 2: Initial demonstration platform.

The results obtained in a very short schedule from this demonstrator confirmed both feasibility and interest from end-customers.

During the same period, we developed a miniaturized remote sensing device able to monitor the mechanical strain and temperature to locally estimate spring aging. The estimation of wear is based on the exploitation of the Wöhler curves derived from the linear damage accumulation model of Palmgren and Miner [1]. The algorithm is implemented on local (on sensor) computing resources, improving the lifetime of operations by reducing drastically the amount of data to be transmitted (power savings), as well as the robustness of the solution when facing communication disruption (continuity of service).

A wireless connection (BLE) allows for reporting wear level, remaining lifetime, maximal stress endured and battery status to a standard terminal (smartphone or tablet). This first approach illustrates the concept in applications where an operator is required to inspect the machinery. This approach also supports the collection of raw data from the sensors in the context of laboratory use.

Depending on applications, other communication schemes of allows for automatized and remote data collection; they are based on long range communication (e.g., LoRa) or integrated within the sensing infrastructure of the end-product. In the latter case, power can be provided wirelessly for unlimited time operations.

The autonomy expected from the system (10 years at first) is not only pushing for an extremely low-power design, but also constraining the selection of the battery. Selecting and assessing commercial solutions required the elaboration of a specific test bench to explore the consumption profiles of the final system. Beyond the expected energy capacity, multiple characteristics like temperature range, self-discharge rate or admissible peak currents must be met simultaneously. A measurement campaign is presently running to assess most promising COTS solutions but also experimental samples soon to market.



Figure 3: Final form-factor prototype opened to reveal electronics.

Finally, the embedded software (firmware) requirements for an industrial implementation are addressed by the use of a proprietary a real-time operating system (RTOS) providing both ultra-low power performances and secure "over-the-air" updates of the device software, compatible with the expected lifetime of operations.

[1] "Fatigue life curve – A continuous Wöhler curve from LCF to VHCF", Rainer Wagener and Tobias Melz in Materials Testings 80 (2018).

Deep Neural Networks vs. Random Features: a Performance Comparison on an Industrial Dataset

L. Biggio, T. Bendinelli, I. Kastanis, P. A. E. Schmid

The popularity of modern Deep Neural Networks is constantly growing. Their application is widespread across several engineering fields, especially when large datasets and significant computational resources are available. However, modern deep learning techniques are often expensive in terms of computational cost and energy consumption. The design of more computationally efficient Machine Learning methods is key in the quest for increasingly sustainable and responsible AI solutions. In this paper, we study the performance of Rocket, a recently proposed method based on random features, on a popular industrial dataset. Its comparison with competitive deep learning baselines shows the advantages of Rocket in terms of the trade-off between accuracy, training time and memory footprint.

The last decade in Machine Learning research has witnessed the rise of increasingly large Deep Neural Network models, characterized by a spectacularly large number of trainable parameters. While such models have undoubtedly raised the bar of the potential of Artificial Intelligence, their training is overly expensive, energy-consuming and requires very large datasets. In times when the quest for socially acceptable technological solutions is pressing, it is apparent that the status of state-of-the-art AI methods is far from being sustainable and responsible. In the context of industrial applications of Machine Learning, deep learning models are still relatively smaller compared to state-of-the-art popular language models, mainly because the lack of large open-source datasets. Nevertheless, their training can still be quite computationally expensive and memory intensive and often requires dedicated hardware solutions. These considerations naturally pose the question on whether cheaper and faster solutions exist and if their performance are somewhat comparable to existing state-of-the-art deep-learning-based models utilized in industrial applications. In this project we make an initial first step toward a positive answer to the above question. We conduct a pilot study based on a thorough experimental evaluation of several deep learning baselines and their comparison with Rocket^[1], a recently proposed technique for time-series classification. Our results on the popular CWRU bearing dataset from Bearing Data Center of Case Western Reserve University^[2], clearly shows that Rocket can provide close-to-optimal performance with drastically reduced training time and memory footprint as opposed to the considered deep learning baselines.

Method. Rocket is based on lifting the input to a high dimensional space by means of random projections and then training a linear classifier on top of the resulting features. In particular, the approach taken by Rocket consists in generating many convolutional filters -- obtained by randomly choosing length, weights, dilation and padding among a pre-defined pool of candidates -- and then training a ridge regression classifier to perform the downstream task of interest. Despite its apparent simplicity, the method has been shown to compete favourably with several deep learning baselines, even though, to the best of authors' knowledge, its application to popular industrial benchmark datasets has never been explored so far.

Experimental Setup. We consider the CWRU dataset, and we compare Rocket with the deep learning baseline methods introduced in. The CWRU dataset is chosen for its popularity in

the Prognostic and Health Management literature and provides access to the bearing data for normal and faulty bearings. The data contains 9 different faults, and the basic task is to map input time-series into the corresponding health class. As an additional level of complexity, for each class the dataset is divided into 4 different working conditions. The goal is to train an algorithm on working condition a and test its performance on b (Task $a \rightarrow b$), to the end of assessing its generalization capabilities. For each working condition, this operations result in datasets divided into 200 sequences of 512 Fourier coefficients.

Results. Table 1 shows the results. The Baseline network consists of a 1.3 million parameter convolutional neural network specifically designed to be a competitive method for time series classification. For each task, reported are the mean and max accuracy across 5 training runs. Note that DANN, MMD, AdaBN implement Domain Adaptation techniques that make use also of unlabelled data from the test domain. Rocket and Baseline do not use such additional information and are thus disadvantaged in their generalization performance. Nevertheless, besides outperforming Baseline in most tasks, Rocket provides very competitive results with all the considered baselines. This is remarkable especially considering the approximately two order of magnitude smaller training time it employs and its dramatically lighter memory footprint.

| Setup | Baseline | | DANN | | MMD | | AdaBN | | Rocket | |
|------------------|-----------------|--------|-----------------|--------|-----------------|--------|-----------------|--------|-----------------|--------|
| | Mean | Max |
| Task 0-1 | 93.49 | 95.45 | 98.76 | 99.30 | 99.38 | 99.50 | 98.87 | 99.35 | 97.56 | 98.00 |
| Task 0-2 | 93.65 | 95.15 | 99.96 | 100.00 | 99.98 | 100.00 | 99.30 | 99.75 | 91.50 | 94.17 |
| Task 0-3 | 91.02 | 94.75 | 99.81 | 100.00 | 100.00 | 100.00 | 99.75 | 99.80 | 87.78 | 88.30 |
| Task 1-0 | 97.93 | 98.30 | 98.73 | 99.05 | 99.31 | 99.40 | 98.82 | 99.05 | 99.68 | 99.80 |
| Task 1-2 | 100.00 | 100.00 | 99.96 | 100.00 | 99.98 | 100.00 | 99.95 | 99.95 | 100.00 | 100.00 |
| Task 1-3 | 98.26 | 99.35 | 99.65 | 99.80 | 99.97 | 100.00 | 99.82 | 99.85 | 99.91 | 99.95 |
| Task 2-0 | 91.63 | 94.40 | 97.70 | 98.25 | 98.61 | 98.65 | 95.89 | 96.40 | 98.81 | 99.09 |
| Task 2-1 | 97.09 | 98.05 | 98.40 | 98.45 | 98.52 | 98.60 | 97.83 | 98.15 | 98.97 | 99.54 |
| Task 2-3 | 99.78 | 100.00 | 99.82 | 99.95 | 100.00 | 100.00 | 100.00 | 100.00 | 99.99 | 100.00 |
| Task 3-0 | 87.96 | 88.25 | 97.62 | 97.85 | 98.72 | 98.90 | 89.27 | 90.30 | 91.68 | 93.47 |
| Task 3-1 | 89.42 | 91.15 | 98.41 | 98.50 | 98.53 | 98.60 | 94.42 | 95.10 | 89.37 | 90.05 |
| Task 3-2 | 99.65 | 99.90 | 99.98 | 100.00 | 100.00 | 100.00 | 99.98 | 99.95 | 99.92 | 100.00 |
| Average | 94.99 | 96.23 | 99.07 | 99.26 | 99.42 | 99.47 | 97.82 | 98.14 | 96.26 | 96.86 |
| Train time | 84 s | | 177 s | | 266 s | | 133 s | | ≈ 2 s | |
| Memory Footprint | ≈ 10 MB | | ≈ 20 MB | | ≈ 10 MB | | ≈ 10 MB | | ≈ 10 KB | |

TABLE I
COMPARISON BETWEEN ROCKET AND DEEP LEARNING BASELINES.

In this paper, we have presented a preliminary demonstration of the potential of Rocket, a recent method for efficient time series classification based on random features, in the context of industrial applications. The results we obtained are particularly interesting considering the significant gains Rocket delivers in terms of training time and memory footprint yet providing close-to-optimal accuracy performance.

[1] A. Dempster, F. Petitjean, G. I. Webb. "ROCKET: exceptionally fast and accurate time series classification using random convolutional kernels." Data Mining and Knowledge Discovery 34.5 (2020): 1454-1495.

[2] W. Smith and R. Randall, "Rolling element bearing diagnostics using the case western reserve university data: A benchmark study," Mechanical Systems and Signal Processing, vol. 64-65, 05 2015.

Safely Applying Auto-tuning to Industrial Controllers

I. Sideris, P. A. E. Schmid, F. Crivelli

Safely auto-tuning typical control policies can have significant financial importance in the industry. This is the goal of many modern optimization algorithms equipped with theoretical safety and convergence guarantees, but, in practice, it is challenging to implement them in industrial assets. To bridge this gap, a software pipeline was designed that offers a consistent way of applying safe reinforcement learning by leveraging previous experience gathered on the setups of interest. Efficient experience transition accelerates the discovery of near-optimal and optimal solutions and strengthens safety guarantees.

Setting the control parameters of a controller is a challenging and time-consuming process. It requires significant domain knowledge and is usually done manually. Many heuristics and rules-of-thumb have been developed to facilitate this procedure and give the response its desired characteristics. However, this usually results in sub-optimal performance and can lead to hardware damages and injuries when applied to critical or unstable industrial plants.

To address and confront these problems, an automated tuning pipeline that safely finds the best gains for a given control architecture was developed. Moreover, for efficiency reasons, the amount of data needed to accomplish autotuning was kept as low as possible. This was achieved using Bayesian Optimization^[1] (BO) and harnessing all the existing prior knowledge available on the controlled plants.

BO is a black-box global optimizer that searches for the optimal solution by iteratively sampling the black-box system at its most promising locations. A surrogate model for the system is constructed with each sample, which further helps define the following sampling locations. Usually, the surrogate is a Gaussian Process (GP). The following samples are found by selecting the points that satisfy a criterion, like the maximization of the upper confidence bound, that considers the mean and the variance of the statistical model. The GP can also be used to sample unknown but mathematically defined constraint functions which can be included in the sample definition to guaranty that the system will not be driven to unstable or generally dangerous function modes.

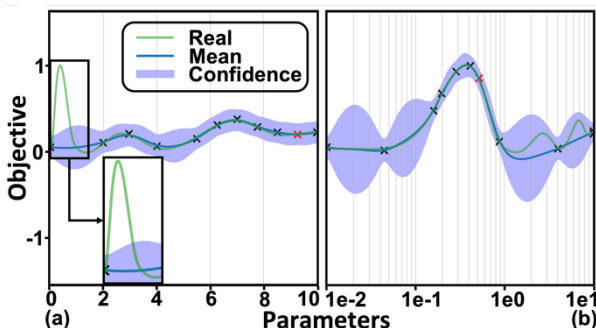


Figure 1: Plots (a) and (b) illustrate how mapping the gains helps express regularity assumptions over multiple orders of magnitude of gains, thus increasing the sensitivity of safeOpt^[3] on every scale.

Because of its agility, BO has been extensively used for various optimization schemes, especially in Safe Reinforcement learning. Some examples from the literature implementing different sampling strategies equipped with safety guarantees and fast convergence are stageOpt^[2] and safeOpt^[3]. However, both algorithms assume that the underlying GP surrogate is well calibrated and that its regularity assumptions are uniformly applicable. This is not the case for most industrial environments where significant uncertainties prevail.

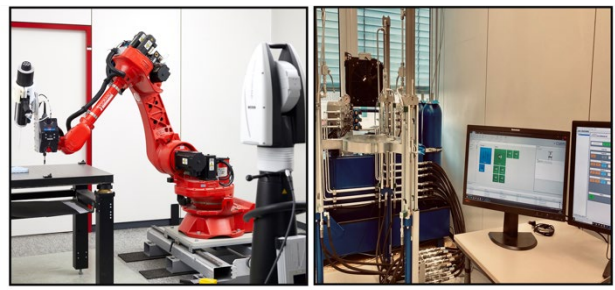


Figure 2: The two setups used to validate our framework

To ensure that the theoretical guarantees will also apply in industrial environments, a pipeline was developed that secures the well-definiteness of the GPs. As a first step, the statistical model is tuned by leveraging underlying knowledge stemming from the industrial setup. This can come in the form of data from previous operations or a simulator that can be used to provide low-fidelity data. This information is used to estimate the regularity and spread assumptions of the GP. After tuning the GP, a transformation is chosen for the optimization problem, which maps the parameter space in an image that conserves the regularity assumptions over the whole search domain. This is further illustrated in Figure 1, where the parameter space is unwrapped, forcing the sampled function to be consistent. Finally, safeOpt was used to find a solution in the transformed domain.

The pipeline was tested on two industrial rigs, one robotic and one hydraulic, as shown in Figure 2, where an 18-parameter and six 3-parameter controllers were tuned. In both cases, the optimizer quickly found good solutions for the controller gains without violating any given constraints. Moreover, tuning the model and modifying the optimization landscape also proved to accelerate the convergence of the optimizer by decreasing the number of necessary samples until reaching the optimal solution.

[1] B. Shahriari, K. Swersky, Z. Wang, R. P. Adams, N. de Freitas, "Taking the Human Out of the Loop: A Review of Bayesian Optimization," in Proceedings of the IEEE, pp. 148-175, 2016.

[2] Y. Sui and V. Zhuang and J.W. Burdick, Y. Yue, "Stagewise Safe Bayesian Optimization with Gaussian Processes" arXiv: 1806.07555, 2018.

[3] F. Berkenkamp, A. Krause, A. Schoellig, "Bayesian optimization with safety constraints: Safe and automatic parameter tuning in robotics." arXiv: 1602.04450v3, 2020.

Spot the Difference – Anomaly Detection using Neural Image Comparison

T. Schöpe, M. Russi, M. Höchmer, P. A. E. Schmid

Anomaly detection in computer vision is a well-established approach for quality inspection in the industrial setting. It does not need time consuming and error prone acquisition and labeling of anomalies as it is only trained using scenarios considered good or normal. When dealing with highly stationary environments, i.e., small part variations, stable illumination conditions, clean working environment etc., state-of-the-art anomaly detection algorithms perform decently and are often a first choice for quality inspection in production lines. Their biggest drawback however is their high sensitivity to environmental changes and need for low part variability. CSEM proposes a new method to perform anomaly detection which can be adapted to environmental changes within a single shot and can easily be trained to be robust against acceptable anomalies like illumination changes.

Anomaly detection networks are often the first choice regarding industrial visual quality inspection algorithms. These networks are trained solely on images considered as normal or good. This has two advantages: Acquiring a large quantity of images of good parts is often done far easier than acquiring images of all possible types of faults. Additionally, as all images used for training are considered as good, no time consuming and error prone labeling process is necessary. The idea of this approach is to learn how a good situation looks and then to mark everything which deviates from this as abnormal or faulty.

The nature of this procedure is that it only works well in situation where the inspected part variation is small (watch, medical) and the environment of the image is highly controllable, i.e., constant illumination and background that are shielded from external influences like sunlight, dirt, or changes in the background. In any other case these algorithms tend to drop either in precision or recall. Optimizing for a good trade-off between these two metrics can become highly challenging, if possible at all.

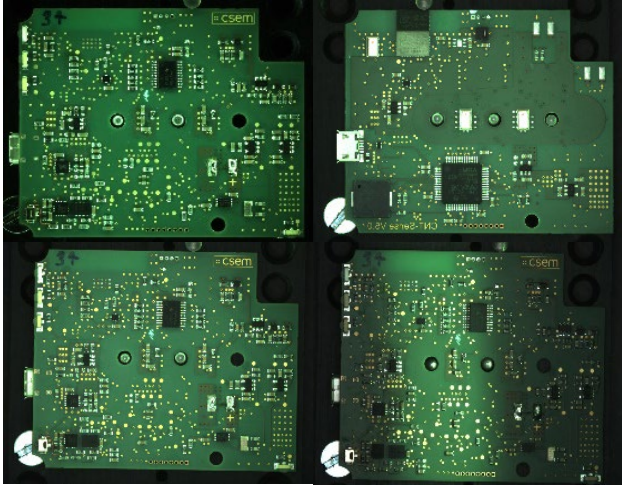


Figure 1: Circuit boards with different circuits (top) and spurious light (bottom). These lab-produced images can be used to test an algorithms performance for use cases with a high part variability and different illumination conditions.

CSEM developed a One-shot learning algorithm that tackles the weaknesses of state-of-the-art anomaly detection. The new approach is particularly attractive for make-to-order production industries or setups, where a controlled acquisition environment cannot be guaranteed, for example because of a high degree of human-machine interaction in the acquisition area. After successfully implementing a version of the algorithm within an industrial project, CSEM launched an internal research project to examine different areas of application and to bring the algorithm to higher industrial maturity.

Different use-cases are considered. One of them is the anomaly detection on circuit boards. Varying circuit designs are examined to test the algorithms robustness to part variability. Additionally, spurious light can be introduced to the setup (see Figure 1).

The algorithm's core idea is a tile-wise comparison of the test image with a given reference of a good part. A twin neural network architecture predicts for each tile-pair, if the two tiles are similar or different, i.e., faulty. This network consists of two parts: Feature extraction and comparison. For feature extraction, both the reference and the test tile run through the same neural network to extract the same feature of both images. After that, a comparator network compares the features of the tile pair to determine if the pair consists of similar samples or not. A schematic of the architecture is found in Figure 2.

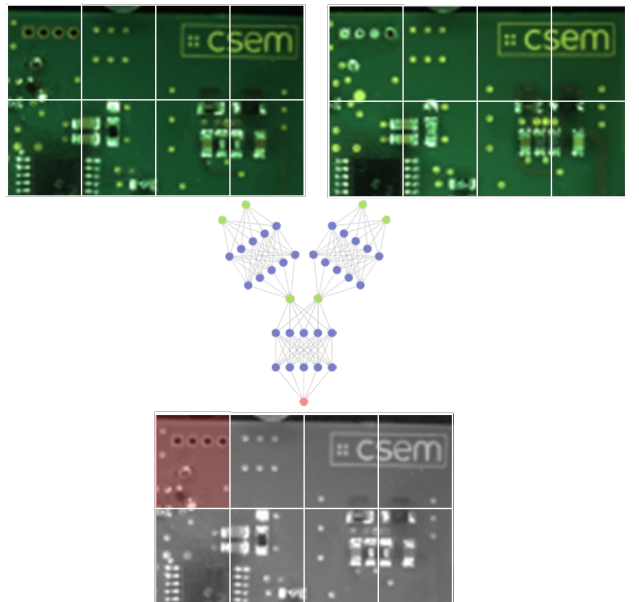


Figure 2: Schematic Neural-Image-Comparison Pipeline. The test image is compared to a reference image. The images are tiled and for each tile, the algorithm predicts if the test tile is similar to the reference.

By using a reference image to describe an image of a good circuit board, the algorithm can be trained to be agnostic to circuit designs as the design is only revealed at runtime. At the same time, the use of a reference enables robustness against environmental changes. If the background of the setup changes, it is sufficient to take a new reference image of a good part and provide it to the network. Further robustness can be achieved by training the network with multiple images of the same part taken with varying acquisition conditions. By using a test image of the same part as the reference, but with introduced spurious light, the algorithm can learn to consider a tile-pair with different illumination as similar and not as faulty.

My Chemical Romance – an AI-Chemist assisting Thermal Analysis

T. Schöpe, T. Bendinelli, C. Beyer, I. Kastanis, M. Höchemer, P. A. E. Schmid

A strong competency in materials science is indispensable in today's industries – spanning from pharma over food to packaging. A sealing ring must not become brittle, a PET bottle cannot deform, and medications need to react within the body at exactly the right time. Across the material science domain, Mettler-Toledo's Differential Scanning Calorimeter (DSC) has become an indispensable tool for many. Using a DSC however requires highly skilled and experienced chemists. Together with ZHAW and Mettler-Toledo, CSEM has developed an AI-based assistant that helps analyzing DSC measurements.

Differential Scanning Calorimetry measures enthalpy changes in samples as a function over temperature or time. These enthalpy changes arise from changes in their physical or chemical properties and are crucial to characterize a material. Mettler-Toledo provides highly precise DSC that can measure even smallest effects. However, the measurement process is only half the battle. Tracing back these changes to their actual physical or chemical roots requires highly educated and experienced chemists.



Figure 1: Differential Scanning Calorimeter. A crucible with the sample material is placed in an oven and its enthalpy changes are measured over time or temperature.

To properly analyze a DSC measurement, three things have to be identified by an expert for each effect: The effect start, the effect end and the effect type. After this identification, Mettler-Toledo's proprietary software STARE provides deeper insights, computing various material characteristics based on the expert's input.

Mettler-Toledo, ZHAW and CSEM joined an Innosuisse project to develop an algorithm which can support the experts by providing an automatic suggestion about effect start, end and type.

As DSCs are used for a vast number of different materials, from metals, plastics to food, a high number of different effect types must be differentiated from each other. Additionally, effects of the same chemical root can look completely different depending on the material type or environmental conditions. Chemists are often experts about the materials they characterize and already have a prior idea about which analysis results to expect. They use this knowledge, consciously or subconsciously, to properly analyze their measurements. This knowledge is so vast and can be so specific that it cannot simply be translated into code. A data-driven solution is necessary. However, the knowledge applied by a chemist can be so complex that extracting it from a dataset would require a very large amount of training data.

The acquisition of this amount of data showed not to be feasible. State-of-the-art simulations can only simulate measurements for the easiest of cases and real-life measurements are typically kept highly confidential by companies and therefore would have to be manually measured. The only measurements within reach were the ones available in Mettler-Toledo's databases and the ones

manually acquired during the project. A big annotation campaign was started by the DSC experts at Mettler-Toledo to annotate the available data, a highly time-consuming and challenging task. This resulted in a dataset with over 2'000 annotated measurements. While this amount is a lot regarding the cost of acquisition, it would still not be enough to confidently extract the many underlying, chemical rules from the data.

In order to cope with this fact, CSEM developed a chemistry-informed neural network. It is trained on the data but has some prior knowledge about the chemical background integrated. This knowledge has been generated and curated by Mettler-Toledo's DSC experts. This combination enables the network to make confident predictions about the effects present in a measurement despite the small training dataset. To further increase robustness of the solution, a sophisticated data augmentation pipeline has been developed to train the neural network. In addition to well established data augmentation techniques, physical knowledge about the different devices sold by Mettler-Toledo can be used to alter the existing measurements. This enables the network to ignore artefacts that might arise from the measurement device itself, which could be the newest model sold last year but as well a 20-year-old device.

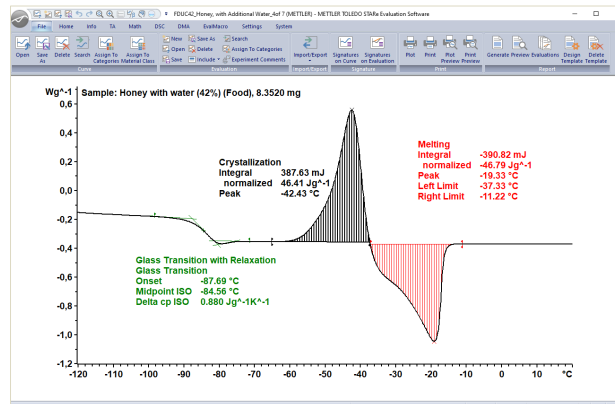


Figure 2: Example DSC-measurement. Heatflow as a function of temperature with marked phase transitions.

The developed algorithm has directly been integrated into STARE software. Newer versions of the algorithm, for example after retraining the neural network, can easily be imported without updating the software itself with a deployment methodology that has been filed for patent.

The product has reached the market in July 2022 and can be bought as AIWizard™ within the STARE software: <https://www.mt.com/at/de/home/library/videos/lab-analytical-instruments/aiwizard-video.html>

LeafEye – Robust Plant Pests' Identification and Classification

S. Widmer, V. Michel*, T. Bendinelli, M. Höchemer, P. A. E. Schmid

A rapid and reliable identification of diseases and pests is crucial for a successful crop protection in modern agricultural production systems. Especially for high value crops grown in greenhouses, the early detection of diseases and pests permits not only a more efficient control but also a reduction of the amount of applied pesticides. In the LeafEye project, CSEM developed a prototype of a portable handheld device that can detect and count invertebrate pests on leaves. This allows for early detection and precise use of pesticide. The device also provides valuable feedback on the success of the treatment.

High value crops are commonly grown in greenhouses. An infestation of pests and fungi can be devastating to a crop. If detected early, it can be well treated, and the crop saved with low costs. Currently, if a farmer suspects an infestation, a biological specialist must investigate and identify the type of problem on the leaves. The LeafEye device enables farmers to autonomously investigate the health of their crops without further external experts.



Figure 1: The LeafEye prototype.

The prototype device consists of a custom-built illumination, two high resolution cameras which are connected to a Nvidia Jetson Xavier NX system on a module. This embedded processor is triggering and acquiring the images from the cameras, processing the pictures onboard and controls the user interaction with the operator.



Figure 2: LeafEye device in use on site.

An additional, integrated GPS module stores exact geolocation along with the images. This way, the spreading of an infestation can be more accurately monitored and assigned to different sections within the greenhouses. A small screen on the back of the device gives the operator a first glance at image quality and detected problem, while a battery at the basis of the handle provides autonomy for up to 4 hours of operation.

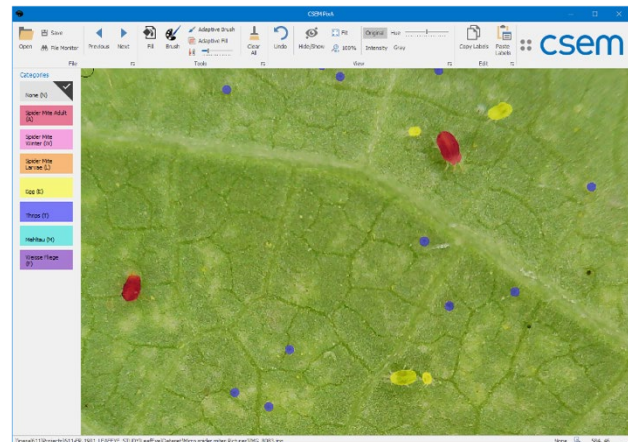


Figure 3: CSEM Labelling tool (Pixa) used by Agroscope for annotation.

CSEM's device uses a custom-made algorithm for detecting and locating different types of pests. The algorithm is based upon a Convolutional Neural Network (CNN) which has been trained to identify and localize pests from camera images. A team of experts from Agroscope collected and labeled data from a variety of pests to train the network using CSEM's labelling tool Pixa.

After numerous iterations devoted to optimizing performance, the final system can detect more than 10 different species of pests accurately.



Figure 4: The algorithm takes an image as input, then outputs a bounding box and the class of each pest detected.

The algorithm is designed to run on an edge-based computer in real-time. The neural network was optimized for embedded processing in regards of power consumption, latency and memory usage. The device is portable and can be used for indoor and outdoor applications. It grants direct access over WiFi using a web interface for updates and logging.

The device provides valuable insights for greenhouse operators and pest control professionals alike. Agroscope is currently discussing potential partnerships to industrialize this proof of concept further.

* Agroscope, Conthey, Switzerland

Industry Guard

M. Russi, M. Höchmer, P. A. E. Schmid

The cost-effective monitoring of industrial plants is a technically demanding task. The plants are widely arranged, inhomogeneous in design and exposed to harsh environmental conditions. The brute force approach corresponds to total monitoring using countless IIoT sensors and Big Data analysis. This approach is costly and complex. The approach presented here tries to enable a superhuman with simple technical tools, which supports the shift workers in the simplest way. Together with Schweizer Salinen and Schweizer Zucker, a generic, portable, anomaly detection platform for pump and hydraulic system failures, consisting of three different sensors, was developed, and tested.

What have the two opposites – salt and sugar in common? Beside that they are found in all kitchens, their productions have many similarities. There is raw material from where the substance gets subtracted (salt in brine / sugar in sugar beets) and there is a crystallization process with lots of energy involved. While the sugar production only runs between October and December, salt is produced all year round. However, in both cases, downtime is catastrophic and costly. One common reason for downtime is failing of pumps. If the viscosity is getting too thick, pumps can easily fail (overheat, burn windings, destroy gearbox), leading to stopping the whole process, flooding the production, or plugging the pipes, which takes days to recover. Standard sensor, like flowrate sensors, failed in the past and are too expensive to be installed everywhere. To early identify these conditions and prevent disasters, Schweizer Salinen and Schweizer Zucker teamed up with CSEM to assess the possibility of a generic, portable, platform to identify pump anomalies. This platform consists of different sensor to evaluate their potential in an industrial setup:

Infrared camera

With the infrared camera, the temperature of the pump and its surroundings can be monitored with the idea that a potential failure changes the working point of the pump and therefore influencing the temperature. Different regions are defined which are analyzed separately, but also altogether over a time of multiple days.

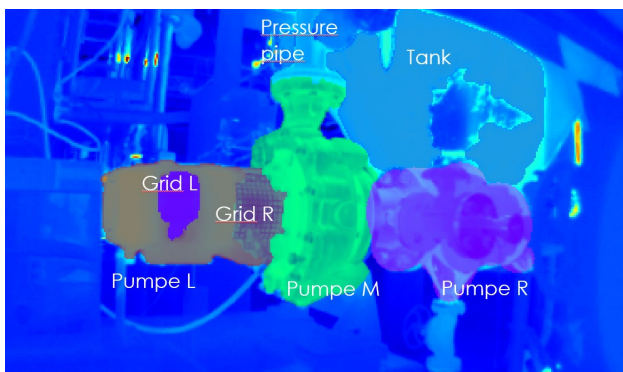


Figure 1: Pump temperature regions.

High frequency microphone

People with lots of experience detect early malfunctions just by listening to the sound and vibrations. A high frequency microphone with frequency range up to 150 kHz and 1 MHz sampling rate is being used to mimic this human sense. The spectrum above 20 kHz is hidden for humans but enables the system to hear metal on metal. The signal is transformed into a spectrogram for frequency analysis and processes with a neural network to identify outliers.

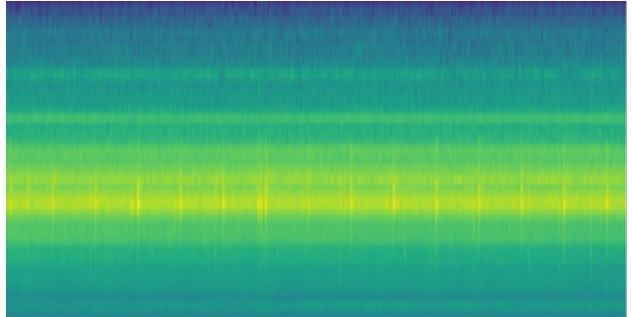


Figure 2: Pump spectrogram of 10s sound (0-150kHz).

Frequency extraction from images

As third sensor, a standard industrial camera operates in a special mode. By defining a small region of interest, the camera can be driven as a high-speed camera. This allows to acquire an image area of 128×128 pixels with over 2'000 frames per second. On all image features are extracted and matched. With tracking these features over the frames, the frequency of their vibration can be calculated. In contrast to the microphone approach, where much higher frequencies can be reached, the location of the actual vibration is adding addition information for subsequent anomaly detection tasks.

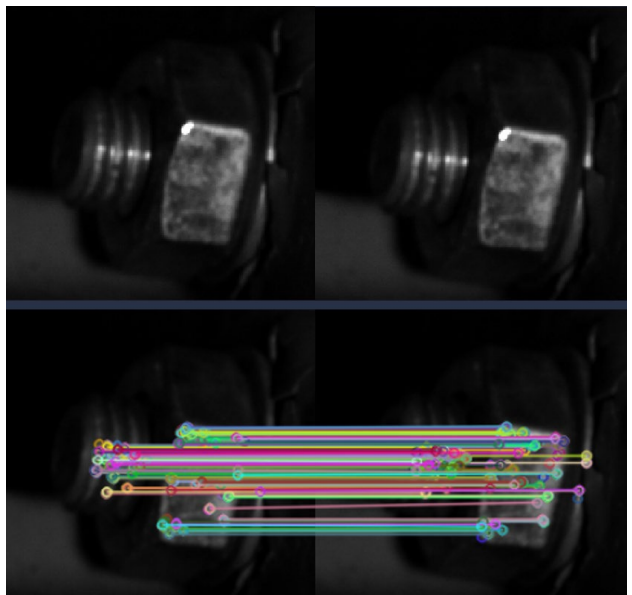


Figure 3: Screw and bolt for two subsequent frames (top); Matched features between the two frames (bottom).

With all three sensors, data is being acquired with healthy pump state as well as simulated failures, such as thickening of the underlying fluid. In the next phase all three sensors will be fused into one neural network as well as evaluating their industrial potential for harsh environment.

Smartphone-based Blood Pressure Measurement during Induction of General Anesthesia

M. Proen  a, G. Hofmann*, G. Bonnier, A. Lemkaddem, U. Christen**, J. F. Knebel**, P. Schoettker*, M. Lemay

Hypertension, or chronically high blood pressure (BP), is the leading risk factor for cardiovascular diseases. With close to 1.5 billion hypertensive individuals globally, the need for accessible and accurate means of screening and monitoring BP is key in fighting this pandemic. Smartphones, which are widely available, could play a leading role. We have previously validated the accuracy and precision of the OptiBP® smartphone app (Biospectral, Switzerland), which runs CSEM's cuff-less BP monitoring algorithm. We present hereafter the trending ability of the app when tested in a very dynamic environment.

High blood pressure (BP), or hypertension, is the main risk factor for cardiovascular diseases and the root cause for approximately ten million deaths each year. By 2025, the number of people suffering from hypertension is expected to reach 1.5 billion. Early detection, prevention, and management of hypertension are essential, but require accessible and accurate measurements.

Smartphones represent widespread, readily available devices for mobile health, with over one third of consumers owning one worldwide. With the potential to measure a photoplethysmographic (PPG) signal at the fingertip using the phone's camera and the recent advances in PPG-based BP monitoring [1], the potential of the approach is huge.

We have previously validated our patented cuff-less PPG-based BP monitoring algorithm [2] during general anesthesia induction using PPG signals from a standard pulse oximeter[3]. Using smartphone-derived PPG signals acquired via a dedicated app (OptiBP®, Biospectral, Switzerland), we have recently demonstrated [4] its compliance in terms of accuracy and precision with the requirements of the ISO 81060-2 standard. In the present study, our aim was to evaluate its trending ability (capability to track changes in BP).

In a clinical study [5] (ClinicalTrials.gov identifier: NCT03875248, Arm 1) in 121 patients scheduled for an elective surgery necessitating general anesthesia, we evaluated the trending ability of our BP algorithm applied to smartphone-derived PPG signals compared to invasive radial BP. One-minute PPG signals were measured every 2 minutes with the app and one BP value was estimated from each one-minute PPG signal. The corresponding synchronous reference BP value was calculated by averaging the invasive BP measurement during that minute. Clinically significant BP changes of at least $\pm 15\%$ occurring between one-minute windows were automatically identified in the PPG and invasive data. The trending ability was assessed via four-quadrant and polar plots, using the concordance rate (CR), the angular CR at $\pm 30^\circ$, and the angular bias and standard deviation (SD) as trending performance metrics.

Figure 1 shows the results for mean BP. The upper panel (four-quadrant plot) depicts good concordance (CR = 95%). The lower panel (polar plot) confirms said concordance (angular CR at $\pm 30^\circ$ of 92%), with an angular bias $\pm SD$ of $-2.0^\circ \pm 17.2^\circ$. By analogy with non-invasive cardiac output monitoring techniques, good trending ability can be claimed with CR > 90-95%, angular

CR at $\pm 30^\circ$ > 90-95%, and angular bias < $\pm 5^\circ$ [6]. Similar figures were obtained for systolic BP (CR = 91%, angular CR = 90%, angular bias and SD = $-2.2^\circ \pm 18.8^\circ$) and diastolic BP (CR = 93%, angular CR = 92%, angular bias and SD = $-0.2^\circ \pm 17.1^\circ$).

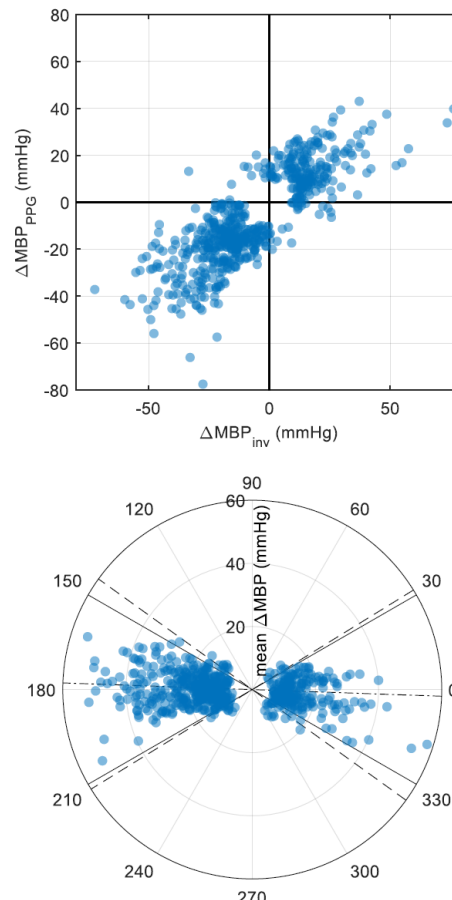


Figure 1: Four-quadrant plot and polar plot demonstrating the trending ability of the cuff-less BP algorithm for mean BP (MBP). The dash-dotted line in the polar plot depicts the angular bias, and the two dashed lines the 95% confidence interval.

Our study demonstrates that our cuff-less BP solution, applied to smartphone-derived PPG signals, can accurately track significant BP changes in challenging hemodynamic conditions. Being ISO 81060-2 compliant in static conditions, the smartphone implementation of our BP solution may become a key tool in the prevention and management of hypertension.

* Department of Anesthesiology, Lausanne University Hospital and University of Lausanne, Switzerland

** Biospectral SA, Lausanne, Switzerland

[1] M. Proen  a, et al., in: J. Sol  , R. Delgado-Gonzalo; The Handbook of Cuffless Blood Pressure Monitoring. Springer, Cham, 2019.

[2] M. Proen  a, et al., WO 2016138965 A1, 9th of September 2016.

[3] Y. Ghamri, et al., Anesth Analg, 130(5):1222-1233, 2020.

[4] J. Degott, et al., Blood Press Monit, 26(6):441-448, 2021.

[5] G. Hofmann, et al., J Clin Monit Comput, in press, 2022.

[6] L. A. Critchley, et al., J Cardiothorac Vasc Anesth, 25:536, 2011.

Introduction of Artificial Intelligence in Cardiotocography Interpretation for the Clinical Use

A. R. Soltani, J. V. Zaen, C. Aguet, H. Sigurthorsdottir, A. Radan*, M. Lemay

Cardiotocography is among the most important medical surveillance methods, particularly for the assessment of the fetal state during labor. Yet, its conventional subjective interpretation mainly depends on the observer's experience which can lead to different interpretations of a same situation. In this article, we present how we have overcome this well-known issue at CSEM by a close collaboration with the Inselspital Bern. We have taken the advantage of Artificial Intelligence to devise a smart system capable of interpreting the cardiotocograms and provide accurate estimation of the pH level of the fetus (as a strong biomarker of hypoxia) as well as the detection of fetal hypoxia.

Cardiotocography (CTG) is the main medical surveillance method used to assess the fetal state during labor. As fetal hypoxia remains an important cause of neonatal morbidity and mortality, the question of suboptimal intrapartum surveillance is still omnipresent in obstetrics. Whereas the main goal of CTG is to prevent poor neonatal outcomes like stillbirth, neonatal acidosis or hypoxia, its impact has been widely discussed ever since its introduction in the late 1960s. CTG interpretation strongly depends on the observer's experience, thus, intra- and interindividual differences in interpreting the CTG are a long-known issue. This offers a suitable background for the use of artificial intelligence (AI) in CTG interpretation, following the resolutions that have occurred in fields of cardiology and radiology. In the literature, there are a few studies such as Petrozziello-2019 [1] and Cömert-2019 [2] who tried to predict fetal hypoxia using AI-based methods on CTGs. Such studies focused only on the prediction of hypoxia and have not provided any estimation of pH values.

In this work, we have designed a hybrid method based on i) digital signal processing and conventional machine learning (DSP), and ii) deep learning models (DL) to estimate the pH level of the fetus and the predication of fetal hypoxia using CTGs. The hybrid method takes the advantage of both DPS and DL methods by providing the pH values as the weighted average of the results of DSP and DL methods. For the DSP method, we have developed several physiological features to represent CTGs and various models (e.g., Bayes, support-vector machine, decision tree). In addition, we have devised and optimized a convolutional neural network (CNN) in the DL method.

The proposed method has been evaluated on a large-scale clinical data consisted of around 14000 CTGs recorded by Inselspital. After a careful data cleaning and screening process, around 6000 CTGs with pH values ranging from 6.7–7.6 have been used to evaluate the method. However, this work is still ongoing, and more data inclusion is expected. As the validation strategy, the data has been split into 60-20-20% portions as the training, validation, and test sets. Table 1 compares the performance of the methods based on DSP, DL, and hybrid for the detection of hypoxia as well as the estimation of pH values.

The results (Table 1a) show that the hybrid method is able to detect hypoxia with an accuracy of 76%. The specificity of the hybrid method is slightly higher than the sensitivity which shows that the method is a bit biased toward the negative class (not

hypoxia). One reason for this might be the imbalanced nature of the training dataset. Comparing the results of DSP, DL, and hybrid methods, the hybrid method is able to keep a proper balance between the sensitivity and specificity and provide a more reliable method. Another important point is the poor sensitivity of the DL method probably due to having limited number of samples, especially for the positive class (samples with hypoxia), in the training set. Compared to the literature, the proposed hybrid model has achieved comparable results where slight differences can be observed, probably since these works have used different and more limited datasets for their evaluations. The results of Table 1b suggest that all three models have almost similar performance in the estimation of pH with MSE, RMSE, and MAE of 0.01, 0.07, and 0.05, respectively.

As future prospective, it has been planned to add more data (around 3500 samples) to the database to make it more suitable for the training of the models, especially for the DL-based models. A bigger dataset would allow better optimization and training of the models and would provide further improvement of the results.

Table 1: Performance of the proposed methods for the detection of hypoxia and estimation of pH level in comparison with the literature.

| a) Hypoxia detection | | | | | | |
|----------------------|--------|-------------------------|------|------|------|--|
| Reference | Method | Model | Acc. | Sen. | Spe. | |
| [1] | DL | CNN | - | 58 | 85 | |
| [2] | DSP | kNN, decision tree, SVM | - | 77 | 93 | |
| CSEM | DSP | Bayes | 72 | 69 | 73 | |
| CSEM | DL | CNN | 77 | 31 | 82 | |
| CSEM | Hybrid | Bayes - CNN | 76 | 63 | 78 | |

Acc: Accuracy, Sen: Sensitivity, Spe: Specificity,
kNN: k-Nearest Neighbour.

| b) pH estimation | | | | | |
|------------------|--------|---------------------------|------|------|------|
| Reference | Method | Model | MSE | RMSE | MAE |
| CSEM | DSP | Support vector regression | 0.01 | 0.07 | 0.05 |
| CSEM | DL | RNN | 0.01 | 0.07 | 0.06 |
| CSEM | Hybrid | Bayes - CNN | 0.01 | 0.07 | 0.05 |

MSE: Mean Square Error, RMSE: Root Mean Square Error, MAE: Mean Absolute Error

This work was partly funded by Canton of Bern. CSEM is thankful for their support.

* Fachärztin FMH Gynäkologie und Geburtshilfe Oberärztin, Inselspital Bern, Switzerland

[1] A. Petrozziello, C. W. Redman, A. T. Papageorghiou, I. Jordanov, A. Georgieva (2019). Multimodal convolutional neural networks to detect fetal compromise during labor and delivery. IEEE Access, 7, 112026-112036.

[2] Z. Cömert, A. Şengür, Ü. Budak, A. F. Kocamaz (2019). Prediction of intrapartum fetal hypoxia considering feature selection algorithms and machine learning models. Health information science and systems, 7(1), 1-9.

Limitation of Calibration-free PPG-based Blood Pressure Estimation

C. Aguet, J. Van Zaen, M. Proen  a, G. Bonnier, M. Lemay

Photoplethysmography (PPG) is a promising technology for non-invasive and cuffless blood pressure (BP) monitoring. In this context, CSEM has recently explored a feature learning approach to automatically extract relevant information from the PPG waveform and estimate BP accordingly. To date, a calibration procedure remains crucial to reach clinically acceptable accuracy. Although this is a weakness of most PPG-based BP monitoring technologies, this research demonstrates the limitations of a calibration-free model and confirms the importance of a calibration to obtain an accurate estimate of absolute BP.

Persistently high blood pressure (BP) or hypertension is a serious condition that greatly increases the risk of developing cardiovascular diseases (CVDs). It affects about one third of the adult population. However, a major concern is the absence of noticeable symptoms in half of the cases. Identifying abnormal BP fluctuations could help in the early detection and prevent eventual complications of hypertension and related CVDs.

Recent advances in acquisition and signal processing have opened new opportunities in photoplethysmography (PPG)-based technologies for vital sign monitoring. The study of the PPG pulse morphology is promising for non-invasive, cuffless and continuous BP monitoring. Previous attempts have mainly focused on features based on conventional pulse wave analysis. However, such approaches are limited by the computation complexity of some features and the requirement of expert knowledge. CSEM recently proposed a feature learning model leveraging convolutional layers to extract key representations from an ensemble average (EA) PPG pulse along with its second derivative (acceleration plethysmogram, APG) to estimate systolic (SBP) and diastolic BP (DBP) accordingly. We demonstrated its ability to extract relevant information related to BP from PPG and APG pulses^[1], as well as its ability to adapt to unseen data from different target populations and PPG sensors^[2].

Subject-specific characteristics or various external factors can affect the PPG waveform morphology. These include tissue composition, age, height, sensor type, contact pressure, or measurement site. A calibration of the system usually helps to cope with the inter-subject variability induced by such factors. As illustrated in Figure 1, the aforementioned model incorporates a calibration procedure based on a single initial PPG measure and its associated BP reading.

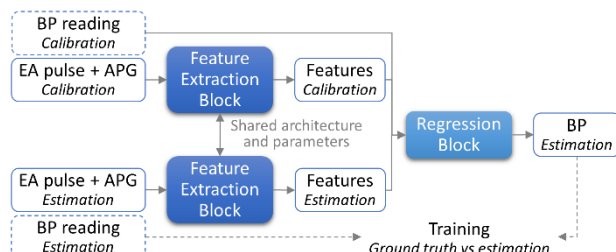


Figure 1: Model structure with an initial PPG-BP calibration measure.

To date, such a procedure remains crucial for achieving clinical acceptable accuracy. However, calibration is often a weakness

[1] C. Aguet, et al., "Feature Learning for Blood Pressure Estimation from Photoplethysmography," Annu. Int. Conf. IEEE Eng. Med. Biol. Soc., vol. 2021, pp. 463–466, Nov. 2021.

[2] C. Aguet, et al., "Generalization Capability of a Neural Network for Blood Pressure Estimation from Photoplethysmography," 2022 Computing in Cardiology (CinC).

of PPG-based BP monitoring technologies, as requiring a measure with an approved standard complicates the measurement procedure. Therefore, we study this limitation by implementing a calibration-free model (Figure 2), while keeping the same structure of the feature extraction block and the regression block as in the previous model. The proposed model is evaluated against the invasive reference in terms of accuracy (bias) and precision of agreement (standard deviation of the error).

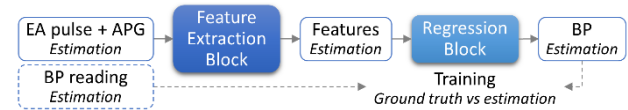


Figure 2: Model structure without calibration.

Our research is conducted on a subset of the open-access VitalDB database^[3] containing arterial BP from an invasive catheter and PPG from a fingerclip sensor (1493 patients and 166'966 EA pulses). The recordings are from patients admitted at Seoul National University Hospital (Republic of Korea) that underwent non-cardiac surgical interventions (NCT02914444 at ClinicalTrials.gov).

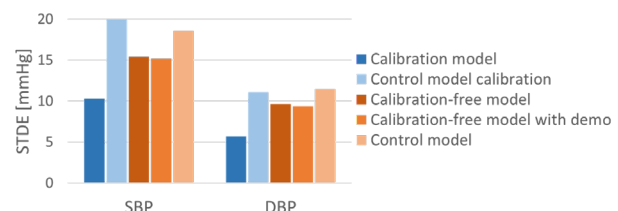


Figure 3: Standard deviation of the error in the test set for SBP and DBP.

Good agreement is found between the proposed PPG-based approaches and the invasive reference, with negligible biases (~1 mmHg). When comparing the calibration and calibration-free methods in Figure 3, the results show that the initial PPG-BP measure helps to improve the algorithm performance in providing absolute BP. It allows for a reduction in standard deviation of the error (STDE) in the test set of approximately 33% for SBP and 47% for DBP estimation. The calibration-free approach might be too limited to fully characterize the inter-subject variability. Furthermore, the addition of demographic information, such as age, height, weight, or gender (calibration-free model with demo) might not be sufficient to reduce the impact of individual physiology.

[3] H.-C. Lee, et al., "Vital Recorder—a free research tool for automatic recording of high-resolution time-synchronised physiological data from multiple anaesthesia devices," Sci Rep, vol. 8, no. 1, p. 1527, Dec. 2018.

Optical Heart Rate Monitoring – Continuous Improvement Strategies

C. Moufawad El Achkar, P. Renevey, M. Proen  a, M. Gerber, P. Theurillat, D. Ferrario, M. Lemay

Optical heart rate monitoring (*oHRM*) has become a staple in today's wearables. Measuring heart rate in daily life is challenging: algorithms must track pulses at rest, during rhythmic activities (e.g., walking, running, biking), and non-rhythmic activities (e.g., typing, cooking). Accurately measuring heart rate requires a robust algorithm that can handle these different use cases in real-time. At CSEM, the development of *oHRM* algorithms has undergone continuous improvement and development for the past 2 decades, keeping up with and anticipating user needs in the realm of physiological tracking. In this report, we describe our continuous improvement strategies and the most up-to-date results of our *oHRM* library.

CSEM's work on optical heart rate monitoring (*oHRM*) goes back to the early 2000s, with the first patent on PPG granted in 2001 [1]. As a main pillar of CSEM's Digital Health activities, *oHRM* is used in different fields ranging from lifestyle to sports to medical applications. Consequently, the maintenance of CSEM's *oHRM* algorithm library became a must to ensure high accuracy with respect to commercially available devices.

The *oHRM* algorithm library was developed for low-power embedded, real-time applications [2]. To cover the widest possible array of use cases, the algorithm extracts information from photoplethysmography (PPG) and accelerometer signals, as shown in Figure 1. The library fuses the classification of physical activity (including movement rhythmicity) and PPG signals to output instantaneous heart rate (HR) values.

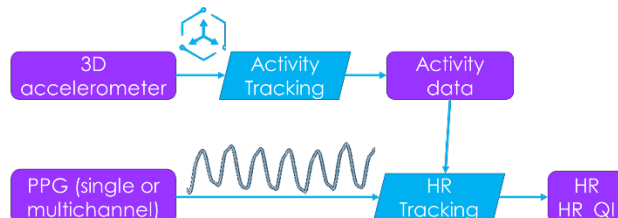


Figure 1: *oHRM* algorithm block diagram.

The *oHRM* library is validated on a large database consisting of more than 740 hours of simultaneous PPG/accelerometer and ECG (electrocardiogram) data obtained from 391 subjects. The database includes a wide range of activities: walking, running, biking, skiing, daily activities, and sleep. The ECG-derived heart rate serves as the reference for comparison.

Over the years, the library has undergone several improvements to ensure high accuracy in widespread use cases, especially during sports and activities of daily life. Therefore, strategies were put in place to automatically track these improvements. The sequence shown in Figure 2 describes this process: when an improvement is identified, the corresponding code development is pushed to a source control management system that performs code verification. Then, the statistical performance of the library's HR output is verified against ECG reference data to ensure that the modifications improve the results. Finally, computation costs and memory footprints are evaluated (Table 1).

Table 1: *oHRM* library computational and memory requirements (RAM: Random Access Memory, KIPS: kilo-instructions/s).

| RAM | Flash | KIPS | KIPS_MAX |
|------|-------|------|----------|
| 6 kB | 30 kB | 10.5 | 13.5 |

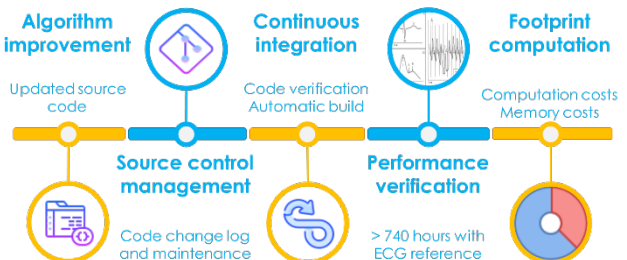


Figure 2: Continuous improvement strategies applied to *oHRM*.

Recently, the following improvements were made on the library:

- Removal of double beat detection at low frequencies
- Stability improvement during activity transitions and sports
- HR estimation improvement during rhythmic activities (walking, running, biking)
- Improvement of HR convergence time

The most recent algorithm performances against ECG reference are shown in Table 1. The performance metrics, especially for lab and outdoor, reveal a decrease in mean absolute error and increase in reliability.

To conclude, CSEM's *oHRM* technology is undergoing constant improvements to maintain high performance and anticipate novel use cases and wearable users' needs. The current results exhibit low errors and high reliability that are perfectly suited to embedded, real-time HR tracking on commercial devices

Table 2: *oHRM* algorithm performance. MAE: Mean Absolute Error, Reliability: % of results < 10 bpm error, both in as mean±standard deviation. Lab and outdoor activities mainly include sports, whereas daily activities may include any type of activity. Bold: results after implementing the improvements.

| | Lab | Outdoor | Sleep | Daily activities |
|-----------------|-----------------------------|-------------------------------|-----------------------------|-------------------------------|
| #subjects | 87 | 146 | 117 | 41 |
| #hours | 72.4 | 123.3 | 483.5 | 62.3 |
| MAE (bpm) | 4.5±2.1 4.3±1.9 | 6.3±5.1 6.1±4.8 | 1.6±1.0 1.6±1.0 | 4.7±3.2 4.8±3.3 |
| Reliability (%) | 89.6±7.1 90.1±6.6 | 83.0±18.2 83.6±17.3 | 97.8±2.4 97.8±2.5 | 87.9±12.2 87.3±12.9 |

[1] C. Verjus, R. Vetter, P. Celka, P. Renevey, "Portable equipment for heart rate measuring and monitoring," EP1374763, Sep. 26, 2007 [Online]. <https://patents.google.com/patent/EP1374763>

[2] R. Delgado-Gonzalo, J. Parak, A. Tarniceriu, P. Renevey, M. Bertschi, I. Korhonen, (2015), Evaluation of Accuracy and Reliability of PulseOn Optical Heart Rate Monitoring Device. In Conf Proc IEEE Eng Med Biol Soc (pp. 430–433).

Compact Long-term 8-channel Electroencephalography with High Functional Sensitivity using Cooperative-sensor Technology with Dry Electrodes

G. Yilmaz, M. Rapin, C. Sainz Martínez, R. Soltani, M. Crettaz, R. Delgado-Gonzalo, M. Lemay, O. Chételat, K. A. Schindler*, J. Jorge

The ability to monitor brain activity from multiple head locations during daily life activities, outside the lab, could bring crucial value to neuroscientists and clinicians. CSEM is exploring its cooperative-sensor technology to enable wearable, long-term, high-quality electroencephalography with 8 channels.

The ability to monitor brain activity with tools such as **electroencephalography (EEG)** in a seamless, long-term manner during daily life activities outside the lab/clinics could prove highly valuable to neuroscientists, clinicians and patients. However, **wearable EEG** is technically challenging for several reasons: (i) a high signal-to-noise ratio is required to measure electrical brain activity, (ii) the presence of hair makes it difficult to achieve good electrical contact, and (iii) the presence of wires and components on the head can be cumbersome and stigmatizing.

Building on its past experience in wearable systems for cardiac and muscle electrophysiology, CSEM has recently developed **ULTEEM**, a highly compact single-channel wearable EEG system that is beginning to demonstrate excellent signal quality in areas such as sleep monitoring. Nonetheless, certain applications, such as the study of epileptic spike propagation, network activity and connectivity, require monitoring multiple head locations at a time, as in so-called **multi-channel EEG**.

In this work, CSEM explored the feasibility and advantages of its **cooperative-sensor technology** to develop a compact multi-channel EEG system with high signal quality, low sensitivity to noise perturbations and low wire density (Figure 1). The system was implemented with 8 sensors connected by a 2-wire parallel bus, and a compact control unit to supply the sensors with power and synchronization signals, and to store measurement data. A dedicated app was developed to control the device via Bluetooth. The sensors were designed with standard snap connectors to allow compatibility with diverse electrode types. Two sensor configurations (i.e., positions) were considered: "**Wake**", with the sensors uniformly arranged in a ring around the head, and "**Sleep**", focused on frontal and fronto-temporal regions (Figure 1).

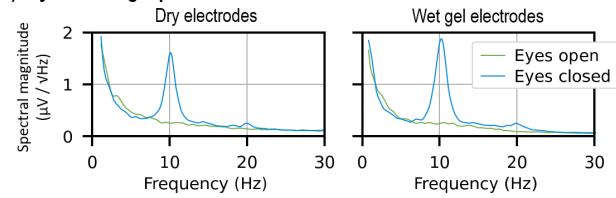


Figure 1: EEG prototype, with two different configurations ("Wake" and "Sleep"), here shown with dry electrodes (pin-type for hair, flat for skin).

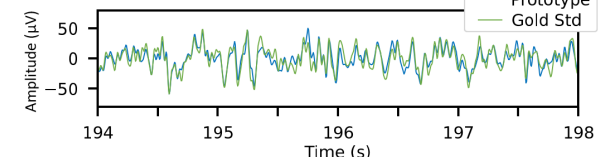
Once tested for electrical safety, the system was tested in human volunteers for signal quality and functional sensitivity, as well as for the feasibility of EEG recordings with dry electrodes. In a first study focused on the **electrodes**, 4 participants were recorded in the "Wake" configuration while undergoing an alternated eyes open/closed protocol (15 s alternations) – known to increase

alpha wave power (8–12 Hz) with eyes closed compared to open. The protocol was run using either dry electrodes (SoftPulse from Datwyler; pin type for posterior, flat type for anterior regions) or wet gel electrodes (NG Gelrodes, Neuroelectrics). Overall, both electrode types allowed a clear detection of alpha modulation (Figure 2a). On average for the group, the baseline noise observed with dry electrodes around the alpha peak was only 16% higher than with gel, while the peak amplitude was comparable.

a) Eyes-closing alpha modulation



b) Comparison to gold standard



c) Oddball frontal modulation

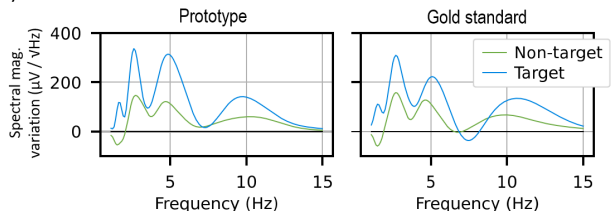


Figure 2: EEG signals recorded from human volunteers using different electrode types (a), and a concurrent gold-standard system (b,c).

In a second study focused on **functional sensitivity**, 2 participants were recorded with both the new prototype ("Sleep" configuration, dry electrodes) and a gold-standard commercial device (64-ch BrainAmp from Brain Products, passive wet gel electrodes), simultaneously. Besides eyes open/closing, an auditory oddball protocol was also run, where pure tones were played in succession – either a lower pitch (termed "non-target", more frequent) or a higher pitch ("target", rare). Overall, the signals measured by the prototype were highly similar to those of the gold standard (Figure 2b), with correlations of 0.89–0.98. Both systems showed similar modulations in the frontal brain response to target versus non-target stimuli (Figure 2c), namely an increase in theta waves (4–7 Hz), as reported in past studies.^[1]

Altogether, the results obtained so far suggest that cooperative sensors can capture meaningful features of brain activity with high signal quality and low sensitivity to noise, even with fully dry electrodes. This project is conducted in close collaboration with Inselspital, Bern, and is partly funded by the Canton of Bern. CSEM thanks them for their support.

* Department of Neurology, Inselspital, SWEZ, Switzerland

[1] Cahn, et al., 2013, <https://doi.org/10.1093/scan/nss060>

ICARUS – a Wearable Platform for Voice-as-a-Digital-Biomarker Applications

G. Yilmaz, M. Crettaz, N. Bonzon, V. Schaffter, J.-A. Porchet, J. A. Lahera Perez, M. Frosio, A. Falhi, M. M. Doss*, O. Chételat

Vocal biomarker research has a huge potential of scalability: today almost all personal devices are equipped with microphones, and they are available to the majority of the public. Clinical validation is an indispensable step before diagnostic technologies appear in our daily lives. ICARUS device aims at providing a complete solution to run large-scale clinical studies: an easy-to-use, modular system capable of acquiring relevant physiological signals, as well as voice, at a quality equivalent to the gold standard references readily used in the clinic for diagnostic purposes.

Digital biomarkers extracted from human voice hold a potential to significantly improve public and individual health. Voice can be acquired by personal devices and the same devices can be used to provide rapid diagnostics or report the progression of a disease to the clinicians. Today, however, the lack of clinical validation remains as a major challenge impeding the deployment of such technologies. Clinical validation requires collecting voice along with clinically relevant measurements (e.g., electrocardiogram, breathing patterns, etc.) on large patient cohorts – and thus requires easy-to-use and -deploy solutions. To address this need, CSEM, in collaboration with IDIAP, developed the integrated sensing platform, ICARUS, which synchronously measures multiple physiological signals and records speech.

ICARUS can measure (i) 1-lead electrocardiogram (ECG), (ii) transthoracic impedance (IMP), (iii) phonocardiogram (PHG), (iv) activity parameters (ACC) based on a 3-axis accelerometer, and (v) record speech. ICARUS device was envisioned and developed with maximum tunability options to allow fast deployment in clinical studies addressing different use cases. More explicitly, the device supports multiple sampling frequencies and resolutions for each signal. Keeping the demand of edge computing in mind, ICARUS device was equipped with an ARM Cortex-M4 processor.



Figure 1: ICARUS device resting on its docking station.

ICARUS device (Figure 1) comprises a measurement unit, a reference sensor, and a 1-wire connection between these two sensors. Thanks to CSEM's proprietary technology (EP2101408), the 1-wire connection does not have to be shielded nor insulated to acquire medical grade ECG. This feature simplifies the assembly and reduces production costs. The sensors can be recharged via the docking station which also allows downloading the recorded sessions to a PC via USB. The sensors can be clipped onto a generic chest belt or a sport bra using the flaps equipped with magnets. The magnets also serve to self-align the sensors to the docking station to ensure a reliable electrical contact during recharging and downloading.

All parts of ICARUS device in contact with the skin are manufactured using appropriate biocompatible materials.

The electrodes are fabricated with medical grade 316L stainless steel and are then over-molded in the housing part (medical ABS) touching the skin. The sensing contact for the phonocardiogram acquisition (electronic stethoscope) is produced with medical grade silicone. The cable connecting the two sensors has a medical PVC outer jacket. Finally, a medical grade epoxy resin is used to glue the top and bottom parts of the housings.

Acquired signals (Figure 2) are recorded on an on-board memory and a down-sampled version of them is transmitted to the tablet (or any other portable device) by means of Bluetooth Low Energy (BLE) communication. An FCC/RED certified BLE module (ANNA B-112, u-blox, Switzerland) is used to ensure compliance with electromagnetic compatibility requirements. On the portable device side, an application was developed (running on Android v11 or newer) to display the signals (ECG, IMP, ACC, PHG, Speech) real-time. Moreover, the application provides additional information such as connectivity status of devices, sampling rate of signals, and battery/memory autonomy. Real-time clock on the ICARUS device is automatically set via the Android application. This feature allows timestamping the signals with a universal internet clock, thus providing a means to synchronize the signals with other devices used in the clinical data collection.

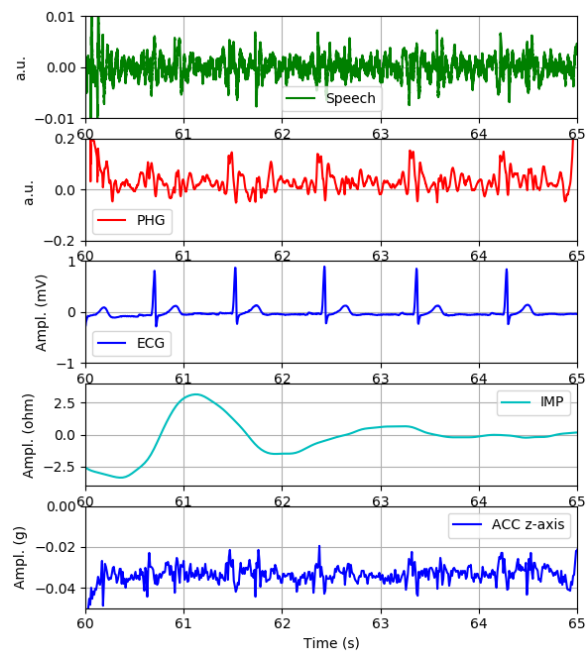


Figure 2: Signals acquired by ICARUS device (position: sitting; a deep breathing at the beginning and then tidal breathing).

ICARUS device is currently used in two studies for validation: stress evaluation and estimation of hypoglycemia. This work was partly funded by Canton of Bern. CSEM is thankful for their support.

* IDIAP Research Institute, Martigny, Switzerland

Lung-monitoring Wearable with Low-power Sensors Seamlessly Integrated in a Garment

B. Sporrer, M. Pons, K. Badami, C. Meier, M. Rapin, B. Bonnal, G. Yilmaz, O. Chételat, N. Bonzon, I. Frerichs*, E. Kaimakamis **, J. Wacker

Respiratory diseases like chronic obstructive pulmonary disease or lower respiratory infections rank among the top causes of death worldwide. Traditional surveillance schemes with intermittent disease follow-ups by physicians are not efficient enough at preventing exacerbations. In the EU project WELMO, comfortable vests with seamlessly integrated low-power sensors were developed to continuously monitor the health status of the lungs through electrical bioimpedance and chest sound measurements. Their performance was successfully verified and validated in benchtop tests and pilot clinical studies.

Lung diseases are classically monitored in clinical settings using stationary or portable approaches (e.g., chest radiography, spirometry, auscultation). WELMO developed and tested sensor vests for remote monitoring of the lungs. Each vest contains 18 sensors which record chest sounds and bioimpedances for electrical impedance tomography (EIT), a non-invasive medical imaging modality. Designers of wearables face three main challenges when integrating sensors in garments: (1) electrically connect the sensors to each other (2) power the sensors with a small battery for long-term measurements (big batteries reduce the wearing comfort); (3) integrate the sensors in the garment so that users perceive no difference to ordinary clothing. Challenge (1) has been solved with CSEM's patented cooperative sensors (CS), a solution which allows connecting a multitude of bio-signal sensors with one or two wires only while at the same time not compromising the signal quality. Connecting biosensors with one or two wires only is far from trivial, since the same wire(s) simultaneously convey multiple electrical impulses, whose amplitudes differ by magnitudes. Employing CS, WELMO tackled challenges (2) and (3) by developing ASICs which reduce the sensor volume by a factor of ~3 and the power consumption by a factor of ~20 when compared to the sensors built with discrete electronic components. As shown in Figure 1 the small sensor size enables their seamless integration in a garment.



Figure 1: WELMO harness containing 18 sensors. Inset: Side view of 2 of the ultra-flat sensors. The packaged ASIC is 6×6 mm small.

The ASIC (die size: 1.8×2.2 mm) amplifies the bio-signals as well as communicates with and harvests power from a central recording and powering unit. The die is produced in a mature 180 nm mixed-signal CMOS process, which offers both low-cost production and sufficient performance for a mostly analog circuit working at frequencies up to 1 MHz.

For EIT, the ASIC must be able to both inject an AC current into the electrode and measure the resulting potential of the electrode versus the ground node ("Fabric connection B" in Figure 2) at defined times of the imaging sequence. Both operations need to be performed while maintaining a very high impedance on the electrode terminal. The signal current injection is optimized for high impedance and additionally decoupled by an external

capacitor to avoid DC leakage. The receiver uses as a first input stage a unity gain buffer, which connects the high impedance input of the buffer to the electrode. The digital state-machine, which is synchronized to the central unit, activates and controls the current sources in the injection circuit and the operation of the receiving chain. All functions of the ASIC have been successfully verified in benchtop tests.

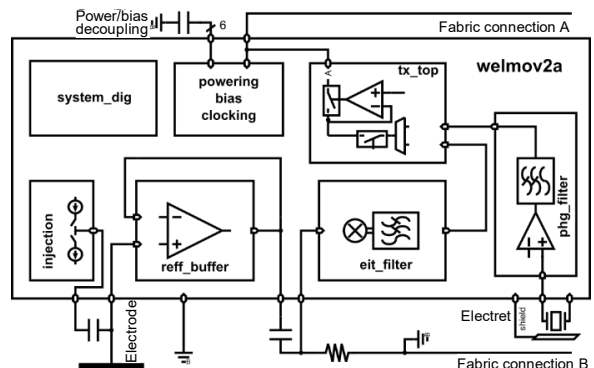


Figure 2: ASIC block schematics and external components. system_dig: digital state machine; tx_top: transmission; phg_filter: sound filter.

In addition to the ASIC, CSEM also developed sensors with discrete components and integrated them in vests (Figure 3). The WELMO sensor vests were validated in two pilot clinical studies which confirmed the WELMO concept (e.g., plausible EIT images present in > 80% of study participants) and highlighted its great potential for long-term monitoring of lung function.

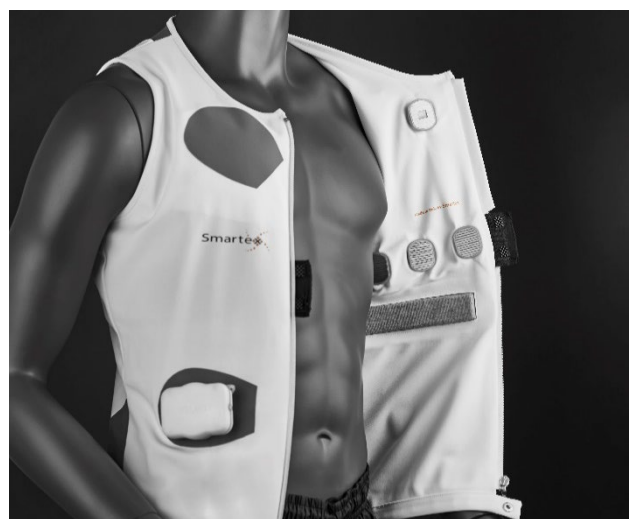


Figure 3: WELMO vest with sensors made of discrete electronics components.

This work was funded by the European Union (Grant 825572).

* Department of Anaesthesiology and Intensive Care Medicine, University Medical Centre Schleswig-Holstein, Kiel, Germany

** 1st ICU, "G. Papanikolaou" General Hospital of Thessaloniki, Greece

A Benchmarking Solution for Edge Devices

S. Narduzzi, D. Favre, L. A. Dunbar

There has been a rapid development of dedicated deep learning inference platforms in the last few years. Today, the deployment of models on hardware is highly fragmented in terms of technology, tools, and usability in contrast to the software libraries for deep learning algorithms. In order to accelerate the uptake of this hardware CSEM has developed a pipeline for automatic deployment of neural networks on different platforms. Here the performances of 3 different edge platforms are compared.

Edge computing is a key tool in harnessing the possibilities of artificial intelligence. Compared to the cloud, edge computing offers lower latency useful for real-time application and connectivity independence, such that there is no need of infrastructure and no transmission of sensitive data, allowing improved security and privacy-preserving applications. However, what may be the most impactful advantage of edge computing, which is as yet little exploited, is its potential in ultra-low-power applications. Ultra-low-power allows always-on IoT devices for seamlessly integrated intelligent systems. Creating edge-based IoT devices often requires limited hardware resources, both in terms of power and on-device memory. Today's intelligence is mainly based on Deep Learning (DL) networks which are power and memory hungry. This conflict has resulted in several emerging technologies and platforms to perform efficient inference at the edge.

Established companies are targeting the IoT market by creating ultra-low-power processors (Intel Loihi, STM32 Cortex-M4), but there are also several other innovative platforms such as DynapCNN and Kendryte K210 specialized for deep neural network inference with minute power budgets. The specialized nature of the platforms requires platform-specific software tools, making the deployment of one neural network (NN) model on several platforms cumbersome, and creating a barrier to technology adoption. Moreover, the lack of hardware standardization coupled with the necessary customization of the software makes it difficult to compare and thus choose the best technology for a given use-case.

To remove this barrier, we must facilitate access to platforms to non-hardware experts. Indeed, the success of DL is essentially linked to the acceleration provided by graphical processing units (GPUs). Currently, only a very small proportion of users have mastered the CUDA programming language used by most GPUs. In most DL libraries, mobilization of the necessary resources can be called in a single command line, without the user having to understand the technology behind it. This kind of single instruction would empower the data scientists in the porting the DL to edge devices.

CSEM has developed a simple tool to deploy NN on specific platforms, allowing the comparison between platforms and the selection of the best hardware for a given application. As an example, a convolutional NN was deployed on 3 different platforms: the STM32 Cortex M4 from ST Microelectronics, the DynapCNN event-based processor from SynSense, and the standalone board Kendryte K210 from Canaan. The selected network was a LeNet-5 architecture trained on MNIST and tested on the first 1000 samples of MNIST. For the DynapCNN processor, the images were transformed to spiking time-series^[1]

and the accuracy was recorded for the first prediction and entire time-series.

Table 1: Inference results on the selected platforms.

| Platform | Kendryte K210 | STM32L4R9 | DynapCNN |
|-------------------|---------------|-----------|------------------------|
| Weight format | float-16 | float-32 | int-8 |
| Size (KB) | 94.2 | 359.2 | 90.5 |
| Accuracy | 97.23% | 98.26% | 94.07% 98.79% (99.09%) |
| Latency (ms) | 54.17 | 80.82 | 36.23 41.3 (294.9) |
| Energy (μ J) | - | - | 144.5 |

The STM32L4R9 was tested on both float-32 and int-8 representation (using post-training quantization). With int-8 precision, the STM32L4R9 was the fastest to compute synchronous frames, while DynapCNN provides the best result with 98.79% of accuracy using only the first spike, and 99.09% using the entire spike simulation sequence.

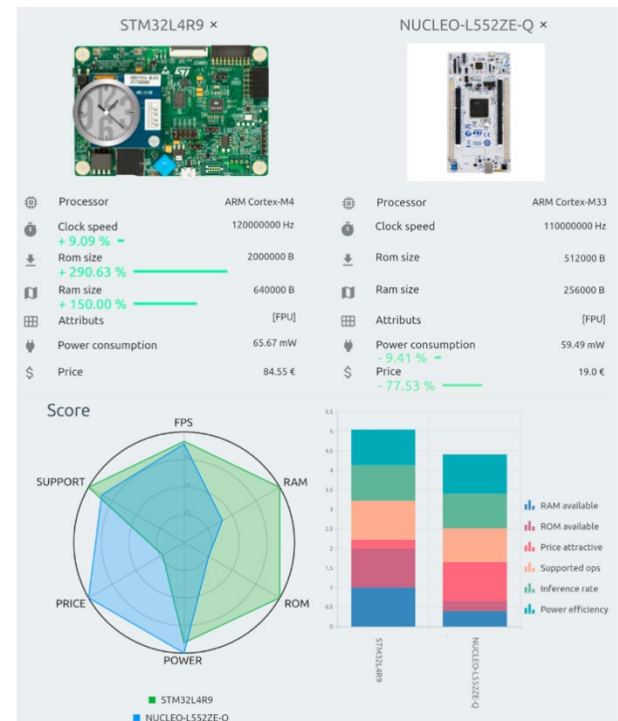


Figure 1: Benchmarking tool for comparison of devices.

To make the deployment of neural networks easier on different devices, CSEM is working on making the library public and on the development of a visualization tool presented in Figure 1. These tools will initially be made available to the partners of the European project ANDANTE, and will then be released to the public in order to help harness the full potential of machine learning for edge devices.

^[1] S. Narduzzi, D. Favre, N. Pazos, L. A. Dunbar, "Deploying a Convolutional Neural Network on Edge MCU and Neuromorphic

Hardware Platforms" (2022) <https://doi.org/10.13052/rp-9788770227902>

Deep Learning Based Detection of Intrauterine Growth Restrictions in Piglets

R. Ruggeri *, M. Dia, L. A. Dunbar

Intrauterine growth restriction (IUGR) is defined as the impaired development of the mammalian foetus or its organs during gestation. It is a major problem in pig production with substantial economic effects on farming. In this work, we develop a non-invasive deep learning-based model that is able to detect IUGR using a full body approach and outperforms current visual inspection based on head morphology.

One of the main economic drivers in pig production is the number of pigs produced per sow per year. The increasing litter sizes observed in modern pig breeds have led to an increased percentage of piglets being born undersized and exposed to different degrees of intrauterine growth restriction (IUGR)^[1]. Early detection of IUGR in piglets is essential to minimize its negative effects and improve the intervention tools in place. In pigs, IUGR results in lower birth weights and a higher brain-to-organ weight ratio due to the "brain-sparing" survival mechanism. A simple on-farm assessment of piglets based on weight and head morphology is usually used to identify IUGR (see Figure 1). However, recent veterinary studies show that such assessment does not represent sufficient phenotypes to reliably detect IUGR compared to invasive methods that consider the association between the brain and other internal organs^[2].

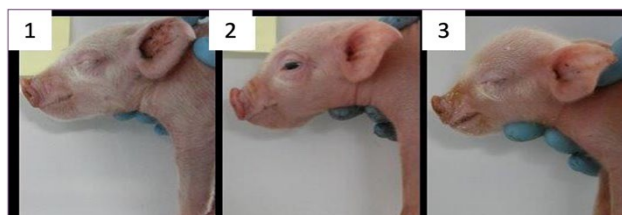


Figure 1: Expert labeling of piglets using visual inspection of head morphology. Score 1, 2, and 3 corresponds to healthy, mild IUGR, and sever IUGR piglets respectively.

In this study, we use computed tomography (CT) scan imaging as non-invasive method to assess the brain-to-liver weight ratio in new-born piglets in order to accurately identify the IUGRs. A deep learning model is then developed to correlate this ratio to visual characteristics of the head shape and body form obtained using profile images of the piglets.

Images of 311 newborn piglets were taken for this study using RealSense camera D435i placed at 40 cm from the piglets. Each piglet was positioned in a hammock and several frames were taken for the whole body with the camera moving from the right lateral side to the top of the piglet. For each piglet we applied two different labelling strategies:

- CT scan images were acquired using a 64-channel multi-slice scanner (Siemens Emotion Duo CT). From these images, the volumes of the brain and the liver were extracted. Using pre-calculated density of the two organs, we compute the brain and liver weights from the volumes extracted by the CT scan images and assess the brain-to-liver weight ratio for each animal. A cut-off value, which is represented by the median plus one standard deviation of the population, is then used to label our piglets into normal and IUGR (see Figure 2).

* University of Bologna (Italy), Agroscope (Switzerland)

^[1] C. F. Hansen, et al., Intrauterine growth-restricted piglets defined by their head shape have impaired survival and growth during the suckling period (2018). Animal Production Science 59, 1056-1062.

- Each piglet included in the study was given a score according to the morphological characteristics of its head (see Figure 1). These characteristics consist of dolphin-like shape of the head, bulging eyes, hair without direction of growth, and wrinkles perpendicular to the mouth. The scores were assigned by two different experts.

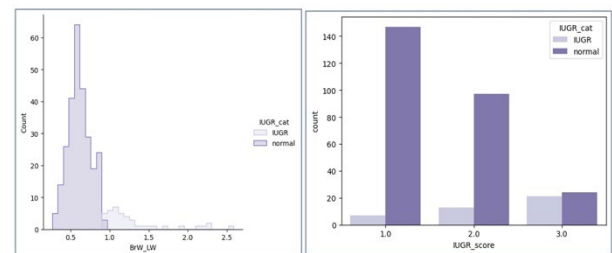


Figure 2: Histogram showing the distribution of brain-to-liver weight ratios with a cut-off value of 0.94 for normal vs. IUGR categories (left). Breakdown of the brain-to-liver binary categories with respect to the scores assigned by experts after visual inspection.

The exploratory data analysis suggests that the diagnosis based on the head morphology is not sufficient. Figure 2 shows that almost half of the piglets which were assigned with a score 3 by an expert because of their head shape, were normal according to their brain-to-liver weight ratio. Furthermore, some of the piglets assigned with the score 1 showed an increased brain-to-liver weight ratio and were assigned to the IUGR category.

After preprocessing the image data (cropping, resizing, outlier removal, data augmentation), a convolutional neural network, which takes as input one frame for each piglet and gives as output a binary classification into IUGR or normal category, was trained. Three convolutional layers of kernel size 3 followed by average pooling were used. Furthermore, batch-normalization was applied to regularize the network and stabilize the training with Adam optimizer. Due to the class imbalance, the cross-entropy cost function was adapted to penalize further the misdetection on the minority class (i.e., IUGR). Moreover, the results were cross validated over 5 runs in order to obtain statistically robust performance. Our model yields an accuracy of 90% on the test data and outperforms visual inspection.

Future investigations will increase the size of the dataset which will reduce the overfitting and improve the generalizability of our model. More data will also increase the input space where a multi-input network can be trained based on various acquisition angles and hence improve the overall performance.

^[2] F. Felicioni, et al., Intrauterine growth restriction: screening and diagnosing using animal models, (2019). Anim Reprod. 2020 May 22;16(1):66-71.

SCA-resistant Implementations of Elliptic Curve Cryptography in Embedded Secure Software

D. Vizár, F. Valencia, L. Besseau, A. Duc

An adversary with physical access to a device might use side-channel attacks (SCA) to recover secret keys used by a cryptographic implementation being executed (ab)using correlation between the key and a physical characteristic, such as power consumption. Implementations resisting SCAs are important in embedded applications exposed to such adversaries. Secure software (SW) implementations allow legacy devices to be retrofitted with SCA resistance. Here a SW, SCA-resistant implementation of elliptic curve cryptography has been developed and tested.

Elliptic-Curve Cryptography (ECC) is based on the mathematics of so-called elliptic curves over finite fields. ECC can be used for encryption, digital signature, key exchange, and other, advanced cryptographic applications. ECC yields the smallest overhead in both the ciphertext/signature size and computational complexity of all public key cryptography today, making it especially suitable for constrained devices. Side-channel attacks (SCA) use the influence an implementation and its inputs have on measurable physical processes in a device to break a cryptographic algorithm. For instance, power consumption generally depends on the handled data (notably the private key). SCA thus target the implementation, bypassing the mathematical hardness of cryptography. A naked-eye inspection of a device's power trace sometimes reveals information about internal data for "text-book" implementations (SPA, Simple Power Analysis). Noise and basic defenses can be defeated by statistical methods using multiple traces (DPA, Differential Power Analysis, CPA, Correlation Power Analysis). If a clone device is available, it is possible to characterize the power consumption, and then to find the best fit for attack traces using the characterization (Template attacks). The two main classes of countermeasures against SCA rely on adding noise to hide the leakage signal, or on breaking the relation between physical variables and secret data. The former can be done by *shuffling*, i.e., randomizing the execution of the code, while the latter is typically done by *masking*, i.e., transforming a function into a functionally equivalent operation with randomized data. Scalar multiplication is the most complex operation underlying most ECC schemes. Typically, a secret scalar (key) is multiplied with a public point on an elliptic curve and the goal of an attacker is to identify the bits of a secret scalar.

Table 1: Performance in clock cycles (measured with $5 \cdot 10^5$ executions).

| Implementation | Mean clock cycles | Overhead |
|---|-------------------|----------|
| MbedTLS | 366.325 | x1 |
| Double-and-Add | 1232.977 | x3 |
| Montgomery ladder | 1670.904 | x4 |
| Exponent 2-splitting | 3364.6 | x9 |
| Exponent 3-splitting | 5393.6 | x14 |
| Random interleaving | 5568.461 | x16 |
| Randomly interleaving + Randomized projection | 5852.538 | x17 |

In this work, the scalar multiplication has been implemented using different technique and with SCA protection strategies, both from literature [1] and custom. For the underlying finite field arithmetic, the low-level routines of mbedTLS [2] have been used. These implementations have been elaborated, with performance benchmarks in Table 1. *Double-and-Add*: One of the simplest scalar multiplication algorithms, it is a loop over of the scalar (key) bits with a conditional operation dependent on each bit's value; it is vulnerable to SPA and DPA. *Montgomery ladder* is a loop over scalar bits with no conditional operations. It is robust against timing attacks but vulnerable to DPA. *Exponent n-splitting* is. Montgomery ladder with scalar (exponent) masking, each mask share requires a Montgomery ladder computation and is robust to SPA and DPA. *Randomly interleaved Montgomery ladder with exponent splitting* is proposed in this work, here the loops of individual shares are randomly interleaved to counter template attacks. The side-channel security has been tested by collecting power consumption traces of the implementations running on the nRF52840 (ARM Cortex M4) using the ChipWhisperer USB oscilloscope, then applying statistical T-test and χ^2 -test methods, measuring the statistical dependence between the public inputs, the secret scalar and the power traces, the statistical test being computed per-sample in the traces. Figure 1 shows the results of specific T-test (using traces obtained with random public points and random secret scalar, grouped by a particular bit of the scalar) for randomly interleaved Montgomery ladder. The absence of samples outside of the red lines indicates there is no leakage with 3000 traces.

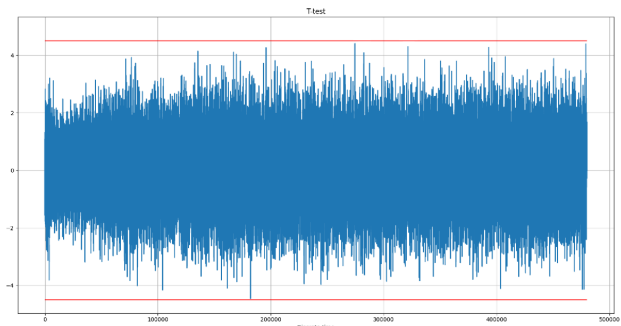


Figure 1: T-test Randomly interleaved Montgomery ladder (3000 traces).

SCA-protected implementations of ECC can be used to retrofit side-channel security to existing systems, notably legacy embedded devices. Tested implementations allow the user to choose a protection strategy that delivers the desired trade-off between security level and acceptable overhead.

[1] J. Fan, X. Guo, E. De Mulder, P. Schaumont, B. Preneel, I. Verbauwheide, "State-of-the-art of secure ECC implementations: a survey on known side-channel attacks and countermeasures," in 2010 IEEE International Symposium on Hardware-Oriented

Security and Trust (HOST), Jun. 2010, pp. 76–87,
doi:10.1109/HST.2010.5513110.

[2] MBedTLS. <https://www.trustedfirmware.org/projects/mbed-tls/>

Applications of Artificial Intelligence in Side-channel Security

D. Vizár, F. Valencia, L. Meier

Side-channel attacks (SCA) allow an attacker to extract secret keys used by a nearby device by observing its physical characteristics, such as the power consumption, when running cryptographic implementations. Embedded devices are often exposed to such adversaries, especially in the internet of things (IoT). Avoiding such attacks requires an (in)security analysis of the implementation of cryptography used. Here, a Python package of SCA harnessing Artificial Intelligence (AI) has been implemented to aid in assessment of embedded SCA security, which goes beyond the state of the art.

Side-channel attacks (SCA) use information leaked through a measurable physical variable, such as power consumption, of a device running cryptographic algorithms, breaking the security of implementation rather than the mathematical security. Profiled attacks use a clone of the target device to precompute a model of data-consumption relation. Unprofiled attacks use generic data-to-power models, e.g., Hamming Weight (HW). Machine learning (ML) techniques can be used in profiled and unprofiled attacks. For profiled attacks, a model is trained, predicting an intermediate value of a cryptographic algorithm that depends on (a part of) the secret key from profiling traces. In the classification phase, the model assigns intermediate values to attack traces, which in turn are used to recover the most probable key bits. For unprofiled attacks, a multitude of models is trained, using attack traces to predict an intermediate value computed based on every possible guess for the attacked key bits. The model with the best learning performance (accuracy or sensitivity) suggests the corresponding key hypothesis is correct. SCA using ML defeats certain SCA defenses and outperform other SCA methods.

A Python package implementing the prominent state-of-the-art ML SCA attacks [1] has been developed. Package structure (Figure 1) facilitates the extensibility and reusability to enable adding new implementations and attack strategies with minimal coding time.

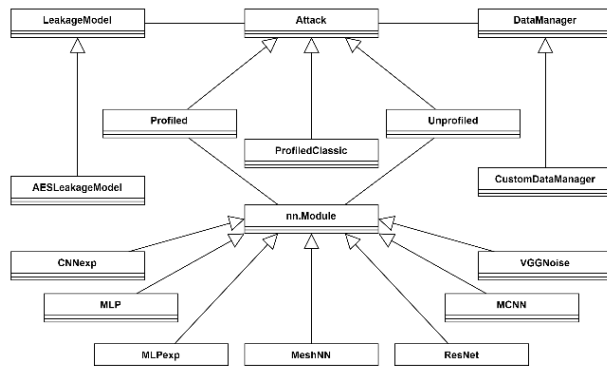


Figure 1: Class diagram of the ML SCA package.

One of the critical points in neural network training datasets is the balancing between classes. When HW is used as power model, the classes are imbalanced. A newly discovered solution for the set unbalance lies in modifying the way the softmax function (mapping output neuron weights to probabilities) is normalized. Instead of normalizing class-wise (so-called "dim 1"), the input-wise (or else trace-wise, so-called "dim 0") normalization has been made and tested experimentally. The experiments confirm dim 0 to have the following effects. *Improve profiled attacks with unbalanced datasets*, reducing the number of epochs necessary for an attack to converge, and even

outperforming other balancing techniques. *Avoid the training penalty due to the initial bias caused by the random seed in profiled attacks with balanced datasets*. *Improve the success rate of unprofiled attacks*. Figure 2 shows a comparison between attacks with dim 0 and 1, in terms of the rank of the correct key hypothesis suggested by the model (0 = best) as a function of the number of epochs needed.

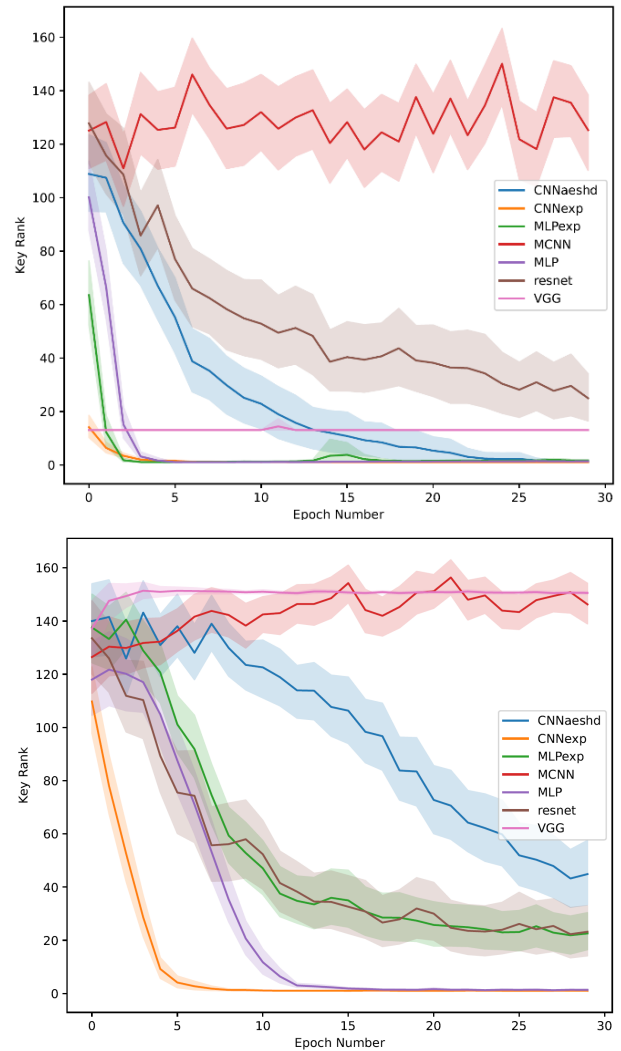


Figure 2: Attack comparison using dimension 0 (top) and 1 (bottom) with different neural network models. Power model is Identity.

The newly developed software package allows any (un)protected implementation to be rapidly checked against multiple ML SCA approaches, providing more insight on leakage sources and countermeasure effectiveness compared with statistical attacks. Normalizing the softmax function with dimension 0 allows to work with imbalanced sets and improves attacks with balanced sets.

[1] B. Hettwer, S. Gehrer, T. Güneysu, "Applications of machine learning techniques in side-channel attacks: a survey", Journal of Cryptographic Engineering, 10(2):135–162, (2019).

Arbitrary-scale Image Generation

E. Ntavelis, M. Shahbazi, I. Kastanis, R. Timofte, M. Danelljan, L. Van Gool

Positional encodings have enabled recent works to train a single adversarial network that can generate images at different scales. However, these approaches are either limited to a set of discrete scales or struggle to maintain good perceptual quality at the scales for which the model is not trained explicitly. We propose the design of scale-consistent positional encodings invariant to our generator’s layers transformations. This enables the generation of arbitrary-scale images even at scales unseen during training. Moreover, we incorporate novel inter-scale augmentations into our pipeline and partial generation training to facilitate the synthesis of consistent images at arbitrary scales. Lastly, we show competitive results for a continuum of scales on various commonly used datasets for image synthesis.

In this work we extend the task of multi-scale generation, using a single generator, to arbitrary continuous scales. To this end, we propose an appropriate positional encoding formulation. While this leads to arbitrary-scale generation, this strategy alone does not guarantee consistency across scales. We therefore further propose a means of enforcing consistency between different scales and resolutions using inter-scale augmentations in the discriminator. Specifically, we generate images at different scales from the same latent code. Then, pairs of generated images at different scales go through channel-mix and cut-mix augmentations. Finally, the discriminator assesses the augmented images. Such an approach encourages the generator to generate scale-consistent images so that the images still look realistic after inter-scale augmentations. Our method can also generate parts of the image in arbitrary resolutions with scale consistency, as visualized in Figure 1.

To summarize our contributions: We (a) design a scale-consistent positional encoding scheme that enables fully convolutional and pad-free generators to generate images of arbitrary scales; (b) introduce a set of inter-scale augmentations that pushes the generator to create consistent images among scales; (c) further facilitate the consistency among arbitrary scales by incorporating partial generation in our training pipeline. We perform experiments on various commonly used datasets characterized by diverse positional priors. Our results indicate that the introduced pipeline permits the consistent generation of images of arbitrary scales while preserving high visual quality. We name our method ScaleParty.



Figure 1: Arbitrary-scale image synthesis using different datasets.

Designing a Scale-Invariant Generator: We guide the synthesis using positional encodings. We use pad-free convolutions for

spatial equivariance. Removing the padding shrinks the convolution’s output feature map. To counter this, we use auxiliary padding on the positional input and clip the output. The encodings are pixel-centred, and we use 2x up-sampling without aligning corners. Our encodings are consistent across both scales and the generator layers’ transformations.

We use inter-scale augmentations between images produced by the same latent code at different scales. We incorporate partial-frame training as a straightforward way to train for a continuum of scales and larger resolutions.

We trained our approach for the commonly used datasets FFHQ [1] and LSUN [2]. We compare with the state-of-the-art baselines in multi-scale image generation: CIPS [3] MSPIE [4] MS-PE [5] and the single resolution StyleGAN2 [1]. As seen in Figure 2, for FFHQ, the baselines methods are either unable to produce images in arbitrary scales or are unable to consistently produce perceptually good results in different scales.

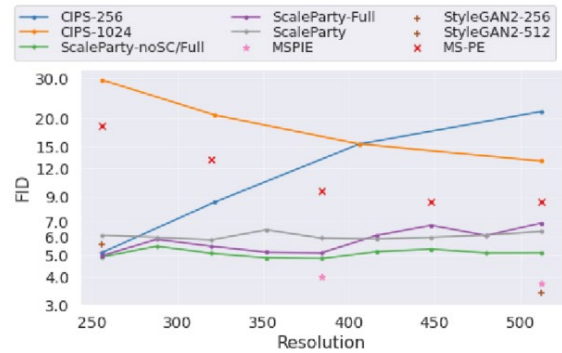


Figure 2: Comparison with base line methods using FFHQ dataset.

We present ScaleParty [6], a novel method for arbitrary-scale image synthesis utilizing a single generative adversarial network trained with positional guidance. Our scale-consistent positional encodings permit a pad-free generator to produce perceptually good results across a continuum of scales. Furthermore, we introduce a scale-consistency objective by applying inter-scale augmentations before presenting the synthesized image to the discriminator network. Incorporating partial generation training in our pipeline further improves consistency. The combination of multi-scale and partial synthesis training teaches the generator a dense representation of positional encodings. During inference, this can be leveraged to create geometrically manipulated images by applying transformations such as warping or stretching to positional encodings.

[1] StyleGAN2 [Karras, et al., CVPR2019]

[2] LSUN [Yu, et al., arXiv2015]

[3] MSPIE [Xu, et al., CVPR2021]

[4] MS-PE [Choi, et al., ICCV2021]

[5] CIPS [Anohkin, et al., CVPR2021]

[6] ScaleParty [Ntavelis, et al., CVPR2022]

Improving the Classification of an Unbalanced Spheroids Dataset by Oversampling with Synthetic Images from Generative Adversarial Network

F. Luongo, C. Netsch, T. Valentin, J. Goldowsky, M. Kirschmann, R. Vincent, D. Van De Ville*

Biological data is often imbalanced and incomplete, decreasing the classification performances of Machine Learning (ML) classifiers. Traditional data augmentation (e.g., by adding noise or changing contrast) can be used to increase the performance of ML classifiers [1]. Here we investigate if Generative Data Augmentation with Generative Adversarial Networks (GANs), can further improve classification performance and to show greater improvements of performance. The use of this technique could be extended to all small, unbalanced datasets.

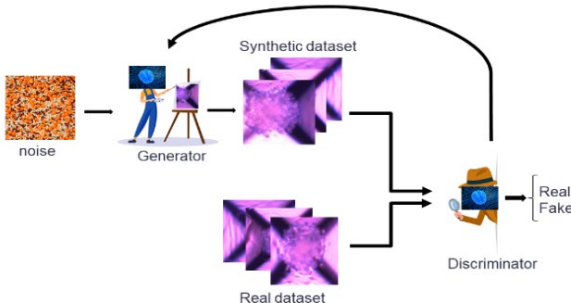


Figure 1: Illustration of a standard GANs Algorithm [2].

Spheroids, spherical cell aggregates, have become increasingly relevant as organ and disease models for biomedical research. Those small spherical tissues have a three-dimensional shape promising an efficient and reliable replication of in-vivo cells [3]. A cell line used for hepatotoxicity studies, the HepG2 spheroids lineage typically exhibit high class imbalance of 1:10 or worse as the rare phenotypes are developing with very low probabilities. For some experiments these spheroids need to be sorted early during the cell culture to remove unhealthy spheroids. Wrongly classified spheroids can pollute entire batches, making it potentially dangerous for subsequent applications.

For efficient experiments high-throughput sorting of spheroids is needed and this can be achieved by automation via microscopy and in-silico classification. As this is a complex image classification task deep learning offers a powerful technique to this. However, to train deep learning models successfully all classes need to be sufficiently represented in the training data. This is problematic for biological entities as spheroids of the unhealthy class as they are less represented in the dataset. Here we investigate if the classification accuracy of unbalanced datasets can be improved by increasing the number of samples of the rarer class by synthetic image generation [1] with three adversarial generative networks (GANs) architectures. An example of the functioning of a GAN is shown by Figure 1.

The data generated by different GAN architecture is compared with a real spheroids' images in Figure 2. The generated data is comparable to the distribution of the real data, experts couldn't distinguish between them. Our results show a significant increase in F1 score of the classification models when augmenting with styleGAN2-ADA [4] -generated images compared to the baselines with and without traditional

augmentation methods. This novel application of GANs can improve the classification of similar unbalanced datasets.

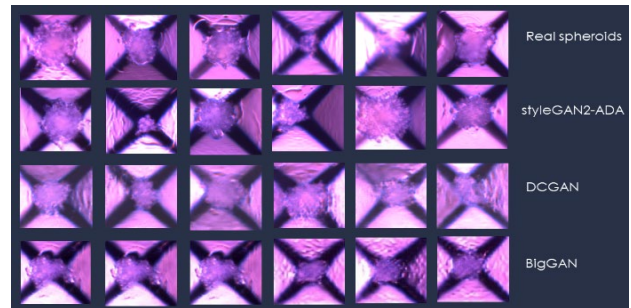


Figure 2: Images of spheroids from the real dataset and synthetically generated with different GANs architectures. Only the first line of images is coming from the real image distribution.

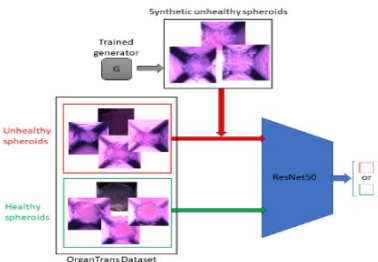


Figure 3: Integration of the generative data augmentation method into the training process. The generator of the GAN is used to produce synthetic images.

The classification accuracy significantly increased with the input of synthetic unhealthy spheroids integrated as illustrated in Figure 3. An increase of F1 score <5% for 10% unhealthy spheroids and <15% for 1% of unhealthy spheroids, for the generative models trained with 200, 2'000 or 15'000 images of unhealthy spheroids.

There are a lot of limitations to include synthetic images (deep fakes) in the medical field, but they could be a potential solution for problems linked to small and unbalance data, helping to understand mechanisms of rare phenotypes and associated diseases.

- EPFL, Swiss Federal Institute of Technology in Lausanne
- [1] Shorten, C. and Khoshgoftaar, T. M. A survey on image data augmentation for deep learning. *Journal of Big Data*, 6, 1–48
- [2] Adapted according to: Silva, T. S. A short introduction to generative adversarial networks. <https://sthalles.github.io>

[3] Ryu, N.-E., Lee, S.-H., Park, H. Spheroid culture system methods and applications for mesenchymal stem cells. *Cells*, 8, 1620.

[4] Karras, T., Aittala, M., Hellsten, J., Laine, S., Lehtinen, J., Aila, T. (2020). Training generative adversarial networks with limited data. *Advances in Neural Information Processing Systems*, 33, 12104-12114.

FETA – a Flexible Low-power AI/ML Accelerator for Time Series Signals

A. Bonetti, S. Devise, S. Emery

Machine learning (ML) algorithms such as neural networks can be extremely effective in performing complex analysis of data from IoT sensors. However, battery-powered devices rarely embed ML functionalities as they often operate on tight power budgets. In this work, we present FETA, a flexible and power-efficient digital accelerator for ML algorithms for any time-series signal.

The large variety of data that is acquired by sensors on mobile, wearable, and IoT devices has enabled numerous new applications such as long-term medical monitoring, fitness tracking, and voice control. ML algorithms such as neural networks (NNs) can be used for processing time-dependent sensor data (time-series) from these sensors. However, very few portable devices embed ML features because of tight power budgets. Thus, the design of ultra-low power NN accelerators is key to enable ML features in any battery powered device and create unprecedented use-cases for edge devices.

FETA is a digital accelerator (Figure 1) that parallelizes the computation of recurrent neural networks (RNNs) which are commonly used in time-series applications being suited for identifying temporal correlation within the input signal. The parallelized computation is enabled by eight processing elements (PEs) which compute multiply-and-accumulate (MAC) operations that are the most common calculations required by RNNs. Additionally, further power savings are enabled with hierarchical processing (e.g., in voice applications).

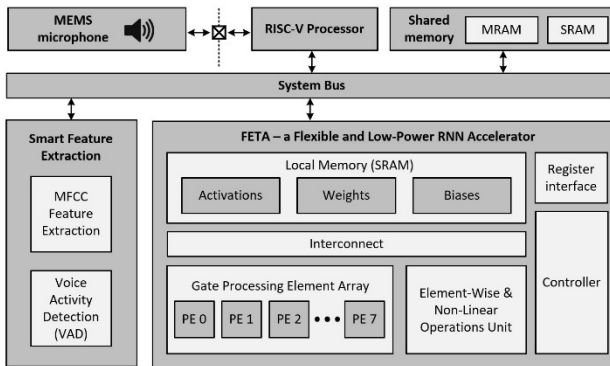


Figure 1: FETA accelerator and smart feature extraction block.

FETA is designed for flexibility to support a wide range of ML time-series applications, such as biomedical signals monitoring, predictive maintenance, and voice control. To achieve this, several parameters can be programmed, such as the number of computed RNN layers, the type of RNN cell (LSTM or GRU), and the non-linear activation function, such as hyperbolic tangent, sigmoid, and rectified linear unit (ReLU). Also, this accelerator can compute fully connected layers to support not only RNNs but also multilayer perceptron (MLP) networks. Quantization of both weights and activations can be programmed to 4, 8, or 16 bits for additional power savings and unlocking memory space while ensuring a sufficient computational precision.

The use of FETA for voice applications is enabled thanks to the integration of a block that extracts voice features as Mel-frequency cepstral coefficients (MFCCs) from the raw data provided by a digital microphone. A voice activity detection (VAD) block can monitor either the raw voice data or the extracted features to enable the RNN acceleration by FETA only when voice is detected while keeping the accelerator in a low-power inactive state in the remaining time. The feature extraction block can also be bypassed to feed FETA with any type of data (e.g., raw audio data, output data from another neural network, etc...).

Beside the ultra-low power computation achieved by FETA, further energy savings are achieved with hierarchical processing (Figure 2). This approach relies on the fact that often battery-powered always-on devices are inactive most of the time. Thus, power consumption can be saved in sleep state and performance should be offered only when needed. With hierarchical processing, a small neural network can be continuously computed for smart and low-power wakeup (e.g., single wakeword) that would trigger the on-demand execution of a large neural network (e.g., set of commands). Energy-constrained market products might offer this flexibility only with costly reconfiguration (i.e., large power consumption and latency due to memory update). Instead, FETA can store an ultra-low-power neural network in the local memory and a more performant network in the shared memory to schedule their execution with hierarchical processing for large system energy savings.

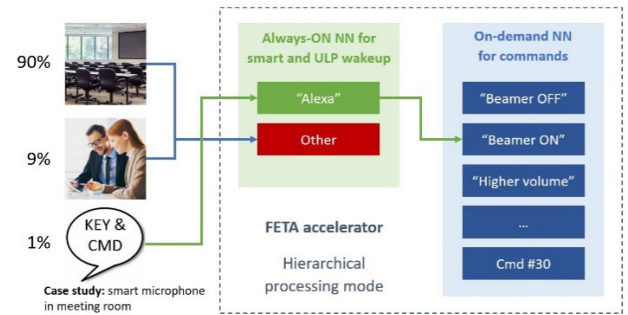


Figure 2: Hierarchical processing in FETA based on always-on and on-demand neural networks.

The performance of a CSEM system-on-chip (SoC) based on the FETA accelerator is compared in Figure 3 with the Syntiant NDP-100, a state-of-the-art low power commercial product for the acceleration of ML algorithms. The FETA SoC consumes 5x lower power and provides more flexibility in terms of supported NNs and computing precision for a similar accuracy in the keyword spotting (KWS) benchmark.

| Blocks | Syntiant NDP-100 | CSEM SoC with FETA |
|---------------------------------------|--|--|
| NN topology | Syntiant FC | LSTM (118 cells) + FC (10 neurons) |
| KWS accuracy (Google 10-word dataset) | 94% | 95% |
| Computing precision | 8 bit | 4 / 8 / 16 bits |
| Core supply voltage | 0.85 V | 0.80 V |
| Process node | 40 nm | 22 nm |
| Single network processing | | |
| Task | 100% of time @ 10-words KWS | |
| Power consumption | 340 µW | 60 µW |
| Hierarchical processing | | |
| Task | 99% of time @ VAD 1% of time @ 10-words KWS | 99% of time @ 2-words KWS 1% of time @ 20-words KWS |
| Average power consumption | 63 µW | 23 µW |

Figure 3: Comparison of FETA-based CSEM SoC with a state-of-the-art market product.

EdgeML Deployment Flow for CSEM's End-to-End Machine Learning Solution

P. Jokic

The proliferation of energy-efficient machine learning chips is extending the range of smart applications that can be processed at the edge (edgeML) on self-sustainable and battery-powered devices. CSEM's latest ultra-low power ML system-on-chip (SoC) demonstrates this by executing state-of-the-art edgeML within 1 mW. We present the deployment flow which enables to transfer the software performance to an optimal hardware implementation.

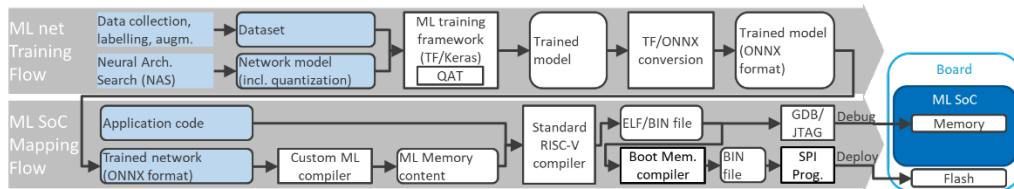


Figure 1: ML compiler flow.

Machine learning (ML) algorithms, like convolutional neural networks (CNNs), are computation-intensive and thus consume significant power for processing. This traditionally made them unsuitable for analyzing data onboard energy harvesting- or battery-powered mobile devices, operating on a limited power budget. CSEM's edgeML SoC^[1] tackled this challenge by providing a highly energy efficient CNN accelerator, combined with a low power-trimmed system architecture, enabling ML processing capabilities in the 1 mW power region, compatible with such power-constrained mobile devices. ML compilers that efficiently deploy the algorithms to the accelerator play an equally important role as the underlying hardware architecture to achieve the low power capabilities built into the chip. This work describes the significance of both components, the ML compiler and the ML SoC, for implementing a low power emotion classification system.

CSEM's ML compiler flow converts trained CNN models into a memory file containing all parameters and settings required by the hardware accelerator to execute the model. Figure 1 illustrates this flow. The generated ML memory content is compiled along with the microcontroller code that implements the application, control tasks and all other non-accelerated tasks using the standard RISC-V GCC compiler. Executable binaries are then either deployed to the ML SoC through the GDB debug environment or further post-processed into a bootable format that the ML SoC can directly boot from when stored in a connected SPI Flash memory (on the circuit board). ML training precedes this flow but is excluded from the compilation for simplicity and modularity reasons. However, the training must also be matched to the hardware by considering constraints like supported precision/quantization options and layer types.

ML model deployment starts by reading the model from an inter-operable ONNX format, as depicted in Figure 2. This allows extracting the layer types, their dimensions and associated trained parameters. The layer-wise memory allocation is then planned based on the layer dimensions. To minimize the memory footprint, an optimized CNN mapping strategy is followed^[2], reducing activations memory by up to 50%. With all memory pointers computed, the layer settings (accelerator instructions) can be derived and finally the parameters can be computed into a hardware-compatible format. Additionally, some arithmetic operations that are subsequently performed in a series of ML layers can be merged into a single hardware-mapped layer, as illustrated in Figure 3. This reduces both the number of

parameters and the execution cycles and allows to maximize the decimal bit-width of fixed-point values for minimal quantization errors (compensated by shift). Finally, all layer settings and compiled parameters are written into a C-header file, which can be directly included by the application code. Thus, the standard GCC compiler can be used for generating the final binary file.

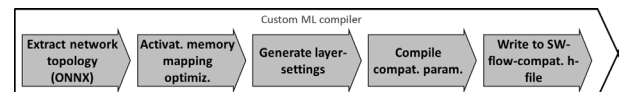


Figure 2: Custom ML compiler stages.

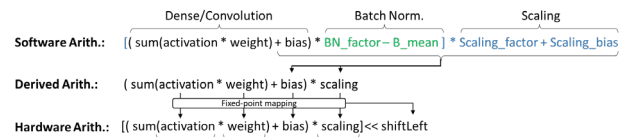


Figure 3: Arithmetic operations mapping.

This flow is exemplified by deploying an emotion classifier on CSEM's latest edgeML SoC platform shown in Figure 4. An 80-layer CNN is employed as classifier, consisting of convolution, pooling, normalization, and dense layers. The compiler automatically converts this into 30 hardware-mapped layers by merging operations. The activation memory optimizer further reduces the activations footprint by 49% to a total CNN footprint of 783kB, freeing memory space for the face detection (303kB) and the application code (46kB) on the available 1.2MB memory. Quantization-aware arithmetic mapping ensures consistent end-to-end accuracy preservation (>95%).

Evaluating the emotional state of a user allows smart interactive systems to optimize the human-machine-interface and adjust the application accordingly. This is demonstrated by detecting faces in the field of view and running the described CNN classifier on the cropped faces to mirror the emotion to the user at a 1 mW power budget, suitable for battery operation. Concluding, the ML compiler is an essential contributor to efficient ML deployment, exploiting the features of the target hardware (accelerator).



Figure 4: Emotion classification application.

^[1] P. Jokic, et al., "A ULP 22 nm System-on-Chip with Dual-engine Hardware Acceleration for Edge ML Inference", CSEM Scientific and Technical Report (2020) 106.

^[2] <https://ieeexplore.ieee.org/document/9142248>

RISC-V Core Extension for Efficient Vector Processing using the X-Interface

M. Imfeld, J.-L. Nagel, V. Moser

Open-source cores and accelerators represent an exciting opportunity for quick development of cutting-edge solutions, while focusing the design effort on high-value elements for CSEM customers. Bringing open-source components to industrial-grade is however a mandatory step towards this goal.

The RISC-V instruction-set architecture (ISA) is an open standard ratified by RISC-V International and comprising a base ISA and several extensions. The benefit of RISC-V ISA standardization is multifold, open-source development and interoperability being not the least. For CSEM, one of the key benefits is the availability of both open-source and commercial programming tools and software, which allow focusing on the development of ultra-low-power hardware.

CSEM is also member of the OpenHW Group, which develops and promotes various open-source cores, the related IPs, tools and software. The CORE-V family of RISC-V cores comprises several industrial-grade cores targeting needs from low-footprint micro-controllers to Linux-capable platforms.

Different projects will benefit from different standard RISC-V ISA extensions, e.g., vector extension for machine-learning applications, security extensions in trusted platforms, etc. An elegant solution developed within OpenHW is the eXtension interface [1] (X-Interface). This interface allows offloading instructions unknown to the base core to an accelerator, in a closely coupled fashion. The advantage, compared to a memory-mapped accelerator, is evident for standard ISA extensions like Floating-Point, Vector, Cryptography or Bit Manipulation. However, the same principle can also be used to extend the ISA of the core with non-standard instructions. Similarly, to the standard ISA extension, these instructions are not recognized by the main core and are simply passed to the accelerator.

Two OpenHW cores (CV32E40X and CVA6) currently support this X-Interface.

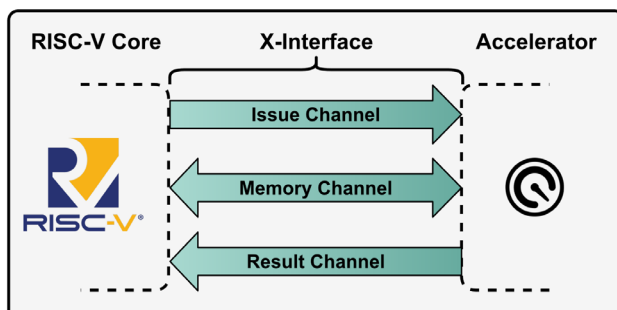


Figure 1: OpenHW X-Interface.

An example of possible extension is obviously the floating-point arithmetic. Another recently standardized extension is the RISC-V vector extension (RVV). RVV comes with a set of registers and a very extensive list of new instructions.

[1] <https://github.com/openhwgroup/core-v-xif>

Standardized subsets of RVV are also available, e.g., removing floating-point capabilities (Zve32x) when targeting low-power applications.

The Vicuna [2] coprocessor is an open-source X-Interface compliant accelerator supporting Zve32x developed at TU-Wien. The accelerator is highly parameterizable so that it can be tailored to specific applications. In particular, the number of parallel execution units and the data-path width of each execution unit can be specified at design time. Since it is compliant with a RISC-V standard extension, it is supported by the most established RISC-V compilers (GCC and LLVM).

CSEM contributed to the Vicuna project by developing an industrial-grade verification framework to assess its quality. This task was carried out by developing a UVM-based environment. The environment emulates the core-side of the X-Interface and thereby drives and monitors the signals on the interface. To verify the correct execution of instructions on the design under test (DUT), the verification environment also monitors certain registers within the DUT. The scoreboard (which is part of the environment) compares the monitored signals to a reference model. In this case, Spike (an open-source RISC-V instruction-set simulator) was used as the reference model. Each retired instruction is registered in the coverage collector and the verification effort is complete once the coverage goal is reached.

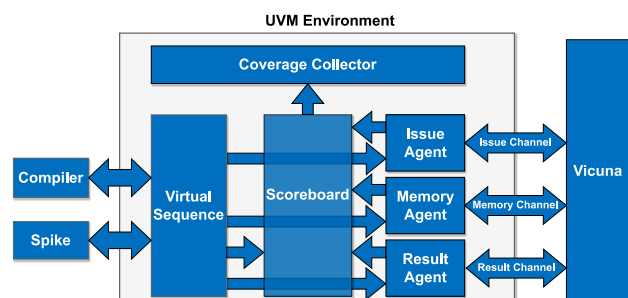


Figure 2: Architecture of the UVM-based verification environment.

The verification framework is not limited to RVV but will be highly reusable with any other accelerator based on the X-Interface. Of course, for accelerating non-standard ISA extensions, a golden model will have to be developed.

This project demonstrates the viability of the X-Interface as a way to connect tightly coupled accelerators to RISC-V cores. A verified vector processor and a reusable verification environment for future accelerators were created.

[2] M. Platzer, P. Puschner (2021). Vicuna: A Timing-Predictable RISC-V Vector Coprocessor for Scalable Parallel Computation.

Implementation of a Cryptographic Function for Hashing and Message Encryption

H.-R. Graf, F. Valencia, D. Vizár

CSEM is implementing cryptographic HW accelerators based on Keccak as IPs for integration in ULP SoCs. Keccak is well-known for being used in SHA-3, the latest SHA standard from NIST, but can be used to implement the full range of symmetric cryptography applications.

CSEM is expanding its portfolio of intellectual properties (IP) for cryptography with dedicated hardware (HW) accelerators for Keccak. Keccak is the name of a family of cryptographic primitives, that includes secure cryptographic hashing, authentication, encryption and more. It is the winner of the latest NIST (National Institute of Standards and Technology) hash function competition and became SHA-3 [1], the best Secure Hashing Algorithm. While the still widely used SHA-1 algorithm is regarded as insecure, NIST does not withdraw its successor SHA-2 yet. But SHA-3 significantly improves robustness against cryptographic attacks, that is required with the expected rise of quantum computers.

The Keccak cryptographic primitives can be implemented very efficiently in hardware, leading to higher throughput and lower power consumption than software implementations. Keccak uses a key-less cryptographic permutation function (also referred as Keccak-f [2]) that can be used in a number of higher-level algorithms, many based on the so-called Sponge construction (see Figure 1, that gets explained afterwards). This can be used in many different cryptographic applications, like secure hashing, extendable output functions (XOF), message authentication, authenticated encryption but also pseudo-random number generators (PRNG). Currently, it is standardized by NIST only for hashing and XOFs but there is a promising and steadily expanding family of cryptographic algorithms based on Keccak, some of them already in consideration by NIST for the upcoming light-weight cryptography (LWC) standard. LWC will become important in a world full of Internet-of-Things (IoT) devices.

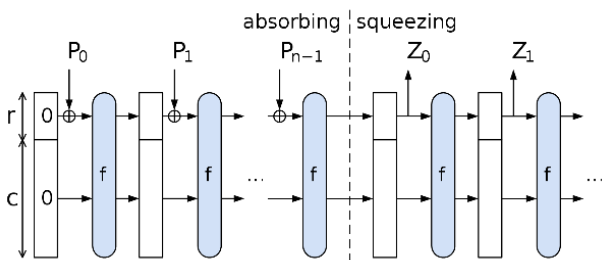


Figure 1: Sponge construction for hashing using permutation function f .

The analogy in Figure 1 to a sponge is that an arbitrary number of input bits are first “absorbed” into its state, after which an arbitrary number of output bits are “squeezed” out of its state. The correctly padded input message P is partitioned into n blocks of r bits, and “absorbed” (input) by XOR operation to the “top” part of the state, block by block. The “bottom” part of the state has an additional capacity of c bits, that provides robustness against various attacks. The permutation function f is applied on

the state for every block, thus updating the state. Later, the output Z is “squeezed” (extracted) from the “top” part of the state, again in blocks of r bits.

The permutation function Keccak-f consists of a number of rounds with 5 individual steps that use simple operations of XOR, AND, and NOT, that are very suitable for HW implementations. The Keccak state is organized as a 3-dimensional array of $5 \times 5 \times N$ bits, with N in $\{1, 2, 4, 8, 16, 32, 64\}$. A slice is a set of 25 bits with same z coordinate in the Keccak state.

For SHA-3, NIST has constrained the Keccak parameters (see Table 1), while the HW accelerators of this work are built for a wider range of applications.

Table 1: Keccak parameters.

| | SHA-3 | CSEM Keccak HW IP |
|----------------------|-------------------------------|--|
| Rate r [in bits] | 224, 256, 384, 512 | Freely configurable (in steps of 32) |
| State size [in bits] | $5 \times 5 \times 64 = 1600$ | All (25, 50, 100, 200, 400, 800, 1600) |
| Rounds | 24 | Freely configurable |

Reduced state sizes are used in light-weight cryptography (LWC). For instance, the NIST LWC finalist Elephant uses a Keccak state of 200 bits and 18 rounds, that has a reduced computation complexity and therefore leads to lower power consumption.

The HW accelerators of this work are targeting the sweet spot of embedded systems with constrained resources. They are optimized for reduced power consumption, dedicated to ultra-low power (ULP) System-on-Chips (SoC) or other application-specific integrated circuits (ASIC). Additionally, CSEM has implemented (fair) shuffling and masking to harden the IPs against side-channel attacks (SCA). An example of SCA is a hacker trying to extract secret keys by observing the power consumption of the device.

Slice-based implementations have been chosen because this is a good balance between area and performance. Furthermore, it allows to implement shuffling of sequentially executed, parallel operations at very little cost. For even higher SCA resistance, an implementation that uses masking, at cost of larger area, was developed as well.

A basic catalog of Keccak IPs with side-channel security results has been compiled. The HW accelerators were prototyped and SCA stressed on a FPGA platform, but also integrated and simulated in a RISC-V SoC.

[1] Federal Information Processing Standards Publication 180-4, Secure Hash Standard (SHS), Information Technology Laboratory, National Institute of Standards and Technology, March (2012), <http://csrc.nist.gov/publications/fips/fips180-4/fips-180-4.pdf>

[2] G. Bertoni, J. Daemen, M. Peeters, G. Van Assche, The KECCAK reference, Version 3.0, January (2011), <http://keccak.noekeon.org/Keccak-reference-3.0.pdf>

ULP 57-66 GHz MIMO FMCW RADAR in 22-nm FDSOI CMOS

S. Cerida Rengifo, F. Chicco, E. Le Roux

The design of a second test chip of the ultra-low power short-range RADAR-on-chip (RoC) has been carried out augmenting the functionalities of the first prototype. The frequency synthesis is now fully integrated, and it is based on an all-digital phase-locked loop (ADPLL). The MIMO system has increased to 4 TX and 4 RX channels. Auxiliary blocks such as crystal oscillator and bandgap voltage reference have also been included to reduce the required off-chip components. The RADAR is integrated in GF 22-nm FDSOI CMOS, consuming only of 40.2 and 101.1 mW for the 1TX/1RX and 4TX/4RX configurations, respectively.

The 60-GHz unlicensed ISM band provides a 9-GHz bandwidth for short-range devices (SRD). This multi-GHz band benefits sensing devices as radars which can achieve a theoretical range resolution of 17 mm. In recent years, the development of radars has been driven mainly by the automotive industry where power consumption is not a hard constraint. However, in the case of portable or battery-powered devices, power consumption is a key factor. In order to address this market gap, a low-power frequency-modulated continuous-wave (FMCW) radar is being developed towards a low-cost low-power fully integrated solution. FMCW is chosen because it exhibits a bandwidth compression at the baseband, thus lowering the operating baseband frequency and relaxing the specifications and power consumptions. After a successful first operating prototype, the second version of the radar test chip has been designed to add more functionalities.

The new radar chip is composed of 4 transmitters (TX) and 4 receivers (RX), taking advantage of the modular design of the TX-RX slices in the first version which enables an easy extension to a larger number of channels. A larger number of virtual channels in the MIMO radar means a higher angular resolution. The theoretical angular resolution for this 4x4 MIMO array, considering an antenna spacing of half wavelength, is 6.3°. In addition to having the MIMO channels, it is necessary to be able to differentiate each TX channel in each RX channel. Therefore, orthogonal BPSK modulations are implemented within each TX channel. At the same time the modulating frequency is used as a low-IF at 2 MHz to translate the beat frequency away from DC offsets and flicker noise.

Further optimization is implemented in both the TX and RX channels. On the TX side, the BPSK modulator and power amplifier are merged into a power mixer, thus saving area and power. On the RX side, a transformer-based passive mixer-first is designed to minimize power consumption since there is no active circuit operating at 60 GHz. The mixer is co-designed with a voltage-mode low-noise IF amplifier and the IF signals are output off-chip using a buffer.

One of the main highlights in this new chip is the full integration of the frequency synthesizer based on an all-digital phase-locked loop (ADPLL). The core of the ADPLL is a digitally-controlled oscillator (QDCO), performing direct synthesis at 60 GHz. The QDCO generates quadrature signals which are required to extract the micro-Doppler signatures of the targets, normally used in gesture recognition and vital signs monitoring applications. The loop is closed by means of a CML divider-by-4 and a dynamic divider-by-12, followed by the time-to-digital converter (TDC), digital-to-time converter (DTC), and digital loop filter. In addition, auxiliary blocks such as crystal oscillator (XO), bandgap reference voltage, and LDOs are also integrated to reduce the number of off-chip components required.

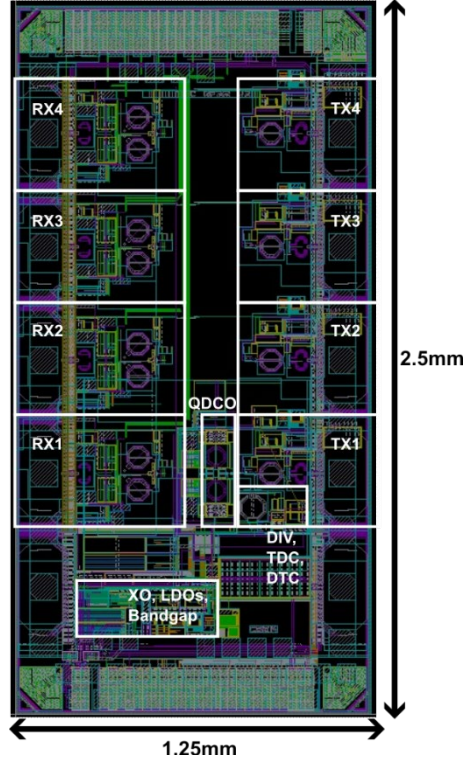


Figure 1: Test chip of the 4-TX & 4-RX 60-GHz FMCW radar.

The 4-TX & 4-RX MIMO FMCW radar is integrated in GF 22-nm FDSOI. The floorplan of the test chip is shown in Figure 1. A record low power consumption is achieved with 40.2 mW in the 1TX/1RX configuration. The power breakdown for the 4TX/4RX configuration is shown in Figure 2, corresponding to an estimated average power consumption per virtual channel of only 6.3 mW. The next steps in the development are to characterize the chip and build a demonstrator.

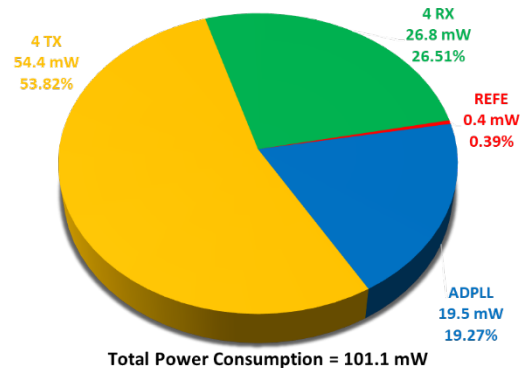


Figure 2: Power consumption breakdown.

Bluetooth® Dual Mode Transceiver Performances in 22 nm Bulk and FD-SOI CMOS Technologies

N. Raemy, F. Chicco, A. Dissanayake, V. Kopta, E. Le Roux, K. Manetakis, F. Pengg, E. Pérez Serna, P. Persechini, C. Salazar Gutierrez, N. Scolari, A. Vouilloz, J. Soldevila Vilarrasa, R. Ravanilla, L. Zahnd, F. Epifano, P. Dal Fabbro

CSEM's Bluetooth Dual Mode transceiver IP program, that started in 2019^[1], reaches today its maturity and provides the ultimate answer to the increasing demand of True Wireless Stereo (TWS), which is boosting the technology for low power Bluetooth wireless. The ultra-low power budget does not compromise the radio performances, reaching state-of-the-art RX sensitivity, high TX output power and excellent interferer rejection, for an optimal audio link (streaming or communication).

The wireless audio market is more and more dominated by Bluetooth standard for its efficiency and availability. After the excellent 2020 performance, the Bluetooth audio shipments were set to a new record of 1.3 billion in 2021. Most of recent smartphone buyers can certify that wired headphones disappeared when unboxing their new mobile phones, confirming manufacturers are promoting instead True-Wireless Stereo (TWS) earbuds. These accounted for 55% of the headphone market in 2021. This scenario represents a great opportunity for TWS earbuds, with a market estimated at 263 million units in 2022, growing to 619 million in 2026.^[2]

CSEM icyTRX-DM IP, a Bluetooth Dual-mode (DM) transceiver combining Bluetooth extended data rate (EDR) along with Bluetooth Low Energy for audio streaming through Classic and emerging LE Audio streaming. In lab evaluation and real-life connection, the icyTRX-DM IP is demonstrating outstanding performance. It is available in 22 nm GlobalFoundries FD-SOI CMOS and also in TSMC ULL bulk CMOS, offering a high valuable choice for CSEM's customers.

Received early 2022, the icyTRX-DM-GF22 silicon has been fully characterized over process, voltage and temperature (PVT). The measured transceiver performances are in-line with the targeted specifications and best-in-class for most of them. As depicted in Figure 1, the 2 Mbps Bluetooth Low Energy (LE) mode, datarate used for LE Audio transmission, exhibits a sensitivity better than -95 dBm, well controlled over PVT variations.

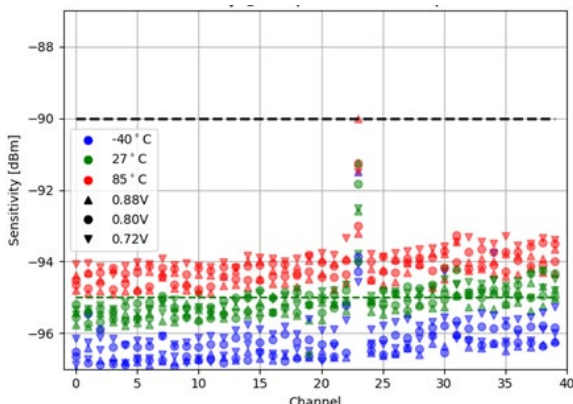


Figure 1: BLE Bluetooth Low Energy 2 Mbps sensitivity measurement in GF 22 nm.

[1] N. Raemy, "Dual-mode Bluetooth Silicon IP in 22 nm CMOS", CSEM Scientific and Technical Report (2019) 108.
N. Raemy, "Bluetooth Dual Mode Transceiver in 22 nm CMOS", CSEM Scientific and Technical Report (2020) 112.

Despite the trade-offs required by the stringent power consumption and size targets, the immunity towards interferers is excellent, as shown in the carrier-to-interferer (C/I) measurement in Figure 2.

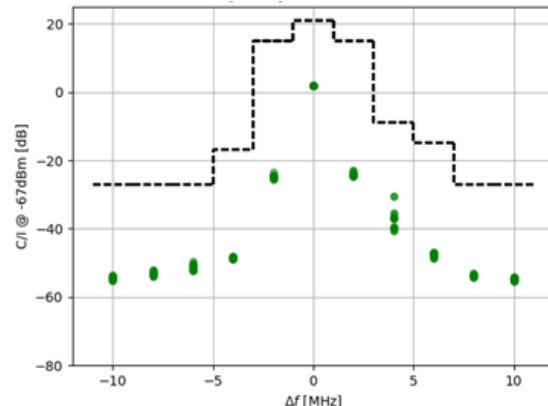


Figure 2: C/I 2 Mbps measurement in GF 22 nm.

For Bluetooth Low Energy 1 Mbps operation, the transmitter has been designed to deliver up to +11.5 dBm (or +13 dBm for TSMC ULL 22 nm) in high-power mode and approximately 4 dBm in low-power mode. The power amplifier (PA) is supplied with 1.6 V core voltage in high-power mode while the whole IP is working at the nominal operating voltage of 0.8 V (PA-included) in low-power mode. The output power accuracy is better than ±1.0 dB over process and temperature.

Due to the peak-to-average ratio (amplitude modulation) intrinsic to EDR modes, the maximum transmit power is +8.5 dBm for EDR 2 Mbps and +7.5 dBm for 3 Mbps (or +10 dBm and +9 dBm, respectively, in TSMC ULL 22 nm).

The IP has been licensed to several customers worldwide who shall launch their products in 2023. Some of them are already looking ahead to next generation IP version for which additional features are required: support to the upcoming Channel Sounding and High Data Rate (HDR) features and higher TX output power to name just a few. CSEM is paying close attention to the market trends and is already working towards the next generation of the icyTRX-DM IP.

[2] 2022 Bluetooth Market Update (www.bluetooth.com)

ASIC-driven Miniature Atomic Clock

S. Karlen, J. Haesler, Y. J. Regamey, D. Ruffieux, S. Lecomte

Chip-scale atomic clocks (CSACs) currently achieve the high level of frequency stability required for today communication systems and localization devices. Thanks to the combination of a dedicated application specific integrated circuit (ASIC) with a microcontroller and a MEMS atomic vapor cell-based physics package, a small, low power and highly integrated solution was demonstrated at CSEM. These results pave the way for the power reduction of CSACs in a near future.

Miniature atomic clocks play an important role in the fields of telecom and navigation. Upon further miniaturization and cost reduction, they are poised to play an ever-increasing role in modern portable and autonomous applications. Several compact and miniature atomic clocks are today available on the market with different levels of miniaturization. All of them make use of discrete electronic components to drive the physics package. Moving electronics to an application specific integrated circuit (ASIC) opens new perspective for further miniaturization, high volume production as well as power and cost reduction.

In the past several years CSEM has developed Rubidium filled MEMS atomic vapor cells with a process compatible with low-cost and large-volume production^[1] (see Figure 1-right), and a flat physics package (PP) was developed for height sensitive applications^[2] (see Figure 1-left). The physics package consists of an LTCC (Low Temperature Co-fired Ceramics) package which includes a proprietary MEMS cell, a 795 nm emitting VCSEL (Vertical-Cavity Surface-Emitting Laser), and a propriety planar waveguide used to route the laser light to the cell and the photodiodes.



Figure 1: LTCC flat-form factor atomic clock physics package, PP (left); Rubidium filled MEMS atomic vapor cell (right).

To tend towards the ultimate clock miniaturization, a proprietary ASIC was developed as well^[3] (see Figure 2). Coupled to a microcontroller, this integrated circuit offers the required functionalities to fully and autonomously operate a CPT atomic clock: RF synthesizer, transimpedance amplifiers, current sources, and lock-in detection. This ASIC was implemented in a standard digital 0.18 μm CMOS. Its total power consumption was estimated to be in the order of 26 mW (without current sources).

A clock prototype which takes advantage of the three elements was assembled as a single compact system. The cell was heated

up to 90°C using the ASIC current sources. The system was operated under vacuum in order to reach this cell temperature as the vacuum encapsulation of the physics is not yet realized.

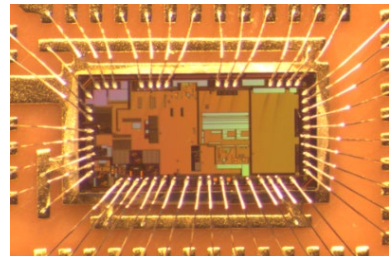


Figure 2: Clock ASIC (3 x 6 mm).

A coherent population trapping (CPT) signal with a full width at half maximum of 1.7 kHz was measured by locking the laser to the rubidium D1 atomic transition and modulating its frequency at 3.417 GHz using the ASIC RF generator. The measured CPT contrast was 0.6%. After locking the local oscillator (quartz) to the atomic clock transition, a short-term frequency stability of 10^{-10} at 1s integration time (see Figure 3) was measured. The long-term stability was not optimized and was limited to 10^{-11} in this measurement.

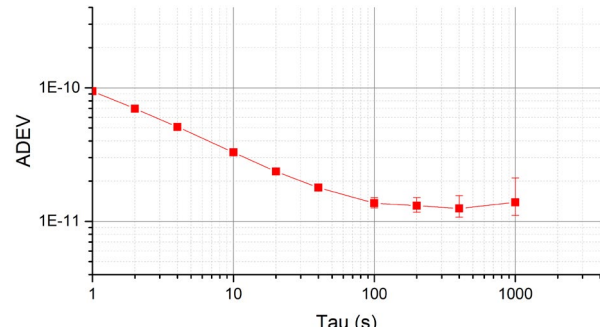


Figure 3: Allan deviation of the ASIC-driven chip-scale atomic clock system.

The measured short-term frequency stability is comparable to the stability of a clock operated with discrete electronics in the same experimental conditions. This verifies the functionality and the operability of the ASIC. Coupled with a low consumption physics package, a full clock draining less than 50 mW of electrical power can thus be reached in a near future.

[1] S. Karlen, et al., "Lifetime assessment of RbN3-filled MEMS atomic vapor cells with Al₂O₃ coating", Optics Express, 25(3), 2187 (2017).

[2] J. Haesler, et al., "Ceramic based flat form factor miniature atomic clock physics package (C-MAC)", 6th International Colloquium on Scientific and Fundamental Aspects of GNSS / Galileo (2017)
J. Haesler, et al., "Low-Power and Low-Profile Miniature Atomic Clock Ceramic based flat form factor miniature atomic clock

physics package C-MAC)", European Frequency and Time Forum & International Frequency Control Symposium (EFTF-IFCS) (2017).

[3] D. Ruffieux, et al., "Towards Portable Miniature Atomic Clocks" In A. Baschirotto, et al., "Frequency References, Power Management for SoC, and Smart Wireless Interfaces" (pp. 83–99), Springer International Publishing (2014).

PRECISION MANUFACTURING

Michel Despont

Precision manufacturing is revolutionizing countless industries, from watchmaking to aerospace. This trend relies on a wealth of advanced technologies, which transform traditional technologies into intelligent components. CSEM's goal is to supply Swiss companies, particularly small to medium size enterprises (SMEs), which represent 95% of Switzerland's economy, with the latest Precision Manufacturing solutions to increase their bottom line.

By mastering the design rules and tools to maximize precision manufacturing benefits, we consider our solutions' implementation in the industrial environment and their integration into industrial systems. Our work has both a technology-related focus (*MEMS, Additive Manufacturing, and Functional Surfaces*) and a system-level focus (*Photonics, Tools for Life Sciences, and Scientific Instrumentation*).

MEMS

CSEM MEMS designs and creates complex monolithic devices and systems, and their integrated electronics and packaging requirements. These technologies are the backbone of multiple disruptive technologies. CSEM currently incorporates its developments into a variety of fields, including "Photonics" (opto-mechanical platform), "Scientific Instrumentation" (silicon compliant structures), "Quantum Technologies" (rubidium vapor cells), and "Energy Harvesting" (thin-film patterning).

With its long history in MEMS fabrication, CSEM is one of the pioneers in this field. Our broad and flexible technology portfolio, state-of-the-art infrastructure and equipment provide SMEs with the unique chance to access technologies that would normally be unavailable to develop customized devices in low and medium volumes. SME's entry barrier to access large commercial foundries or to internalize these technologies is often too high, especially considering what they need to invest in terms of money and knowledge.

CSEM MEMS offers Swiss industry solutions along the entire innovation chain and beyond, including small-scale production fulfilling quality requirements in accordance with ISO-9001 standards.

Additive Manufacturing

Additive manufacturing (AM) is shaping a new era of technologies and creating new opportunities to increase performances and merge several functions into a single part. By pushing advanced materials to new limits in our state-of-the-art facilities, CSEM can exploit every aspect of the AM ecosystem, from advanced design and prototyping to the preproduction of components and systems.

We develop parts with high added value for the aerospace, watch, and medical technology industries. We create this value through precision mechanics, whose high accuracy and small-size geometries would be impossible to create with traditional technologies. Examples of our work include compliant mechanisms for space applications, microfabrication for the watch industry, and microfluidic applications for life sciences. With integrated functions, we have created sensing parts with integrated electronics and sensing for in-situ monitoring in the aerospace domain and vibration damping to withstand harsh

environments. Besides, the development of AM processes for enabling materials makes it possible to produce parts that have never been conceived before (e.g., self-actuated compliant mechanisms based on shape memory alloys).

Functional Surfaces

Surfaces and interfaces play a crucial role in numerous chemical and physical processes and are vital in exploiting new materials' full potential. As a cross-disciplinary topic, the most critical challenge faced by surface and interfacial engineers is developing a deep understanding of atomic and molecular-scale interfacial phenomena and their translation in engineering large-scale surface and interfacial properties, processes, and materials.

CSEM Functional Surfaces provides its know-how in surface structuration, modification, and interfacial engineering and assists partners in manufacturing and upscaling developed processes. We tailor our developments to the needs of a wealth of applications, from space and aeronautics, watchmaking, and energy harvesting and storage to life sciences and MedTech. We provide expertise in formulating and depositing novel materials into functional thin films, developing sensing platforms with molecular recognition abilities, and coatings with non-stick, antimicrobial, self-cleaning, or barrier properties. CSEM has developed a unique platform combining surface structuration and functionalization, fostering innovation through the hybridization of technologies. CSEM continuously works to further its vacuum coatings capabilities in strategic domains (e.g., horology, photovoltaics, medical technologies), while our liquid-based coatings are increasing the robustness of watch components and optical sensors. Lastly, our work in Interfacial engineering is critical to improving the performance, stability, and scaling-up of multi-layered systems e.g., solar cells or batteries.

Photonics

Photonics, the science and technology of generating, manipulating, steering and detecting light, is recognized as a critical technology for the 21st century. And it is already having a transformative impact on how we communicate, manufacture, and measure. Photonics is poised to continue its massive expansion in many technical areas and new applications.

We focus on novel optical elements and systems based on micro & nano-optics, integrated photonic circuits (PICs), photonic sensing in microfluidics, image sensors enhanced with artificial intelligence, high-performance laser sources, and laser-based instruments. This broad set of competencies is in line with the diverse needs of Swiss industry and their high-performance and high-added-value products. We develop three vital photonic areas: (1) Lasers and metrology – including laser sources and laser-based instruments. (2) Intelligent imaging and sensing – image sensors coupled with artificial intelligence, machine learning and enhancing micro-optical components (spectral filters) that bring novel capabilities to deeply integrated miniature devices. (3) Photonic Integrated Circuits (PICs) – CSEM is focusing on a novel platform called lithium niobate on insulator (LNOI), with high potential benefits for telecommunications, quantum technology, and sensing domains thanks to their electrooptic modulation capabilities and wavelength conversion.

Tools for Life Sciences

Tools for life sciences encompass the development of instruments, engineered biosystems, smart labware, sensors, and other technologies used in drug-testing, diagnostics, and regenerative medicine. Life sciences companies face distinct challenges with their highly visible role in diagnosis, drug pricing, and access to medicines. Their major technical challenge is developing cost-effective interfacing tools for different biological materials.

CSEM Tools for Life Sciences provides the necessary tools and devices for handling and monitoring body fluids and cells, and our technologies aim to improve patients' quality of life. We have long-standing experience in surface functionalization and structuring, biomaterials, microfluidics, fluid control, MEMS, biosensors and artificial intelligence.

From concept to prototyping and validation in biosafety level II laboratories, CSEM helps industry innovate and develop new products across different application domains, including: (1) Automated cell microsystems – standardization and parallelization of microphysiological systems. (2) Biomonitoring – proprietary low-cost fabrication technologies for sensing and sample preparation. (3) Laboratory automation and AI – tools for reliable handling and pre-treatment of samples including making use of the interpretation of data.

Scientific Instrumentation

CSEM Scientific Instrumentation aims to meet the demands of complex systems with ever-higher precision and new features in space, astrophysics, metrology, watchmaking, and industrial instrumentation. CSEM's competencies in the design, simulation, development, and testing of complex, miniature, hybrid, and precision systems have led to quantum leaps in performance compared to existing systems. The resulting advantages include sub-micrometric and reproducible motion patterns and a far smaller number of movable parts thanks to advanced manufacturing technologies that can avoid friction and premature wear.

For the last 30 years, CSEM has developed sound expertise in designing, simulating, manufacturing, integrating, and testing high-precision micro-mechatronic systems based on compliant structures. CSEM Scientific Instrumentation is organized along the three application-oriented topics. (1) High-precision mechanisms – developing sub-micrometric instruments, working in harsh environments within scientific missions. (2) FlexMEMS that benefit from compliant mechanism (Flextec) and MEMS design, paving the way to a wide range of small new scale silicon mechanisms for the watchmaking domain and medical applications. (3) Lidar for space and bathymetry applications, including flash imaging and frequency-modulated continuous wave lidar.

Direct Laser Writing Maskless Photolithography Equipment

J. Schildknecht, G. Bergonzi, O. Dubochet

In 2022, CSEM installed a cutting-edge maskless photolithography tool. This equipment allows to expand our capability in photolithography with an increase in performance while offering a high flexibility and suppressing the need to purchase photolithographic masks.

Photolithography is a key process in micro-fabrication which applies to all MEMS based products and developments such as the manufacturing of sensors, microfluidic devices, the production of micromechanical watch parts or photonics components.

Digitalization affects all activities in society and industry. Micro-manufacturing processes are no exception to this trend. The conventional photolithography equipment with exposure of photosensitive resists through a semi-transparent mask is gradually being replaced by digital systems of direct writing by a laser beam into the resist from a computer file. This method offers great flexibility and significantly reduces the tooling costs (mask manufacturing) while reducing the environmental footprint of this process step.



Figure 1: Direct Laser Writer (DLW) Heidelberg MLA150 cassette to cassette.

The main advantages of a DLW over a conventional mask aligner are the following:

- Minimum writing resolution of 0.6 µm
- Alignment accuracy improved by a factor of 4 (<0.5 µm topside and <1 µm top to backside). Advanced alignment options allow to perform a re-alignment for each die or for a specific area thus allowing to compensate for the potential curvature of the substrate.
- Reduction of the defectivity. There is no mechanical contact with the photoresist surface thus avoiding surface defects during photolithography.
- Reduction of the ecological footprint. DLW does not require the fabrication of photolithographic masks anymore.
- Gain in agility and flexibility: DLW allows to directly transfer the CAD file to the machine without the need to order a photolithographic mask, which usually takes 7-10 days thus reducing the cycle times in R&D. The design can virtually be modified for every exposure.

The system available at CSEM from Heidelberg Instruments features a minimum resolution of 0.6 µm. The system is equipped with a cassette-to-cassette wafer loader and pre-aligning station capable of handling square substrates up to 7"x 7" and wafers up to 200 mm. The automatic alignment can be performed on both sides of the wafer.

The laser diode is emitting at 375 nm with a power of 7.4 W. A special high aspect ratio option allows the exposure of thick resists >20 µm.

The tool is already qualified for several resists. Figure 2 below demonstrates the 0.6 µm writing resolution in 0.8 µm thick AZ1505 resist.

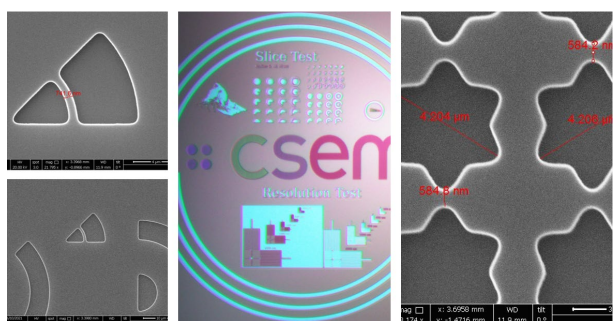


Figure 2: Results of the resolution tests on CSEM direct laser writer Heidelberg MLA150. Critical dimensions down to 600 nm can be properly exposed and developed.

The overall writing time depends on the layout and the resolution. The full writing time for a 150 mm wafer in high resolution mode can take up to 140 minutes per wafer. The automatic loader allows however to use the tool over-night thus increasing its productivity.

Further developments are on-going to expose thicker resists. A specific option allows to adjust the focal length during exposure thus allowing to optimize the sidewall angle for thick resists. Another advantage of this mode is the ability to expose resist in a cavity or on a substrate exhibiting a severe topography.

The machine is also capable of grey scale exposure in 128 gray levels. This option allows to modulate the intensity of the laser beam thus allowing to create tri-dimensional structures. This technique can for example be used for applications in the field of micro and nano-optics.

Another advantage of contact-less lithography is the possibility to work with new type of materials that need to be exposed in viscous form. This is for example the case of OSTEMERS® which aim to replace PDMS in microfluidic applications. As the sensitive layer is liquid before exposure, it cannot be brought into contact with a mask. Direct laser exposure is therefore the best option for structuring these materials.

With this new system, CSEM expands its photolithographic process capabilities and gains in flexibility for all its development activities.

First Measurements of High-temperature Silicon Carbide-based Sensors

A. Hoogerwerf, G. Spinola Durante

Silicon carbide (SiC) pressure sensors can operate at high temperatures, which makes them excellently suited for the monitoring of, amongst others, gas turbines and airplane engines. A first characterization of piezo-resistor sensors in SiC at temperatures up to 400°C yielded stable resistance with parabolic temperature dependence. Back-side leak-tight reference cavities for pressure sensor have been realized by laser bonding (LADB) of SiC-lids onto SiC-MEMS test vehicles. Fully functional MEMS pressure sensors, bonded with Ag-paste, will be measured to check performances up to 650°C.

Of all the physical parameters measured by sensors, pressure is one of the most important ones. Numerous pressure sensors exist for a wide variety of applications. Most of the pressure sensors in use today are made of micromachined silicon. Silicon is an excellent mechanical material and has therefore been widely used. However, the maximum operating temperature of silicon pressure sensors is limited by several factors, amongst which the plastic deformation of silicon above 300°C and 1 GPa^[1].

Silicon carbide is much more resistant to high temperatures and does not deform plastically below 800°C^[2]. It is therefore suited as a material for high temperature pressure sensors. Moreover, SiC is chemically stable which makes its processing more difficult. Another challenge consists in the metal-to-SiC contact resistance which should not drift in the operating temperature window of up to 650°C.

This far, the high temperature characterization has been carried out on test structures. The most important measurements are the measurements of the temperature derivatives of the piezo resistors. These measurements have been carried out in a temperature range between 20°C and 400°C due to equipment limitations. The resistances clearly show a parabolic temperature dependence with a minimum value at 150°C as shown below (Figure 1).

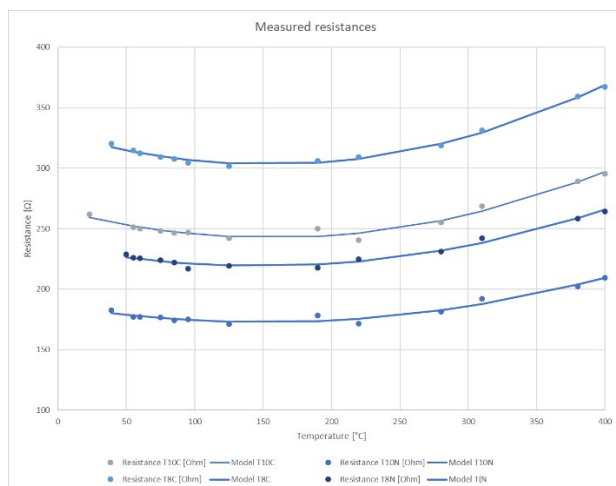


Figure 1: The measured temperature dependence of SiC piezo resistors.

We have therefore developed a full fabrication flow for SiC pressure sensors that is compatible with the high temperature operation. Sensors have been fabricated and characterized at room temperature^[3]. The sensors have a sensitivity of 130 μ V/bar and the noise level is in the tens of μ V.

The pressure sensors need a hermetically sealed reference cavity to be used as absolute pressure sensors. The manufacturing of a reference cavity was achieved by laser assisted diffusion bonding^[4] (LADB) of a SiC-lid with a Pt-ring on a SiC MEMS test vehicle (Figure 2).

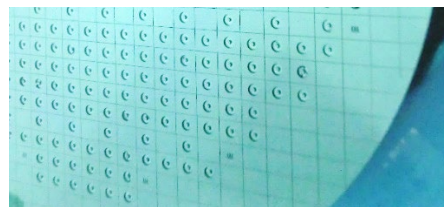


Figure 2: SiC MEMS test vehicle sensor (back-side) wafer Pt-metallized.

The leak-tightness of LADB bonding has been validated on SiC MEMS test-vehicle samples. However, the LADB bonding of sensor chips needs further improvements as the quality of the bonding interface is key to achieve high yield. The improvements currently under investigation consist in adjusting the masking material and etching recipe for SiC etching to guarantee particle-free mask removal and hence clean surfaces for bonding.

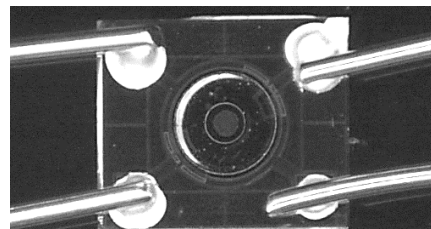


Figure 3: SiC MEMS absolute pressure sensor with reference cavity and Pt-wire bonds assembled (by hand) with Ag-sintering paste.

Functional MEMS pressure sensor prototypes were packaged by exploiting a back-up solution i.e., by using a silver sintering paste for both back-side reference cavity bonding and for Pt-wires interconnections on the front side. These MEMS prototypes will be measured to confirm sensitivity and stability of the pressure sensor up to the operating temperature of 650°C.

This work has been supported by InnoSuisse.

[1] J. Castaing, P. Veyssi  re, L. P. Kubin, J. Rabier, "The plastic deformation of silicon between 300°C and 600°C", <https://doi.org/10.1080/01418618108235821>

[2] K. Niihara, "Slip systems and plastic deformation of silicon carbide single crystals at high temperatures", [https://doi.org/10.1016/0022-5088\(79\)90161-9](https://doi.org/10.1016/0022-5088(79)90161-9)

[3] A. Hoogerwerf, et al., "Silicon Carbide Pressure Sensor Characterization", CSEM Scientific and Technical Report (2021) 64.

[4] R. Jose James, et al., "Low temperature hermetically sealed, optically transparent miniature packages: from medical to space", <https://doi.org/10.1109/ECTC32696.2021.00265>

PMUT-based Acoustofluidic Devices using Highly Piezoelectric AlScN Layers

E. Vuille-dit-Bille, M. Dubois, D. Bayat, T. Overstolz, S. Heub, G. Weder, M. Despont

Piezoelectric materials find numerous applications in life science. Particularly, they are integrated in acoustic-based devices for sensing, imaging, and manipulation of objects. The manipulation of big biological entities such as microtissues is crucial for the growth of personalized medicine. Therefore, CSEM is combining its expertise in piezoelectric layers and life science to develop an acoustofluidic platform to manipulate and position microtissues.

In the past years, a new piezoelectric thin film material, aluminum scandium nitride (AlScN) has attracted increasing attention due to its improved piezoelectric performances compared to its predecessor aluminum nitride (AlN). The substitution of some Al atoms by Sc in the lattice has been demonstrated to considerably increase the piezoelectric coefficient of the layer. Consequently, AlScN thin films are becoming a serious competitor of the well-established PZT thin layers. One major advantage of AlScN over PZT is its relatively moderate sputtering temperature which enables deposition on a large range of materials including polymers. Additionally, thanks to its good piezoelectric performance, AlScN layers can be used in miniaturized devices.

The deposition of AlScN is challenging as the process needs to be carefully optimized in order to avoid the growth of abnormal non-piezoelectric grains and reduce internal stress. On membrane-based devices, a not fully controlled process can lead to stress variation in the range of 1 GPa. CSEM has mastered the necessary process steps (the bottom electrode material, the growth by reactive sputtering at moderate temperature and the etching of these layers) to produce high-quality piezoelectric films with a Sc content of 30% and is now incorporating this technology in devices.

Acoustophoresis is a well-established technique that uses non-contact forces arising from sound pressure fields to manipulate various suspended particles such as bubbles, nanoparticles, or biological entities. By vibrating, piezoelectric materials generate acoustic standing waves, thereby creating zones of minimal pressure to which cells and microtissues are pulled and trapped. Common piezoelectric transducers used in acoustophoresis are PZT bulk transducers or interdigital transducers made of lithium niobate. CSEM intends to leverage the potential of AlScN thin films to create innovative miniaturized membrane-based devices to manipulate and position microtissues.

Due to the big size of microtissues, ranging from 100 μm to a few mm in diameter, large forces are required for their manipulation. Sufficient acoustic power is achieved by producing silicon membranes which are deflected by thin $\text{Al}_{0.7}\text{Sc}_{0.3}\text{N}$ layers. These layered membranes are called piezoelectric micromachined ultrasound transducers (PMUT). CSEM is developing an acoustofluidic platform (Figure 1) containing a PMUT array to levitate microtissues into a single plane and arrange them in defined patterns. The platform is closed by a glass lid, which reflects the acoustic waves generated by the membranes and produces vertical standing waves.

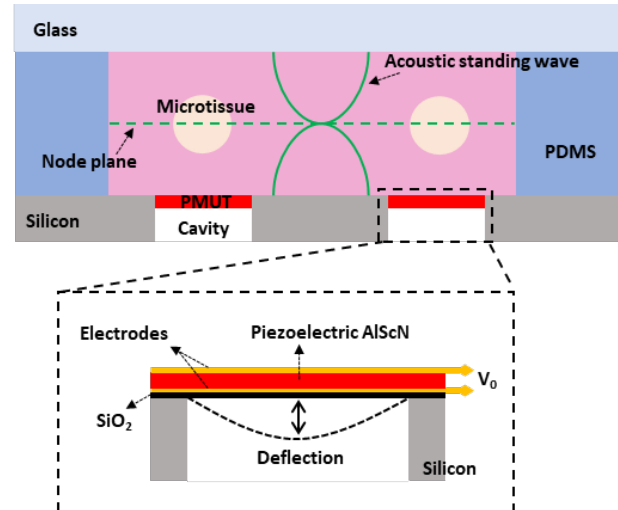


Figure 1: Schematic view showing the acoustofluidic positioning device and PMUT layout. [1]

A FEM software (COMSOL Multiphysics) was used to study the performances of the platform. The Gor'kov potential, i.e., the potential associated to the acoustic force, was simulated for a device containing four PMUTs in a row (Figure 2). With an optimized design, four Gor'kov minima are forming above the PMUTs. These regions serve as strong acoustic traps for microtissues. Additionally, simulations have shown that trenches around the PMUTs are required to achieve sufficient acoustic power for levitating 200 μm diameter microtissues. The mechanical decoupling between the edges of the PMUTs and the substrate results in large membrane deflection and thus high acoustic power. In conclusion, the FEM study showed that microtissues can be levitated on a unique plane and in a defined pattern using AlScN thin films.

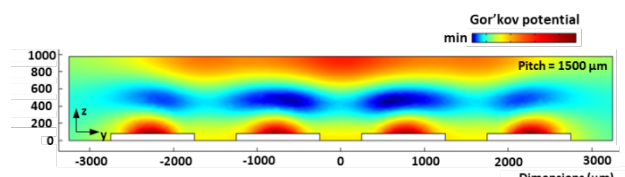


Figure 2: Gor'kov potential generated by 4 PMUTs at $f_{\text{res}} = 777 \text{ kHz}$ and $V = 50 \text{ V}$. Color indicates the intensity of the potential. [1]

The acoustofluidic platform is under further development and test devices are currently produced to verify the simulations on microtissues positioning.

[1] E. Vuille-dit-Bille, et al., 2022 Acoustofluidic conference, Glasgow, Scotland. Reproduced with permission from the Chemical and Biological Microsystems Society (CBMS). Copyright 2020 CBMS.

Coolers for RF and LF Power Modules

A. Hoogerwerf

The ever-increasing power density of power electronics necessitates innovative solutions to remove the generated waste heat. We are currently working on using MEMS-based two-phase fluidic coolers that will have heat conduction properties that are better than copper or silver. Moreover, the MEMS-based technology uses silicon or silicon carbide substrates that match more closely the thermal expansion coefficients of the electronics than the metals do. The packages based on these coolers are aimed for use in satellites but will also find their way in terrestrial applications.

The evolution of semiconductor technology has led to ever-improving performances of the fabricated transistors. This leads to higher density circuits that switch even higher amounts of power. The drawback of this is that high power density "hot spots" become more frequent in these circuits. An effective removal of this waste heat is necessary to limit the temperature rise in these areas, as the temperature increase leads to a degradation of the circuit and reduces its lifetime.

An effective way of removing heat is presented by oscillatory heat pipe loops. The functioning of such loops is schematically presented in Figure 1. The top side of the structure is attached to the heat generating device and the bottom one is attached to a heat sink. The structure is partially filled with a liquid under low pressure. Once the heat is turned on, a part of the liquid evaporates to form gas bubbles. The design of the loop with its alternation of wide and narrow parts, makes that the bubbles move back and forth in a chaotic way between the hot and the cold part of the structure. Each time a bubble reaches the cold side of the structure it condenses (partially), giving off the latent heat of evaporation of the fluid that it has obtained during the bubble formation on the hot side. The physical movement of the bubble therefore moves the heat from the hot side to the cold side. If the cross-sectional area of the loop channels is small enough, the effect of the orientation on the functioning of the structure is minimal and it can be used in micro-gravity environments, such as space. Moreover, the heat pipe loop can be made small enough, so that it has the size of a power electronics package and can therefore become a part of it.

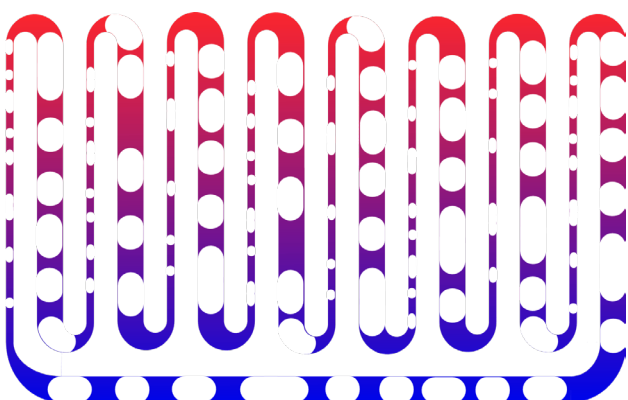


Figure 1: Schematic representation of an oscillatory heat pipe loop.

Within the EU project HEATPACK (<https://heatpack.eu/>), the oscillatory heat pipe loop is pursued for two high-power electronics packages for use in satellites. In a first phase, test structures have been made out of silicon-glass sandwiches. The glass is a poor thermal conductor and, therefore, in a second phase, has been replaced by silicon carbide (SiC). SiC is a good thermal conductor and is also optically transparent. It is bonded to a structured silicon wafer using gold-gold thermo-compression bonding. For this reason, the SiC wafer is covered with a gold layer that is patterned to only leave the gold in the bonding areas. A silicon wafer is structured with the heat loop pattern and the inlet port on its backside. The wafer is subsequently covered by

gold on both sides. The SiC and silicon wafers are aligned and then pressed together at high temperature in order to achieve the thermocompression bonding. A schematic cross-section of the resulting structure is shown in Figure 2. The gold on the backside of the silicon wafer allows for easy attachment to the heat generating circuit.

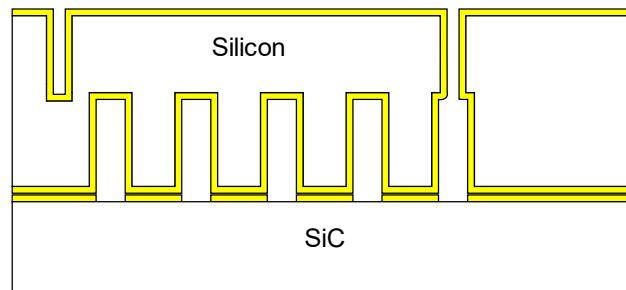


Figure 2: Schematic cross-section of a bonded Si-SiC cooler.

The heat pipe layouts etched in the silicon wafer correspond to the base and top plates of RF and LF power electronics modules developed in the HEATPACK project.

A picture of the patterned SiC wafer just prior to bonding is shown in Figure 3a. The black areas on this picture are actually transparent. A die after bonding is shown in Figure 3b

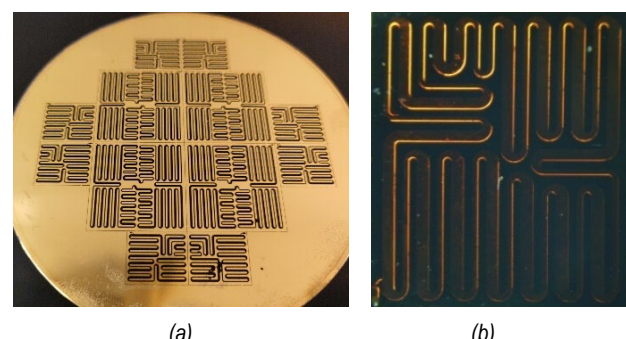


Figure 3: a) Patterned SiC wafer just prior to bonding, and b) die after bonding.

The bonded dies will be filled with the coolant liquid and the inlet will be closed before being integrated in the HEATPACK modules.

CSEM acknowledges funding from the European Union's HORIZON 2020, Space Research Program, Technologies for European non-dependence and competitiveness, under grant agreement No 821963.

Laser Assisted Wafer Level Encapsulation / Benchmarking with State-of-art Technologies

R. Jose James, M. Renggli, G. Spinola Durante, K. Krasnopolski

Hermetic sealing is very important for long term reliable functioning of microsystem components like micro-electro-mechanical systems (MEMS). There is a lack of scalable sealing methods, which can be realized at low temperatures of less than 150°C. CSEM has developed a sealing technology based on localized heat application using a cost-effective continuous wave (CW) / millisecond pulsed fiber laser. This sealing process has been scaled to wafer level and successfully tested for long term reliability, low temperatures sealing and high throughput.

Hermetic sealing has become an integral part in manufacturing of electronic devices. There are many different reasons for using hermetic sealing, such as having specific atmosphere, or vacuum for improvement of the quality factor of a MEMS resonator or a reference cell containing Rubidium gas for an atomic clock. The main reason why hermetic sealing is widely used for electronic devices, however, is to protect it from moisture, which is a requirement for long term reliable operation [1].

Commonly applied state-of-art (SoA) hermetic sealing methods with proven scalability are solder-based bonding, glass frit bonding, anodic bonding and thermo-compression bonding. The bonding technology needs to be selected based on the application requirement and applicability. There are many different parameters that need to be considered for applicability of a sealing method for a specific device. Key parameters in this respect are bonding temperature, area needed for bond frame on the wafer, complexity of applying the bonding layer, achievable bond strength, vacuum suitability, and throughput. Most of SoA technologies require a temperature of more than 300°C to achieve a hermetic bond.

A laser-based sealing technique named 'LADB' [1] was developed for low temperature sealing. The sealing is achieved by localized heating to bond a lid on to a substrate with a cavity, so that sensitive components inside millimeter scale compartments are kept at low temperatures of less than 100°C. With a bond frame width as low as 30 µm, using only thin film deposition techniques for bonding layer deposition, a high bond strength of 195 MPa (on sapphire packages), both high hermeticity and processing speed, LADB outperforms SoA technologies in key aspects and has proven to be equivalent in many others. The main advantages of the method in comparison to SoA are clearly the low temperature (<100°C versus >300°C) and throughput (few minutes versus tens of minutes up to an hour).

This process was initially developed on chip level for packaging of temperature sensitive components for use in Active Implantable Medical Devices (AIMDs) and space applications. Some examples of manufactured chip level packages with integrated devices using this technique can be seen in Figure 1.



Figure 1: Sealed glass and sapphire packages with VCSEL and micro-lenses integrated inside (left); Implantable sapphire packages (right).

These packages were tested for reliability in space relevant conditions and for applicability in AIMDs as can be seen in Table 1. The packages successfully passed all these harsh tests. The bonding was also tested to be stable up to 500°C.

Table 1: Reliability tests carried out on packages.

| Test | Thermal cycling | Glass cracking test | Mechanical shock | Vibration testing | Saline immersion | Moisture resistance |
|------------|---------------------------|---|---------------------------|-------------------------------|---------------------------------------|--|
| Parameters | -40 to 125°C, 1000 cycles | 2°C to 98°C cold/hot bath in 3 seconds, 10 cycles | 1000 g, 0.5 ms, 30 pulses | 5 Hz up to 2000 Hz, 12 Sweeps | Physiological saline, @95°C for 1000h | 65 °C and 90 % RH, 10 cycles, 3 h Dwell time |

The technology was scaled to wafer level (100 mm diameter) as can be seen in Figure 2. Here, we could see the second advantage of the sealing method, which is the throughput. One wafer can be sealed in less than 10 minutes (process time).

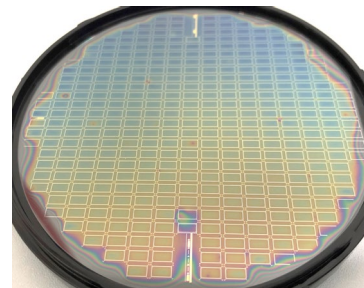


Figure 2: Glass wafers bonded using laser bonding technique.

The prototype stage wafers have an average dicing yield of 95%, which is expected to increase largely in a dedicated production environment. The diced parts as seen in Figure 3 were subjected to liquid penetration testing, shear testing and helium leak tests. An average shear strength of 94 MPa with a standard deviation of 5 MPa was achieved on bonded glass wafers. No leaks were detected during liquid penetration testing or helium leak tests.

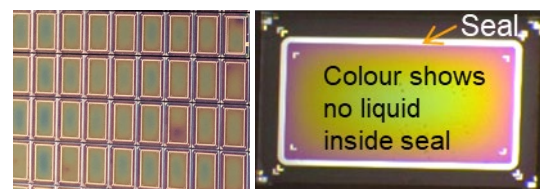


Figure 3: Diced wafer (left); liquid immersion leak testing (right).

Further ongoing investigations on process modifications reveal even faster wafer bonding in less than a minute using this technique, which is much faster than SoA processes.

We acknowledge the financial and technical support provided by European Union, European Space Agency and Switzerland State Secretariat for Education, Research, and Innovation.

[1] R. J. James, et al., "Low temperature hermetically sealed, optically transparent miniature packages: from medical to space," IEEE ECTC, 2021, pp. 1673-1681.

High Aspect Ratio 3D Pyramidal Probes on CMOS MEA's for in vitro Tissue Model Study: Fabrication and Biological Validation

P. Surbled, J. Schildknecht, F. Cardot, O. Dubochet

CSEM SA in collaboration with 3Brain AG develops high aspect ratio 3D pyramidal probes on CMOS multi-electrode arrays (MEAs) for the characterization of brain cells and other type of cells. Manufacturing technologies have been modulated to obtain probes of different shapes and aspect ratios, which are tested on various tissues. The first 3D probes showed good results with a higher sensitivity than 2D probes.

Brain diseases are one of the biggest challenges in our society, impacting one-third of the population and undermining the sustainability of the healthcare system. Advanced biotechnologies such as human stem cells or 3D cultures (e.g., spheroids, organoids) promise to improve brain drug discovery. However, the appropriate instruments to measure those samples are not yet on the market.

The company 3Brain develops high-resolution CMOS-based devices to be implemented in a new generation of instruments allowing to characterize brain cells. CSEM participates in this development, adding in a post-process on CMOS wafers 3D probes that penetrate in the tissues and increase the measured signal level. Different types of probes are tested by varying the height, width, and stacking of the probes as well as adding a passivation layer. Some examples are schematized in Figure 1.

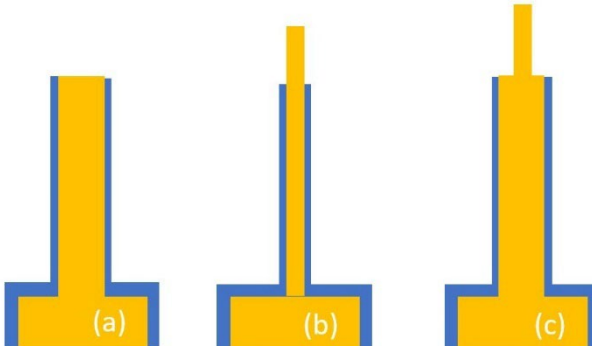


Figure 1: Schema of long probes (a) passivated, (b) fine and partially passivated, (c) with a second probe on the first one.

As displayed in Figure 2, a SU-8 dry film is laminated on a CMOS wafer covered previously with a thin titanium layer. The dry film is exposed, baked in oven, and developed in a PGMEA solution (A). After etching the Ti layer in the openings, the SU-8 mold is filled with electroplated gold and planarized (B). These steps can be repeated to form a pyramidal pillar shape as depicted in Figure 1c. After removal of the stack of SU-8 dry-films and Ti layers, parylene is deposited on the whole wafer (D). For the opening of this insulation layer, the wafer is levelled with a plating step. Subsequently the wafer is planarized which removes the parylene cap at the top of the probes (E). The parylene can then be removed along the upper segment of the probe between the plated layer and the gold probes (F). At the end the plated metal is removed, releasing the passivated probes. Examples of passivated probes are shown in Figure 3a, 3b, and 3c.

The CMOS chips were packaged and tested. Figure 4 shows the spiking activity recorded from the same cerebellar slice, measured respectively with planar (2D) chips (top row), and with 3D chips (bottom row). The 3D chips are showing a far better performances with an increased number of sensed cells and a better signal-to-noise ratio.

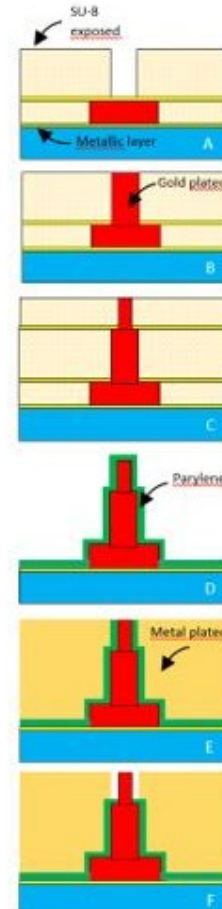


Figure 2: Process flow 3-level plating in dry film SU8 moulds and passivation.

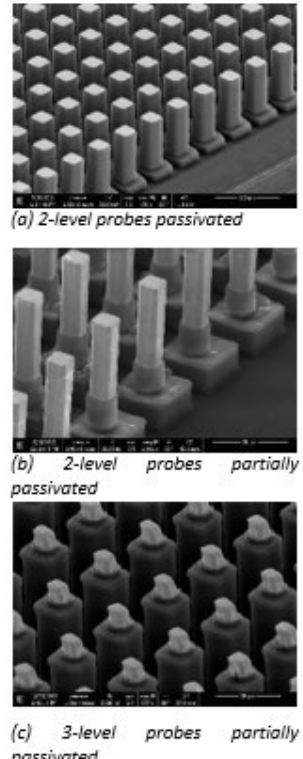


Figure 3: Various kind of probes partially or completely passivated.

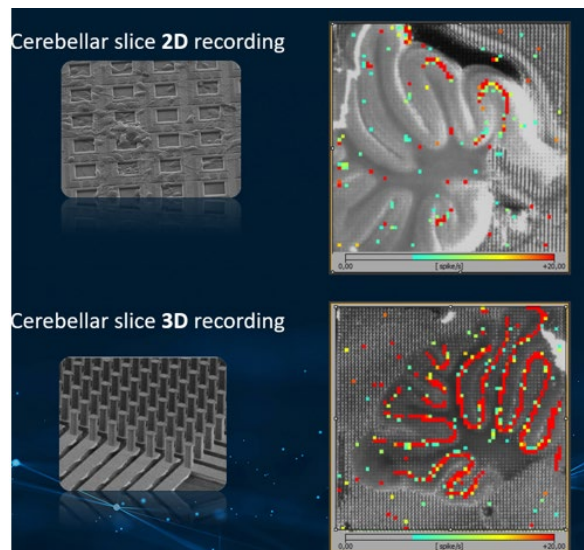


Figure 4: Recording of cerebellar cells using 2D (top) and 3D chips (bottom).

Elaboration of the Reliability Assessment Methodology for RF Electromechanical Relays in Space Applications: Bi-parameter Thermal – Mechanical Stress Testing

I. Marozau, S. Unterhofer, M. Dagon, O. Sereda, M. Berry*, P. Gonin*, G. Aubry*, A. Flaceau*, R. Enquebecq*

The reliability of the developed radiofrequency (RF) miniaturized electromechanical relays (MEMR) against a simultaneous application of thermal and mechanical stresses was studied. These stresses are likely to simultaneously occur during the spacecraft launch phase. The main aim was to elaborate the reliability methodology and to evaluate the MEMR performance under mechanical loads at various elevated temperatures. The developed methodology was applied to identify the limits at which the mechanical MEMR robustness is in accordance with the defined product requirements for space applications. This approach allows to define the mechanical load margins under different thermal conditions that are closer to the possible real operation conditions as opposed to the state-of-the-art room temperature testing.

Reliability testing and qualification for space applications is traditionally based on the existing ESA standards (e.g., ESCC). Each standard generally represents a fixed single stress factor testing under well-defined conditions at which the device has to perform without failure. In real operations, however, a combination of different environmental factors influences the reliability of components, with the risk of overstressing them beyond the nominal single stress parameter requirement. Some of the currently applied test procedures for space evaluation do account for such scenarios: combination of humidity and high temperature; combination of electrical load and temperature.

One of the most overseen and underestimated combinations is mechanical loads at high temperature. This kind of stress factors are likely to simultaneously occur during the spacecraft launch phase. However, there is no existing reliability standard that targets this scenario.

Within the framework of SELECTOR EU project (grant number 821973), CSEM has developed a test program that can be used for the reliability assessment and evaluation of the RF MEMR components under mechanical loads at high temperature, which was approved by the MEMR device manufacturer Radiall. The test program consists of two tests:

- Thermal – mechanical vibration: sine sweep and random
- Thermal – mechanical shock

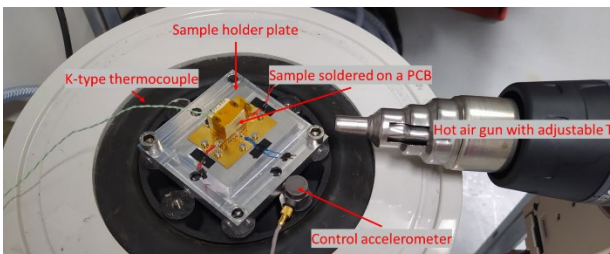


Figure 1. Arrangement of the device during the thermal-mechanical vibration testing.

The tests are performed at discrete temperature steps (from room temperature up to the maximum specified operation temperature). Within each temperature step the mechanical load is progressively increased until the device failure occurrence (or until the maximum possible equipment load is reached). A special setup was designed and constructed for carrying out the thermal-mechanical tests (Figure 1). The setup allows to change and control the device temperature while performing the required mechanical test. Failure evaluation was performed by measuring

the RF and DC characteristics of the device before and after the test. The electrical state of the MEMR was also in-situ monitored during the test using a specially designed test bench.

The developed bi-parameter test program was applied for the MEMR switches from Radiall, which were designed for the primary use in space applications. In the first stage, 3 samples were subjected to progressively increased mechanical vibration loads (sine sweeps and random) at consecutively increased temperature steps of 50°C, 75°C, and 100°C. All devices have successfully passed the tests at the maximum possible vibration acceleration level of 50 g at each temperature.

A similar procedure was also applied for the combined thermal – mechanical shock testing. Three groups of 3 samples each were subjected to progressively increased mechanical shock loads at three temperatures, respectively.

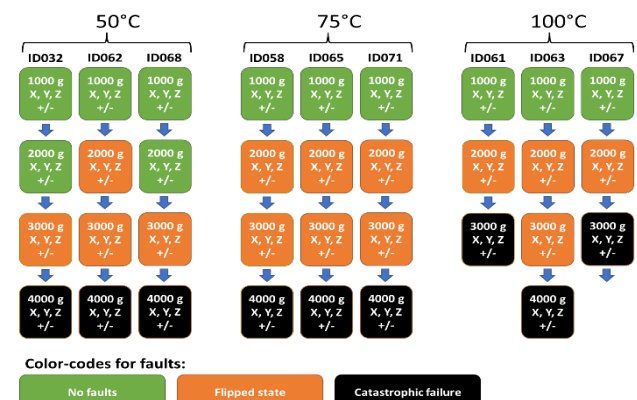


Figure 2. Results of thermal – mechanical shock tests at the temperature levels of 50°C, 75°C, and 100°C.

The obtained results are shown in Figure 2. At the temperature levels of 50°C and 75°C all tested devices withstood the required shock acceleration of 3000 g, whereas 2 out of 3 DUTs tested at 100°C failed at 3000 g. This indicates that the mechanical shock resistance of the MEMR starts to deteriorate at temperatures above 75°C. The shock acceleration level at which the relay state flipping (non-catastrophic fault) was observed also gradually decreases with the temperature increase.

The developed bi-parameter testing approach allows to define the mechanical load margins under different thermal conditions that are closer to the possible real operation conditions as opposed to the state-of-the-art room temperature testing. The developed MEMR devices have demonstrated a very good robustness against mechanical loads at high temperatures.

• Radiall, Aubervilliers, France

Ultra-sensitive Photonics Accelerometers for Next-generation Seismic Sensor Networks

A. Manzoor, F. Ebrahimi, H. Sattari, D. Bayat, A. Hoogerwerf, M. Despont, A. H. Ghadimi

Seismic sensors are powerful, highly versatile, and cost-efficient tools used in a wide range of applications with specific requirements in terms of frequency response and sensitivity. In this SNF funded project, CSEM joins forces with the Swiss Seismic Institute at ETHZ, to develop and field test a new generation of opto-mechanical accelerometers and seismic sensors capable of reaching nano-g level sensitivities with ultra-high bandwidths.

Seismic sensors can record seismic waves with frequencies from 1 Hz to more than 1 MHz and can be used in two modes: 1) Imaging of seismic events and their evolution with time, which are related to transients in material properties, fluid flow, and stress evolution; 2) Monitoring of tiny fractures, cracks or micro-earthquakes that are an indication of material fatigue or accelerating failure processes. Sensors can be deployed on concrete or steel, for example, for structural health monitoring of buildings, dams, bridges, or wind turbines. They can also be deployed in deep boreholes, detecting micro-earthquakes during the reservoir creation of geothermal sources, oil and gas exploration, and operations, or monitoring mining operations and the integrity of nuclear repositories. Moreover, they can also be used as scientific instruments to better understand fluid-rock interactions or the initiation and propagation of catastrophic natural and induced earthquakes. Finally, these sensors may be deployed in future space missions.

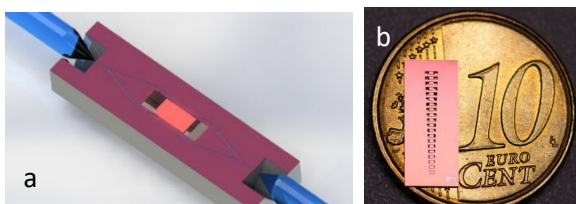


Figure 1: a) Schematic 3D design of OPOSSUM sensors showing optical fiber and waveguides (blue) and test mass at the center (red). b) Optical image showing an array of 20 fabricated test masses on a silicon chip illustrating a central silicon mass suspended with SiN tethers providing high Q (image on top of 10 cent Euro coin for scale).

The OPOSSUM (OPtOmechanical Seismic Sensor for Ultra-high-resolution Monitoring) project exploits theoretical and experimental advances in the field of opto-mechanics in the last decade as well as a significant improvement in microfabrication and modeling of high-quality integrated photonics circuits (PIC) and ultra-high Q (UHQ) mechanical resonators (Figure 1a). These two technological building blocks are at the core of a new generation of miniaturized, fully integrated ultrasensitive seismic sensors that are developed at CSEM, with capabilities far exceeding the current generation of sensors in numerous ways:

- Ultra-low noise thus ultra-sensitive [$<100 \text{ ng}/\sqrt{\text{Hz}}$]
- Ultra-wide frequency range [1 Hz - 50 kHz]
- High dynamic range [$>140 \text{ dB} \equiv 24\text{bit digitizer}$]
- Low-cost at large manufacturing volume
- Absolute amplitude calibrated → [Reliable magnitudes]
- 3D directionality with more than 20 dB reduction of off-axis signals
- Passive recording, optical fiber readout → Enabled for harsh environments (high temperature, pressure, low power, and lifetime not limited by embarked electronics)
- Optical data transmission → Long distance recordings
- Multiplexing capability → Sensor array on one single fiber
- Small form factor [$<1 \text{ cm}^3$] → Deployment in tight spaces

The combination of these capabilities is truly unique on the market and will enable us to push the current limits of existing applications and enable new applications currently not possible or not even envisioned. It will, for example, have the capability to enhance GeoEnergy reservoir developments and risk mitigation strategies greatly.

To achieve this level of performance in noise floor and sensitivity, all optical, electrical, and mechanical noise sources have to be addressed. While some of these noise sources are fundamental (e.g., thermo-mechanical noise of the test mass and shot noise of the laser), others are technical (e.g., electronics Johnson noise). At the fundamental limit, the thermo-mechanical noise of the test mass often limits the performance of the accelerometers, especially at lower frequencies.

The aim of the first year of this multi-year project was to simulate, optimize, implement, and measure the mechanical test mass capable of achieving the target performance. Three different sensors are envisioned with different resonant frequencies: 1 kHz, 10 kHz, and 50 kHz. Each of these correspondingly has a different bandwidth and a different required noise floor of 5, 30, and $100 \text{ ng}/\sqrt{\text{Hz}}$, respectively. The thermo-mechanical noise is dependent on the quality factor, resonance frequency, and test mass. The ultra-high-quality factor is made possible using prestressed ($\sim 1 \text{ GPa}$) silicon nitride nano-beams, while a central silicon block provides large enough mass to achieve the target sensitivity. Moreover, a series of compliant (spring-damper) elements constraining the motion of the resonator mass in other directions provides high directionality.

The sensing scheme also requires uni-axial sensitivity, i.e., the resonator would need to be primarily sensitive to vibrations in only one direction. This must be the direction of its fundamental vibration mode that has the most energy, while the frequency of its higher order modes has to be pushed to higher frequencies. Thus, it is essential to ensure that the frequency of the second mode is sufficiently larger than the first mode. This fact ensures that the only significant motion is that of the primary mode. Multi-directional sensing is possible by using 3 different sensors oriented orthogonally to each other.

A simulation study was done to obtain 3 different resonator geometries corresponding to each of the 3 resonant frequencies, and corresponding noise performances. A novel design for the resonator mass was considered for this project, allowing a fair frequency separation (frequency ratio $f_2/f_1 = 2$), and a sufficiently large mass for low thermal noise while constraining it to the right resonance frequencies.

Finally, devices are fabricated using a unique silicon micro-machining technology (Figure 1b) and have to be measured using optical interferometry in high vacuum ($<10^{-6} \text{ mbar}$) to prevent gas damping of the mechanical vibrations.

Packaging of PICs for Fluidic Applications

M. Fretz, R. Arnet, S. Graf

Novel adhesive bonding techniques developed at CSEM allow for leak-tight integration of photonic integrated chips (PICs) in fluidic systems. Our economical approach helps to bring down the costs of disposable fluidic/diagnostic devices. Such units may be deployed as diagnostic tools in health care at the point of care or e.g., as a photonic biosensor platform for use in aquaculture.

With the advent of photonic integrated chips (PICs), quantitative measurement of biomarkers (e.g., pathogens, proteins, antibodies) is no longer restricted to central laboratories with expensive equipment. Today small and inexpensive disposable units are becoming deployed in the field. Whereas lateral flow assays require labeled reagents and provide semi-quantitative results at best, PIC based units may provide label-free quantification with high sensitivity at the point-of-care (PoC) [1].

As a member of the EU-project PHOTO-SENS, CSEM and its partners develop a single-use fluidic cartridge as part of a biosensor platform for the detection of e.g., pathogens in aquaculture. These disposable units require the integration of photonic biosensor technology in the shape of PICs. The combination of fluidic as well as electronic integration pose new technical challenges to the integration process. Furthermore, the envisaged use as a disposable cartridge at the PoC requires an assembly process compatible with mass manufacturing.

Novel adhesive bonding techniques allow for such a low-cost integration process of the PIC. Following aspects are important when designing the cartridge for mass production:

- Automatic pick and place of PIC
- Electronic signal to/from PIC top and bottom surface (might not apply to all PICs. Some or even most will feature all electrical contacts on a single side)
- Alternatively, some PICs will feature optical facets instead of electrical connections. These must remain unblocked and free of adhesives
- Leak-tight seal of the sensor area of the PIC in the fluidic channel

The PIC may feature both a sensitive area to be integrated in the fluidic channel as well as electric connections to the outside world on the top surface. These areas must be separated in a leak-tight fashion. The PIC in the here-presented cartridge has electric connections on both sides. Therefore, the integration process requires following steps:

- Application of an adhesive on the substrate for PIC bonding. This must be applied selectively. The adhesive layer needs to provide openings for the electrical connections.
- Dispensing of electrically conductive adhesive (ECA) on the substrate to provide electrical connections to the bottom contacts of the PIC. The ECA is applied in the openings of the adhesive layer (see first step)
- Pick and place of the PIC. This step also provides electrical connection to the backside contacts of the PICs via the previously dispensed ECA

- Placement of a plastic sheet containing fluidic channels and connections over the PIC.

The assembled prototype is shown in Figures 1 and 2. Through the inlet the sample liquid is brought over the PIC to the outlet. Only the active area of the PIC is within the channel, which poses a challenge to the leak-tight seal. CSEM has overcome this problem with various novel sealing techniques involving the application of double-sided tapes and/or liquid adhesives.

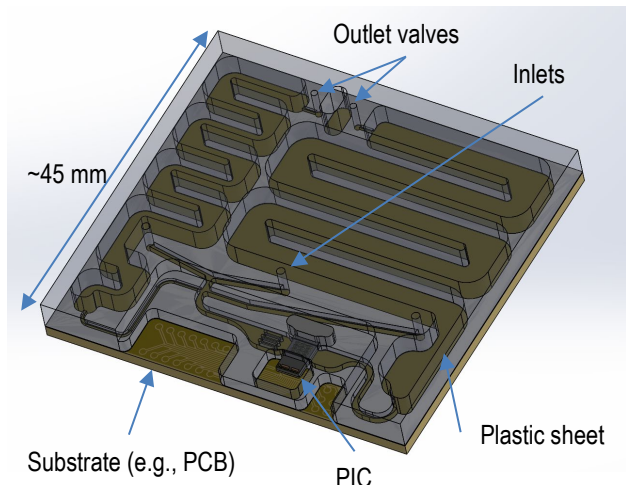


Figure 1: CAD drawing of the single-use cartridge with integrated PIC as part of the biosensor platform. The top transparent part is the plastic sheet with fluidic channels.



Figure 2: Assembled demonstrator from Figure 1. Part of the PIC extends beyond the fluidic channel to expose the electrical connections.

This project has received funding from the European Union's Horizon 2020 research and innovation program under grant agreement No 965643.

[1] D. J. Steiner, B. L. Miller, "Photonics-enabled lateral flow assay diagnostics", Proc. SPIE 11662, Frontiers in Biological Detection: From Nanosensors to Systems XIII, 116620F (5 March 2021).

Additive Manufacturing of Metal Matrix Composites for Space Applications

G. Bernard, V. Pejchal, R. Logé, L. Pambagui, O. Sereda

Metal Matrix Composites (MMCs) offer the toughness and ductility of a metal with the high stiffness and strength of a brittle reinforcement phase (usually ceramic) that allow to engineer the needed properties for a specific application. Specific Young's modulus is improved since the applied load is borne by the stiff reinforcement^[1]. Titanium alloys are materials of choice for space applications due to their high-stiffness-weight ratio and corrosion resistance. Whereas titanium carbide is interesting as reinforcement because no fragile phases are formed, and good particle-matrix bonding can be obtained. The present study showed excellent mechanical properties improvement. LPBF titanium based MMC parts exhibited Young's modulus of 149 ± 17 GPa ($33 \text{ GPa} \cdot \text{cm}^3 \cdot \text{g}^{-1}$), an improvement of more than 27% compared to the conventional titanium alloys.

This study focused on titanium specific stiffness improvement by producing MMC by Additive Manufacturing. In particular, LPBF was used to produce Ti matrix reinforced by 12 vol.% of TiC, namely Ti12TiC. The raw powders used were: (i) Ti grade 2 gas atomized ($D_{50}=31 \mu\text{m}$), (ii) aggregated TiC pseudo-spherical particles ($D_{50}=167 \mu\text{m}$). The powder blends were mechanically mixed.

The following section focus on development of LPBF process for Ti12TiC MMCs. Firstly, single-line walls (consecutive layers of single-track) were studied to narrow down the laser power and scanning speed window (Figure 1a). Design of experiment (DoE) was performed to optimize the recipe and study the effect of laser power, laser scanning speed and hatch distance on the relative density of cube specimens (Figure 1a). Among the best parameters, several cubes were printed to assess the repeatability of the process. The porosity of material cubes with the highest overall density showed relatively variability in the range of 0 to 0.8%. A representative microstructure of tensile bar printed with the best parameters is shown in Figure 1b) where TiC is observed in both forms: (i) un-melted stoichiometric TiC particles and (ii) sub-stoichiometric dendrites. It is assumed that the lower size fraction of TiC is dissolved into molten Ti during the LPBF process and precipitated as dendrites during the rapid cooling of the sample. Tensile bars were subsequently heat-treated at 880°C to coarsen and homogenize the TiC microstructure as well as relieve residual thermal stresses. Figure 1c and 1d show, respectively, an observed microstructure after 24hs and 196hs of heat-treatment.

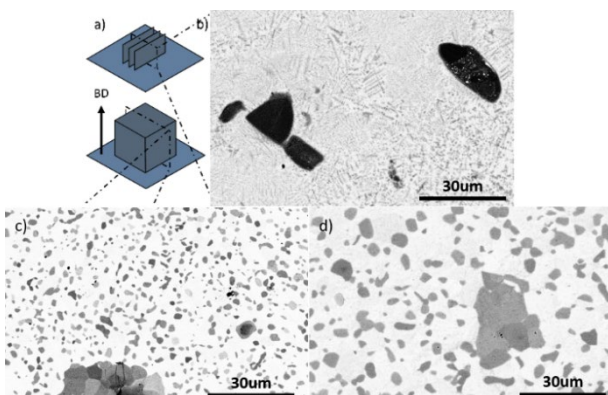


Figure 1: a) schematic illustration of single-line walls ($4 \times 6 \text{ mm}^2$) and cubes ($5 \times 5 \times 5 \text{ mm}^3$); SEM micrographs of mirror polished cross section of b) as-built Ti12TiC, c) 24h heat-treated Ti12TiC d) 196h heat-treated Ti12TiC.

Mechanical properties of as-built and heat-treated MMCs as-well as as-built Ti reference were measured using tensile test experiments, see Figure 2. The Young's modulus of the MMC was increased to 149 ± 17 GPa in as-built condition. It is more

than 25% increase compared to the reference Ti sample in the same condition (117 ± 7 GPa). The specific Young's modulus calculated for the latter, using the theoretical density, was $33 \text{ GPa} \cdot \text{cm}^3 \cdot \text{g}^{-1}$. Similarly ultimate tensile strength was increased from 576 ± 4 MPa to 723 ± 19 MPa in as-built condition. On the other hand, the elongation drastically dropped to $0.7 \pm 0.1\%$. The heat treatments induced a grain growth from $1.7 \pm 0.5 \mu\text{m}$ to $6.4 \pm 1 \mu\text{m}$. It also allowed to increase elongation to $1.4 \pm 0.2\%$ after 24h and $3.1 \pm 0.3\%$ after 196h. This is explained by the TiC grain growth as well as the stress relieve induced by the heat treatment. A smaller effect was observed on ultimate tensile strength with an increase to 891 ± 8 MPa after 24h and to 850 ± 19 MPa after 196h. Young's modulus was not influenced by heat treatments.

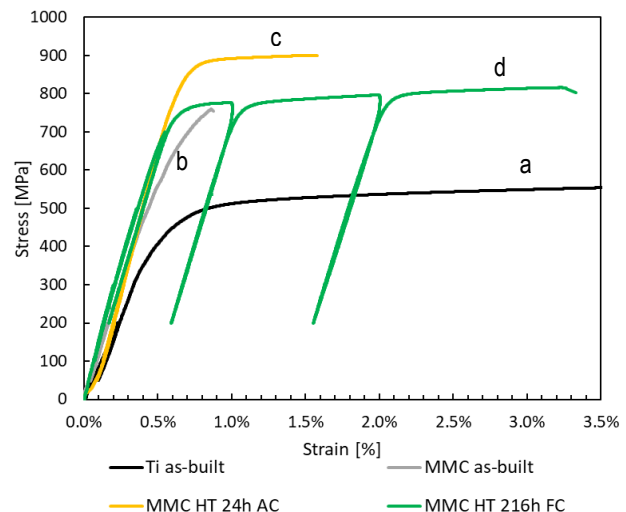


Figure 2: Tensile stress-strain of as-built and heat-treated MMCs as well as Ti reference with a) Ti in black, b) as-built Ti12TiC in grey, c) 24h heat-treated Ti12TiC in yellow, and d) 196h heat-treated Ti12TiC in green.

In conclusion, this study shows a process to produce near net-shape and extremely low porosity Titanium reinforced by Titanium Carbide MMC. The mechanical properties of this MMC are strongly improved compared to the pure Titanium reference sample. In particular, an outstanding specific Young's modulus of $33 \text{ GPa} \cdot \text{cm}^3 \cdot \text{g}^{-1}$ was achieved. It is 27% higher compared to the typical titanium alloys^[1,2]. Thanks to those improved mechanical properties, new designs of lightweight parts become available which will contribute more efficient space exploration. Further studies on the topic will be undergone to improve even more mechanical properties and refine the process.

This work was partly funded by ESA. CSEM thanks them for their support.

[1] A. Hauert, et al., J. Mech. Phys. Solids 57 (2009) 473-499.

[2] D. R. Lide, ed. (1999). 'Commercial Metals and Alloys'. CRC Handbook of Chemistry and Physics (80th ed.).

MADAM – Damped Flexures Based on Additive Manufacturing

L. Salamin, H. Saudan, F. Cosandier, L. Kiener, E. Klauser, N. Blondiaux, F. Boudoire, N. Kalentics, S. Henein*, L. Tissot-Daguette*

This project is part of the research on precision compliant mechanisms relying on additive manufacturing. It consists in designing, manufacturing and testing a novel type of flexures that integrates a damping action. Indeed, as compliant mechanisms are sensitive to vibrations and shocks, developing robust and reliable damping systems is of prime importance. The impressive damping performances observed during this project open opportunities in numerous domains such as space, watch making, robotics, metrology, or automotive. Beyond mechanism applications, this elementary damped flexure element could be tailored in terms of shape and size and used as a building block to develop new structural damper topologies.

The novel flexures designed in this project were double blades with lattice features^[1]. As illustrated in Figure 1, the double blades are composed of a master blade which is thicker to lead the double blade motion and a thinner slave blade. The idea behind this concept of two blades of different thickness is to avoid a stiffness loss effect that appears when a flexion with rotation of the blade is implemented.

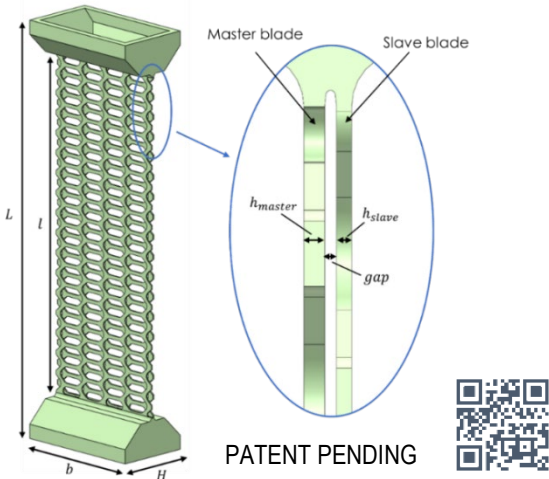


Figure 1: Flexure architecture with the dimensional parameters which are listed under the following table. Scan QR code to watch video.

Table 1: Flexure parameters

| Parameter | Symbol | Value | Unit |
|------------------------|--------------|-------|------|
| Length | l | 47.6 | mm |
| Width | b | 18.2 | mm |
| Thickness master blade | h_{master} | 220 | μm |
| Thickness slave blade | h_{slave} | 160 | μm |
| Gap | gap | 125 | μm |

The flexures were additively manufactured in 17-4PH stainless steel using Laser Powder Bed Fusion process. Then, after undergoing a 600°C stress relief treatment and being cut from the build-plate, the flexures were impregnated with an elastomer. After this process, the impregnated flexures were ready to be tested in vibration.

From the gathered data illustrated in Figure 2, one can observe that adding an elastomer on a flexure greatly enhances the

damping performances. Indeed, the motion amplitude of the reference decreases significantly in hundreds of seconds while for the impregnated blades about ten seconds only are required.

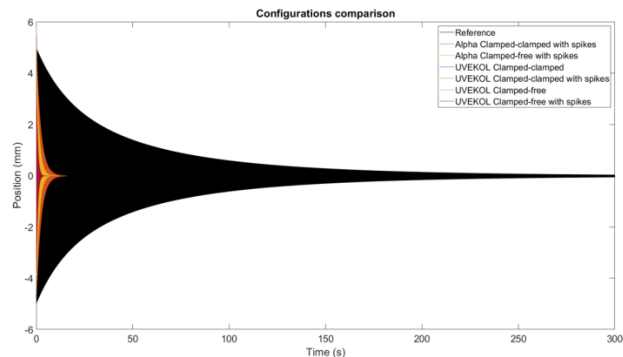


Figure 2: Free oscillation test results.

Following an exponential curve fitting process on the measured time-domain datapoints, the damping parameters listed in Table 2 are obtained from the mean values of four different free oscillation tests performed for each blade configurations.

Table 2: Results of the free oscillation tests

| Blade configuration | Elastomer | Quality factor Q | Actual damping c [kg/s] | Resonance frequency f_0 [Hz] |
|-----------------------------|-------------|--------------------|---------------------------|--------------------------------|
| Reference | - | 1250 | 0.002 | 8.6 |
| Clamped-clamped | UVEKOL S | 24.3 | 0.198 | 13.9 |
| Clamped-clamped with spikes | UVEKOL S | 23.8 | 0.204 | 14.1 |
| | Alpha gel C | 66.6 | 0.047 | 9.1 |
| Clamped-free | UVEKOL S | 19.5 | 0.234 | 13.2 |

The quality factor Q is reduced up to 64.2 times and the calculated viscous damping coefficient c is increased by a factor of 97.5 for the impregnated blades compared to the simple reference. Therefore, the impregnated lattice blades produced are a promising solution to withstand vibrations and shocks for precision compliant mechanisms.

* EPFL, Instant-Lab, 2000 Neuchâtel, Switzerland

[1] M. Lautenbacher, "Etude d'éléments flexibles innovants réalisés par impression 3D métallique", EPFL - CSEM, 2020.

Post-processing Development for High-performance mm-Wave Antennas Manufactured by LPBF Process

S. Unterhofer, A. Vorobyov, G. Andreatta, A. Finelli, M. Dadras *, O. Sereda

Laser Powder Bed Fusion (LPBF) Additive Manufacturing (AM) process opens new horizons for the fabrication of high-precision waveguide (WG) mm-wave antennas that are difficult or impossible to be produced with traditional machining. Material choice was investigated to achieve a lower level of radio frequency (RF) losses, which was finally applied to an Aluminum Silicon alloy allowing a surface roughness (R_a) of all surface orientations of ~6 to 10 μm after printing (As-Built) and below ~4 to 6 μm after surface treatment (chemical polishing and metal plating).

Fabrication of mm-wave components is nowadays limited in shape complexity, thus performance. AM opens the possibility to increase the complexity to costs ratio, since traditional manufacturing of WG antennas usually includes manual assembly steps. Additive manufacturing brings advantages that can overcome the production process: a repeatable quality and fewer assembly steps.

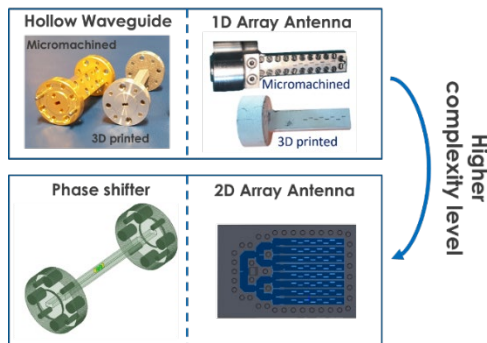


Figure 1: Simple components tested to establish the full procedure of fabrication.

Material choice was first investigated, producing testing parts with printing parameters already tuned for each material. To measure RF losses, simple hollow WG has been printed and measured without any post-process (PP) for bronze (Cu-10-Sn) and two aluminum alloys (Al-12-Si and Scalmalloy).

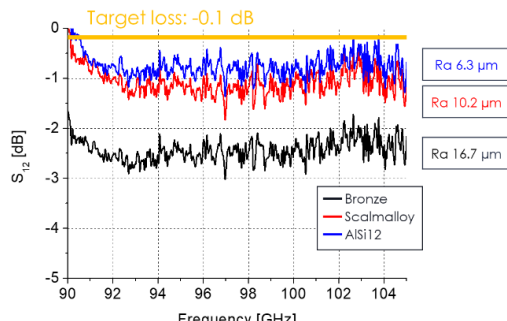


Figure 2: Measured losses in the mm-wave hollow waveguides for different alloys evaluated.

RF losses showed that post-processing is a must, and Al-12-Si was the best material to continue the study. To increase electrical conductivity and decrease surface roughness of as-built samples, the following post-processes are tested:

1. Heat treatment
2. Chemical and mechanical polishing
3. Silver-plating

Heat treatments on AM components decrease residual stress and change MP. Al-12-Si alloy is a precipitation hardening alloy. Heat treatment of printed Al-12-Si alloy leads to increase the electrical conductivity due to decreasing of Si content in solid

solution by Si based precipitates formation. This accompanying by decreasing yield strength and increasing the ductility. Long treatment at high temperature would lead to recrystallization and grain growth.

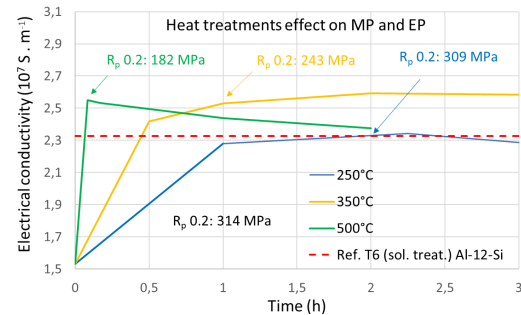


Figure 3: MP and EP measured at different heat treatment conditions for Al-12-Si.

Another advantage of having bigger grains size is the improvement of chemical etching, which is used to decrease roughness of internal channels. Surface roughness of as-built parts depends on the used process parameters and printing orientation. R_a of ~6 - 7 μm are reached with optimized printing parameters for Al-12-Si on surfaces printed at 90° to the respect of the building direction. After chemical polishing, R_a decrease below ~4 - 5 μm .

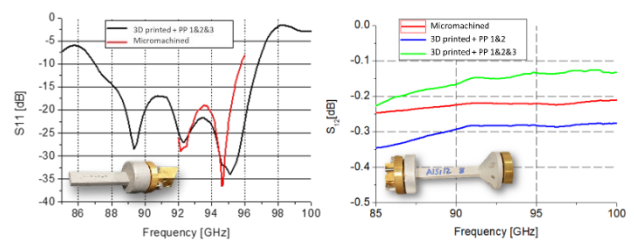


Figure 4: RF performances of mm-wave hollow waveguides and 1D linear array designed by TTi, fabricated, and characterized at CSEM after the full process.

Electroless silver plating developed internally, is the last post-process performed to increase the surface electrical conductivity of internal channels.

The RF performances of simple AM mm-wave components showed in Figure 4, after consecutive heat treatment, chemical polishing, and silver-plating, are comparable to WG antenna made by traditional manufacturing. More complex geometries will be assessed in future.

The research has received funding from the Clean Sky Program under grant agreement no. 886696 and was carried out in the frame of the 3DGUIDE project (Feasibility demonstration of 3D printing for a new efficient production method of mm-wave WG antenna).

Precise Controlling of Transformation Temperature in Nitinol

O. Klok, O. Sereda, M. Dadras, F. Gigon*

Nitinol is an alloy which can show superelasticity and shape memory properties depending on the phase composition and temperature. One of the ways to control Nitinol phase transformation temperatures and subsequently its properties is a heat treatment. This study shows the effect of the heat treatment on the phase composition and austenite transformation temperatures of Nitinol for defined application. Several complementary techniques were utilized to provide an in-depth understanding of the microstructural changes in the alloy.

Nitinol is an alloy of Ni and Ti, which is well known for its good corrosion resistance and biocompatibility as well as unique properties such as superelasticity and shape memory^[1,2]. The latter properties are defined by the alloy phase composition and its ability to phase transformation. The application of Nitinol depends on the temperature at which the phase transformation occurs and often must be in a strictly defined range. The heat treatment is one of the ways to modify transformation temperatures in Ni-rich Nitinol by forming the secondary phases. The present study shows that Nitinol austenite finish temperature (Af) can be increased by the heat treatment. The comprehensive evaluation of the effect of heat treatment on NiTi properties and microstructure was performed using several complementary techniques.

Differential scanning calorimetry DSC was used to evaluate the temperature transformation behavior of NiTi. Figure 1 shows that raw NiTi has one-step transformation austenite → R-phase upon cooling and reverse transformation R-phase → austenite upon heating. After the heat treatment, phase transformation occurs in two steps, i.e., austenite → R-phase → martensite with reverse two-step transformation martensite → R-phase → austenite. Heat treatment leads to increase of Af from 21°C to 35°C.

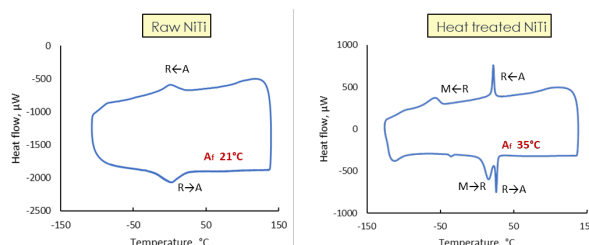


Figure 1: DSC temperature profiles of raw and heat treated NiTi alloy.

To understand the microstructural changes, a transmission electron microscopy (TEM) with energy dispersive spectroscopy (EDS) was performed. This technique was chosen based on the tendency of the alloy to develop fine phases in the nanometers range^[3], which might not be visible with optical microscopy or scanning electron microscopy (SEM). The obtained results in Figure 2 show that raw NiTi has homogeneous distribution of Ni and Ti with the chemical composition close to 57 wt% Ni and 43 wt% Ti. After the applied heat treatment, Ni₄Ti₃ phase appears, while the matrix Ni content decreases to 55 wt%.

X-ray diffraction (XRD) results in Figure 4 show that at room temperature, the studied NiTi alloy is austenitic, while the heat treated one is a mixture of R-phase as main phase and austenite (in agreement with DSC results). Additionally, formation of Ni₄Ti₃ phase in heat treated alloy is confirmed by XRD.

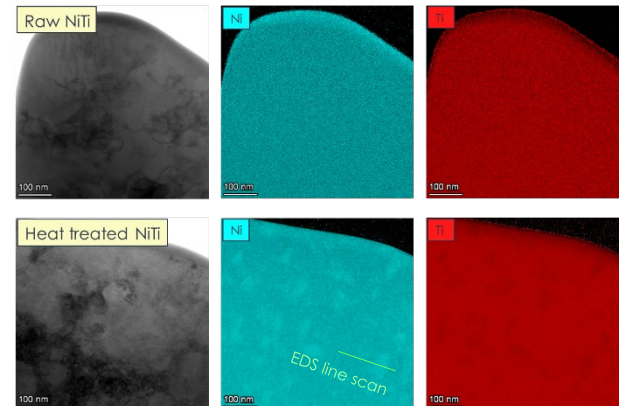


Figure 2: TEM micrographs and EDS chemical mapping of the raw and heat treated NiTi alloy.

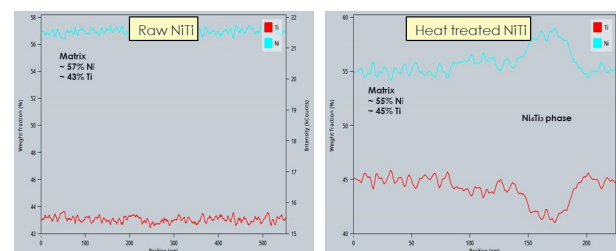


Figure 3: TEM/EDS line scans showing chemical composition of the raw and heat treated NiTi alloy.

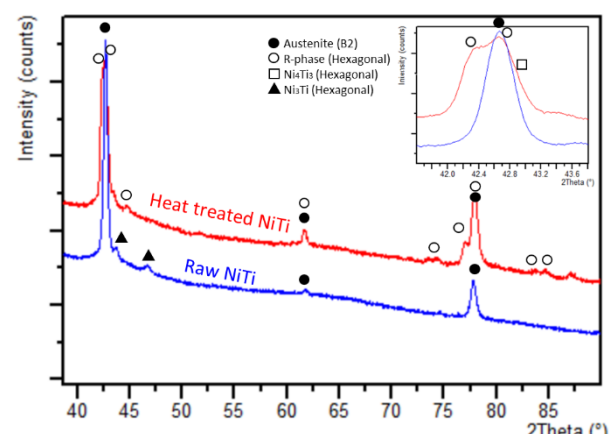


Figure 4: XRD phase analysis of raw and heat treated NiTi.

The obtained results show that the applied heat treatment leads to the increase of Af, which is caused by the decrease of matrix Ni content due to the formation of Ni₄Ti₃ phase. The main phase changes from austenite to R-phase. Thus, the heat treatment can be used as an effective way to tailor transformation temperature of Nitinol needed for specific application.

* FKG Dentaire Sàrl

^[1] J. W. Mwangi, et al., J. Manuf. Process. 38 (2019) 355-369.

^[2] A. Wadood, Adv. Mater. Sci. Eng. (2016) 1-9.

^[3] S. Jiang, et al., Trans. Nonferrous Met. Soc. China 25 (2015) 4063-4071.

MANUELA – Additive Manufacturing using Metal Pilot Line

G. Perruchoud, D. Novo, E. Onillon, V. Pejchal, O. Sereda

Metal additive manufacturing (AM) allows, by enabling use of advanced design, production of high added value components, at design levels that cannot be reached with conventional manufacturing techniques. Still, the AM-based manufacturing sequence implies large amounts of critical steps – design for AM, AM fabrication, post processing, quality assurance – compared to conventional production sequences. In order to ease the usage of Metal Additive Manufacturing, the H2020 Manuela project aims at implementing an open-access pilot line facility, covering the whole production sequence, to show full potential of metal AM for industrial AM production.

Coordinated by the Chalmers University, the H2020 research project MANUELA deploys, together with 20 other EU partners, an open access pilot line covering Laser Powder Bed Fusion (LPBF) and Electron Beam Melting (EBM) manufacturing capabilities offered at the three sites the Chalmers University, the Politecnico di Torino and the Friedrich-Alexander Universität. It is supported by the postprocessing center RISE Research Institute. Postprocessing covers machining, heat treatment, powder cleaning, 3D scanning and blasting. Within MANUELA, CSEM acts as a Design for AM (DfAM) expertise center and quality assurance expertise focused on raw material and final product qualification, and pilot line standardization. CSEM relies on its heritage of design for additive manufacturing, covering manufacturability analysis, part specific process flow selection, part optimization (such as minimizing geometric distortions and weight, and support structures where needed). The part design is done with respect to the specific manufacturing and post-processing flow, ensuring the "first time right" production. CSEM design activities were performed using a dedicated software suite, that allows generative design, topology optimization and manufacturing process simulation. Additionally, CSEM established the acceptance criteria for raw materials, quality assurance procedure, and works on standardization of the pilot line processes as well as identification of the AM standardization gap analysis.

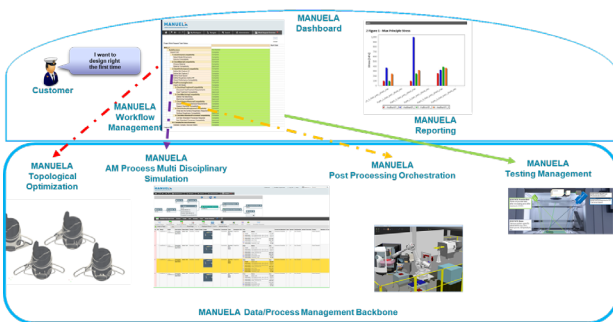


Figure 1: MANUELA's design and process dashboard.

In the frame of the activity, CSEM coordinates the development of six validation use cases, including specification collection, DfAM, pilot manufacturing and part acceptance. In the following the different use cases of the industrial partners are described:

- Avionics use case (QIOPTIQ): Helmet mounted displays (HMDs) components intended for aerospace applications. Material: Aluminium A20X.
- Space use case (BEYOND GRAVITY): optimized slip ring assemblies based on AM. Sliprings allow energy and signal transfer from rotating element (e.g., solar panel) to static element (e.g., satellite platform). Material: Pure Copper and A20X.

- Medical use case (CEIT): custom-made cranial implants created by the usage of titanium alloy. Material: Ti6Al4V ELI.
- Power use case (ENEL): power plant machinery components subjected to high thermo-mechanical stresses. Material: Ni alloy
- Automotive use case (OEB): rocker for motorsport competition. Material: Titanium Ti6246.
- Energy use case (SIEMENS): gas turbine heat shields. Material: Ni alloy.

Example of achievements are depicted in the following figures.

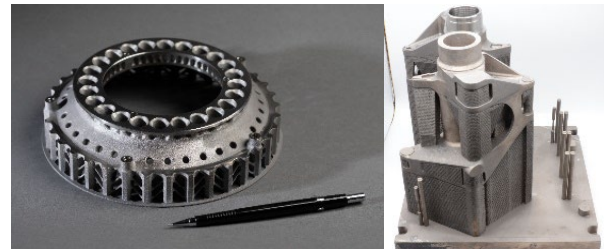


Figure 2: Automotive parts.



Figure 3: Space parts Slip ring assemblies' parts (rotor and stator).

The MANUELA pilot line commercial services are planned to be launched Q2-2023, offering full chain DfAM, AM and post-process services for the European Industry with RISE as single-entry point. The key MANUELA partners will support RISE to provide the pilot line services, CSEM acting as Design for AM center.

The project is financed partly by the European Commission under the H2020 program, grant number 880774, as well as the Swiss Secretariat for Education, Research and Innovation (SERI) and for which we would like to thank for their support.

New Approach to the Generation of Compliant Mechanisms Designs for the Space Industry

G. Lang, J. Rouvinet

The design of compliant mechanisms is a complex process, and the rise of additive manufacturing capabilities broadens the tools of the designer. Indeed, parts' complexity are no longer restricted by the manufacturing capabilities. In collaboration with the Product Development Group Zurich (ETHZ), a PhD thesis has been set up to develop a design's methodology for generating solutions fitting space industry's needs.

Compliant mechanisms use deformation to achieve displacements. These mechanisms have the advantages of displaying no wear, no backlash, no friction, and they have a longer life cycle compared to conventional mechanisms. Such technology is thus well-suited to spaceborne precision mechanisms, for which trajectories shall be finely controlled, perturbations avoided, and systems operational for years.

The emergence of Additive Manufacturing (AM) has opened the door to a new design freedom. Indeed, the layered approach of AM allows to manufacture intricate and freeform parts without increasing the manufacturing complexity and cost. Along the years, the design of compliant mechanisms has been adapted to the capability of conventional machining. To take advantage of this unique environment introduced by AM, novel approaches and methodologies shall be developed.

CSEM has demonstrated its ability to design and manufacture viable compliant mechanisms by additive means [1]. However, the design process is complex, time consuming and costly. Therefore, a PhD thesis has been setup in collaboration with the ETHZ Product Development Group (PdZ). Its main objective is to develop an automatized methodology to support engineers during the design for AM compliant precision mechanisms.



Figure 1: COMAM, a compliant mechanism for high precision pointing instruments, manufactured by additive means at CSEM.

[1] L. Kiener, H. Saudan, F. Cosandier, J. Kruis, G. Perruchod, V. Pejchal, P. Spanoudakis, J. Rouvinez, "Innovative Concept for Additive Manufacturing of Compliant Mechanisms," EASN (2019).

[2] J. Rouvinet, A. Ummel, F. Cosandier, D. Nguyen, V. Schaffter, "PULSAR: Development of a Mirror Tile Prototype for Future Large Telescopes Robotically Assembled in Space," SPIE 11451 (2020).

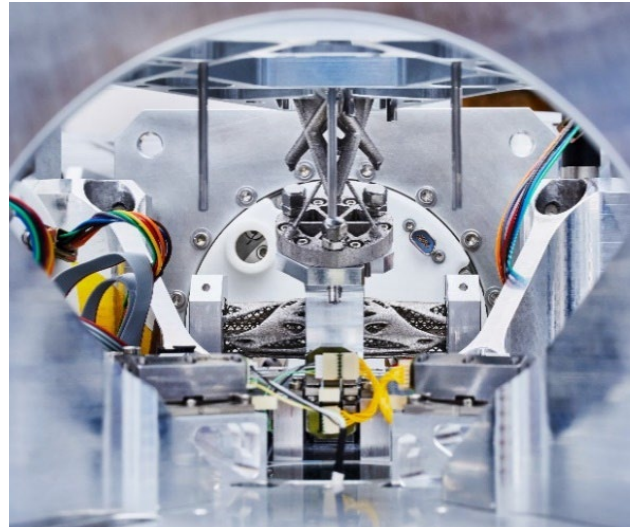


Figure 2: Integrated AM compliant pivots and universal joint implemented during the project PULSAR [2].

The combination of metallic AM and topology optimization has proven worth in the specific field of spacecraft structures. However, the compliant problem seems to be impermeable to this approach. PdZ used a knowledge-based engineering (KBE) approach to tackle similar design for AM problems such as multi-flow nozzles and fluidic manifolds [3]. By combining rules, heuristics and databases, KBE synthesizes designs based on prior expertise. Thereby, engineers keep control on the design process, but repetitive and heavy tasks are automatized. This thesis aims to expand the KBE framework to include CSEM's expertise in the field.

Furthermore, in technical systems such as spacecrafts, the selection of an ideal configuration cannot be based on performance alone. Indeed, other criterion such as costs and risks are involved. KBE's parametric nature provides the perfect framework to support such system engineering activities.

In brief, this thesis aims to develop a tool to synthesize ready to manufacture precision compliant mechanisms. Instead of generating a sole design, the tool will provide the engineer with multiple solutions fulfilling the requirement. For each solution, secondary criterion will be evaluated to provide insights for the trade-off process.

We would like to thank ETHZ and the Product Development Group for their contribution and collaboration.

[3] M. Biedermann, P. Beutler, M. Meboldt, "Automated Design of Additive Manufactured Flow Components with Consideration of Overhang Constraint," Additive Manufacturing Vol. 46 (2021).

Full Chain Process Development for 4D Printing of Two-way Shape Memory Alloy for Space Applications

N. Sohrabi, V. Pejchal, A. Manzoor, Y. Puyol*, O. Sereda

Shape Memory Alloys (SMAs) are an interesting class of metallic materials that can recover their initial shape after deformation upon heating above a certain temperature. There has been a growing interest in the additive manufacturing (AM) of SMAs, which are considered promising materials for applications in many industrial sectors. This is true for Nitinol (NiTi), one of the most commercially successful SMAs commonly available only in a limited number of shapes due to difficulties in fabricating parts using conventional methods. In this regard AM promises much needed versatility in design using SMAs, thus developing new potential applications including novel actuators. The aim of the project was to fabricate the flexural pivot demonstrator for space applications through the development of an optimized process-flow of NiTi-based 4D printing technology.

The quality of the NiTi feedstock is crucial for printability and showing shape memory effect (SME) at room temperature ($M_f > 20^\circ\text{C}$). Therefore, several gas-atomized NiTi powder feedstocks were characterized with respect to their morphology, flowability, chemical composition, and transformation temperature. The selected powder feedstock exhibited $D_{v90}=50\mu\text{m}$ with a chemical composition of Ni 50.25 at.% ($M_f > 20^\circ\text{C}$), excellent flowability.

Laser powder-bed fusion (LPBF) process was conducted using TruPrint1000 (Trumpf GmbH) at CSEM. Design of experiment (DOE) was performed to optimize the process parameters and study the effect of laser power, laser scanning speed, and hatch distance on the relative density of specimens. After the optimization, parts with a density higher than 99.5% were achieved (Figure 1a) and 600 μm thin blades were manufactured for further characterization. The observed melt pool (Figure 1b) shows a start of keyhole mode, which is the ideal case to achieve the highest density^[1].

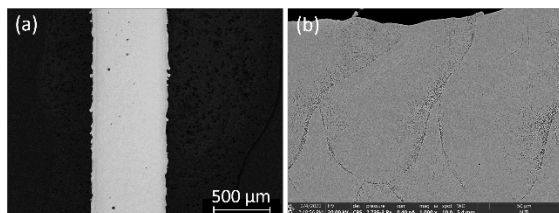


Figure 1: a) cross-section of a blade with optimized processing parameters, and b) melt pool of the optimized processing parameters.

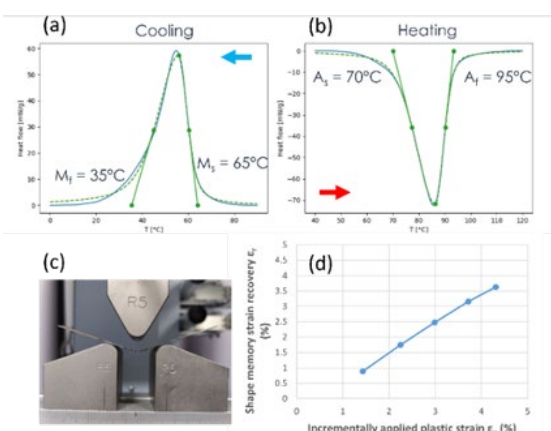


Figure 2: (a-b) DSC peaks upon cooling and heating of the fabricated part, (c) three-point bending set-up, (d) shape memory strain recovery measured as a function of applied plastic strain in three-point bending.

The transformation temperatures of the fabricated samples were measured using DSC (Figure 2a-b). The fabricated parts showed SME at room temperature since M_f was higher than 25°C . Shape

memory strain recovery was measured based on the three-point bending procedure as 3.6% (Figure 2c-d). The blades showed an ultimate tensile strength of 510 MPa with strain to failure of 5.3%.

Two-way shape memory effect (TWSME) is not inherent to NiTi or other SMAs but can be induced by a bespoke thermo-mechanical treatment, the so-called training. The training method used in this project was the constrained cycling of deformed martensite, in which the sample was deformed and constrained in the cold state (martensite phase) while 100 thermal cycles (between 0°C and 120°C) were applied. A demonstrator was printed (Figure 3a), and the training process was applied as mentioned above. Since the strain was localized in the central hub of the demonstrator, to actuate the TWSME after training, two heaters were attached to the front and rear sides of the demonstrator (Figure 3b). The demonstrator was installed on a test bench to precisely measure the actuation angle upon heating and cooling. TWSME of the demonstrator is shown in Figure 3c, which was stabilized around 7° of actuation after 30 cycles.

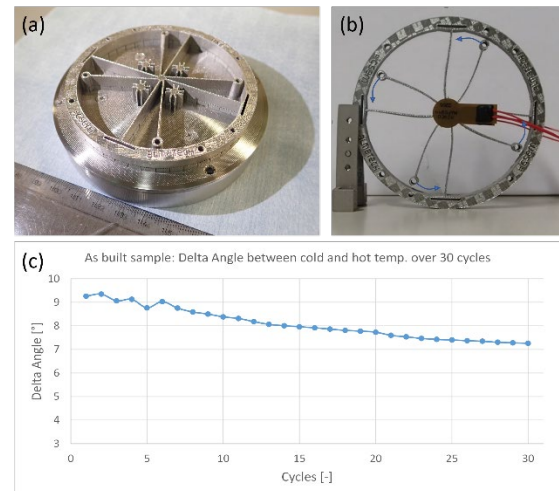


Figure 3: a) Printed demonstrator before training b) trained demonstrator with integrated heaters, and c) TWSME measurement of the demonstrator upon heating and cooling.

In conclusion, a shape memory pivot actuator with a density higher than 99.5% was fabricated via LPBF, exhibiting SME at room temperature with almost 4% of strain recovery. The fabricated demonstrator showed a 7° two-way actuation after training without need of using bias springs, which was more than twice the initially aimed TWSME (3°). To the best of the authors' knowledge, this is the first study in the literature showing significant TWSME of SMAs fabricated via AM. This work was supported by SERI (REF-1131-61001).

• ALMATECH SA

[1] H. Ghasemi-Tabasi, et al., Addit. Manuf. 36 (2020) 101496

Additively Manufactured Flexure Pivots for Space Cryo Application

L. Kiener, G. Lang, H. Saudan, F. Cosandier, N. Kalentics

Flexible pivots made by metal additive manufacturing were developed, manufactured, tested and delivered for cryogenic testing. Thanks to this novel production technology, the final parameters have been tuned according to customer specifications and produced within three weeks, including the final machining to cope with conventional high-precision dimensions for interfaces.

The Centre Spatial de Liège (CSL) in Belgium is developing a new mechanism following SPICA mission requirements. The Mode Selector Mechanism needs to move a flip mirror that will pick-up either low- or high-resolution beam and direct it into the instrument light path. This mechanism must ensure an accurate and reliable positioning of the flip mirror in two fixed and stable positions (meaning unpowered). The mirror will be mounted between two flexible pivots providing a small angular displacement (+5/-2°) with a low spring torque.

Based on CSEM background in design and manufacture of precise Additive Manufacturing (AM) metallic flexible parts [1], the optimization of the flexure geometry was performed to cope with the specifications. To benefit at most from the AM possibilities, the design is integrating interlocked lattice flexible pivot. This allows to increase the performances compared to commercial off-the-shelf products. The design is integrating special features to ease the machining, which is performed to ensure precise tolerances at the interfaces (i.e., external diameter, length and concentricity).

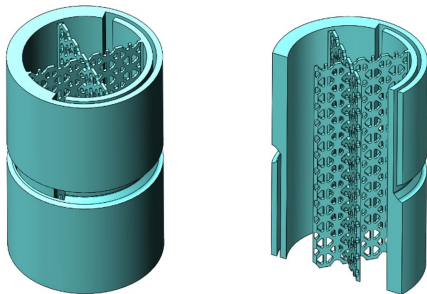


Figure 1: AM flexible pivot concept (right: cut view).

In parallel with the design activities, a first batch of representative fatigue test samples was manufactured and tested to assess the lifetime limits and the influence of different thermal treatments.

The main challenge was to design and manufacture small parts with high accuracy, e.g., thin blades of 200 µm. The flexure blades are not machined; therefore, their surface roughness shall be as low as possible to ensure a high fatigue limit.

The complete process workflow – design, manufacturing, and post-processes such as cleaning, thermal treatments, machining, characterization, acceptance – was established and verified to ensure fulfilling the requirements. In total 12 flexible pivots were 3D printed in stainless steel. Half of them were delivered to CSL for integration in the mechanism. The cryogenic testing at 4K is foreseen end of 2022. After this, the pivots will be measured

again to verify that the main parameters are still within specifications.

Table 1: Flexible pivots characteristics.

| Parameter | Specification | Measurement | Unit |
|-----------------------------|---|---------------|---------|
| Diameter | 12.7 0/-0.015 | 12.68 - 12.69 | mm |
| Length | 20.32 ±0.05 | 20.32 - 20.36 | mm |
| Mass | none | 6.6 | gram |
| Flexible blades thickness | 200 - 220 | 210 - 215 | µm |
| Angular stiffness | 1.7 - 4 | 4 ±0.4 | mNm/deg |
| Fatigue limit at room temp. | 230 MPa for infinite lifetime, 450 MPa for 1e4 cycles, determined on representative bending samples | | |
| Material | 316L stainless steel | | |



Figure 2: AM flexible pivots after machining.

The project demonstrates that flexible mechanisms can be designed, optimized and produced by metallic additive manufacturing. The main advantages are the design freedom, the possibility to tune the characteristics according to a specific need and the fast production time.

The project partner is Centre Spatial de Liège (CSL), Belgium. CSEM thanks them for their support.

[1] L. Kiener, H. Saudan, F. Cosandier, et al., "Compliant mechanism based on additive manufacturing" CEAS Space J (2021). <https://doi.org/10.1007/s12567-021-00394-0>

Protective Coatings on Anodized Aluminum Oxide for Watch and Medical Components

X. Bulliard, M. Crenna, J. Gay, R. Pugin, J. F Laithier*, C. Storrer*

Anti-corrosion sol-gel coatings have been successfully applied onto Anodized Aluminum (AAO) components for the watchmaking industry and for biomedical tools. Two deposition routes are considered: dip coating and spray coating. Both techniques lead to an improved protection to corrosion over a large range of pH in aqueous media, from pH 2 to pH 11. In addition, the coatings are homogeneous, mechanically resistant with good adhesion on the parts after curing. This ensures the mechanical integrity over prolonged time. These protective properties open new market perspectives for medical tools that must resist successive cycles of sterilization at basic pH.

A good protection to corrosion of AAO components over a large range of pH is critical for the watch and medical components markets (Figure 1). A target application is medical tools, for example for dental or spine surgery, that must resist several cycles of sterilization at high pH. A sol-gel anti-corrosion coating was formulated to be effective over a wide range of pH between 2 and 11 through a careful choice of alkoxide precursors in solution. The formulation was further optimized in terms of types and concentration of catalytic agent and of water amount to obtain a sol-gel solution that can be stored several weeks before use. In the CERANO project, funded by Innosuisse, the processability of the sol-gel solution on different components, which often possess complex geometries, is considered. The mechanical integrity, durability, and color stability after coating is also evaluated.



Figure 1. Examples of colored watch components and medical components.

Two different techniques were chosen for the deposition of the sol-gel formulation: dip coating or spray coating. When using dip coating, the thickness of the coating on the AAO substrate is tuned by controlling the withdrawing rate from the solution and the viscosity of the sol-gel solution. Drying and gelation occur, leaving a smooth film on the AAO substrate. For fixed solution parameters (i.e., viscosity and surface tension), the thickness depends solely on the withdrawing speed, as illustrated in Figure 2. The coating thicknesses were approximately 0.8 µm for a withdrawing speed of 50 mm/min and 1.46 µm for 100 mm/min. The thickness increased with speed following the Landau-Levich model. For complex shapes, the components were oriented so that the differences in the flow rates of the meniscus on the shapes are minimized to avoid material excess.

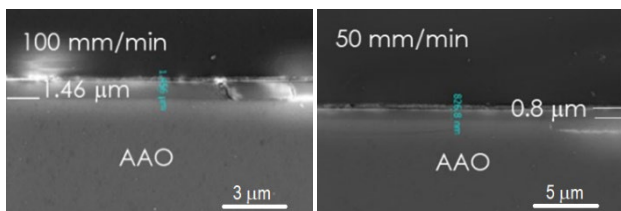


Figure 2. Cross section by FIB-SEM of the sol-gel coating on the AAO substrate for different withdrawing speeds, at 50 mm/min and 100 mm/min.

Spray coating was carried out with a mini-spray valve mounted in an automated robot. The viscosity of the sol-gel solution was adapted to the other spray parameters, i.e., the flow rate, the deposition speed and the distance between the spray head and the AAO substrate, to control the material amount deposited on the substrate. The thickness was mainly controlled by the flow rate and the number of spray repetitions. For one spray pass, it was approximately 1 µm. In both spray and dip coatings, a final step consisted in curing the coated samples. After curing, the anti-corrosion properties were found to improve over the native boehmite layer formed on the AAO substrates. The mechanical adhesion was measured by carrying out scratch test (Taber indentation scratch tester) and was similar to that of the native boehmite layer.

Another aspect of the work is the aesthetics, especially for watch applications. In the manufacturing process, coloration of AAO is achieved by migration of dyes into the porous structure of the AAO before sealing. The sol-gel topcoat should not affect the transparency, the gloss, and the color of the components. Color changes were evaluated by measuring the L*a*b values in the CIELAB color space before and after coating. L* represents the perceptual lightness while a* are related to the opponent green-red color, and b* to the opponent blue-yellow color. For most of the colors shown in Figure 3, the variation in the L*, a*, and b* were below 1 or 2 points after dip or spray coating.



Figure 3. Examples of different colored parts after sol-gel deposition by dip coating (color changes were evaluated on these samples).

In summary we implement dip- and spray-coating techniques for the deposition of a protective topcoat on AAO components of complex shapes for watch and medical applications. After curing, the coated parts show better anti-corrosion properties and similar mechanical properties when compared to the anodized components. Sol-gel coatings are particularly adapted to add other functionalities to the treated parts. A future perspective is the development of antibacterial coatings.

* Coloral SA, Cressier, Switzerland

UV-patterning of Phosphonic Acid Monolayers for Copper Electroplating on Solar Cells

J. Gay, A. Lachowicz, N. Blondiaux, A. Faes, C. Allebé, G. Andreatta

The photovoltaic industry is expected to consume 30 to 50% of the global silver supply by 2030, indicating the need of using other materials for solar cell metallization processes. CSEM has developed a low-cost and scalable mask of phosphonic acid (PA) self-assembled monolayers (SAMs) on indium tin oxide (ITO) for nickel and copper electroplating on heterojunction solar cells. PA were deposited with different procedures and characterized using cyclic voltammetry and etching resistance tests to assess the barrier properties of the SAMs. Patterning of SAMs was performed using UV radiations to achieve selective electroplating of nickel and copper on ITO. The process was upscaled on M2 (156.75×156.75 mm) solar cell precursors.

The PV industry is rapidly expanding with an actual production of more than 100 GW/year, growth rates at 25% in the past two years, and is expected to reach 2 TW of annual production around 2032 [1]. Currently, the PV industry uses 20 tons of silver per GW produced. Although silver consumption per cell is expected to decrease, a PV production of 1 TW/year will require at least 50% of the global world silver supply, indicating the necessity of using other materials for the metallization of solar cells [2]. The low resistivity of electrodeposited copper offers an interesting alternative to screen-printed silver solar cells.

CSEM has developed a patented copper electroplating process using self-assembled monolayers (SAMs) as mask for heterojunction solar cells (Figure 1). Self-assembled monolayers (SAM) of organic molecules are molecular assemblies formed spontaneously on surfaces by adsorption. Thiol, carboxylic acids, silanes and phosphonic acids are well known chemistries for SAM preparation. Phosphonic acids (PA) were found to bind strongly on various metal oxides, including indium tin oxide (ITO). In comparison to conventional organic resists, SAMs present the advantage of strongly reducing the material consumption.

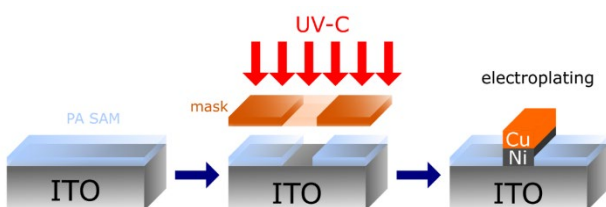


Figure 1: Process summary for selective copper electrodeposition on ITO using SAMs as a mask.

The insulating properties of SAMs vary depending on chemistry, self-organization, and the deposition process itself. Several scalable deposition processes were investigated. SAM produced using two different PA chemistries and varying processes were characterized by cyclic voltammetry, which is very sensitive to film defects (Figure 2). A low "maximum current intensity" indicates better insulating properties, therefore better masking.

The SAM-coated samples were photopatterned using UV-C (254 nm) radiations through a silicon hard mask. Indeed, upon UV-C exposure, scission of the C-P bond of the phosphonic acid molecules occurs. For a silicon hard mask opening of 130 µm, the measured width of the photopatterned area was measured to be equal to 180 µm [3].

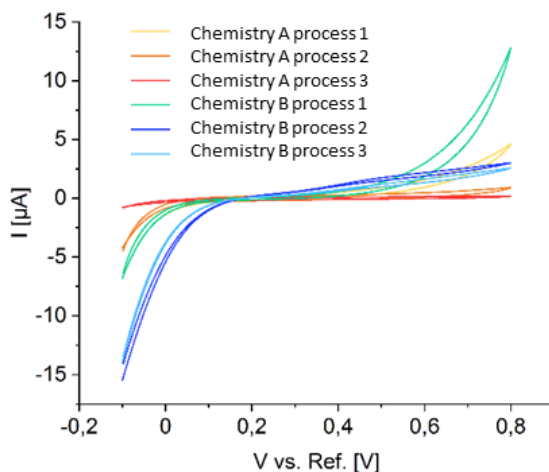


Figure 2: cyclic voltammetry curves of SAM-coated ITO electrodes deposited via different procedures.

Electroplating processes were then performed on the patterned monolayers showing the most insulating properties. On ITO deposited on a polished silicon wafer, selective electroplating of nickel and copper was obtained (Figure 3) with excellent selectivity. A scale-up of the method was then investigated. The first tests show less selectivity with the presence of parasitic plating. The higher amount of parasitic plating observed on full-scale solar cells was explained by the different SAM deposition procedures, SAM-covered areas, surface roughness and contacting methods.

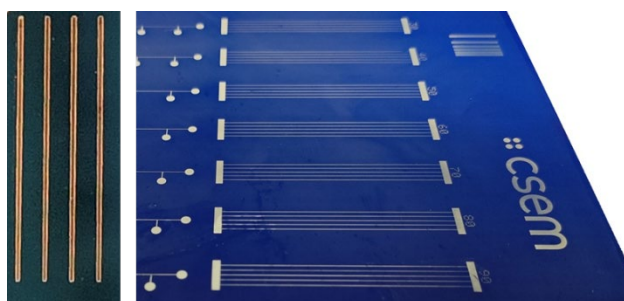


Figure 3: (left) Electroporation of Ni and Cu metal lines using a PA SAM as a mask; (right) Ni plating on a 156.75×156.75 mm textured solar cell.

Future work aims to improve patterning and electroplating processes on solar cells, further reducing parasitic plating.

[1] P. J. Verlinden, "Future Challenges for Photovoltaic Manufacturing at the Terawatt Level", *J. Renew. Sustain. Energy* (2020), 12, 053505.

[2] A. Lachowicz, N. Badel, J. Gay, G. Andreatta, *et al.*, "Reinforcement of Screen-Printed Copper Paste by

Electrodeposited Copper for Metallization of Silicon Heterojunction Solar Cells. 10th Met. Interconnect. Workshop (2021).

[3] J. Gay, A. Lachowicz, N. Blondiaux, G. Andreatta, "Selective Copper Electroplating on Patterned Self-Assembled Monolayers for Photovoltaic Applications", *ACS NanoMaterials* (2022), <https://doi.org/10.1021/acsanm.2c04291>

Mechanically Resistant Antibacterial Coatings for Medical Tools

X. Bulliard, M. Crenna, A. Finelli, X. Lefèvre, R. Pugin, J. F Laithier*, C. Storrer*, T. Zwingelstein **, V. Humblot **, A. Figarol **, A. Marguier **, F. Chérioux **

Medical tools made of anodized aluminum (AAO) are coated with an antibacterial coating based on a sol-gel formulation. In addition to antibacterial properties, the coating has a protective purpose to avoid chemical and mechanical degradation during the sterilization of the medical tools. The antibacterial properties are generated by the addition of silver or silver precursors to the sol-gel coating. Depending on the form of silver, the antibacterial effect is induced by the gradual release of silver ions or by direct contact to silver metal.

Antibacterial properties can be generated by different mechanisms, such as preventive action by limiting the adhesion of bacteria, or by bactericidal action. For the protection of medical tools based on anodized aluminum (AAO) antibacterial coating must have protective properties as well to avoid corrosion or to improve the durability of the toll after multiple sterilization steps in severe basic environments. In the project METEOR, antibacterial coatings were specifically designed to have long-term durability and efficacy. For that purpose, silver was incorporated into a sol-gel coating.

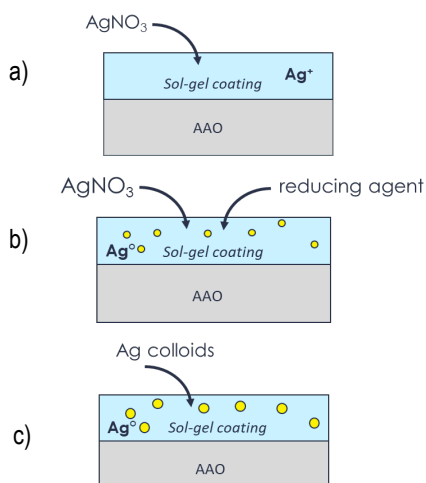


Figure 1. Three approaches to incorporate silver in the sol-gel coating: a) silver nitrate in the coating, b) in-situ growth of particles from precursors, c) addition of Ag colloids.

Three approaches were chosen to incorporate silver inside the sol-gel coating. In the first one, a silver precursor (silver nitrate, AgNO_3) was mixed to the sol-gel solution before coating on AAO (Figure 1a). In the second one, a sol-gel coating was first deposited on the AAO substrate before dipping in successive baths of silver nitrate and a reducing agent. This led to the in-situ growth of finely dispersed nanoparticles into the sol-gel coating. In the third approach, silver colloidal particles were directly mixed with the sol-gel solution before coating on the AAO. Silver is thus present in different forms in the coating, i.e., as Ag^+ ions in the first approach, as Ag° (and remaining of Ag^+ ions that have not been reduced) in the second one and as Ag° in the third one.

For the first approach, the antibacterial effect was induced through Ag^+ release. The antibacterial properties were confirmed by contact tests on Escherichia Coli bacteria. For this test, the coating was applied on a transparent substrate to characterize visually the antibacterial effect. For the reference sol-gel coating, no antibacterial properties could be detected (Figure 2a). At 0.5% of AgNO_3 , most of bacteria in contact with the samples were killed (Figure 2b), while at 2.5%, a halo of killed bacteria was further observed around the sample (Figure 2c).

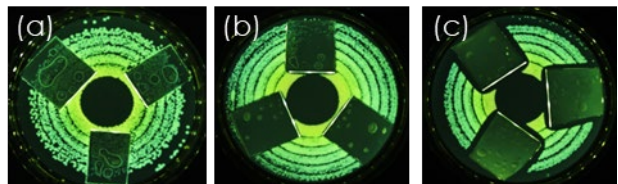


Figure 2. Antibacterial contact test against *E. coli* bacteria: a) bare sol-gel, b) sol-gel with 0.5% AgNO_3 , c) sol-gel with 2.5% AgNO_3 .

To evaluate the potential toxicity on cells, cytotoxicity tests were carried out by exposing Normal Human Dermal Fibroblast (NHDF) to Ag^+ solution. The cells remained unaffected up to a concentration of 3.5 mg/L and were stressed above (Figure 3). The exact amount of Ag release was measured by ICP-AES (Inductively Coupled Plasma Atomic Emission Spectroscopy), and allowed us to determine a window for which the antibacterial properties are effective, while the cells are still viable.

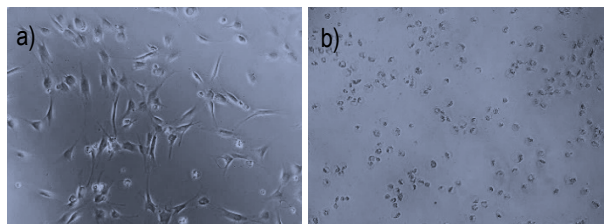


Figure 3. Cytotoxicity tests on Normal Human Dermal Fibroblast cells: a) unaffected at $C(\text{Ag})$ of 0.65 mg/L and b) stressed at 3.5 mg/L.

For the second approach, the particles were too small and finely distributed inside the coating to generate the antibacterial effect, while for the addition of Ag colloids in the third approach, an antibacterial effect could be observed for large particles only ($<1 \mu\text{m}$). In that case, enough particles were present at the surface to have a direct action on the bacteria by contact killing. For this last approach, the durability of this antibacterial coating was evaluated by corrosion tests at $\text{pH}>11$ that mimic sterilization. The coating kept its functionality and mechanical integrity.

In summary different approaches based on silver incorporation in a sol-gel layer were successfully tested as an antibacterial coating. The sol-gel coatings were designed for either prolonged release of silver ions or for the distribution of silver throughout the coating for long-term effect. Coating durability was confirmed by corrosion tests mimicking sterilization procedures of medical tools.

METEOR project is supported by the Interreg France-Suisse 2014-2020 program and has benefited from the European Regional Development Fund (FEDER), and on the Swiss side from federal and cantonal grants (Neuchâtel, Vaud). CSEM thanks them for their support.

* Coloral SA, Cressier, Switzerland

** UFC-FEMTO, Besançon, France

Optical Oxygen Sensor for Monitoring Water Quality

R. Pugin, X. Bulliard, A. Grivel, J. Gay, A. Finelli, M. Crenna, R. Ischer, J.-A. Porchet, S. Heub, M. Maurel*, F. Nguyen*, V. Girardet*, M. Derbois*, C. Lemoine*

Over the past years CSEM has developed optical oxygen sensors based on the selective quenching of luminescent dyes in the presence of oxygen. The sensor is highly customizable and allows the continuous monitoring of oxygen concentration in a wide range of environments. Beyond its use for measuring dissolved oxygen in cell culture devices, the sensor is currently integrated into new systems dedicated to water quality monitoring.

The company Neroxis provides turnkey solutions for monitoring the water quality of supply networks and for the protection of surface resources such as rivers and lakes. Among Neroxis products, the modular, fully stand-alone SWARM buoy allows continuous monitoring of changes in conductivity, temperature, speed, depth, dissolved oxygen, pH, turbidity, organic matter, chlorophyll A, phycocyanin and phycoerythrin. Coupled with weather data, SWARM data are an excellent indicator of the water quality of the resource. It also helps anticipating events such as algal blooms and adaptation of drinking water treatment. Today, one limitation of SWARM is the prohibitive price and "rigidity" of its dissolved oxygen and pH measurement devices (10% of the Buoy), which limits the deployment of this technology.

Over the past years, CSEM has developed and patented a new range of optical oxygen sensing systems which consist of luminescent-reactive dyes embedded in a hierarchical porous matrix (Figure 1).^[1]

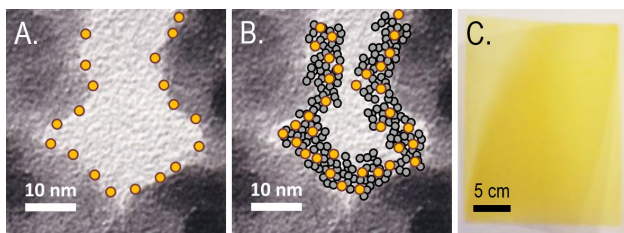


Figure 1: SEM micrograph of the sensing layer based on silica nanoparticles showing the difference between the incorporation of dyes either in a single level (A) or dual level (B) of porosity. The yellow dots represent the dyes encapsulated in the nanoporous structure of the sol-gel matrix (grey dots). The sensing layer is deposited on A4 sheets (C).

The sensors have shown advantages compared to current commercial solutions in particular high sensitivity and selectivity, enhanced reliability and robustness of the sensor as well as cost-effectiveness of its production. These oxygen sensors are disposable and coupled with a portable reading device. The reader includes a light source (LED), a detector (photodiode), low consumption electronics, a battery, and a communication module. All together the system provides high-precision, reliable, non-invasive, and reversible oxygen sensing.

Typical sensor performances are the following:

- Working range 0.1% - 21% O₂
- Accuracy 0.1% at 2% O₂
- Precision ±0.3%
- Shelf life 12 months

* Neroxis, Neuchâtel, Switzerland

[1] E. Scolan, B. Wenger, R. Pugin, "Optical sensor for detecting a chemical species", EP3184994B1.

Recently CSEM has integrated such O₂ sensors in various systems for Life Science applications such as an objective-like device for microscope or fiber-based devices to monitor oxygen in bioreactors and incubation chambers.^[2]

The objective of this project was to adapt the technology to allow monitoring of water quality in rivers and lakes. New generation of O₂ sensors as well as a compact optical transducer have been integrated on the SWARM buoy to measure O₂ concentration with high precision/accuracy, and at different water depth (Figure 2). The capability to extend this technology for monitoring of pH and different nitrogen derivatives is currently under evaluation.

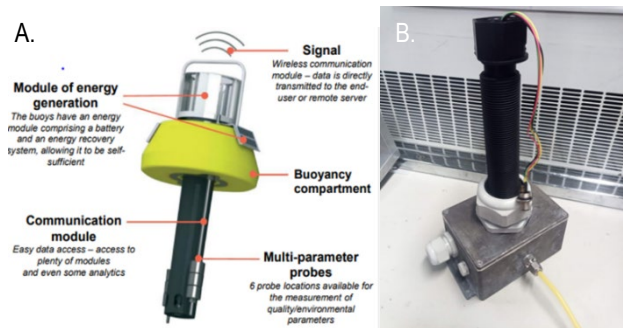


Figure 2: Scheme of the SWARM buoy produced by Neroxis (A) Neroxis probes equipped with CSEM O₂ sensor (B).

These new sensors will also be used to measure oxygen in environments close to submerged archaeological structures. The obtained measurements will be analyzed and correlated with aging and degradation of archaeological woods. More specifically we will demonstrate how oxygen, pH, and ion monitoring provides understanding of oxidative degradation process and helps predicting algal bloom or mussel colonization.

Neroxis and CSEM would like to warmly thank the Canton of Neuchâtel (Département de l'économie, de la sécurité et de la culture) for their financial support.

[2] S. Heub, et al., "Non-invasive optical oxygen sensing for life sciences and environmental monitoring", CSEM Scientific and Technical Report (2019) 45.

Protective, Passivating, and Selective Transport Layers in Perovskite/c-Si Tandem Solar Cells

M. Dussouillez, A. Paracchino, X.Y. Chin, A. Walter, G. Andreatta, C.M. Wolff*, K. Artuk*, D. Türkay*, S.J. Moon, F. Sahli, N. Blondiaux, B.A. Kamino, C. Ballif, Q. Jeangros

The Swiss National Science Foundation project PAPET brings together the Photovoltaics and Thin-Film Electronics Laboratory (PV-lab) of the Ecole Polytechnique Fédérale de Lausanne and CSEM to develop high-efficiency perovskite/c-Si tandem solar cells, a technology which should promise affordable photovoltaic electricity costs. This four-year project focuses on understanding and mitigating performance-loss pathways, especially those occurring at the interfaces between the perovskite absorber and the neighboring contact materials. Through a careful optimization of materials and processes, the partners were able to produce the first perovskite/c-Si tandem solar cells exhibiting an efficiency >30%, hence validating the performance potential of the technology. In addition, the project identified and mitigated various degradation pathways affecting the long-term stability of the technology.

The low cost of crystalline silicon (c-Si) solar modules has enabled photovoltaics to take larger shares of the electricity market. Increasing the efficiency of c-Si modules by implementing more advanced solar cell designs is and will continue to be the main driver to continue this deployment, providing this efficiency gain comes at affordable extra production costs. There is an incentive to increase the number watts produced per unit area to lower the cost of electricity as the cost of a photovoltaic system is dominated by the balance of system components and not by the solar cells. This approach will however lose its effectiveness soon as c-Si cells are capped by a theoretical limit of around 29.5%, a value already approached by record devices made in the laboratory (26.8%). While there is still some margin in the short term to increase the efficiency of industrial c-Si cells and modules, a change in strategy will be required for the longer term. The most promising approach to overcome the performance limitations of c-Si and other single-junction solar cells involves stacking several solar cells to form a multi-junction device. This advanced solar cell design enables a better usage of the incoming photons energy and has been validated experimentally using III-V materials, highly efficient yet scarce and expensive materials with production cost almost 500 times higher per watt than c-Si. As of today, the only known multi-junction design that has the potential to combine low production costs and high device efficiencies consists in pairing c-Si with metal halide perovskites.

The materials contacting the metal halide perovskite absorber in a tandem solar cell should ideally combine several properties to maximize the performance and stability of the device: they should not only be selective to one type of carrier, either electrons or holes, but also passivate defects present on the surface of the perovskite, be optically transparent to the parts of the solar spectrum that need to be collected either in the perovskite or in the c-Si absorber, be electrically conductive to not hinder the transport of charge carriers to the electrodes, form a continuous layer free of shunts, provide a suitable template layer on which to grow the perovskite, and also protect the fragile absorber against the egress and ingress of species. The contact materials used today do not fulfill all these criteria, a limitation that the project PAPET aims to lift. More specifically, the project has been focusing on understanding, through advanced characterization, and optimizing the growth mechanisms and resulting properties of the perovskite and contact layers. From this understanding, a new surface passivation approach that also tunes the microstructure of the perovskite material has been developed. In addition, the hole contact located below the perovskite could be optimized. Thanks to these innovations, two types of perovskite/c-Si tandem solar cells with an efficiency >30% could be demonstrated by EPFL PV-lab with

support from CSEM. The previous record was at 29.8%. First, a tandem device featuring a Si wafer flat on its front and textured on its rear and a solution-processed perovskite absorber reached an independently certified efficiency of 30.93%. Second, the photocurrent produced by the solar cell could be increased further by depositing the perovskite on a Si wafer textured on both sides using a hybrid method combining physical vapor deposition and solution processing. This latter design reached an efficiency of 31.25%, a world record independently certified by the National Renewable Energy Laboratory in the USA.

These high device efficiencies, currently achieved with an active area of 1 cm², will only translate into commercial products if similar values can be achieved with industry-relevant dimensions and if these devices remain stable in operational conditions. This second challenge is also a central research focus of PAPET and there again the contact materials play a key role. Thanks to advanced characterization, the chemistry of the NiO_x hole transport layer was found to evolve in time when at 85°C, temperatures typical of the IEC 61215 damp heat test. This change in the NiO_x results in the formation of a charge extraction barrier and hence in a severe loss in the solar cell performance. By modifying the NiO_x stoichiometry and doping it with another element, cells remaining stable >5000 hours in damp heat conditions (85°C in 85% relative humidity) could be demonstrated (Figure 1), corresponding to five times the standard qualification test done for c-Si photovoltaics. The project is now focusing on the investigation and mitigation of degradation pathways occurring in perovskite cells when these are subjected simultaneously to illumination and high temperatures (>60°C).

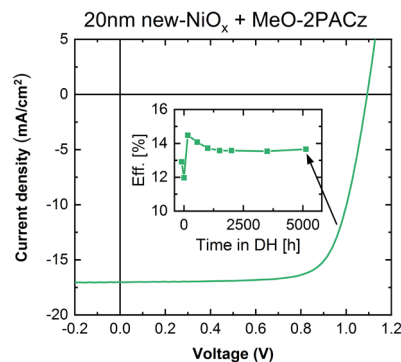


Figure 1: Current-voltage properties of a 1-cm² encapsulated perovskite single-junction solar cells after 5100 hours of damp heat testing, highlighting the long-term stability of devices featuring a modified NiO_x hole contact in these conditions.

Acknowledgements: this work was supported by the Swiss National Science Foundation (200021_197006).

* EPFL PV-lab

Nanoimprint Lithography of Polyimide for Very Thin and Flexible Medical Technologies

G. Basset, M. Kraus, C. Eggenspiller

Thin polyimide (PI) films are used more and more in advanced medical technologies to fabricate a wide range of very thin and flexible devices, such as cardiovascular catheters, stent delivery devices, brain stimulation electrode arrays, and drug delivery systems. PIs are high performance polymers which have become a material of choice due to their outstanding mechanical characteristics, long-term reliance, and robustness allowing them to sustain aggressive sterilization processes on top of having good biocompatibility^[1]. The fabrication of thin film PI electronic devices for medical applications relies on printed circuit board (PCB) or semiconductor manufacturing processes and had limited improvements in the last decades. New processing technologies developed at CSEM enable cost-effective 3D-structuring of PI at the wafer scale using nanoimprint technologies.

CSEM has more than 30 years of experience in the microfabrication and microstructuring of a wide range of materials using various nanoimprint lithography (NIL) technologies^[2,3]. While UltraViolet-NIL (UV-NIL) fabrication technologies are widely used for micro and nanooptics fabrication at the wafer or chip scale^[3], thermal NIL is widely used for the manufacturing of polymer substrates.

Due to its very high thermal stability, PI imprinting has not been used so far in the manufacturing of thin flexible medical devices. Processing relied only on photolithography, masking, and dry plasma etching to selectively remove the material, resulting in binary geometries. Such fabrication methods are time-consuming, costly and limit the geometries.

To overcome these limitations, following requests from MedTech customers, CSEM has developed a new process flow to 3D pattern PI thin films at the wafer scale, as described in Figure 1:

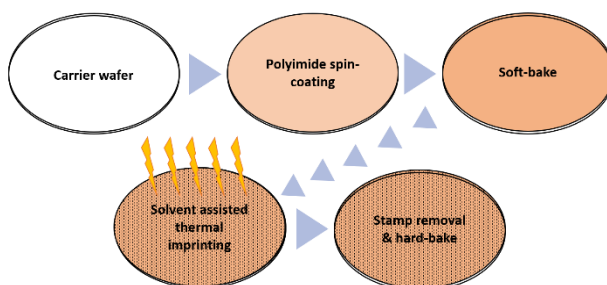


Figure 1: Main steps of the thin film polyimide imprinting process flow on carrier wafers.

The thermal imprinting is solvent assisted. Specific imprinting temperatures and temperature ramps are used, combined with a nano-porous mold and a custom imprinting stack to progressively reduce the solvent concentration during the imprinting.

The resulting PI films exhibit very low roughness and high topographical fidelity to the targeted geometry provided by the mold. As an example, micro-cavities with flat bottom and rounded edges were structured. The rounded edges were purposefully created on the mold to ease further assembly work. The flat area,

flat bottom, and the rounded edges are well structured in the thin PI over 150 mm wafer as visible in Figures 3 and 4.



Figure 2: Detail of a PI imprinted film structured with micro-cavities.

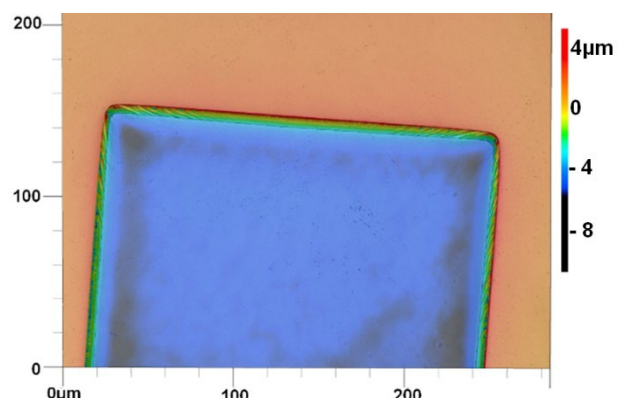


Figure 3: Topography map made by 3D laser confocal microscopy of a PI thin film imprinted with a micro-cavity.

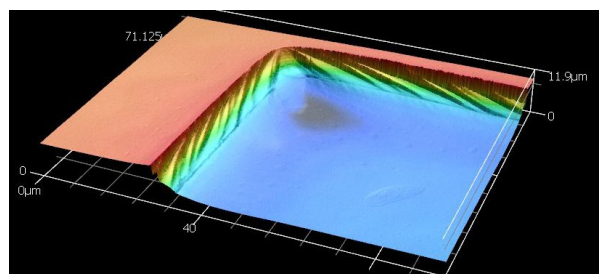


Figure 4: Detail of a cavity corner realized in PI using nanoimprint lithography, imaged by 3D laser confocal microscopy.

These novel polyimide imprinting processes open the door for more complex and cost-effective manufacturing of a variety of flexible medical devices.

-
- [1] C. P. Constantin, M. Aflori, R. F. Damian, R. D. Rusu, "Biocompatibility of polyimides: A mini-review". Materials, 12(19), 3166 (2019).
 - [2] M. T. Gale, "Replication technology for micro-optics and optical microsystems". In Gradient Index, Miniature, and Diffractive Optical Systems III (Vol. 5177, pp. 113-120). SPIE (2003).

- [3] F. Zanella, G. Basset, C. Schneider, A. Luu-Dinh, S. Fricke, A. M. Madrigal, M. Zahir, "Microlens testing on back-illuminated image sensors for space applications" App. Opt., 59(12), 3636-3644 (2020).

Manufacturing of LIGA Parts with Functional Sidewalls

N. Blondiaux, R. Pugin

LIGA process is a well-known microfabrication method allowing the manufacturing of microparts and microstructured surfaces. As of today, single or multi-level microstructures have been demonstrated and parts of increasing complexity are being produced for various markets. To give more functionality to LIGA parts, CSEM recently developed and patented a method for the surface-structuring of the sidewalls of the parts. The process is based on the fabrication of submicrostructures of well defined lengthscales on the sidewalls of LIGA mold features, which are then transferred in the part during electroforming. Several properties are targeted such as surface-wettability tuning, friction, and the control of the aesthetics of the parts.

LIGA process (german acronym for Lithographie, Galvanoformung, Abformung), is a well-established technique used to manufacture precision microparts or parts presenting microfeatures. This industrial scale process covers various markets: pharmaceutics with the manufacturing of microsieves integrated in inhalators^[1], watch industry with the production of a variety of microparts and bearings, and manufacturing of precision molds for the plastic industry.

As this process is based on photolithography and electroforming, production is done at standard wafer scale and is generally used to make 2D parts. Since its invention, several improvements have been done to produce high aspect ratio structures, multilevel microparts, and hybrid parts^[2]. To add functionality to the parts, some examples have been shown with microparts faces presenting a hierarchical structure, for instance for anticounterfeiting applications^[2]. However, in many applications, the functionality of the microparts actually arises from its sidewalls. As photolithography cannot be used in this case, standard finishing techniques need to be used as a post process to tune surface topography of the final part.

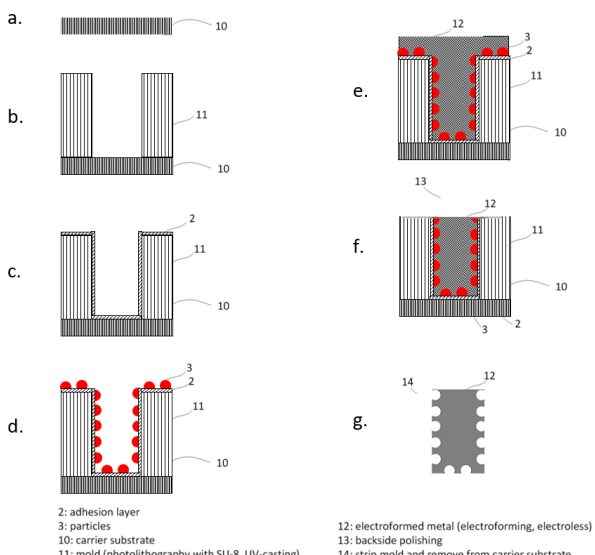


Figure 1: illustration of the process flow proposed to manufacture electroformed parts with structured sidewalls.

- [1] C. C. Huang, 8th Annual IEEE International Conference on Nano/Micro Engineered and Molecular Systems, 2013, pp. 490-493.
- [2] G. Genolet, H. Lorenz, UV-LIGA: From Development to Commercialization. *Micromachines* 2014, 5, 486-495.
- [3] N. Blondiaux, et al., "Micro-nanostructuring of 3D Surfaces: on the Manufacturing of Functional Parts for the Medical and

During the last decade, CSEM has been developing processes for the surface structuring of various materials such as silicon, glass, and metals. One of the key processes developed is nanosphere lithography which consists in the deposition of micro- or nanoparticles of well-defined dimensions to control the lateral dimensions of the structure followed by a wet or dry etching step to transfer the structures into the substrate^[3]. This process has recently been adapted to modify the surface of LIGA molds to produce nanostructured electroformed parts^[4]. Figure 1 presents the main steps of the process. After the fabrication of a SU8 mold on a wafer, particles with diameters ranging from 100 nm to 1 micrometer are deposited using a self-limiting process to produce a monolayer on the surface of both the SU8 mold and the substrate. After an electroforming step, the parts are released and cleaned, which results in the negative structure on the sidewalls of the metal part.

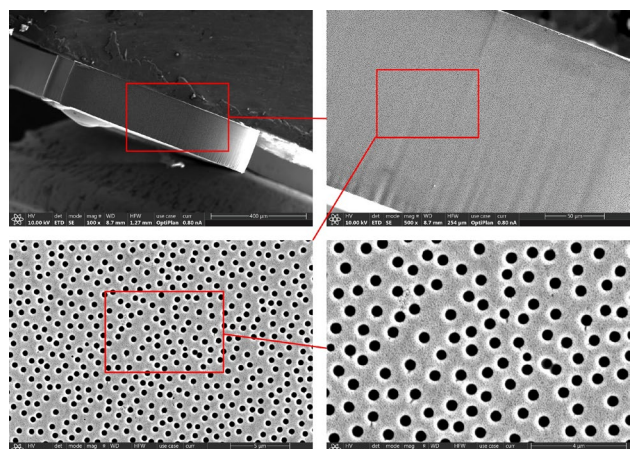


Figure 2: SEM images of resulting nickel part electroformed on SU8 coated with 500 nm particles.

Figure 2 presents the results obtained for a nickel part with 500 nm structures. A highly homogeneous coverage of the sidewalls and a good replication of the structures during the electroforming step were obtained. The process has been upscaled to 150 mm wafers.

Next steps will concern the optimization of the process for complex LIGA molds and its application to various cases studies.

"Watchmaking Industry ", CSEM Scientific and Technical Report (2020) 34.

[4] EP3578508A1: methods for manufacturing micromechanical components and method for manufacturing a mould insert component.

Broadband Atmospheric Gas Sensing with State-of-the-Art Supercontinuum Light Source and Machine Learning Spectral Analysis

L. Balet, S. Chin, S. Denis, E. Muntané Calvo, J. van Zaen, G. Borque Gallego, L. Giriens, C. Hofer, M. Gumy, D. Novo, S. Lecomte

Air pollution is one of the largest risk factors for disease or premature death globally. The European TRIAGE consortium develops a smart, compact, and cost-effective air quality sampling sensor network for the simultaneous broadband detection of all relevant atmospheric pollution gases.

Air pollution has been linked to severe health conditions, such as strokes and lung cancer, and the World Health Organization (WHO) estimated it to be the cause of 4.2 million premature deaths in 2016^[1], i.e., corresponding to 7.6% of all the deaths worldwide in that year. Wildlife, plants, ecosystems, and even our climate are affected by degraded air quality. Monitoring the pollution level and identifying the source of pollutant is thus of upmost importance, and governmental bodies have passed regulations on the subject.

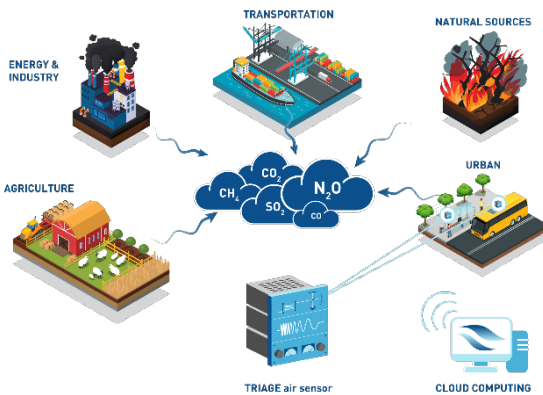


Figure 1: Illustration of the TRIAGE concept. The TRIAGE detectors monitor the air quality at different location and transmit the measured target gas concentrations in real-time to a cloud-based system for further analysis based on machine learning.

Currently, several methods are used to monitor air quality. They are often based on expensive laboratory equipment for precise analysis, and a series of low-cost sensors, targeting single gas species with reduced accuracy and dispersed over a territory. The TRIAGE^[2] system aims at replacing this myriad of detectors with a single high resolution portable system. The project builds upon a state-of-the-art ultra-broadband coherent light source, called a Supercontinuum, to perform absorption spectroscopy over the 2–10 μm spectral region known as the fingerprint region, where most gases present in the atmosphere absorb light with unique and distinctive features. The spectroscopic analysis is usually performed by fitting the measured absorption with reference spectra found in a database. For TRIAGE, we developed machine learning based analysis algorithm^[3] that can simultaneously fit several gas species, and is robust to measurement noise, including baseline fluctuations and spectral shifts.

Benefiting from excellent spatial coherence, the supercontinuum light interacts with the atmospheric air through a 30 m long multipass cell folded in a 40 cm long enclosure. The light is then

analyzed in a Fourier Transform Spectrometer, whose outputs are detected by a balanced detection system for improved SNR^[4]. An industrial mini-PC equipped with a 4G network card performs the analysis locally and sends the raw and analyzed data to a remote repository for further processing and analysis, including data aggregation from multiple sensors, generation of concentration maps from discrete measurement locations and alarm generation based on predictions.

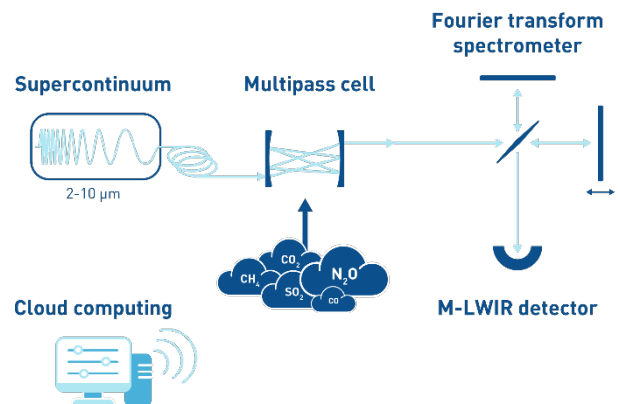


Figure 2: The detector prototype uses a supercontinuum light source with a target bandwidth between 2 and 10 μm . The gas-light interaction occurs within a 30 m multi-pass cell, and the transmitted light is then analyzed in a Fourier transform spectrometer. Balanced detection with a custom designed detector is processed electronically and the absorption spectrum is analyzed.

In this collaborative work, several CSEM teams are involved in the design, assembly, and testing of 3 generations of compact detector prototypes, as well as for the big data management and the development and implementation of the different machine learning algorithms. Currently the first prototype has been designed and is under fabrication. First results are expected by December 2022 and will be used to validate the machine learning algorithms. The system will then be shipped to our partners for precise assessment of the limits of detection for a range of predefined gas species, before being used at different locations, including a wastewater treatment plant, waste incinerator, urban environment, and a natural methane release site.

This work is funded by Horizon 2020, the European Union's Framework Programme for Research and Innovation under grants No. 101015825 (TRIAGE) and has been carried out in close collaboration with VIVID Components (DE), DTU Fotonik (DK), NKT Photonics (DK), Radboud University (NL), Senseair (SE), NORBLIS IVS (DK), Linköping University (SE), and VIGO photonics SA (PL).

[1] WHO Fact Sheet 2018 Ambient (outdoor) air pollution (available at: www.who.int/news-room/fact-sheets)

[2] B. Napier, *et al.*, "Ultra-broadband infrared gas sensor for pollution detection- the TRIAGE project", *J. Physics-Photonics* 3, 31003 (2021)

[3] A demonstrator is available at <https://triage.tk/>

[4] M. A. Abbas, *et al.*, "Fourier transform spectrometer based on high-repetition-rate mid-infrared supercontinuum sources for trace gas detection", *Optics Express* 29, 22315-22330 (2021)

Ultrastable Low-noise Optical Frequency Ruler

S. Kundermann, L. Karlen, E. Onillon, S. Lecomte

Frequency combs are versatile systems to phase coherently connect optical and RF frequency domains. Most prominent application is optical atomic clock in which an optical frequency, stabilized to an atomic transition, is divided into the RF domain to provide the clock output signal. We have realized a system in which a frequency comb is stabilized to multiple references and used as ultra-stable and low-noise optical frequency ruler for characterizing the exquisite frequency stability of lasers for the future LISA mission aiming at detecting gravitational waves in space.

Active hydrogen masers are among the most stable commercially available frequency references for long term applications. Using frequency combs, the stability of these masers can be transferred to the optical domain. In this case both repetition rate and carrier envelope offset frequency of the comb are locked to the maser with phase locked loops (PLLs). The shortcoming of such approach is that as in a standard frequency synthesizer, phase noise of the reference is multiplied by the ratio between output frequency and reference frequency. In the present case stable laser reference optical output frequencies at ≈ 200 THz and ≈ 300 THz corresponding to wavelengths of 1560 nm and 1064 nm are required to stabilize the reference and to measure frequency noise of the LISA laser head. With a maser output frequency of 10 MHz, the phase noise of the maser will be multiplied by a factor of $2 - 3 \cdot 10^8$. In this case, the frequency noise of the optical reference above 3 mHz would be higher than the requirement on LISA laser head noise. We thus use a high-finesse ultrastable optical cavity (shown in Figure 1) to which we lock a low noise 1560 nm cw laser as an optical local oscillator.

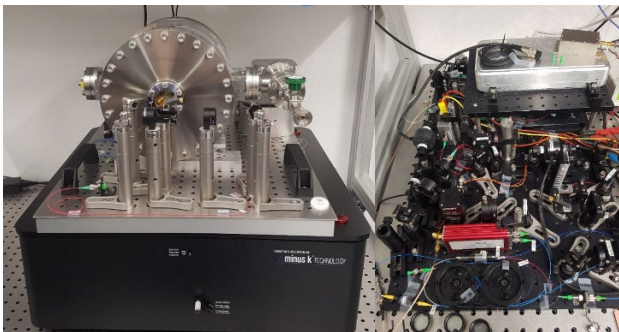


Figure 1: optical reference cavity (left), frequency comb (right).

This setup provides very low frequency noise at Fourier frequencies above 3 mHz. For the LISA laser head however frequency noise down to 30 μ Hz needs to be measured. The inherent drift of such an optical cavity prevents required high stability at low Fourier frequencies. To compensate for the drift of the cavity the cw laser is locked to an optical frequency about 100 MHz offset from the optical cavity reference frequency. This is achieved via a dual phase modulation of the laser light incident onto the cavity, where one frequency is the tunable offset frequency f_{offset} to the cavity and another frequency f_{PDH} is the modulation frequency for the Pound Drever Hall laser locking. A 1560 nm, 600 MHz homemade frequency comb acting as an optical to RF frequency divider is locked to the cw laser while at the same time its carrier envelope offset frequency is locked as well to the maser. The repetition rate of the frequency comb is compared to the maser frequency and kept constant in a PLL acting on f_{offset} . This compensates the frequency drift of the

optical cavity (about 60 mHz/s) and results in transferring the frequency stability of the maser at low Fourier frequencies and the frequency stability of the cavity at high frequency to both the cw laser and the frequency comb. After spectral broadening of the 1560 nm femtosecond pulses from the frequency comb, we obtain an ultra-stable optical frequency ruler providing optical reference spectral lines between 150 and 300 THz. This is very convenient as it allows for characterization of low noise laser sources over all this optical frequency range spanning from wavelength from 1000 nm to 2000 nm.

This setup has been used to characterize the LISA laser head provided by NASA against the very stringent frequency noise requirements of the laser head optical frequency^[1]. The challenge of those requirements is the extremely low required frequency noise of the laser head at frequencies in the 100 μ Hz to 1 Hz range where the metrology setup needs to be even more stable than the laser head under test.

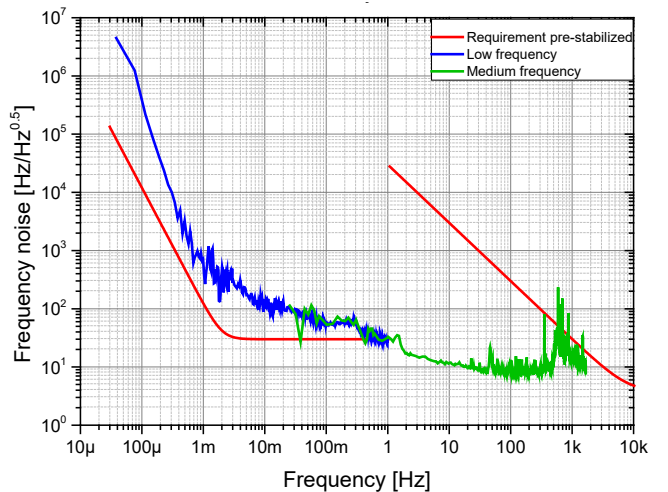


Figure 2: Frequency noise of NASA LISA laser head measured with CSEM ultra-stable ultra-low noise optical frequency ruler.

Figure 2 shows the frequency noise measurement of the NASA laser head when using CSEM's optical frequency ruler. The frequency noise specification is depicted by the red curves. The blue and green curves have been obtained with two different acquisition techniques and show an excellent overlap. While in specification for Fourier frequencies for 1 Hz and above, the laser under test is out of specifications for lower frequencies. This is due to the strongly drifting optical reference used to stabilize the laser under test. This optical reference will be improved in the near future.

CSEM is grateful to ESA and the Canton of Neuchâtel for funding this high-end laser metrology activity.

^[1] L. Karlen, et al., "Gravitational wave observatory metrology laser development and characterization", Proc. SPIE 12188, p. 121881K.

High-power fs Pulse Amplification with an Yb:YScO Crystal

N. Torcheboeuf, C. Hofer, L. Karlen, S. Lecomte

High-power femtosecond laser systems with pulse durations below 300 fs and record average powers are developed for emerging industrial laser applications. Such a short-pulse high-power laser system can be based on ytterbium doped sesquioxide crystals that have a unique set of properties in terms of gain bandwidth and thermal conductivity. Currently such crystals are not commercially available. CSEM, together with NKT Photonics Switzerland GmbH, Mateck GmbH, WZW Optic AG and the Leibniz-Institut für Kristallzüchtung in Berlin, developed high quality crystals and characterized them in a short pulse amplifier operating in the 100 W regime.

Femtosecond lasers have been developed at CSEM for applications like metrology, spectroscopy and microwave photonics since more than a decade. Over the last few years, high-power femtosecond lasers for industrial applications are also in CSEM's focus. The main driver to generate ultra-short pulses and high average power is to reach high peak power for high-precision micro-machining and more and broader range of industrial applications.

To achieve this new level of performance, the Eurostar FEMTOXIDE project, regrouping many industrial and academic partners, explores amplification stages based on a presently not commercially available crystal. Today, the most used material is YAG crystal, thanks to its easy-growth, high-gain cross-section and thermomechanical properties. This development led to a breakthrough in terms of laser crystal production and laser systems performances. The choice of gain materials for ultrashort lasers with high average power is usually a trade-off between broad emission spectra required for the generation of ultrashort pulses and good thermal properties required for an efficient thermal management. Yb:YScO can be this candidate: it has a broader emission spectrum (12 nm FWHM vs 8.5 nm for Yb:YAG) and its thermal conductivity is similar with Yb doping (4.4 W/mK for YScO and 7 W/mK for YAG @2.4% Yb). Thus Yb:YScO allows for the amplification of significantly shorter and similar energetic pulses than Yb:YAG. Currently, sesquioxide laser crystals are not commercially available, such a development can open new markets.

Both high peak and average powers are needed and as such the approach of chirped pulse amplification (CPA) provides the best solution. The system is seeded by a 1037 nm, 40 MHz fs NKT Photonics Origami oscillator. The 250 fs pulses are temporally stretched to avoid non-linear effects in the amplification chain, and a pulse picker controls the repetition rate of the output pulses. A first power amplifier stage is based on an aeroGAIN fiber amplifier module provided by NKT Photonics that allows the system to deliver an average output power of up to 70 W from 1 to 40 MHz pulse repetition rate. At this step we reach the highest energy level for standard aeroGAIN fiber amplifier.

Stretched and amplified pulses pass directly through the tested Yb:YScO rod. This gain medium is forward pumped by 104 W of pump power at a center wavelength of 976 nm. The optimization of the beam diameter, the beam propagation in the rod and the thermal management of the rod are crucial for achieving maximum output power as well as an excellent output beam quality. The maximal average output power from the Yb:YScO rod is 93.5 W, by pumping continuously with 104 W, that includes a 23 W power extraction through the rod. There is no inflection on the power extraction curve, for all repetition rates from 1 to 40 MHz. That means that the pulse energy increases proportionally with the pulse picking ratio, no saturation appears at full power or for low repetition rates. Through thermally induced aberrations within the rod, a portion of the amplified light

is depolarized. This depolarization depends directly on a thermally induced birefringence resulting from the pump absorption in the rod and the gradient of temperature caused by the thermal conductivity of the crystal. The typical signature of depolarized light was observed with the four lobes shown below in the beam profile. The amount of depolarized light was less than 2% of the extracted power from the booster crystal.

After the Yb:YScO amplifier stage, the pulses are recompressed in a grating compressor down to a FWHM pulse duration of 274 fs at 40 MHz. The beam quality factor M² is measured to be under 1.3 at the output of the crystal.

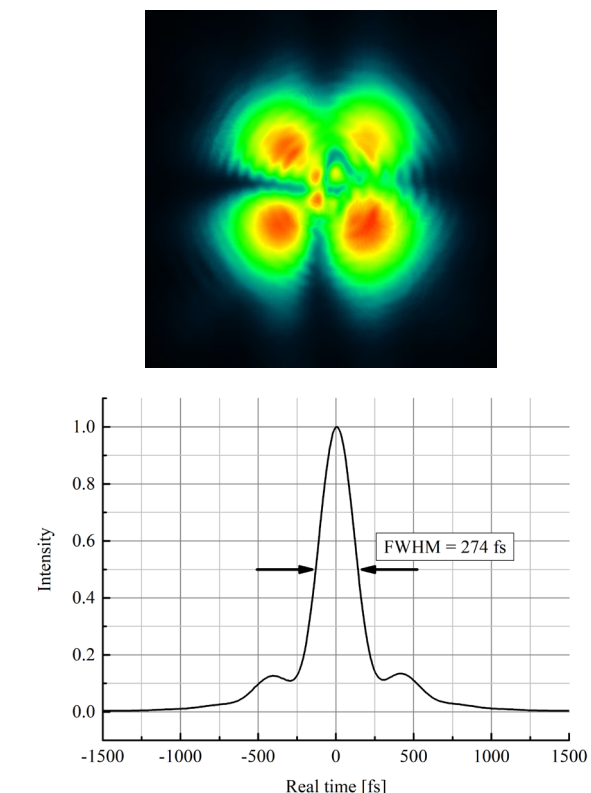


Figure 1: (top) Pattern of the depolarized beam profile out of the crystal at 93.5 W of output power. (bottom) Autocorrelation trace after recompression retrieving a pulse duration of 274 fs assuming sech² pulses and with a repetition rate of 40 MHz.

CSEM would like to warmly thank Dr. Maxim Gaponenko from NKT Photonics Switzerland GmbH for the collaboration in the laser system development, Dr. C. Kränkel from IKZ in Berlin and Dr. H. Schlich from Mateck for the expertise in all theoretical and practical aspects of crystal growth and WZW for further preparation of samples for initial laser tests. This work has been conducted with support from Eurostar with co-founding from the European Union Horizon 2020 program under the project E!12341 – FEMTOXIDE.

Wafer-scale in-plane Micro-optical Interconnects for Fiber arrays

R. Krähenbühl, M. Renggli, S. Mohrdiek, G. Bassett, I.-L. Bundalo, A. H. Ghadimi

A novel wafer-scale, compact, *in plane* solution for interconnecting optical devices with fibers and fiber arrays in a self-aligned “plug-and-play” style is presented. In particular, micro-optical structures on glass wafers, as well as on SiN waveguide grating couplers were designed, optimized, and fabricated. The micro-optical structures are based on re-directing light (reflection) elements, combined with integrated comb like fiber self-alignment structures, fabricated using wafer scale reflow and replication processes. Successful assembly of a 12-fiber ribbon is demonstrated. Excess losses of these structures as low as 0.35 dB are obtained.

Photonics packaging remains one the most challenging steps in the optoelectronic system industry and is therefore oftentimes responsible for more than 80% of the total cost of a of a fully assembled device. Moreover, there is increased demand for compact solutions with the trend for increased data throughput and the resulting demand for multi-fiber connectivity. This leads to an increasing need for miniaturized, compact, cost effective, optical interconnects to fiber arrays.

In this project, we proposed and realized compact “plug-and-play” interconnects based on micro-optical structures. They are based on reflection elements, fabricated from reflowed cylindric structures. To easily enable passive fiber array coupling, these reflecting elements were combined with fiber alignment walls. The resulting micro-optical interconnect is sketched Figure 1.

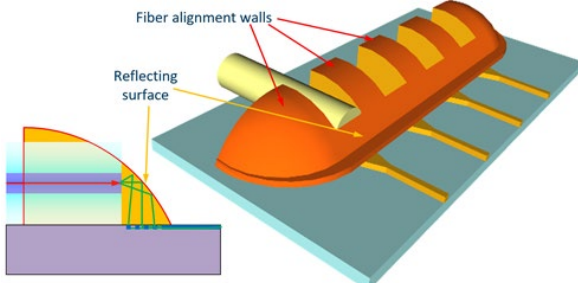


Figure 1: 3D visualization of the proposed “plug-and-play” micro-optical interconnect for an optical fiber array of four fibers into waveguide gratings together with the corresponding optical path.

To fabricate these micro-optical interconnects (Figure 2), we used UV wafer-scale replication into chemically stable polymers, one of the most cost-effective fabrication technologies for volume production.

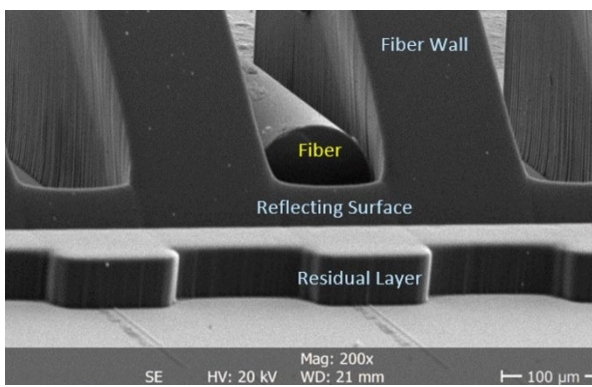


Figure 2: Scanning Electron Microscope (SEM) image of such a realized micro-optical interconnect on a SiN waveguide grating chip.

A dedicated flexible setup was built to be able to characterize the reflecting micro-optical element integrated onto glass substrates or waveguide PICs. The setup consists of an input and an output fiber each on a three-axis micro stage together with a substrate holder (Figure 3). It can handle most commercially available optical fiber (SMF-28 E9, MMF G50, H200, etc.) and covers a

wide wavelength range (400 nm – 1700 nm). Furthermore, it can easily adjust angles (0-90 deg.) of input and output fiber.

Results on glass substrates showed negligible excess loss into a MM G50 fiber (<0.35 dB) and agreed well with the predicted output beam deflection of 100 deg.

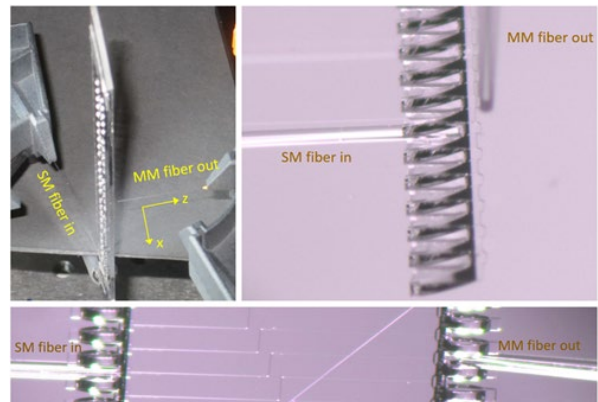


Figure 3: Right angled optical characterization setup used to measure the beam quality, beam deflection angle and excess loss (top row), as well as the straight fiber-PIC (waveguide)-fiber arrangement to measure fiber-to-fiber transmission (bottom row).

In the final step, glass substrates with the fabricated and characterized micro-optical interconnects were assembled to a 12-fold fiber array. The ribbonized fiber patch cord had an MT style connector on one side. The fibers were then introduced into the micro-optical interconnects using a similar setup as for the characterization of the replicated structures.

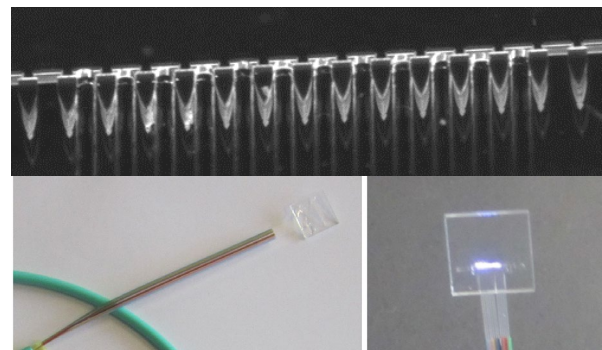


Figure 4: Picture of fully assembled fiber array and corresponding patchcord assembly with its optical output on the substrate back side.

The implementation of such a replication technology will enable the production of reflecting micro-optical interconnects with extreme compactness, thus providing significant technical advantages for both component suppliers and device/system integrators.

Wafer-scale Fabrication of Low-loss Waveguides in Lithium Niobate on Insulator (LNOI) Integrated Photonics Platform

J. Leo, M. Hayati, F. Ebrahimi Agri, G. Choong, Y. Petremand, I. Prieto, O. Dubochet, M. Despont, H. Sattari, A. H. Ghadimi

Lithium niobate on insulator (LNOI) is one of the most promising emerging platforms for photonic integrated circuits (PICs) that comprises a unique set of interesting optical properties: a high electro-optic coefficient, high intrinsic 2nd and 3rd order nonlinearities, and a large transparency window (350 to 5500 nm). In this project, we present a wafer scale fabrication of low-loss LNOI waveguides at C-band and the statistical measurements of resonances. Quality factors exceeding 2.5×10^6 have been measured, corresponding to a waveguide loss below $< 0.14 \text{ dB/cm}$.

Lithium niobate (LiNbO_3) has attracted a lot of attention since the 1970s as an electro-optics material, however, most of its industrial success in photonics domain has been so far limited to devices made from bulk crystals in the form of free-space or fiber-coupled components using ion-implanted waveguides. Recent advancements in bonding of single crystal thin films of LiNbO_3 onto silicon substrates (LNOI), opened a new avenue to explore the advantages of LiNbO_3 in the context of PICs and benefit from the cost reduction, manufacturability and integration aspects offered by integrated circuits [1]. Here waveguides are fabricated using reactive ion etching (RIE) in a LiNbO_3 thin film which allows for significantly higher refractive index contrast ($\Delta n \sim 0.7$) and hence small mode volume. Such a tight confinement not only results in more efficient and faster modulators, but also significantly smaller bending radius and PIC footprint. This ultimately allows designing complex PICs with tens of components in small millimeters-sized chips.

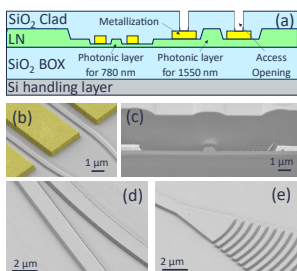


Figure 1: a) Cross section layout of CSEM's LNOI PIC platform. SEM images of b) an electro-optical modulator (false coloured), c) the cross-section showing the LNOI waveguide with the electrodes forming a phase shifter, d) coupled waveguides, and e) grating coupler.

However, so far, LNOI technology has been limited to few academic groups around the world. This is mainly because currently there are no PIC foundry that offers LNOI technology as standard platform to the industry. Establishing a reliable, high yield fabrication process for LNOI PICs is the key to ensure wide spread of this novel technology. CSEM is set to establish an open LNOI foundry based on a reliable process design kit (PDK) library.

One major milestone towards a reliable LNOI PIC platform to realize low loss waveguides, crucial to on-chip routing and enabling high performance passive and active components. Over the last three years, an LNOI etching recipe based on ICP RIE Ar+ milling has been optimized to achieve smooth sidewalls that are highlighted in Figure 1. Here, we present the results of our statistical measurement of waveguides losses in telecom C-band that are fabricated in a wafer-scale fabrication technology.

To characterize the propagation loss, an extensive measurement campaign is required to obtain a statistical value for losses, which would be elusive by measuring only a few numbers of waveguides. In this work we measured a set of racetrack resonators which encompasses a sweep of racetrack resonators

with identical bending radius but varying the straight section lengths. The resonator waveguide width is fixed to 1500 nm. In such a configuration, the linewidth/quality factor of the resonator will reflect the total loss in the ring resonator. By extracting the trend in the intrinsic quality factor of the series of the resonator, we can extract the propagation loss of the straight waveguide section.

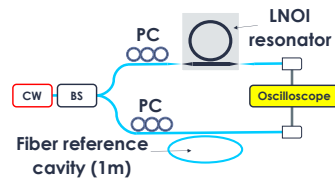


Figure 2: Schematic of the measurement setup to characterize LNOI resonators.

Figure 2 schematically illustrates the fully automated setup to perform measurements and gather the statistics through thousands of resonance measurements from many resonators of different geometries. This provides us with information about our process repeatability and the geometry variation, helping us to understand the different sources of propagation losses and focus our efforts in develop an optimized fabrication process that maximizes the performance of our devices.

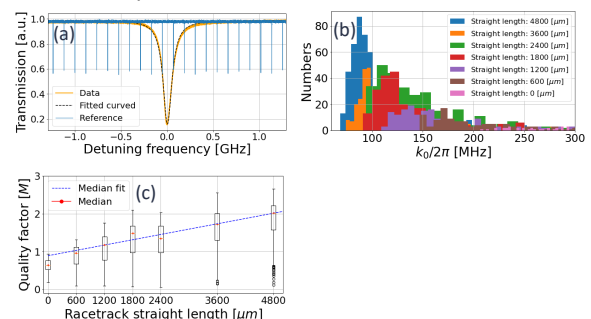


Figure 3: a) LNOI racetrack transmission (orange) with Lorentzian fitting (dashed black) and fiber-loop referenced resonator (blue) with calibrated free spectral range of 118 MHz; b) Histograms of racetrack propagation decay rate loss vs. straight line length; c) Boxplots of racetrack intrinsic quality factor vs. straight line length.

Results are presented in Figure 3. Particularly the histograms of intrinsic linewidth (Figure 3b) and plot of intrinsic quality factor vs. resonator's length (Figure 3c) show a clear trend in which lower linewidth (= higher quality factor, Q) is achieved in racetracks with longer straight section. This can be a strong indication that the Q is limited in our devices by the bending losses at the two ends of the racetrack resonator rather than the propagation losses of the straight waveguides. Indeed, with an intrinsic quality factor greater than 2.5×10^6 , corresponding to a linear waveguide loss below $< 0.14 \text{ dB/cm}$ is obtained. These results have been presented at ECOC 2022 conference.

[1] D. Zhu, et al., Adv. Optics & Photo., 2021,
doi:10.1364/AOP.411024

Toward an Open Access Integrated Photonics Foundry for Lithium Niobate on Insulator (LNOI)

A. H. Ghadimi, H. Sattari, J. Leo, H. Zarebidaki, D. Grassani, I. Prieto, G. Choong, Y. Petremand, O. Dubochet, S. Lecomte, M. Despont

Lithium niobate on insulator (LNOI) is one of the most promising emerging platforms for photonic integrated circuits (PICs) that comprises a unique set of interesting optical properties: a high electro-optic (EO) coefficient, high intrinsic 2nd and 3rd order nonlinearities, a large transparency window (350 to 5500 nm) and a strong piezo electric coefficient. CSEM is set to establish the first open access LNOI foundry based on a reliable high-yield fabrication process as well as an optimized process design kit (PDK) with a library of standardized building blocks. These endeavors are highly supported by EU and National public funds and the results of this multi-year project will pave the way for the creation of the first open European PIC foundry for LNOI that will be available to all stakeholders in coming years.

Lithium niobate (LiNbO_3) has attracted a lot of attention since the 1970s as an electro-optics and nonlinear photonics material. Recent advancements in bonding of single crystal thin films of LiNbO_3 onto silicon substrates leading to so-called LNOI stack, opened a new avenue to explore the advantages of LiNbO_3 in the context of PICs and benefit from the miniaturization, cost reduction, scalable manufacturing, and integration aspects offered by integrated circuits. Tight confinement of light in $<1 \mu\text{m}$ cross section, reactive ion etching (RIE) manufactured waveguides not only results in more efficient and faster modulators, but also significantly smaller bending radius and PIC footprint. This ultimately allows designing complex PICs with tens of components in small mm-sized chips.

Due to its unique material properties an LNOI-based PIC platform can serve a vast range of applications including telecom, metrology, LiDAR, sensing and furthermore leveraging nonlinear photonics for signal processing, spectroscopy, quantum computing and other quantum technologies. LNOI is a platform that not only outperforms other PIC platforms in areas such as ultra-fast modulators, but also enables new functionalities that are currently beyond the capability of other PIC platforms such as: sum or difference frequency generation, second harmonic generation (SHG) and acousto-optics modulators (AOMs), which are needed for advancing novel quantum and sensing technologies.

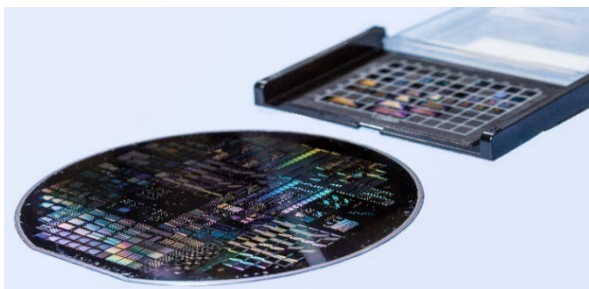


Figure 1: LNOI PIC platform at CSEM based on 150 mm wafer-scale fabrication technology offered as pre-commercial MPW service.

Despite all the mentioned advantages, so far there is no PIC foundry that offers LNOI as a standard PIC platform. CSEM is set to change that by developing the first industrial scale PIC foundry for LNOI technology based on a reliable high-yield fabrication process as well as a library of optimized building blocks that are offered as a process design kit (PDK). This endeavor has been supported by EU and Swiss National funding and here we will present the scope and objectives of the most important ones.

1. **ELENA** ^[1] is our main flagship EU project on LNOI activities which is funded under H2020 project and is coordinated by CSEM. In ELENA, CSEM joins forces with an international consortium of 10 partners with the vision of developing the first European PIC platform for LNOI as well as a fully European supply chain for the LNOI industry. This includes activities ranging from LNOI wafer manufacturing and PIC design software to packaging and several demonstrators. In this project, CSEM will develop a wafer-scale fabrication process for LNOI waveguides with target losses below 0.1 dB/cm and a PDK of active and passive components (Figure 2).

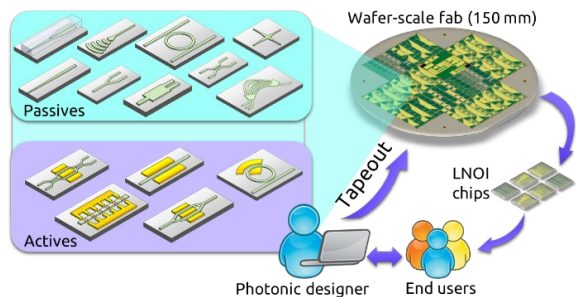


Figure 2. Schematic illustration of passive and active building blocks that will be developed in the context of ELENA project.

2. **PATTERN** ^[2] is EU project funded under Horizon Europe program. In PATTERN, we aim at heterogeneous integration of InP gain chips and photo detectors (PD) with LNOI via methods such as micro-transfer printing for implementation of fast InP-LNOI hybrid tunable lasers. Also, the focus of PATTERN is to push the device technology edge to ultra-high frequencies above 100 GHz including modulators, photodetectors, packaging and software expertise. In PATTERN we will also develop new building blocks such as acousto-optic modulators (AOMs) by combining surface acoustic waveguides (SAWs) and optical waveguides as well as magneto-optic isolators through hybrid integration of yttrium iron garnet (YIG) and LNOI.

3. **LOLIPOP** ^[3] is an EU project under Horizon Europe program with the aim to integrate LNOI with SiN platform and generate light at new wavelengths in visible and near infrared (NIR) via nonlinear wavelength conversion in LNOI. Moreover, CSEM develops several demos using such hybrid integration such as FMCW LiDAR engine and quantum key distribution systems.

4. **SPRINTER** ^[4] aims at applications of high speed LNOI modulators in telecom systems in industrial environments. SPRINTER is also funded under Horizon Europe program and includes a consortium of 12 different partners.

[1] <https://www.project-elena.eu/>

[2] <https://pattern-project.eu/>

[3] <https://horizon-de-lolipop.eu/>

[4] <https://horizon-de-sprinter.eu/>

Increasing the Quantum Efficiencies of Quantum Devices with Microlens Arrays

F. Zanella, C. Schneider, L. Ceric, N. Morales, P. Galli, G. Basset

Microlenses replicated on front-illuminated single-photon avalanche diodes (SPAD) or back-illuminated CMOS image sensor are found to be stable to temperature variations, exposure to humidity, mechanical shocks and vibrations, as well as irradiation by UV, protons and gamma rays (e.g., for space applications). They highly improve the effective fill-factor, on front-illuminated SPAD-based image sensors, and the parasitic light sensitivity on a back-illuminated CMOS image sensor. Their broad transmission spectrum from NUV to NIR, combined with the wide geometrical space available to fabricate microlenses on various active substrates (150 mm wafer or die down to 2x2 mm²), make them suitable for a wide range of quantum photonics applications.

CSEM has more than 20 years of experience in the fabrication and replication by UV nanoimprint lithography (UV-NIL) of micro and nano optical structures, and in particular of microlens arrays (MLAs). MLAs are key components of many optical systems such as photolithography tools or telecom fiber interconnects. MLAs can also be monolithically integrated by UV-NIL onto active substrates (wafers or bare dies) to serve two purposes. Firstly, to concentrate the incident light in the photosensitive area of advanced photodetectors/imagers such as charge-coupled device (CCD), CMOS, single-photon avalanche diode (SPAD) or silicon photomultiplier (SiPM). Therein, the MLA increases the pixel effective fill-factor (i.e., external quantum efficiency) for brighter and more contrasted images in life science, space^[1] and quantum applications. Secondly, to shape/collimate the beam emitted by integrated light sources (micro-LED, VCSEL).

CSEM has been working on the origination of microlens by thermal reflow targeting nearly gapless MLA, as illustrated in Figure 1, and on qualifying such MLAs for space, as previously reported^{[1][2]}. Therein, MLAs were found to be stable to temperature variations (100 cycles from -55°C to 125°C passed), exposure to humidity, mechanical shocks and vibrations, as well as irradiation by gamma rays. Other microlens materials have been screened since then and successfully tested in the 300-2000 nm spectrum range for UV stability, as shown in Figure 2 (up to 15 kJ/cm²), and proton irradiation stability (up to 100 kGy).

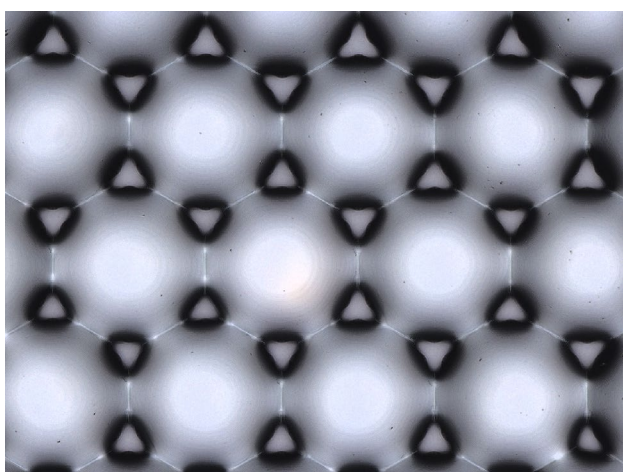


Figure 1. Nearly gapless microlens array with 23 μm pitch.

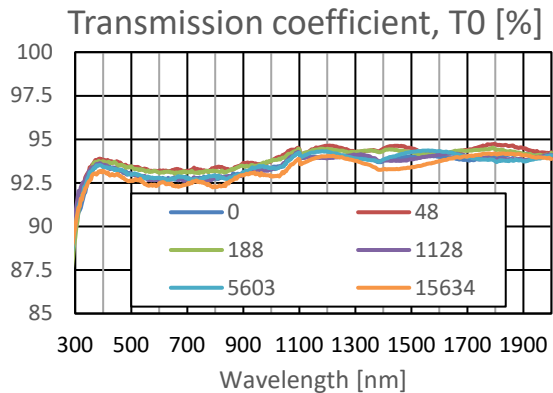


Figure 2: Example of a UV stable microlens material. Doses in J/cm². Optical stack: 30 μm microlens material deposited on quartz.

For all these reasons, EPFL Laboratory for High Energy Physics (LPHE) is currently evaluating CSEM's microlenses on SiPM arrays for the upgrade of the LHCb^[2] detector at CERN's LHC accelerator. Measurements at room temperature of the first prototypes exhibit an increase in the photon detection by 15% which is in good agreement with simulation results. The characterization of a second prototype batch at room temperature is on-going, and testing at cryogenic temperatures previewed in the next step.

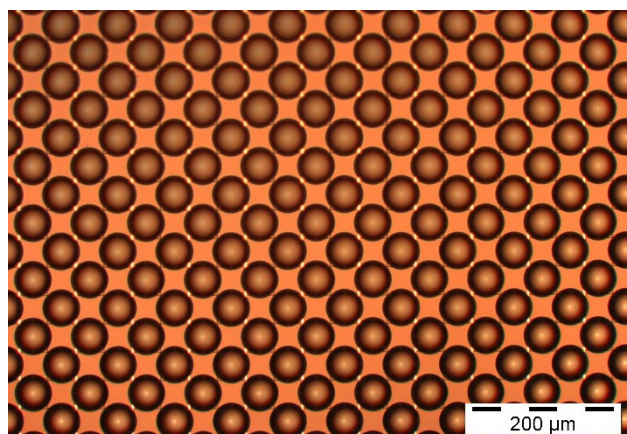


Figure 3: Microlenses on EPFL's silicon photomultiplier array^[2].

The UV stability test campaign was funded by the EU H2020 project Phabulous (grant 871710) and the shown nearly gapless MLA by the Innosuisse project SPADLens (agreement 2155010564). CSEM thanks them for their support.

EPFL LPHE conducted the proton irradiation test at SWAN Isotopen, Bern. CSEM thanks them for the fruitful collaboration.

^[1] F. Zanella, et al., "Microlens testing on back-illuminated image sensors for space applications", Applied Optics 59 (12), 3636-3644 (2020).

^[2] C. Tripli, et al., "Microlens-enhanced silicon photomultiplier arrays for LHCb SciFi Tracker Upgrade 1b", Nuclear Inst. and Methods in Physics Research, A, 1040, 167216 (2022).

Manufacturing Acceleration of Free-form Micro-optical Arrays

T. Offermans, F. Zanella, O. Fernández

Free-form micro-optical arrays (FMOAs) gain increasing interest because they can overcome some limitations of rotationally symmetric optical components, and thereby enable better performance and compactness of optical devices. However, the complex and segmented surface shapes bring fabrication challenges. Here, we present computer-aided design (CAD)-based tools that help analyzing FMOA designs for manufacturing constraints.

Micro-optics manufacturing technologies cannot produce features of any size. Particularly, some origination technologies have a limitation on the smallest feature they can produce. In diamond turning, for instance, such limitation is often linked to the size of the cutting tool, whose size is never zero: accordingly, the concave connection between micro-lenses in the master (which become convex tips on the imprints) show a curvature radius which is linked to the cutting tool radius.

To locate the areas where the size of the feature is below the smallest possible, a new design tool was created in both Grasshopper and Rhinoceros scripts. Based on the 'largest empty sphere'-approach, the scripts extract boundary curves from a single surface object and find the narrowest section. The Rhinoceros script was further optimized to handle multi-surface objects, see the results with the three green circles obtained from a FMOA in Figure 1.

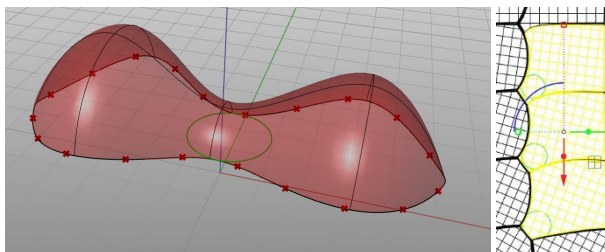


Figure 1: Minimum feature size script output (green circles): Grasshopper on a single surface (left) and Rhinoceros on several lenses of a FMOA (right).

The script output is however dependent on the number of points used to discretize the boundary curves and on the shape topology. To avoid this limitation, and, particularly, for origination techniques based on diamond turning (DT), another script was implemented, which provides the maximum curvature i.e., the required minimum tool radius. In these cases, the minimum radius of curvature of the connections between features (facets, lenses) in the areas of the mold masters manufactured in a row (without changing the location of insert parts or tool) is limited by such tool radius.

This script requires a CAD file in which all connections between features have been filleted, to account for the actual cutting process, which, in DT, cannot produce sharp edges. The results are shown in Figure 2.

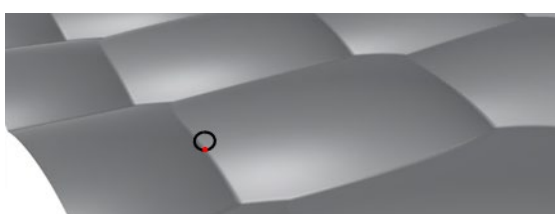


Figure 2: Minimum tool radius extracted over the whole FMOA. The contact point found, is shown in red, and the radius is visualized by the black circle.

Rhinoceros offers a set of built-in functions able to convert a point cloud into a surface, such as "patch" and "Surface from Points". However, the application of these, directly on the point-cloud of a free-form mini- or micro-lens array tend to yield imperfect conversions. The conversions can fail, when using chaotic point-clouds, with points not sorted in any way, or with a non-uniform density of points. In some cases, the resulting surfaces cannot follow the actual shape in sharp transitions.

To tackle some of these problems a further design tool was developed for data-healing, applied prior to running the most accurate Rhinoceros functions to produce surfaces from point-clouds. The data healing includes the removal of points prone to produce problems (noisy points from measurements, clearly out of the surface due to errors in one or more coordinates, for instance) and the re-arrangement of points in a rectangular parametrization allowing "Surface from Points" functions to produce optimal results. The latter is done with a gridded Piecewise Cubic Hermite Interpolating Polynomial before running the script. The result is shown in Figure 3b.

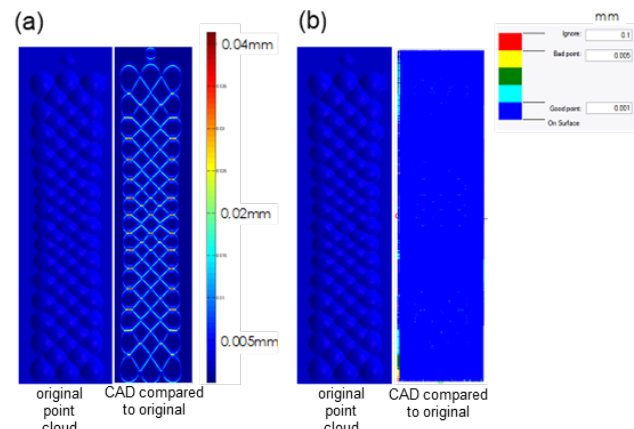


Figure 3: a) Imperfect point cloud-to-surface conversion without point healing; b) If the point-cloud is healed (removal of "conflict" points and re-arrangement of points in a rectangularly-parametrized grid), the results are almost perfect, as shown on the right, where no more deviations are visible except for a small subset of isolated points.

The presented tools make it possible to evaluate designs at an early stage, which speeds up the manufacturing assessment and facilitates the necessary corrections before proceeding with often expensive manufacturing trials.

This work has been carried out within the PHABULOpS project (<https://phabulous.eu>) and was published at the SPIE (doi: 10.1117/12.2597089). The project has received funding from the European Union's Horizon 2020 research and innovation programme under grant agreement n° 871710 in a public-private partnership with Photonics21.

Nanoimprinted Metasurfaces for Foldable and Rollable Displays

B. Gallinet, D. Kazazis*, J. Heidler, M. Kraus, D. Pires **, F. Federspiel **, R. Frantz **

Phase retarders maximize the contrast in displays. Future display technologies will enable production of increasingly thin displays, enhancing versatility and enabling storage by folding or rolling. One obstacle is however the thickness of current phase retarders. In this work, an ultra-thin phase retarder based on dielectric metasurfaces is designed and fabricated with a scalable process.

Future displays in devices such as tablets or smartphones will be foldable or rollable to simplify consumer use and storage. These displays must be extremely thin to have the flexibility of a foil. Reduction of back reflection from ambient light is crucial to maximize the display contrast. This is currently done with a polarizer and a quarter waveplate (Figure 1). Standard phase retarding materials have typical thicknesses of a few microns. Metasurfaces have the potential to overcome the limitations of phase retarding materials, as they can strongly alter the phase of the electromagnetic field within a single micron [1].

In this project, dielectric metasurfaces are designed, fabricated and integrated as colorless and highly transmissive quarter waveplate. The nanostructures are originated with electron beam lithography and replicated using nanoimprint lithography (NIL), which is widely used to replicate nanostructures cost-efficiently and at large scale.

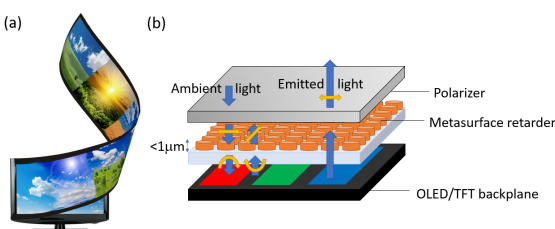


Figure 1: a) Rollable display concept. b) Metasurface retarder for minimization of reflected ambient light and maximization of contrast.

To maximize phase delay, the nanostructure aspect ratio and refractive index are maximized. Two approaches based on nanoimprint lithography are investigated (Figure 2).

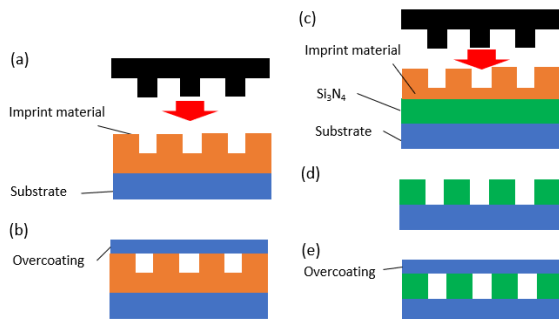


Figure 2: Two fabrication approaches investigated in the project. a) Direct nanoimprint. b) Nanoimprint and etching into a silicon nitride thin film.

The first approach uses direct nanoimprint lithography adapted to high aspect ratios [2]. The nanoimprint material has a refractive index larger than 1.9.

The second approach is based on nanoimprint on a thin film of silicon nitride, followed by transfer etching. It requires more process steps but allows for larger aspect ratios. Figure 3 shows electromagnetic simulations of optical retardation for both approaches. The required retardation is 0.25 ± 0.05 waves over the visible range, corresponding to a quarter wave. The required retardation over the visible spectra comply with requirements over incidence angles up to 50° .

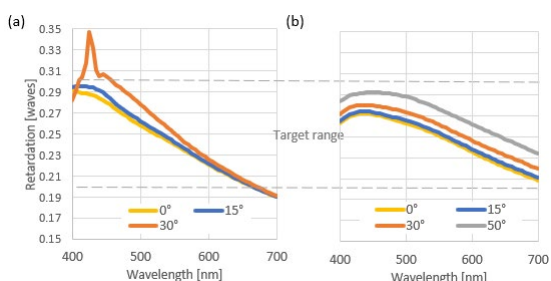


Figure 3: Simulations of optical retardation from two fabrication approaches. a) Direct nanoimprint of index above 1.9. b) Nanoimprint and etching into a previously patterned silicon nitride thin film.

The nanoimprint master is realized with electron beam lithography and etching into a silicon wafer (Figure 4a). Roll-to-plate UV nanoimprinting technology is used for the direct replication on thin foil, which enables industrial scale production. First tests show successful replication of the desired nanostructure in a high refractive index imprint material (Figure 4b).

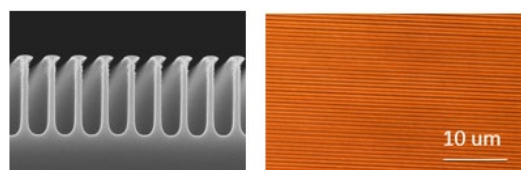


Figure 4: a) Scanning electron micrograph of the silicon nanoimprint master. b) Microscopic image of a nanoimprinted structure into a high refractive index material.

Further work will include fabrication process development and optical measurements of phase retardation, and integration in a demonstrator. This metasurface technology can also be applied in other segments of the consumer electronics market, for example as flat imaging elements. Funding from SNI Nano-Aargovia is gratefully acknowledged.

* Paul Scherrer Institut, Forschungstr. 111, 5232 Villigen PSI
** ROLIC Technologies Ltd, Gewerbestrasse 18, CH-4123 Allschwil

[1] A. Arbabi, *et al.*, Nature Nanotechnology 10, 937- 943 (2015).

[2] F. Lütolf, *et al.*, Optics Continuum 1, 1051- 1059 (2022).

Contactless Water Quality Monitoring for Sewers

K. Preitner, S. Blanc, C. Kündig, D. Honzákko, P. Pad, L. A. Dunbar

We demonstrate a contactless water quality monitoring system tailored for wastewater. The combination of multispectral imaging and machine learning at the edge allows us to measure the turbidity and the chemical oxygen demand with a cost-effective and almost maintenance free solution. The dedicated illumination was specifically tailored to this application, and multiple machine learning models were tested to optimize and predict the water quality, giving results beyond state-of-the-art.

Realtime monitoring of water quality in urban drainage systems and in waste-water treatment plants is essential to assess the pollutants that might contaminate the environment [1] and to effectively manage treatment plants operation. Nowadays monitoring is achieved via manual sampling campaigns or with spectrophotometric probes immersed in water [2], these procedures are difficult to operate and maintain [3] and can result in delayed reaction causing unnecessary harm to the environment and/or facilities.



Figure 1: Typical sewer with low level water flowing through.

Water quality can be assessed by measuring the turbidity (TUR) and the chemical oxygen demand (COD), an indicator of the organic concentration of the water.

By using multispectral imaging combined with machine learning algorithms, we are able extract spectral characteristics to predict the water quality. This technique uses the diffuse reflectivity of the water, allowing a contactless measurement of the water.

A laboratory setup was developed as a proof of concept. Consisting of an active illumination of 13 LEDs ranging from 250 nm to 700 nm, and a grayscale camera sensitive to the same range and a resolution of 2046×2048 pixels. A custom control unit drives the LEDs in sequence to acquire a multispectral cube.

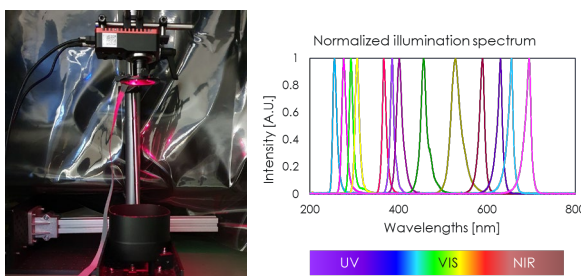


Figure 2: Left: acquisition setup; Right: normalized illumination spectrum.

Twenty-seven water samples were made with different concentration of standard solution of TUR and COD, from 75 to

[1] Alice Botturi, et al., "Combined sewer overflows: A critical review on best practice and innovative solutions to mitigate impacts on environment and human health" Critical Reviews in Environmental Science and Technology, 1585-1618 Volume 51, (2021).

950 NTU and 33 to 900 mg/l respectively, which corresponds to the range observed in sewers.

Multiple models such as partial least squares (PLS), support-vector machine (SVM) and rain forest (RF) were evaluated. The most promising model is the PLS, where an R^2 of 0.99 for TUR and 0.93 for COD are achieved.

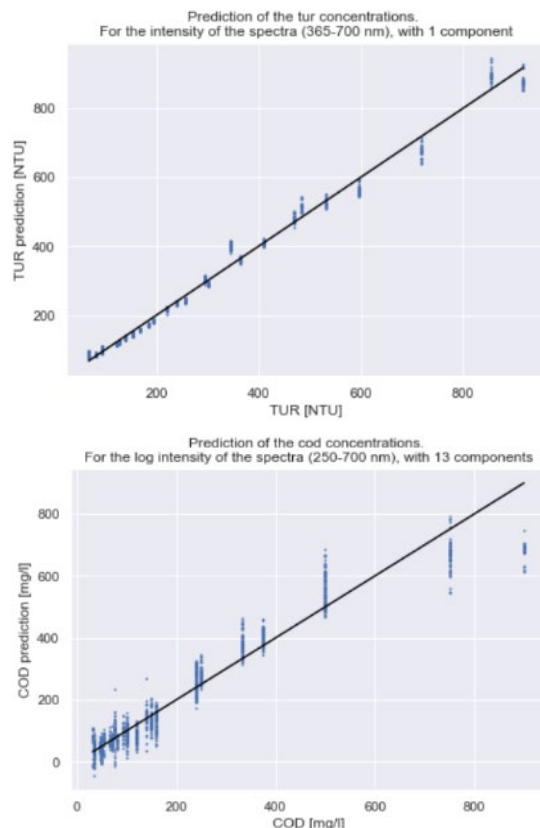


Figure 3: Turbidity (top) and chemical oxygen demand (bot) prediction.

Figures 2 and 3 show the excellent predictions which go beyond state-of-the art. The remaining investigations will tackle the challenge to obtain robust results in situ.

CSEM multispectral imaging systems provide application-specific solutions. The advantage of dedicated solutions is that they are optimized in aspects such as data rate, physical size, accuracy and cost.

[2] R. Salgado Brito, et al., "In situ UV-Vis spectroscopy to estimate COD and TSS in wastewater drainage systems" Urban Water Journal, 261-273 Volume 11, (2014).

[3] G. Gruber, et al., (2006) "Practical aspects, experiences and strategies by using UV/VIS sensors for long-term sewer monitoring" Water Practice and Technology.

Tools for Controlled Positioning of Organoids

S. Heub, E. Vuille-dit-Bille, D. Ledroit, J. Goldowsky, S. Boder-Pasche, T. Valentin, G. Weder

Organoid models are playing an increasing role in the development of personalized medicine for both drug testing and regenerative medicine. While several solutions for standardized production of organoids in large scale are existing, there is currently an urgent need for handling and positioning tools. CSEM is developing various solutions for the controlled positioning of organoids using hydrodynamic, surface modification and non-contact active forces (acoustophoresis) approaches.

Organoid technology is revolutionizing disease modeling, drug testing and organ replacement. These mini-organs, based on stem cells, exploit the potential of multicellular assemblies to self-organize into three-dimensional structures that mimic *in vivo* architecture and functions. The combination of microphysiological systems and autonomous self-assembly (organoids) is emerging as the next generation of tissue models.

In the past decade, researchers have focused on developing easy-to-use, large-scale production platforms to generate reliable organoids, tumoroids, and spheroids. It is indeed the first step towards implementation in the industry. However, unleashing their full potential now requires access to effective positioning methods, particularly to model diseases, test drug sensitivity, examine tissue morphogenesis and form complex tissues for transplantation^[1]. Organoid positioning with precise spatial orientation is critical to build multi-organoid assemblies and for high-throughput analytical processes. Methods must be easily integrated with standardized workflows while enabling safe, automated, and parallelized operations.

CSEM Tools for Life Sciences is elaborating specific labware to enable controlled positioning of organoids for their entire life cycle.

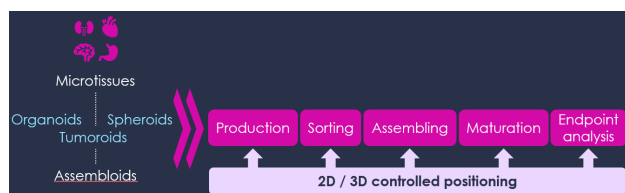


Figure 1: CSEM roadmap on tools for organoid technology illustrating the increasing need of controlled positioning from production to endpoint analysis.

HistoBrick^[2,3] is a hydrogel-based microwell plate designed to facilitate the precise co-planar alignment of microtissues for high-throughput micro-histology (Figure 2a), developed in collaboration with FHNW. Results of paraffin embedding and thin sectioning, obtained using 200 µm HepG2 microtissues on the 96-well format, showed that 75% of samples have their center located in average ±40 µm from the best fitting plane (forming 0.2-0.3° angle with sectioning plane). In partnership with the Institute of Molecular and Clinical Ophthalmology Basel (IOB)^[4], the HistoBrick approach is now being extended to the positioning and embedding of larger & non-spherical organoids (1.5-3 mm) (Figure 2c), as well as cryosectioning. Automated pick and place organoid transfer is currently being implemented.

Hydrodynamic methods, such as a microfluidic trapping device made of hydrogel are also investigated (Figure 2d). The approach enables high-precision positioning of multiple organoids of similar size inside a channel. The organoids are immobilized and can be exposed to various static and dynamic test conditions, enabling testing of multiple replicates in a single channel and direct observation under a microscope.

CSEM is exploring acoustophoresis for precise positioning and orientation of heterogeneous organoid populations in various water-based media using MEMS technologies (Figure 2e). The technology based on piezoelectric micromachined ultrasonic transducers (PMUT) provides geometry and patterning flexibility with low frequencies. The use of external forces offers the advantage of contact-free manipulation in 3D.

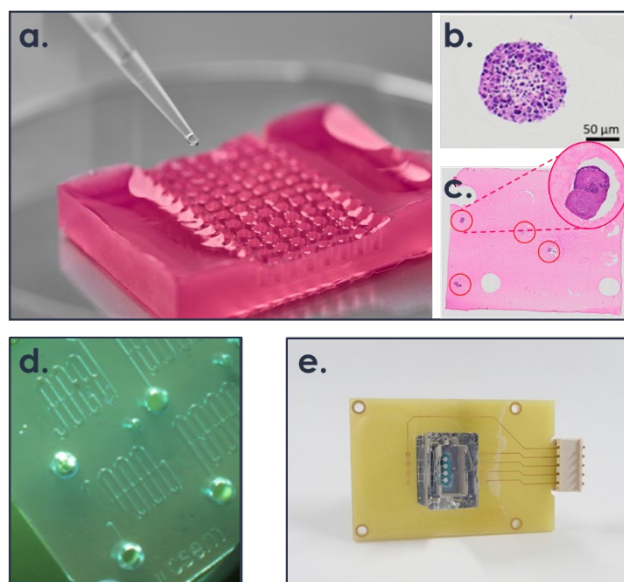


Figure 2: a) 96-well agarose-based HistoBrick, and b) resulting histological section of an HepG2 microtissue; c) Histological section of a 1.5 mm retina organoid obtained with 24-well HistoBrick; d) Hydrogel microfluidic trapping chip; e) Acoustofluidic positioning chip based on PMUT technology.

The standardization of the complete life cycle of organoids comprising production, handling, sorting, positioning, maturation, and analysis is mandatory to enable their industrialization and adoption by the pharma and biotech industries.

^[1] E. Vuille-dit-Bille, et al., "Tools for manipulation and positioning of microtissues", Lab Chip, 2022, 22, 4043-4066.

^[2] Innosuisse project 39848.1 IP-LS

^[3] S. Heub, et al., "Coplanar embedding of multiple 3D cell models in hydrogel towards high-throughput micro-histology", Sci. Rep. 12, 9991 (2022), doi:10.1038/s41598-022-13987-4

^[4] Innosuisse project 57515.1 IP-LS

High-precision Membranes for Cell Isolation

J. Heidler, M. Kraus, M. Zinggeler, L. Tomasova*, Z. Guttenberg*, S. Riethdorf**, K. Pantel**, T. Brandstetter*, J. Rühe*, F. Kurth

We recently reported the successful development and production of both metal and polymer high-precision porous membranes^[1]. The manufactured membranes have the advantageous properties of commercially available track-etched polymer membranes (low-cost, scalability, flexible materials) as well as those of expensive silicon semiconductor membranes (high pore density, homogeneous structure control, customized layouts). Herein, we report the application of our membranes for single cell isolation from complex fluids.

Microfiltration membranes are widely employed for the filtering or up-concentration of cells and micro-particles. Commercially available track-etched membranes are merely semi-suitable for such applications due to low porosity and pore overlap thereby limiting filtration throughput and isolation specificity. Silicon semiconductor process-derived membranes overcome these limitations at the expenses of high costs and stiff and brittle properties. Our previously reported fabrication routes for scalable and cost-effective nickel and polymer high-precision membranes overcoming these challenges set the stage for scalable and cost-effective fabrication processes for large-area and flexible high-precision membranes. While the metal membranes are based on electroplating processes, the polymer membranes are derived by hot embossing, both highly scalable and controllable fabrication routes. The tuned pore sizes (3-8 µm) are suitable for the isolation of single cells from solutions and complex cell suspensions, and this report evidences the isolation of circulating-tumor-cells (CTCs) from blood highly relevant for clinical diagnostics as a proof of concept.

The metal high-precision membranes are now in production on 6-inch wafer scale with full area cylindrical pores, 23% porosity (at largest pore size), and 20 µm thickness. This allowed us to develop initial prototypes for customized arrangements adapted to existing analysis tools and laboratory instruments, e.g., well plates of standard SBS format (Figure 1). Hereby, cut membranes (5.8 × 1.9 cm) form highly dense pore arrays not only capable of size-selective CTC filtration but simultaneously allowing for the homogeneous positioning of isolated CTCs, aligned with the membrane pore layout. Conjunction with subsequent sub-compartment isolation facilitates high density downstream molecular analysis. Furthermore, the surface chemistry and nano-topography of the membranes can be tuned for specific requirements.

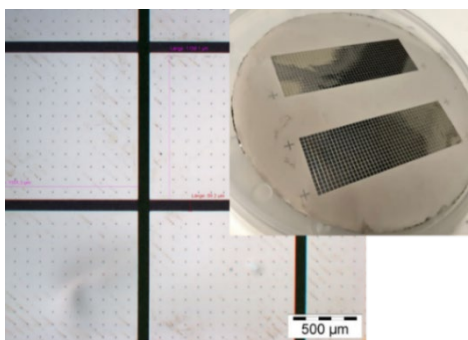


Figure 1: Metal membrane prototype adapted to SBS well-plate format at the size of a microscope slide.

One of the most limiting factors for the isolation of CTCs from whole blood is the filtration time. Available systems can process

a standard blood sample (~7.5 ml) within 2 h, which does not only limit diagnostic capacity, but same time critically impacts cell quality, a prerequisite for clinical data integrity. Embedding our membranes (25 mm diameter) in simple, commercially available filter capsules allowed to successfully isolate CTCs spiked in whole blood at high recovery rates (Figure 2) and at an extraordinary processing time of 40 s for 7.5 ml. Optimizing the fabrication process already allows us to double the available membrane diameter and we are continuing to increase it further for high blood volume processing for the benefit of short processing time and optimal cell quality.

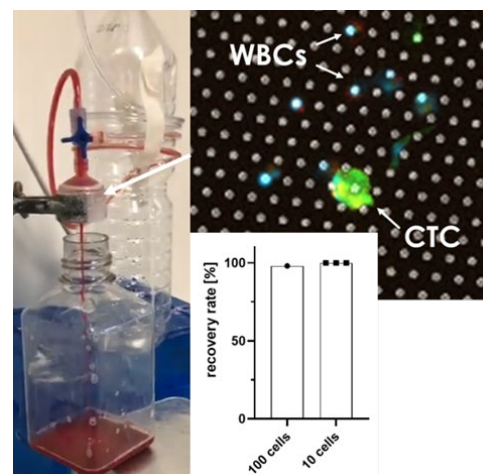


Figure 2: High-precision membranes for the isolation of CTCs from blood. Left: filtration setup. Top right: fluorescent micrograph of isolated cells on membrane [white blood cells (blue): WBC, CTC (green)].

Next to the metal membranes, we successfully upscaled the polymer membranes up to 50 mm in diameter in a single embossing step requiring no time-consuming post-processing, e.g., etching to open pores (Figure 3). Moreover, the molding tools and processing parameters are now optimized for simplified embossing and subsequent demolding from the master mold.

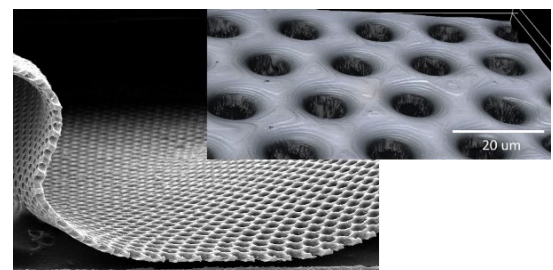


Figure 3: SEM of flexible polymer membrane (left) and optical 3D metrology image of pore size (top right).

Our project partners are supported by funding by the BMBF, Germany (CTC-Decoder, FKZ-# 031B0843A).

* Ibidi GmbH
** Universitätsklinikum Hamburg-Eppendorf (UKE)
* IMTEK Freiburg

[1] Zinggeler, et al., "Development of Scalable Fabrication Methods for High-precision Membranes", CSEM Scientific Technical Report (2019) 52.

Microfluidic SMART LIDS for Safe and Standardized Processes in Multi-well Plates

S. Graf, S. Heub, N. Schmid, R. Ischer, H. B. Atakan, M. Garzuel, J. Rohrer, S. Boder-Pasche, G. Weder, V. Revol

Cell culture applications in drug testing, organ-on-chip, and organoid culture require fluid control systems for media exchange, perfusion, sampling, injection, or pooling. For high throughput, these cell cultures are performed in multi-well plates. Traditionally, the lid of the multi-well plate is removed for manual pipetting or automated liquid handling. CSEM's SMART LIDS offer the liquid handling functionalities directly integrated in the lid while maintaining sterile conditions for long-term incubation. Using this strategy, regular medium exchange, continuous perfusion, and small volume sampling for biomonitoring can be performed in a safe and standardized cell culture process.

A common need in all cell culture is regular **medium exchange**. The medium exchange lid^[1] (Figure 1.2) enables automated media exchange. The technology readiness level of the polystyrene-based lid manufactured by injection molding has increased significantly. Various biological use cases are currently being tested.



Figure 1: Collection of CSEM's SMART LIDS.

In the frame of the EU Horizon 2020 project OrganTrans (<http://www.organtrans.eu>), CSEM has developed a microfluidic lid for the **perfusion** and maturation of bioprinted liver constructs in sterile conditions^[2] (Figure 1.1). The polycarbonate 6-well lid is fabricated via injection molding and ensures tight sealing of the sample chamber for continuous perfusion over several weeks, with possible fluid recirculation.

In the context of a collaboration with the laboratory of Bart Deplancke at EPFL and supported by the SNF Bridge CSEM has developed a **pooling** lid for genomics applications^[3] where suspended bar-code labeled RNA fragments from individual wells are pooled into one vessel for later sequencing. Two pooling lids were developed for 96- and 384-well plates (Figures 1.3 and 1.4), demonstrating high efficiency and simultaneous collection and gathering of small liquid volumes (<50 µl), providing a new tool for medium to large scale sample preparation for RNA-sequencing processes.

The **sampling and sensing** lid developed in the ECSEL project Moore4Medical repeatedly samples 6 µl from a 384 well plate and passes it to an inline glucose sensor before being automatically discarded (see Figure 2). This cycle can be continuously performed on all 24 channels sequentially. One application is to measure the glucose level in the culture medium to monitor the interaction of liver and pancreatic islet spheroids, which is enabled by the interconnected wells and gravitational flow in the InSphero Akura™ Flow plate.

Current developments are focusing on the integration of **low volume injection** functionality on a smart lid. The objective is to simultaneously inject 10 to 100 µl of a solution into multiple wells, typically needed for drug injection. In addition to the development of the dispensing prototype, CSEM has developed and compared methods based on colorimetry and air flow based for the precise quantification of small volumes. The methods enable parallel or sequential read-out directly in well-plates. Two colorimetry-based methods use pre-filled dye solutions in wells. The change of concentration induced by the injection of a small liquid volume results in an absorbance or fluorescence change which can be used to calculate the volume within each well with ±0.1 µl precision using the calibration curves as shown in Figure 3. Alternatively, CSEM's VentSens (patent pending) can be used to directly measure the dispensed volume into the sealed well plate by measuring the exhausted air from the well plate.



Figure 2: Sampling and glucose sensing lid installed on an InSphero Tilter operating the Akura™ Flow 384 plate.

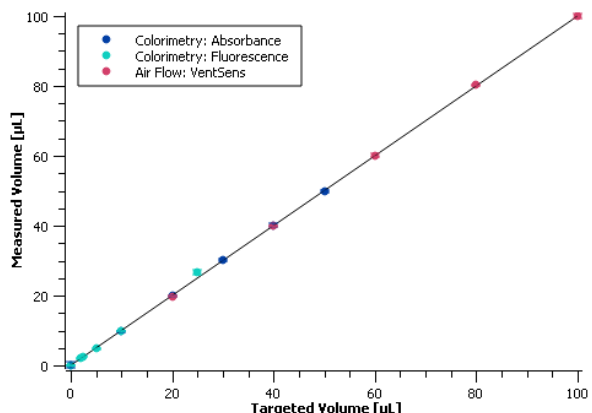


Figure 3: Calibration curves of three methods to measure small liquid volumes (range of 0.1 to 100 µl) dispensed into a well-plate.

In a next step, new functions such as mixing will be integrated into future SMART LIDS Lids.

[1] S. Heub, et al., "SMART LIDS—Standardized Cell and Tissue Culture in Multi-well Plates", CSEM Scientific and Technical Report (2021) 83.

[2] T. Valentin, et al., "Perfusion Platform for Bioengineered Tissues", CSEM Scientific and Technical Report (2022) 94.

[3] S. Boder-Pasche, et al., "Automated Microfluidic System for High Throughput Genomics", CSEM Scientific and Technical Report (2022) 95.

Perfusion Platform for Bioengineered Tissues

T. Valentin, S. Boder-Pasche, S. Heub, H. Baris Atakan, J. Goldowsky, R. Ischer, D. Ledroit, M. Garzuel, G. Weder

Tissue perfusion is a critical need when using organ-on-chip solutions for drug testing and also for regenerative medicine. Perfusion is essential to producing functional models or tissues as they supply oxygen and nutrients during the maturation, and provide the flow needed to encourage vascularization. As part of the OrganTrans EU project (No. 874586), CSEM's Tools for Life Sciences team is developing solutions for unidirectional and continuous medium perfusion through engineered, vascularized tissues. In this context, a platform was developed to perfuse and mature a bioprinted organoid-based liver construct for transplantation.

Perfusion systems aimed at mimicking in-vivo conditions are essential to recreating a physiological micro-environment for in vitro tissue maturation. Unidirectional and continuous medium flow through the engineered tissue is required to provide oxygen, nutrients, and encourage the growth of a vascularized network. In this context, a platform was developed to perfuse organoid-based bioprinted liver constructs for liver transplantation. The system is compatible with multi-well plates and leverages CSEM's microfluidic "smart lid" technology platform for perfusion enabling automated medium circulation, ensuring long-term tissue growth and maturation.

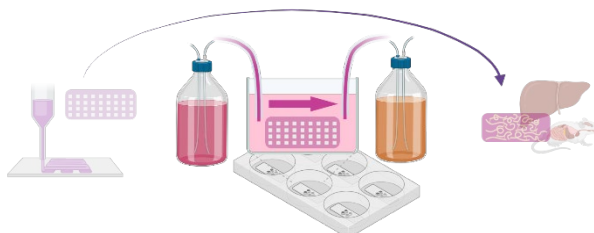


Figure 1: The biofabrication process starting with bioprinting of the liver construct, maturation of the construct in a physiological microenvironment under continuous and unidirectional perfusion, and finally in-vitro tests and transplantation in an animal model for in-vivo tests. Figure generated using BioRender.

The perfusion platform was designed to perfuse six liver constructs in parallel, continuously flowing cell culture media through the tissue. It consists of a sterile lid with integrated microfluidic features that is sealed onto the disposable inserts and creates a closed perfusion chamber (Figure 2a). Six disposable sterile inserts, into which the liver constructs are printed, fit into a standard 6-well plate (Figure 2b-c).

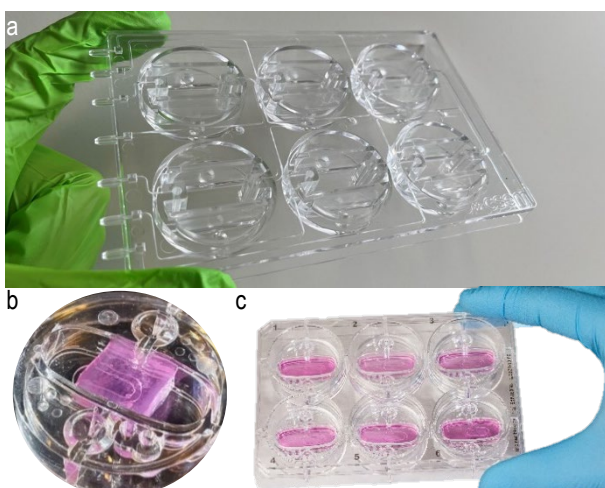


Figure 2: a) Microfluidic lid that allows sustained, long-term perfusion of the bioprinted tissue constructs. (b-c) Disposable inserts for a 6-well plate that hold the bioprinted tissue constructs.

The integrated perfusion platform integrates a peristaltic pump, fluidic components, and an electronic control system. Biocompatible materials were used for all parts that are in contact with the tissue and cell culture media (Figure 3). The perfusion platform enables continuous and unidirectional flow through six wells in parallel, with tunable flow rates ranging from 10 to 500 µl/min without any leakage. Perfusion of 2D cell culture was demonstrated for two weeks in an incubator, to verify the device biocompatibility, showing cell proliferation and no impact on cell viability. Continuous perfusion of six $1 \times 1 \times 0.5 \text{ cm}^3$ freshly printed spheroid-loaded bioconstructs with 10 to 50 µl/min of medium is currently being tested and characterized.



Figure 3: Full OrganTrans tissue perfusion system consisting of a control unit, microfluidic perfusion lid, disposable inserts, tubing, a peristaltic pump, a 1-to-6 manifold, and reservoir bottles for fresh and waste medium.

Going forward, the perfusion platform will be used to test and tune the maturation process of bioprinted liver constructs for several weeks, ensuring a sterile and closed environment. The platform can be easily adapted to other tissues, geometries, and well plates thereby serving both regenerative medicine and drug testing applications.

This work is supported by the EU Horizon 2020 research and innovation program under the project OrganTrans (grant agreement No 874586, www.organtrans.eu).

Automated Microfluidic System for High-throughput Genomics

S. Boder-Pasche, S. Graf, R. Ischer, N. Schmid, S. Heub, H. Baris Atakan, F. Kurth, V. Revol, G. Weder

Large-scale RNA sequencing is emerging as a promising technique to develop drugs and biomarkers. Adapted technologies are needed to enable simple, cost-efficient, and reliable library generation from cells or blood samples. An automated system was developed to address the challenge of sample preparation for high throughput genomics. The technology is based on a microfluidic smart lid that is compatible with standard multi-well plates and enables the simultaneous pooling of barcoded samples in a single step.

High-throughput genomics are of increasing fundamental biological interest. In particular, the development of new biomarkers and treatments requires the generation of molecular data from large collections of samples such as biobanks and drug libraries. In this context, the transcriptomic market focuses on gene expression before gene regulation. Exploiting the benefits of next generation sequencing (NGS), RNA sequencing (RNA-seq) has become a standard in the field for measuring genome-wide gene expression in biological samples. The sample preparation is however cumbersome, including RNA extraction, conversion to cDNA and amplification, and prevents the high-throughput translation of RNA-seq technologies. To face this limitation, bulk RNA barcoding and sequencing (BRB-seq) enables sample preparation in multi-well plate format [1].

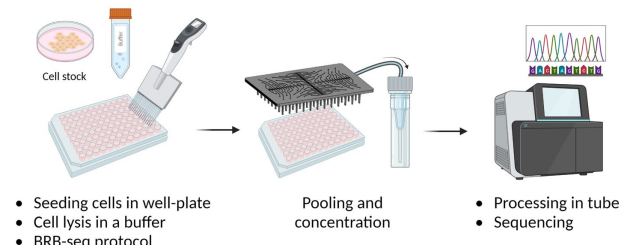


Figure 1: Concept for sample preparation for RNA-seq [2].

In collaboration with the laboratory of Bart Deplancke at EPFL [3], we aim at a complete end-to-end microfluidic solution for BRB-seq, including full integration and automation, from cell suspensions to enriched and indexed DNA libraries. To complement EPFL's process flow, the collection of all barcoded samples from a multi-well plate into a single tube will enable further steps in a single solution, thereby increasing the throughput of the sample preparation. To address this need, a technology was developed to simultaneously pool all the multi-well samples into one tube.

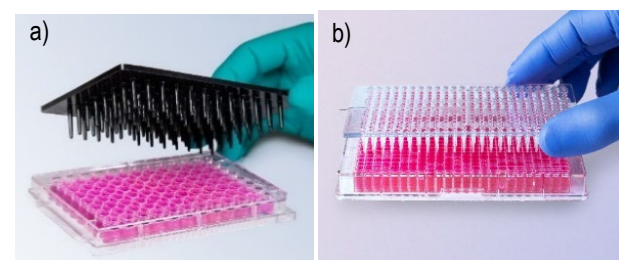


Figure 2: a) Smart lid with microfluidic channels adapted to b) 96-well plate (injection molded), and c) 384-well plate (3D-printed).

First, the technology relies on a smart labware with specific functions: a smart lid comprising microfluidic features to transport the liquid, which is adapted to standard 96- or 384-well plates

(Figure 2). The microfluidic design along with small pins enables liquid collection from all wells. The smart lids for the 96-well plate are manufactured using injection molding in polystyrene (PS), closing channels with a PS plate by laser welding. Industrial manufacturing allows disposable pooling lids. Proof-of-concept prototypes for the 384-well lids were fabricated either by milling or 3D printing.

Second, a dedicated standalone platform enables a controlled and parallelized pooling (Figure 3). The lid is connected to a vacuum pump and to the collection tube. Then, it is placed on the multi-well plate pre-filled with 10 to 80 µl of reagent. A negative pressure is applied for 2 min, which enables to empty all wells and collect all liquids through the lid into a standard plastic tube. A recovery of 88% with 4% standard deviation between similar injection molded lids was measured after 2 min pooling from a 96-well plate filled with 20 µl/well. The pooling recovery was shown to depend on the volume per well and on the lid design as well as the fabrication technique. The pooling process can be parallelized to, e.g., four plates by connecting all tubes with a manifold into the tube. Parallel pooling of four 96-well plates led to the same volume recovery in 2 min. The same set-up can be used to pool 384-well plates, by using the right lid format.



Figure 3: Standalone platform for the parallel pooling of up to four 96-well plates; the plates with the lids are placed in the drawer system on the left whereas the collection tube and the pump are in the right box.

The technology was tested with DNA barcodes to demonstrate its value in supporting high-throughput barcode-based sequencing. 96 different DNA barcodes were pooled directly from a standard well-plate followed by processing within the common sample pool and sequencing.

This new pooling technology shows great potential to address medium throughput needs in the BRB-seq workflow, thereby addressing the challenge of large-scale and cost-efficient sample preparation for RNA-seq.

[1] <https://alitheagenomics.com/>

[2] Created with BioRender.com

[3] Supported by the SNSF and Innosuisse (Bridge grant 40B2-0_187102).

Digital Lateral and Vertical Flow Assays

M. Fretz, S. del Giovane, N. Glaser, H. Chai-Gao, M. Wipf*, L. Burr, S. Paoletti, F. Kurth

We present digital lateral and vertical flow assays (LFA and VFA respectively) with electrochemical sensors based on cheap and scalable production methods. We developed low-cost point-of-care immuno-flow assays providing quantitative measurements of relevant biomarkers for the early detection of preeclampsia. Improving accurate and early diagnosis of this medical condition affecting pregnant women and their unborn babies will prevent complications and save lives and health care costs.

Biosensing is a crucial factor in diagnostics. The detection of proteins and other biomarkers has a myriad of applications in life sciences from the control of emerging pandemics to the diagnosis of medical conditions based on quantitative measurements. LFAs represent the cheapest and fastest diagnostic point-of-care (POC) test available. However, conventional LFAs have several limitations including poorer sensitivity and lower specificity than laboratory tests^[1] and their semi-qualitative results are often insufficient to indicate early disease progression.

Together with our partners Momm Diagnostics and Fachhochschule Nordwestschweiz (FHNW) we develop enzyme-linked flow assays with a signal amplification mechanism highly improving the limit of detection. The vertical and lateral flow approaches have been developed to enable quantitative detection of the analyte of interest using electrochemical detection. Full integration of components will allow for easy sample handling for future in-vitro diagnostic tools. The developed digital flow assays consist of several key elements: (1) immunoassay, (2) signal amplification, (3) electrodes, (4) fluidic system, and (5) readout unit. Whereas the immunoassay is specific to the targeted biomarker, the other components are designed to be compatible with a variety of applications.

In the present work, the biosensing process based on an electrochemical sensor has been developed for the detection of the placental growth factor (PIGF). Screen printing offers a cheap and scalable fabrication route to produce electrodes for signal readout of electrochemical assays. Similar to the material components of a conventional LFA, the printed electrodes are printed on a large sheet first. The digital LFA (here called eFlow) is then derived by 1) lamination and bonding of the hydrophilic film multilayer on top of the printed electrode sheets, 2) cutting the lateral flow strips, and 3) assembly in a fluidic cartridge with electrochemical readout. Figure 1 (left) shows a set of individual LFAs prior cartridge integration, and Figure 1 (right) is a comparison of a PIGF measurement with the eFlow and a conventional LFA. The LOD at the lower limit is increased by a factor of ~10.

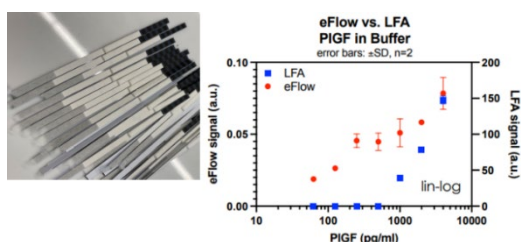


Figure 1: Lateral flow strips equipped with electrodes (left). Comparison of PIGF measurements derived by eFlow and conventional LFA (right).

* Momm Diagnostics

^[1] Y. Liu, et al., ACS Nano 2021 15 (3), 3593-3611.

CSEM also develops a VFA with a dual chamber approach (patent pending). The assay procedure is two-fold: first, the sample is added on top of the first chamber compartment. This first compartment contains all layers a lateral flow strip contains, however, stacked on top of each other so that the sample flows from the top to the bottom (Figure 2, top). A functionalized and laser perforated electrode is implemented into this layer stack and the target analyte binds on it, while other biomolecules pass by into the absorption pad. Once the immunoreaction is performed, the electrode is slid sideways into the detection chamber, in which the amplification assay is initiated by the addition of the reaction solution. This setup allows to minimize background signals thereby improving the assay sensitivity and reduces the number of incubation and washing steps to a total number of 2 (compared to a 10-step reaction with a bare electrode). The assay was first optimized for the detection of c-reactive protein (CRP) diluted in buffer as a model system and a limit of detection of 33 ng/ml could be achieved in a first proof of concept study (Figure 2 bottom).

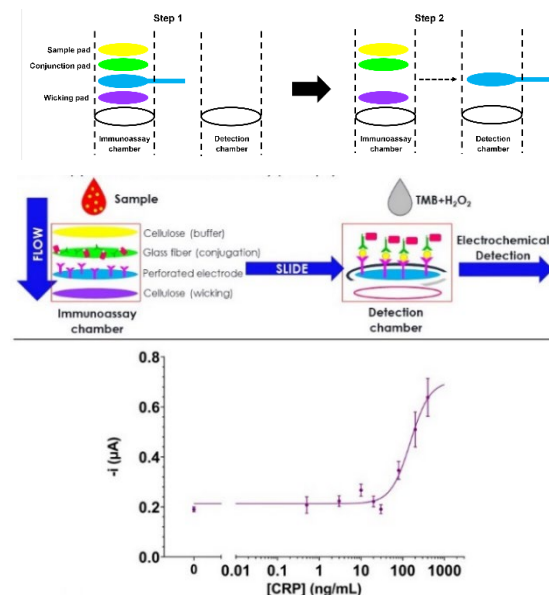


Figure 2: (Top) Principle of the two-step electrochemical immunoassay approach with assay workflow. (Bottom) Calibration curve for the quantification of CRP in blood serum using the eVFA.

Finally, the digital assays require circuitry to collect the electric signals generated by the assay and present them in a user-friendly way. CSEM has thus developed a read-out board for both amperometric and potentiometric measurements. The circuitry may be trimmed to specific needs, and it fits in a hand-held device so portability is facilitated^[2].

This project is partially funded by Innosuisse (35477.1 IP-LS) and the Swiss Nanoscience Institute, SNI (A16.13 PEPS).

^[2] I. Stergiou, et al., "Modular Electronic Readout Platform for Electrochemical Sensing", CSEM Scientific and Technical Report (2021) 93.

Urine – Non-invasive Matrix in Human Biomonitoring

D. Migliorelli, N. Glaser, R. Junuzovic, L. Mühlebach, C. Seitz, L. Burr, F. Kurth, S. Paoletti

Urine is a non-invasive source of liquid biopsy samples and in addition, urine-based tests are more advantageous than clinicopathological parameters for periodic monitoring. We developed easy to use urine analyser system addressing the need for quantitative and costless multi-parameter urine analysis for both, relevant clinical environment as screening method, and at home as informative

Evaluation and measurement of biochemical markers plays an important role in accurate diagnosis helping to adopt appropriate therapeutic methods that improves clinical outcomes. Clinically, urinalysis is crucial in the diagnosis and management of various diseases that are of either metabolic or systemic origin. Many disorders can be diagnosed in their early stages by detecting abnormalities in the urine [1]. These abnormalities include increased concentrations of constituents that are not usually found in significant quantities in the urine such as glucose, protein, red blood cells, ions, or changes in pH. Urine dipstick testing is typically performed as a point-of-care test, with interpretation of the results generally based on a vision-based colorimetric reaction, although newer automated systems for dipstick testing have been introduced.

CSEM is active since years in developing technologies to enable quick and quantitative urine analysis in different environments such as in hospitals (NUTRISHILD 2017), on-field camps (NIIDS 2019), at home (SUMIT 2021) or industrial environments (MIRA 2022). The proposed solutions were explored to tackle different necessities, specifically:

A point of care diagnostics for diagnosis and surveillance of diseases in refugee camps: A novel integrated diagnostic system for diagnosis and surveillance of diseases in refugee camps. Glucose, pH and sodium sensors have been developed and demonstrated good accuracy with a single calibration point.

- Personalized nutrition with a focus on lactating mothers and diet: A 6 channel electrochemical reader has been developed and coupled with screen printed electrodes for measuring pH in urine (Figure 1). Within the EU project Nutrishield, several analysers for different analytes have been developed to evaluate associations between the mother's milk composition and diet. The electrochemical reader enables measuring up to 6 urines in parallel with 50 μ L sample volumes. No sample preparation is required, however a nL volume of additive is needed to regenerate the pH-sensitive surface of the electrode. More than 500 urines total from infants and mothers have been analysed and benchmarked with a commercial pH-meter showing a good accuracy. (Figure 2). The sensors can be used at least with 10 different urines without being recalibrated.
- Smart toilet for at home urine analysis: an add-on module to be mounted on any toilet bowl. A prototype of a urine sampling device has been made to collect urine from the toilet (Figure 1). The disposable sensing cartridges consist of 4 sensors for general health indicators and may be used for up to two weeks. It is planned to extend the cartridge with additional customer specific sensors. Good stability and

accuracy have been achieved by using a single calibration solution for all the sensors, results related to sodium and glucose sensors are shown in Figure 3.

- Multisensor array: A miniaturized multi-sensor array for urine monitoring. Miniaturized, screen printed electrodes are tailored and functionalized for measurement in urine and other complex media. Sensors for the detection of harmful compounds and dysfunction markers with complex matrix compensation are combined in a single, digital dipstick. Machine learning is being used to train the sensor readout for more accurate and reliable sensors to improve upon commercially available semi-quantitative colorimetric urine dipsticks.

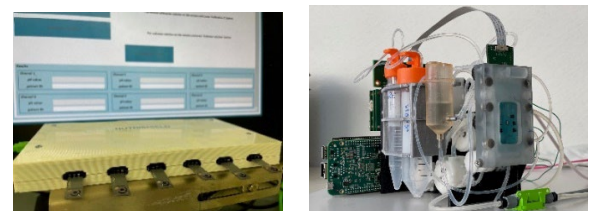


Figure 1: Prototype devices developed in Nutrishield (left: 6 channel reader with pH sensors) and SUMIT (right: add-on module for urinalysis in toilets).

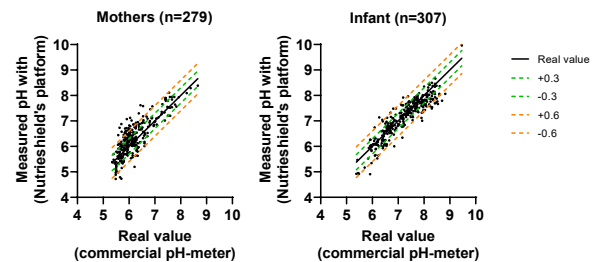


Figure 2: pH measurements: mothers and infants urines measured with Nutrishield's device and benchmarked with a commercial pH-meter.

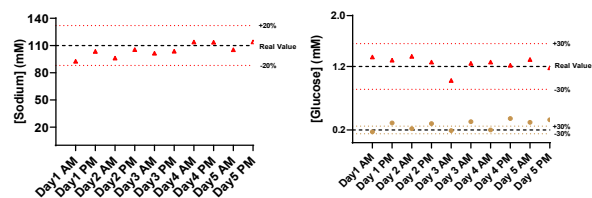


Figure 3: Glucose and Sodium measurements performed along 5 days, twice per day, with the SUMIT's cartridge device and benchmarked with the standard Laboratory analysis.

[1] E. W. Glissmeyer, E. Kent, J. Wilkers, J. E. Schunk, X. Sheng, A. J. Blaschke, C. L. Byington, Pediatrics 2014;133; e1121; 28; doi:10.1542/peds.2013-3291.

Functional Printing

N. Glaser, S. Khan, J. Disser, R. Pugin, F. Kurth

CSEM offers a diverse range of printing technologies to fabricate thin and thick film electrodes for sensors or other functional devices, such micro heating elements. Printing can occur directly on device parts, even 3-dimensional-substrates, or on flexible films to be employed as stand-alone devices or integrated into complex cartridges. We present recent examples of CSEM capabilities and refer to previous projects for further reading.

Screen-printed sensing and actuation electrodes: Electrodes made of graphite, silver, or silver-chloride may be printed for multi-analyte analysis^[1] for diagnostic use-cases or for biomonitoring, e.g., in organ-on-chip applications^[2]. Electrodes as small as $0.4 \times 0.4 \text{ mm}^2$ can be functionalized with various assays and the printed plastic film can be bonded to single- or multiuse disposable cartridges. Figure 1 shows an example of an electrode array in a fluidic channel for the simultaneous recording of 5 analytes. Sheet of electrodes with multiple printed layers and materials can be fabricated at relatively high throughput at CSEM. Well established processes can deliver series of hundreds to few thousand sheets of electrode arrays as seen in the picture.

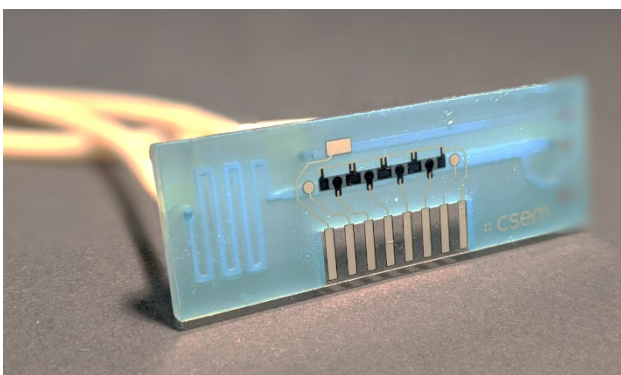


Figure 1: Screen-printed sensor array & disposable fluidic for the simultaneous recording of 5 analytes.

Positive temperature coefficient ink, commonly named "PTC", deposited on a finger silver structure offers the possibility to design a thin, flexible, and self-regulating heating element. PTC ink can be heated up to a self-regulating temperature threshold varying between 40°C to 100°C. A dedicated electronic driver to regulate the maximum temperature consequently becomes superfluous. PTC inks are easily screen printable, allowing CSEM to manufacture thin (20-100 µm) and cost-effective microheaters as shown in Figure 2.

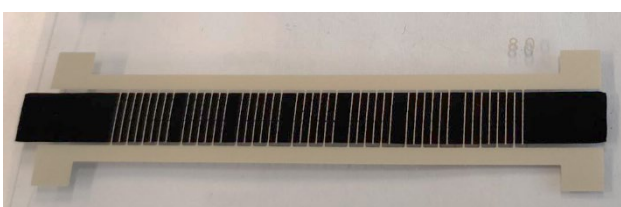


Figure 2: Screen printed micro-heaters with 7 heating zones. Shape and size are customizable from few mm^2 to several dm^2 .

Highly pure inkjet-printed platinum: Metal electrodes or photoactive materials can be printed with an inkjet process. Our platinum electrodes passed cytotoxicity tests and may be used for impedance measurements in-vitro or in-vivo^[3] or may be used as electrochemical transducers for first generation enzymatic sensors^[2]. Electrodes can be printed on A4 format with a resolution of 0.1 mm, harnessing the full advantage of the digital printing process.

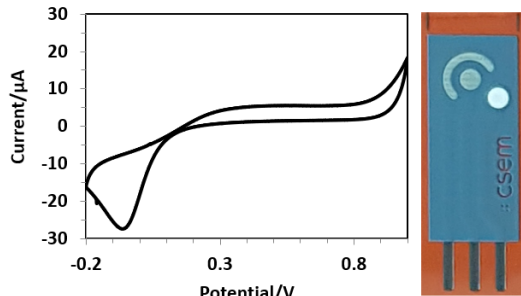


Figure 3: Inkjet-printed platinum electrodes and their response to H_2O_2 .

Functional aerosol jet printing (AJP): Many materials with wide viscosity ranges can be processed through AJP including metallic nanoparticles, epoxies, polymers & carbon-based inks (CNTs & graphene), encapsulants, sol-gel and biological materials. CSEM employs AJP to print inks such as Au, Ag, Pt, polymeric conductors (PEDOT-PSS), and quantum dot formulations on planar surfaces as well as on complex 3D topographies. High-resolution printing of Au (20 µm width) is applied to develop temperature sensors (as RTDs) and microheaters on 3D printed metallic parts for space applications. Further, an ultrasensitive X-ray photodetector has recently been developed through AJP technology at CSEM by using hybrid halide perovskite materials. Printing metallic interconnects on 3D shaped objects is another exciting feature of AJP incl. a 5-axis motion system. The large area deposition through AJP for planarization purposes is appealing for micropatterning on rougher surfaces potentially developed through 3D printed processes. Deposition of planarization and encapsulation layers on larger areas are demonstrated to show the multi-layer stacking of dissimilar materials, as shown in Figure 4.

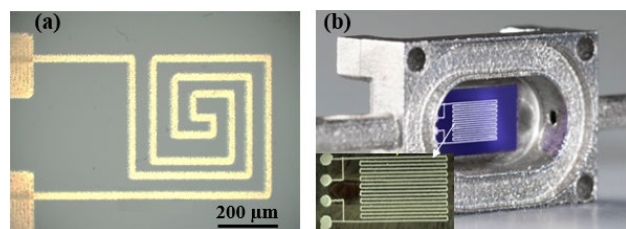


Figure 4: a) Au microheaters on PI substrate for gas sensing, b) Ag/Au RTDs in 3D objects for space application.

[1] N. Glaser, et al., "Cartridge for Digital Urine Analysis with Electrochemical Sensors", CSEM Scientific and Technical Report (2021) 92.

[2] S. F. Graf, et al., "SenseCard—a Disposable Parallel-sensing Card for Advanced In-vitro Models", CSEM Scientific and Technical Report (2021) 53.

[3] E. Borda, et al., Adv. Eng. Mater. 2020, 22, 1901403.

Machine Learning-powered Digital Support to Avoid Mistakes in the Lab

R. Limacher, T. Schöpe, F. Auf der Maur, B. Platerrier, M. Höchemer, P. Schmid, V. Revol

DeckCheck™ for lab techs is a deep-learning vision system developed by CSEM and integrated in Tecan's Fluent® automated workstation. DeckCheck™ displays discrepancies such as missing plates or incorrectly loaded tip boxes and allows the operator to correct the situation.

Laboratory workstations, whose liquid-handling robots automate complex workflows, still rely on the manual setup of labware. The inaccurate configuration of trays, tubes, and plates can result in ruined tests, broken kits, costly delays, and lost patient samples. Tecan set its sights on a digital solution for detecting mistakes with exceptional accuracy for any given workflow. CSEM was asked to develop a vision system powered by a deep learning algorithm for integration into Tecan's lab automation platform.



Figure 1: Typical worktable of a liquid handling robots with equipment and various labware such as tips, multi-well plates and tubes.

CSEM developed a completely new neuronal image comparison approach that can deal with arbitrary variations in labware while being robust to environment changes (illuminations, shadows, reflections) as well as minor allowed variations on the labware due to part variability. The new method is capable of "One-Shot Learning" – meaning it just needs a single image of a new configuration to perform robust anomaly detection on it.

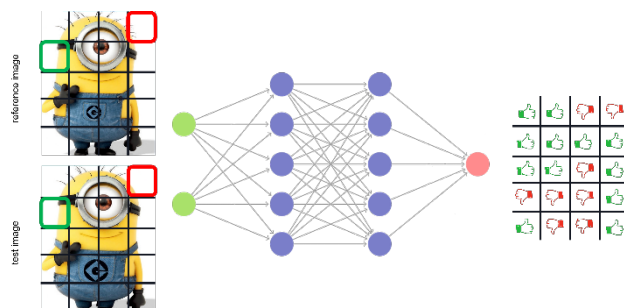


Figure 2: By dividing the images into multiple tiles, the algorithm provides a heatmap of the detected anomalies in the test image compared to the reference image.

The developed algorithm learns to detect differences with respect to a reference image. By dividing a test image into multiple smaller tiles, a heatmap can be generated, depicting the locations of anomalies within the image. The neural network has been trained in a broad range of lighting conditions and arbitrary worktable configurations – without the need for an error prone and time-consuming labeling process.

The algorithm analyses images, flagging up discrepancies in labware objects and positions that it has compared to a reference

image in under 1.5 seconds with 95% reliability, reducing risks and operators' workloads [1].

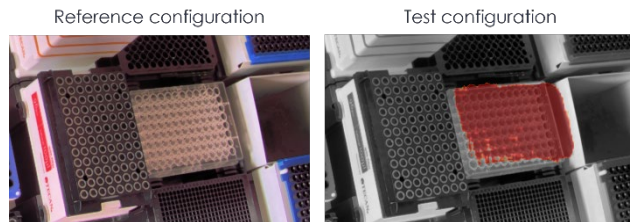


Figure 3: The newly developed approach "One-Shot Learning" allows to compare a test configuration to a reference configuration with a single image. In the present example, a lid is wrongly added on top of the multiwell plate. The comparison considers changes in illumination, accepted tolerances, and normal variations of the labware.

DeckCheck™ has been commercially launched by Tecan in April 2022. Discover more on the product by looking at the promotion video [2].

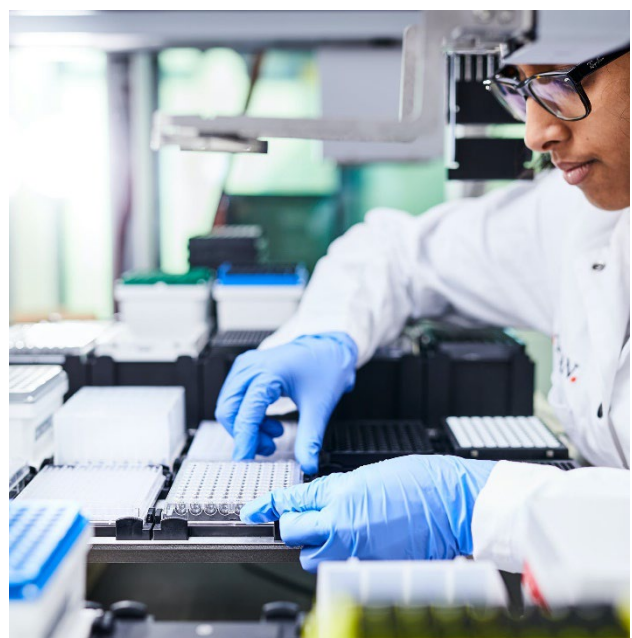


Figure 4: Thanks to DeckCheck™, the lab operator gets direct feedback in case of misplaced labware or other interferences.

The new algorithm's potential does not end there, however. CSEM has already used it for a project in the field of quality control for electronic components and envisages wider applications. The neuronal image comparison approach is also highly relevant to sectors such as security and surveillance where you want to make sure that an object remains where it should be and understand what an image of the object will look like in different light conditions.

[1] <https://www.csem.ch/en/news/digital-support-for-lab-techs-helps-them-avoid-mistakes>

[2] <https://www.tecan.com/vid-by-id?wid=akkhmq0frw&wtit=Fluent+DeckCheck%E2%84%A2>

SLOTT – Straylight Lidar OGSE Verification Tool

A. Ummel

Straylight is a major issue in any astronomical telescope design. The limitation on current analytical and test techniques are making the characterization of straylight and the identification of its sources hard to do early in the telescope development. Under a mandate from ESA, CSEM is leading the development of a breadboard OGSE (Optical Ground Support Equipment) made to acquire time-correlated straylight measurements. Such a tool would provide essential information about the straylight origin allowing to improve the design of the tested telescope.

For astronomical space telescopes, straylight represents a major issue and can seriously degrade image quality and performance. During the development of a telescope, being able to identify the origin of straylight is essential to implement mitigations and design improvements, thus reducing the straylight and improving the telescope performance.

While simulation tools can provide some information about the straylight path, they suffer from the typical limitations of most simulation tools: significant efforts are needed to perform the processing and the simulation results sometimes deviate from the measured performance due to assumptions made, consciously or unconsciously, in the model. On the other hand, state-of-the-art straylight measurement setups provide good measurements of the resulting telescope performance, but they provide very little to no information about the origin of the observed straylight.

Following the results obtained in a previous study, CSEM is developing, with the support of LusoSpace, CSL and TAS-CH, a breadboard OGSE to characterize straylight in telescopes using time-of-flight measurement. Such a tool would provide essential data about the origin of straylight in the tested telescope thus helping devising solutions to reduce and mitigate straylight.

To fulfil its purpose, the SLOTT breadboard emits laser light pulses into the tested item and measures the outcoming light intensity and time of flight. Thus, it is composed of:

- An illumination module, equipped with a Femtosecond Laser and a scanning mechanism.
- A detection and timing system, equipped with a Single-photon detector and associated time of flight measurement electronics.
- A control computer to operate the various subsystems.

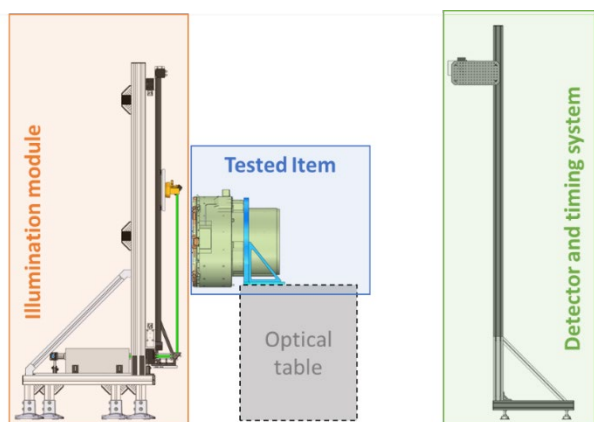


Figure 1: SLOTT breadboard overall CAD implementation.

The tested item is placed between the illumination module and the detector system. The overall design of the SLOTT breadboard is illustrated in Figure 1 and Figure 2.

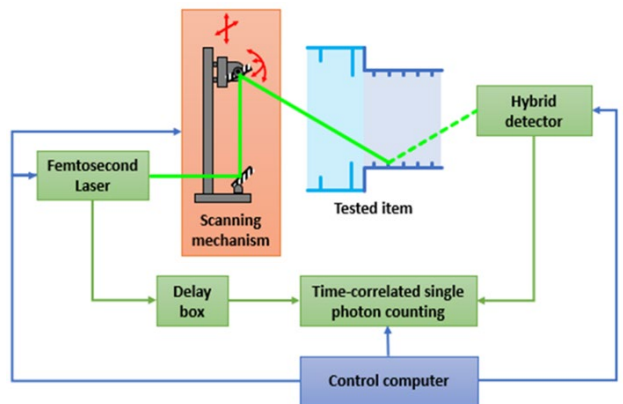


Figure 2: SLOTT breadboard overall architecture.

The main parameters expected of this design are collected and presented in Table 3.

Table 3. Main parameters of the SLOTT breadboard.

| | Parameters | Value |
|--|----------------------------|---|
| Laser parameters | Wavelength | 520 nm |
| | Laser average power | 3 W |
| | Repetition rate | 40 MHz |
| | Laser pulse energy | 75 nJ |
| | Illumination beam diameter | Adaptable: 2, 6.7, 10, 16.7 and 26.6 mm |
| Detection and timing system parameters | Expected time resolution | < 20 ps (~ correspond to 6 mm) |
| | Quantum efficiency | 10 % (@520 nm) |
| | Active area | Ø 3 mm (7.06 mm ²) |
| | Dark count | 50 cps |
| Scanning mechanism parameters | X-axis translation range | 1 500 mm |
| | Y-axis translation range | 1 250 mm |
| | Translation repeatability | 0.5 mm (X and Y) |
| | Ox-axis gimbal range | 0° to -65° |
| | Oy-axis gimbal range | -65° to +65° |

With the ongoing SLOTT activity, CSEM and its partners are developing a promising straylight measurement tool. The upcoming test results are expected to demonstrate the potential of such techniques, hopefully establishing new methods to characterize and reduce the straylight propagation in future space-based telescopes. Such results are expected towards the end of the SLOTT activity planned in January 2024.

AUDACITY – a Novel Actuator for Aeronautics Applications

F. Barrot, D. Grivon, M. Gumi, S. Droz, J. Rouvinet, E. Dominé

In the frame of the Audacity EU's H2020 funded project, CSEM has worked, together with its partners Cedrat Technologies (France) and Universita di Roma (Italy), on a new generation of piezoelectric actuator targeting the aerospace market. In the frame of this collaboration, CSEM has been in charge of the thermo-elastic analysis of the novel Audacity piezoelectric actuator, the design of the Ground Support Equipment needed for its characterization and the environmental testing of the resulting TRL4 prototype.

To reduce weight and consequently fuel consumption of aircrafts, the aviation industry is, among other challenges, targeting the replacement of hydraulic and pneumatic systems with electric ones. The EU-funded project Audacity is a contribution to this strategy as it aimed to design and demonstrate, for the first time in Europe, a powerful, compact and reliable piezoelectric actuator to be used for locking applications in landing gear systems.

Piezoelectric motors offer many advantages for applications in numerous industrial sectors: they are non-magnetic, radiation compatible, exhibit a high force/volume ratio, are characterized by a good unpowered stall force and a low power consumption.

The concept of long stroke piezoelectric actuators, which is required for the application targeted by the Audacity project, is not new but several technical challenges abound with the targeted working conditions: forecasting and validating its performance over a large temperature range [-55°C;+71°C] is the main challenge addressed by CSEM in the frame of Audacity.

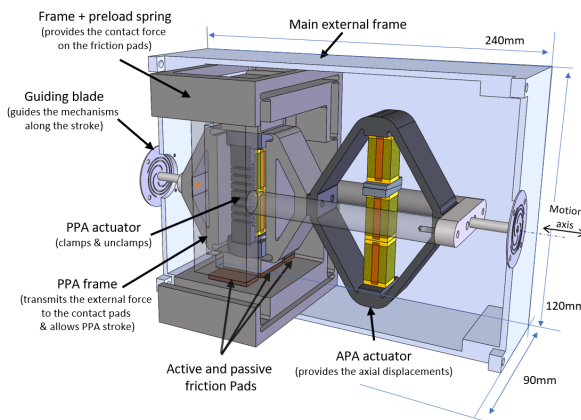


Figure 1: Audacity actuator and its main constitutive parts.

The actuator developed in the frame of Audacity [1] is an improved inchworm actuator capable to move and clamp/sustain a very high load (500 N) to guarantee a good uplock behavior in future landing gear systems. This actuator is made of two piezo elements: a piezo extender to move the mobile part, and a piezo clamp which transfers the blocking force between passive clamps and active clamps; A passive preload mechanism is implemented to guarantee the unpowered stall force at rest.

One of the challenges of this design is to make sure that the piezo actuator performances are stable over the whole temperature range; A careful design and selection of materials are required to guaranty manufacturability and the thermal stability of the critical mechanical plays involved in the operation of this friction-based

inchworm actuator. In particular, a careful thermal design as well as a high precision machining and assembly are essential to guarantee the accurate gap required between the active and passive clamping elements.

| Performances | Values |
|--------------|----------------|
| Stall force | 500N |
| Max weight | < 2kg |
| Stroke | 15mm |
| Speed | > 9mm/s |
| Life | 130 000 cycles |
| Temperature | -55 to +71°C |

Figure 3: Audacity actuator performances.

After a detailed thermo-elastic analysis, required to fine tune the design of the actuator and forecast its performances, CSEM has undertaken the design of the Ground Support Equipment (GSE) required to validate the behavior of the actuator under realistic working conditions. Based on the produced GSE, CSEM carried out dynamic (9 mm/s with a 350 N pushing force) and static tests (500 N load) over the whole temperature range [-55°C;+71°C].

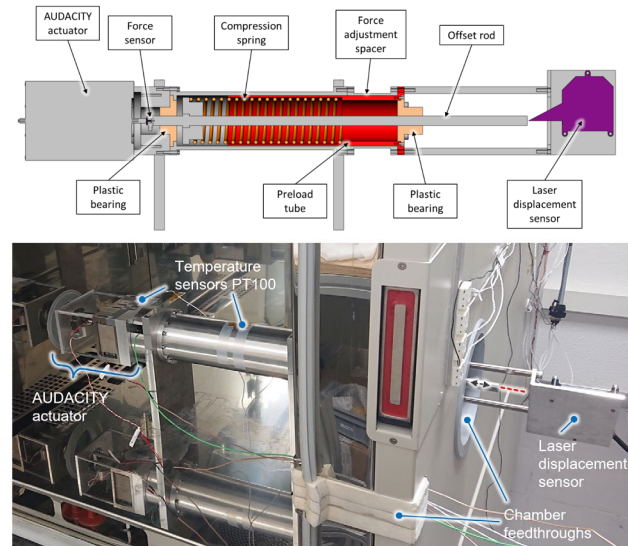


Figure 2: Audacity actuator integrated in its Ground Support Equipment.

After a thorough experimental campaign, the Audacity actuator proved good dynamic and static behaviors, successfully validating its performances in a representative thermal environment.

AUDACITY project has received funding from the European Union's Horizon 2020 research and innovation program through CleanSky2-CFP08-2018-01 under grant agreement No 831795.

[1] E. Betsch, et al., High power density Piezo motors for critical environments, *Actuator* 2022., p 71-75.

LUPINE – High-resolution Position Sensor for Space Applications

D. Grivon, P. Renevey, A. Ambühl, G. Borque Gallego, E. Onillon

In the space market, especially in science and Earth observation, a clear need for high-resolution and reduced cost position sensors has been established. Indeed, future missions will require very demanding pointing stability, accuracy, and control of micro-vibrations for instrument payloads. Existing commercial solutions are either dominated by optical encoders with price around 200 kCHF for the high-end market or covered by potentiometer that cost 15 kCHF for lower end applications. The LUPINE sensor aims to adapt Giant Magneto Resistive (GMR) sensor to fill the gap between the actual sensing position solutions, providing simultaneously competitive price while meeting the most stringent requirements.

Today, nanoTRONIC AG (nT) – CSEM partner in the LUPINE InnoSuisse project – ambition is to develop and commercialize a novel space qualified Giant Magneto Resistive (GMR) sensor, meeting the most stringent performance requirements with a target price of 30 kCHF. Benefiting from an exclusive license agreement with Sensitec to extend their sensor developed for terrestrial application to space applications, nT will be in a unique position on the market, offering a new generation sensor. nT and CSEM join forces to push the boundaries in GMR sensor resolution (by a factor 10 to compete with optical encoders), while maintaining its low production cost (range of potentiometers).

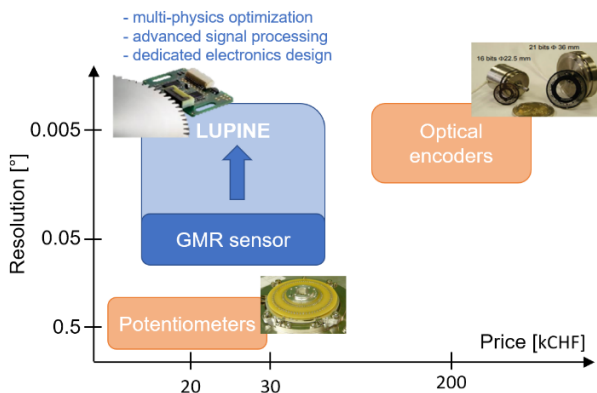


Figure 1: LUPINE's target (top left, courtesy of Codechamp, top right, courtesy of RUAG).

At the end of the project, the resulting sensor, including associated reading and processing electronics will reach TRL6.

Magneto-resistive effect is related to the variation of the resistivity of a material as a function of an external magnetic field. The resistance variation of the 8 GMR cells embedded in the sensors is measured using two Wheatstone bridges. The relative motion between the toothed target ferromagnetic structure and the sensor produces a variable magnetic field seen by the GMR elements. The latter, if correctly arranged, originate the raw output sinusoidal-like signals (Sin/Cos).

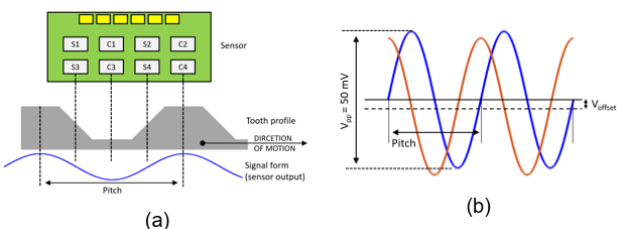


Figure 3: a) Sensor layout and tooth profile, with output signal. b) Typical output signal from the sensor with a supply $V_{CC} = 5V$.

A multi-disciplinary approach combining electromagnetic analysis and signal processing was put in place to achieve the challenging requirements. Firstly, a Finite Element model was developed and correlated with measurements. Also, first available data were processed with preliminary algorithms to assess the system baseline performances as well as to define

the sources of criticalities and possible improvements, both from the mechatronic point of view (optimal tooth profile shape, and optimal sensor position) and as well from the signal processing part.

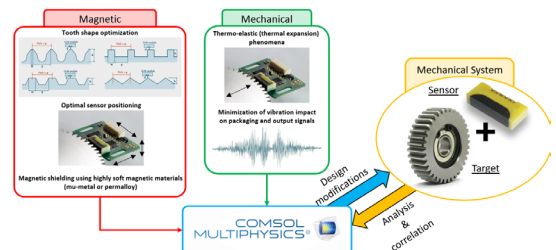


Figure 2: FE approach to analyze and improve the sensing system from the mechatronic side.

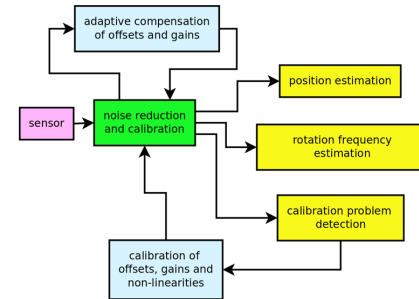


Figure 3: Block diagram define the approach intended to improve the sensor performances trough signal processing.

The first part of the project was successfully completed. The system showed to be particularly sensitive to manufacturing defects and to misalignments. An optimal tooth shape and optimal sensor placement was proposed with the aim of reducing the impact of eventual manufacturing and assembly defects and a second iteration of the target toothed structure is under manufacturing. A second model was developed to include all the sensors non-ideal behavior and harmonic distortions (seen on the measurements and on the FE model). It is used to simulate output data on which develop the signal processing algorithms to extract the target position. Based on these findings, an estimate of the achievable resolution was derived, which is $<0.001^\circ$, in line with the projects' stringent requirements. First versions of the algorithms were delivered to nT, towards their implementation on a spatial grade FPGA. In case the improved system still exhibits parasitic phenomena biasing the sensor outputs, additional signal processing features are foreseen. Tests on the final system in representative environment are planned at CSEM premises by the end of the year 2022.

This work was partially funded by Innosuisse, the Swiss Innovation Agency. CSEM thanks them for the support.

Configurable Slit Mask Unit for the MIR MOS instrument

P. Spanoudakis, M. Gumi, P. Schwab, Y-J. Regamey, P. Theurillat, G. Baderet, V. Schaffter

First phase: design, manufacture, and test in cryogenic conditions of a working prototype of the CSU actuation assembly.

MIR MOS (Magellan Infrared Multi-Object Spectrograph) is a multi-object and integral field near-infrared spectrograph. It is designed to be attached directly to the Nasmyth Rotator of one of the two identical single-mirror reflecting 6.5 m Magellan Telescopes (Figure 1) of the Las-Campanas Observatories (LCO).

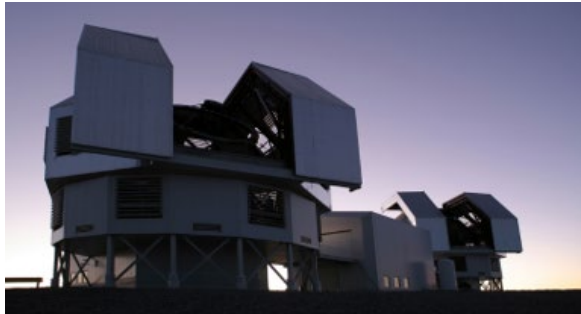


Figure 1: Las-Campanas Observatories.

The MIR MOS instrument will integrate a reconfigurable slit mask unit (CSU) which is a mechanism allowing to generate a multi-slit configuration, a long slit, and an imaging field of view (FOV) aperture at the focal plane of the telescope.

The MIR MOS CSU (Figure 2) is based on design heritage from the successful MOSFIRE CSU in operation on the Keck Observatory since 2012. The selection of a heritage design was based on the outcome of a feasibility study which reviewed various concepts compatible with the instrument specifications. The MOSFIRE CSU design was adapted for use on the Magellan Telescope and doubling the number of slits generated within the FOV.

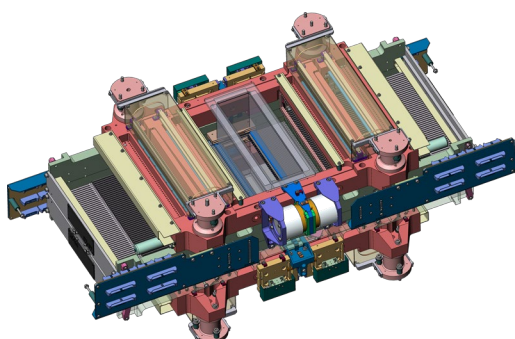


Figure 2: The MIR MOS CSU.

The baseline design is shown above, and it essentially consists of two indexing stages (top and bottom) which allow the masking bars to be staggered and thus doubling the linear slit density within the field of view. The main features are:

- MOSFIRE CSU full heritage design (doubled)
- Actuation provided by indexing stage with a short stroke actuator and an LVDT per stage
- All bars actuated by indexing stages
- Stroke of each bar ± 35 mm
- Actuators double sided

The core of the design is the ratchet and brake clutch bar actuation system working on an inchworm principle to displace the bars which is identical to the MOSFIRE CSU. A slit is formed by moving opposing masking bar pairs across the field to any location along the 70 mm FOV, with a precision of $\sim 5 \mu\text{m}$. The major difference for the MIR MOS design is that a dedicated guide bar is used for the indexing function and the masking bar is attached to the guide bar.

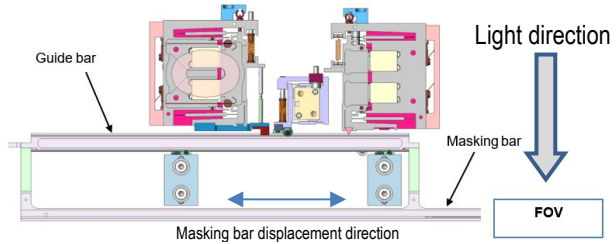


Figure 3: Illustration of the core actuation sub-system to displace bars across the field of view of the instrument.

Development prototype

To test the various functions and operations of the CSU mechanism, a three-bar side-by-side prototype mechanism (Figure 4) will be built that can index bars across a similar field of view. It will not be able to generate slits but nonetheless all bar motion and position performances can be evaluated. The prototype will be fully representative of all critical components (ratchet and brake clutches, guide rollers, limit switches, actuators, sensors, etc.) as well as interfacing with the control system and electronics. This development model will validate the new guiding bar/masking bar combination.

A test campaign at room and cryogenic (-150°C) temperature will enable the rapid evaluation of all critical parameters pertinent to the CSU operation to be manufactured in the subsequent Phase 2 of the project.

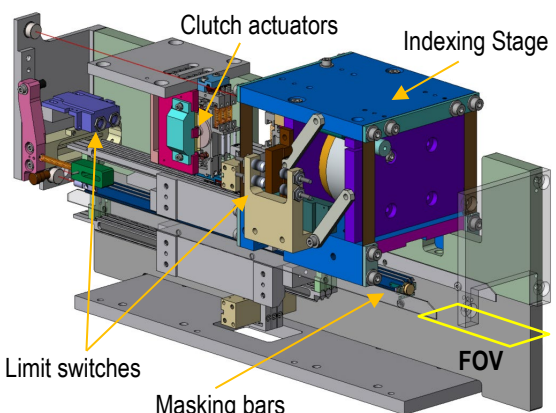


Figure 4: Three-bar prototype indicating some of the critical functions.

MIR MOS instrument will be built at Carnegie Observatories with support from the Instrument Development Group (IDG) at John Hopkins University. This work is funded by CIS (Carnegie Institute for Science). CSEM thanks them for their support.

Fast Steering Mirror for Line-of-Sight Stabilization

J. Rouvinet, P. Spanoudakis, P. Schwab, Y.-J. Regamey, E. Haenni, I. Kjelberg

The fast-steering mirror (FSM) developed at CSEM is a compact design mechanism whose purpose is to control the position and stability of a plane mirror. Compact FSMs have a wide range of applications including satellite communication systems, Earth observation missions and scientific space missions.

The fast-steering mirror mechanism is based on a compact design with the goal of controlling the position and stability of a planar mirror. The mechanism was designed with the objective to ease the manufacturing process, accommodation, actuation, and to reduce the overall costs while achieving exceptional stability over the ± 2.4 mrad tip/tilt optical range. The simplest mirror shape is circular, but an elliptical shape can be considered. The actuation of the mirror is done with the use of three voice coils arranged at 120° . CSEM designed and developed, under its own founding, a fast-steering mirror (FSM) mechanism represented in Figure 1.

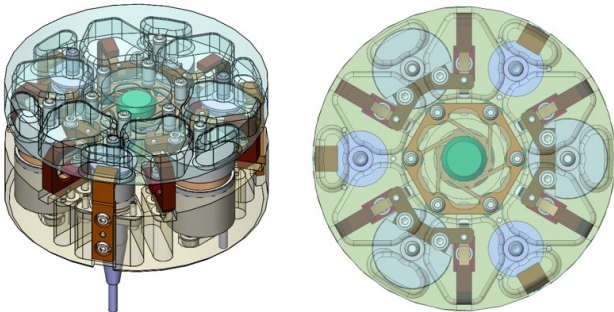


Figure 1: FSM concept baseline, isometric view (left), upper view (right).

A central mirror-flexure membrane supporting the mirror is implemented ensuring the tip/tilt and piston movements starting from a neutral position.

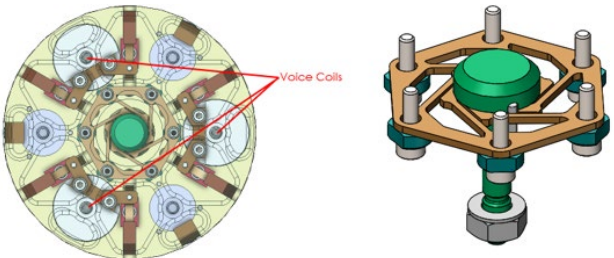


Figure 2: Three voice coil actuators positioned at 120° (left); Flexure membrane with its fixation and central tie rod (right).

Highest sensitivity and resolution capacitive sensors with bandwidths up to 10-20 kHz measure the mirror position which is then controlled in closed loop.

A low noise current amplifier was custom developed to ensure the highest possible accuracy of the voice coil drive current with a measured noise level below $0.2 \mu\text{A}$.

A breadboard mechanism was produced and assembled at CSEM, replacing the SiC or Zerodur mirror by a representative Aluminum dummy, shown in Figure 3.



Figure 3: Picture of the FSM breadboard.

The mechanism properties and performance measurements on the breadboard mechanisms are summarized in the table below:

| Characteristics | FSM performance |
|--|--|
| Controlled DOF | 2 (tip and tilt) |
| Optical angular range (Funct/Max) | ± 2.4 mrad / ± 5.8 mrad |
| Actuator type | Voice coil |
| Number of actuators | 3 |
| Sensor type | Capacitive |
| Mirror diameter | 60 mm |
| Typ. Resolution in closed loop | 0.34 μrad |
| Typ. Stability | 0.3 (analog)- 0.16 (digital) – 0.02 (up to 100Hz) μrad |
| Typ. Repeatability | 1 μrad |
| Typ. Non-linearity | 1.7 μrad (uncompensated) – 0.12 μrad (compensated) |
| Dimensions | $\varnothing 60$ mm x 45 mm |
| Weight | <200g with Zerodur mirror |
| Stiffness in Z | 0.508 N/ μm |
| Resonant frequency | 130 Hz |
| Operation Voltage/control signal | ± 10 V |
| Operating current | ± 2.5 A |
| Command param. Resolution | Analog |
| Sensor acquisition frequency | 7800 Hz |

Compared to other mechanisms on the market, CSEM's FSM is distinguished by its relatively large mirror size, large angular stroke, and high relative accuracy. In addition, its versatile design allows it to be easily adapted for a wide range of applications such as satellite communication or Earth observation.

Future developments of the mechanism will consist of small adaptations of the design for space missions that will be proposed by ESA or space primes in the near future.

Applications of Coherent FMCW Lidar on Surface Metrology

S. Chin, S. Lecomte, C. Pache

The COLIDE project aims at the development of a coherent FMCW LiDAR at $2\text{ }\mu\text{m}$ using an on-chip vernier external cavity laser implemented on photonic integrated circuits with a hybrid GaSb-Si platform. This laser provides a unique wide wavelength tuning range greater than 120 nm and mode-hop-free frequency sweep range of 5 nm (or 375 GHz). It has a large potential for low SWaP-C surface metrology, i.e., additive manufacturing process monitoring.

In the framework of the Eurostars COLIDE project, CSEM collaborated with the company Brolis Sensor Technology, Lithuania, to develop a frequency-modulated continuous-wave (FMCW) LiDAR sensing system at $2\text{ }\mu\text{m}$ for high-resolution surface metrology and gas sensing applications.

Light detection and ranging (LiDAR) remote sensing systems became one of the most fascinating topics in optics and photonics since LiDAR has high capability to perform high resolution 3-dimensional (3D) depth imaging. Recently, LiDAR sensors have been implemented for various applications, even extended to autonomous vehicles, unmanned aerial vehicles and surface metrology. In fact, those applications require essentially strict restrictions on industrial operation conditions, referenced to optimizing the size, weight, power and cost (SWaP-C). To satisfy mentioned characteristics, the FMCW LiDAR is considered as a promising technique as it takes inherent advantage of noise immunity to the solar radiation and cross-talk with other LiDARs; hence, improving the signal-to-noise ratio.

The COLIDE team developed an eye safe FMCW LiDAR at $2\text{ }\mu\text{m}$ with high resolution and performance. Moreover, this wavelength provides inherently higher sensitivity for gas sensing applications, compared to LiDARs at visible and/or near-infrared wavelength. Thanks to the recent advancement in silicon-based photonic integrated circuits technology, the hybrid integration between silicon waveguides and GaSb gain chip was efficiently demonstrated. The amplified spontaneous emission from the gain chip is coupled to a Vernier-type external cavity, consisting of two silicon microring resonators (MRR) with slightly different round trip lengths. The wavelength tuning is realized by the individual thermal control on the MRRs and the injection current applied to the gain chip. The wavelength of the laser output can be broadly tuned with mode hopping over $>120\text{ nm}$ by the thermal control of one of the MRRs. On the contrary, the laser wavelength can be continuously tuned without mode hopping by simultaneously controlling both MRRs (Figure 1). Due to the slow response of the thermal control, the maximal achievable wavelength tuning range was measured to be $\sim 5\text{ nm}$ ($=375\text{ GHz}$) at 1 Hz sweeping speed and $\sim 2\text{ nm}$ ($=150\text{ GHz}$) at 1 kHz .

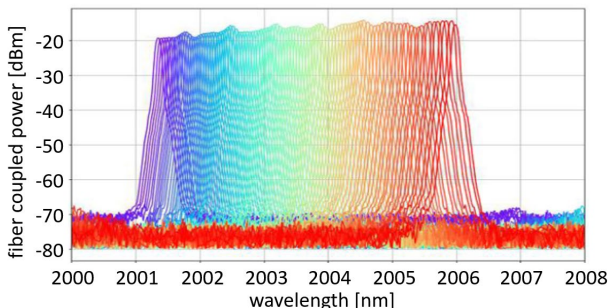


Figure 1: Laser spectrum measured by optical spectrum analyzer while continuously tuning the wavelength over $\sim 5\text{ nm}$ at $2\text{ }\mu\text{m}$.

In parallel to the development of a FMCW LiDAR at 2-micron wavelength, a benchmark FMCW LiDAR operating at $1.5\text{ }\mu\text{m}$ was developed, using a commercial semiconductor laser with DC

tuning rate of -22 pm/mA , equivalent to -2.75 GHz/mA . The injection current to the laser was directly modulated at 1 kHz , resulting in a frequency sweep range of 260 GHz , corresponding to an axial resolution of $600\text{ }\mu\text{m}$.

To validate the performance of the benchmark LiDAR, the light emitted from the sensor was focused with $30\text{ }\mu\text{m}$ beam waist at the surface of the rugotest sample (see Figure 2a) and was scanned by $250\text{ }\mu\text{m}$ step over the whole surface of the sample, using a motorized 2D translation stage. Figure 2b depicts the measured 3D depth image of the sample without averaging; hence 1 ms measurement time for each pixel, showing a perfect agreement. The height of the letters was measured to be $263\text{ }\mu\text{m}$.

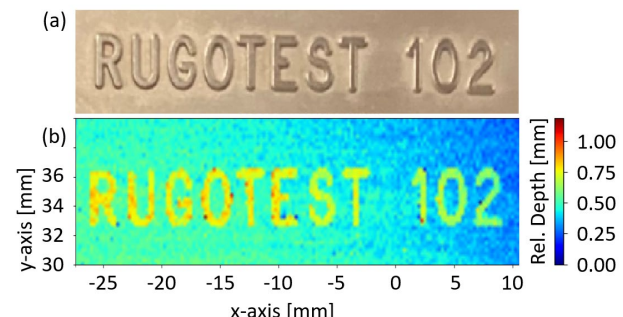


Figure 2: a) Picture of sample for surface metrology. b) 3D depth image of the sample, measured at 1 kHz by the benchmark FMCW LiDAR.

To further evaluate the LiDAR performance, a fixed position on the sample surface was continuously measured. According to the statistical analysis out of 200 consecutive measurements, the precision of distance ranging at 1 kHz was measured to be $50\text{ }\mu\text{m}$, as shown in Figure 3. However, we believe that the achieved sensing precision will be better than this value since the sensor head and the sample were exposed to the environmental vibration of the laboratory. The flat response at the averaging time of 10 ms in Allan deviation can be attributed to the external perturbation. Using 8-step stairs sample, the accuracy was also measured to be $9\text{ }\mu\text{m}$, demonstrating the high performance.

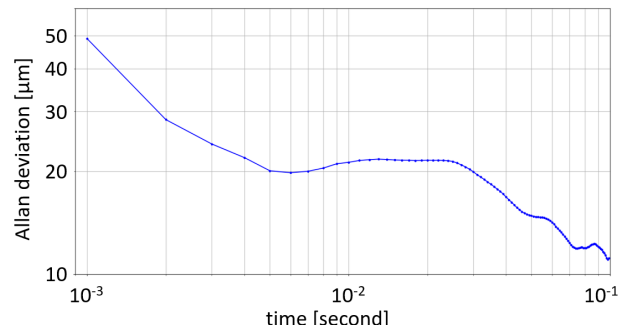


Figure 3: Allan deviation of the distance measurement precision of the benchmark LiDAR at $1.5\text{ }\mu\text{m}$ as a function of averaging time.

This project has received funding from Eurostars and State Secretariat for Education, Research and Innovation (SEFRI).

SUSTAINABLE ENERGY

Christophe Ballif

Over the past decade, photovoltaics (PV) and energy management technologies have drastically increased their global prevalence. Digitization has further boosted these technologies, and their popularity is expected to grow in coming years as the need to decarbonize our energy system keeps growing.

Several developments in the renewable energy field stem directly from research being carried out in Europe, including the industrialization of solar cells and modules by several companies based in Switzerland. Preparing the next-generation solar technologies, CSEM and EPFL's (Swiss Federal Institute of Technology in Lausanne) PV-lab reached a power conversion efficiency of 31.25% on a perovskite-on-silicon-tandem device, breaking for the first time the 30% efficiency barrier with low-cost materials. A pioneer in developing and commercializing colorized solar modules, CSEM is transforming PV panels into building materials. Moreover, our lightweight PV solutions are now being used in multiple stratospheric missions (including weather balloons for the National Centre for Space Studies in France and the SolarStratos airplane). Other applications benefitting from CSEM's PV expertise include airplane containers, specialty blinds for buildings, lightweight façade elements, and high-quality energy-harvesting solutions.

Our expertise further extends into the fields of energy management and storage. The wind energy sector has already used our data-driven maintenance solutions, and we are reducing people's cost of living through our NRGMaestro™ platform. CSEM is also driving forward the energy storage industry with its advanced battery management systems with breakthrough hot-swappable technology, as well as with advanced battery cell concepts using specialty layers and polymers.

PV & Solar Buildings

CSEM PV & Solar Buildings aims to support the TW-scale deployment of PV energy, primarily in Switzerland and Europe, by developing incremental and disruptive technologies to outclass the current mainstream PV products in terms of conversion efficiency, production costs, reliability, aesthetics, and sustainability.

CSEM develops innovative PV solutions featuring higher-power conversion performance, longer lifecycles, lower costs and environmental footprint – in customized sizes, shapes and colors tailored to mainstream PV electricity generation or for integration into buildings (BIPV) and agriculture (AgriPV). Our technologies focus on four activities covering the entire PV value chain, from individual solar cells to bespoke, fully integrated PV modules. (1) In solar cells, we are researching incremental and disruptive upgrades to extend the power conversion efficiency curve of PERC (Passivated Emitter and Rear Cell) technology, e.g., perovskite-on-silicon tandems, (back-contacted) silicon heterojunction, and passivated contacts on tunnel oxide. (2) Our contacting technologies & encapsulation materials operations are uncovering new metallization materials, such as electroplated copper. Besides, we are advancing contacting concepts for individual solar cells, which we scale up into workable PV modules. (3) CSEM uses its polymer platform to

compound and extrude tailored encapsulants to achieve maximum module durability. (4) Lastly, our BIPV (Building Integrated Photovoltaics) solutions activities offer advanced colored foils in an extended color palette to achieve aesthetically pleasing roof and façade integrated elements, fulfilling customers' architectural, technical, and legal requirements.

Energy Harvesting

CSEM Energy Harvesting is dedicated to harvesting light-energy. It is divided into three major topics: (1) Thin-film PV cells for wearables in watches, consumer electronics, logistics, and autonomous internet of things devices, like sensor nodes for mobile or static applications. (2) Lightweight PV modules and advanced materials for packaging in sectors like transport, telecommunication, and active skins. (3) Cross-functional encapsulation materials, with a focus on robust, lightweight modules.

Solar energy harvesting for mobile applications is garnering attention from various industries. As light is widely available, its conversion to electricity can extend battery lifetime, potentially avoiding any external connection of the mobile device and, in optimal cases, enabling the complete removal of the battery from the system. CSEM has developed a first-generation batch of small-scale thin-film silicon solar cells that can be integrated into watch dials or wristbands.

The transport industry is globally responsible for 22% of human-induced CO₂ emissions. With the transition to electric vehicles and the availability of cost-effective, high-performance solar cells, all mobility applications will benefit from integrating PV. Trucks, boats, containers, high-altitude drones or airplanes can profit from the aesthetics produced by curved, integrated, reliable and lightweight solar modules developed at CSEM. Even 24/7 operational drones could become a tangible possibility thanks to the PV and battery improvements. Lightweight solar modules can also be used like active skin on constructions with limited surface load, movable parts, or curved shapes.

Lastly, all new PV wearable and lightweight applications need advanced materials combination and encapsulation schemes, to provide high reliability and extended lifetime in extreme conditions, which we develop in-house at CSEM.

Digital Energy

Energy digitalization describes the transformation of energy conversion and distribution connectivity, data, analytics, and artificial intelligence. Digitization is expected to increase the energy system's resilience and efficiency, and it is intrinsically linked to its planned decarbonization. Digital transformation is vital to manage the increased complexity introduced by distributed energy resources (DERs), e.g., PV and wind turbines. DERs are heterogeneous, have orders of magnitude smaller than conventional generators, and are weather dependent. The challenges associated with this complexity relate to the scalability of solutions, the handling of consumer-grade data to perform industry-grade automation, and the operation under uncertainty and partial observability. Since the energy system is

a critical infrastructure, digitization need reach much higher security and reliability levels than in other sectors.

At CSEM, we focus on making available the power of the internet of things and the full spectrum of artificial intelligence methods to companies that promote a low-carbon energy system. These companies range from small component manufacturers starting their digital transformation to major utilities looking to introduce new services. Graph machine learning, initially created in the context of social networks and recommendation systems, is a promising approach to exploiting the spatiotemporal correlations among DERs for data processing and forecasting. Learning-based control is also a way to automatize and optimize the operations of energy conversion and distribution assets at scale. It can improve energy efficiency by 20% and unlock new capabilities, like demand-side flexibility. Secure delivery builds on software techniques and system architecture to make digital solutions trustworthy by ensuring privacy, reliability, and cybersecurity.

Energy Storage

CSEM Energy Storage is motivated by the need for adequate storage solutions linked to the massive introduction of renewable energy sources scheduled within the Swiss Energy Strategy 2050. Our current research focuses on electrochemical storage solutions, which have recently gained scientific and economic interest due to the rapid uptake of e-mobility applications. As battery is the single most expensive component, we develop hardware and software solutions that can improve battery performance, extend lifetime, and enable second-life applications. We are also exploring how future technologies with increased gravimetric and volumetric energy densities together with enhanced sustainability and safety can benefit the domain.

CSEM focuses on three research activities covering the entire battery value chain. (1) We develop processes and interfaces dedicated to the manufacturing aspects of next-generation battery technologies. We currently work on applying thin-film coatings and suitable electrolytes for upcoming 4th generation (e.g., solid state and Lithium ion-metal) batteries. (2) We are advancing battery models for current and future-generation battery technologies. We use electrochemical impedance spectroscopy (EIS) for improved in-situ and in-operando diagnostics of electrochemical phenomena and their evolution. (3) Our work in smart management systems exploits battery models and their associated algorithms. At CSEM, we focus on exploiting sensors and actuators to optimize battery-cell usage over their lifetime.

Toward Sustainable PV: Activities at the Sustainable Energy Center

A. Barrou, L.-L. Senaud, A. Lachowicz, C. Ballif, B. Paviet-Salomon

Photovoltaic (PV) systems are the lowest cost technology to produce electricity with a limited impact on the environment compared to fossil fuel technologies. However, the production of PV systems uses resources (water, fossil fuels and minerals) which are limited, including critical raw materials (CRM) such as indium and silver. Using life cycle assessment (LCA) methodology to assess the environmental footprint of products, CSEM supports the development of sustainable PV products by providing recommendations for PV manufacturers based on key parameters and scenarios evaluations.

Photovoltaic (PV), which produces electricity thanks to the energy of the Sun, is poised to be the key pillar of the future low carbon energy mix^[1], with crystalline silicon (c-Si)-based technologies called to take the lion's share of it^[2]. In Europe alone, over 8 terawatts (TW) of installed PV capacity is required by 2050 to fulfil the net-zero carbon emission objectives^[3]. Today, widely acknowledged technological roadmaps for PV^[4] mostly focus on the race to higher efficiency and lower cost. However, to reach a sustainable TW-scale deployment, environmental aspects as well as resources scarcity should be considered which lead CSEM to develop its own analysis tools.

For instance, CSEM performed an analysis with the major past (Al-BSF) and current (PERC) technologies, comparing them to one higher efficiency technology (HJT), using up-to-date and accurate data for LCA computations. For this study, two functional units (FU) are used: (i) a kilowatt-peak (kWp) FU, representative for PV manufacturers as it focuses on main production steps of PV; (ii) a kilowatt-hour (kWh) FU, representative for LCA experts as it represents the impact of the PV system over its entire life, but which depends strongly on the place (irradiance) and type of PV installation.

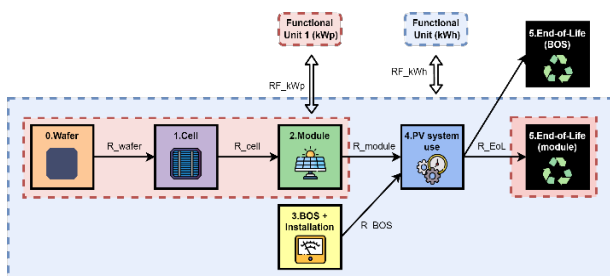


Figure 1: Simplified PV model process tree.

Figure 2 shows that the carbon footprint of the Al-BSF technology was strongly reduced between 2010 and 2020. Remarkably, HJT has the lowest impact (35 gCO₂-eq/kWh) among the three PV technologies under study (due to higher module efficiency).

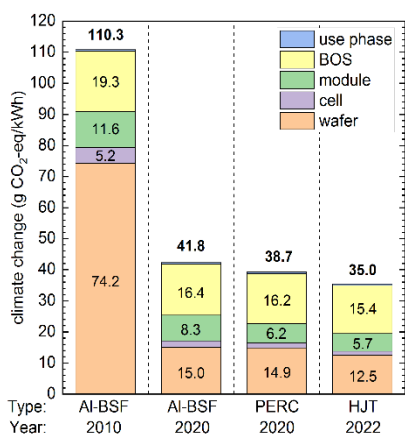


Figure 2: Carbon footprint per kWh of the c-Si technologies (Al-BSF, PERC, HJT)

In addition to carbon footprint, other impact categories sensitive for PV are analyzed (see Figure 3-left). Figure 3 right shows the relative environmental impact of each building blocks of HJT. Importantly, the use phase has a negligible impact, while BOS+Installation represents more than 30% of PV impact for all categories (up to 81% for RUM).

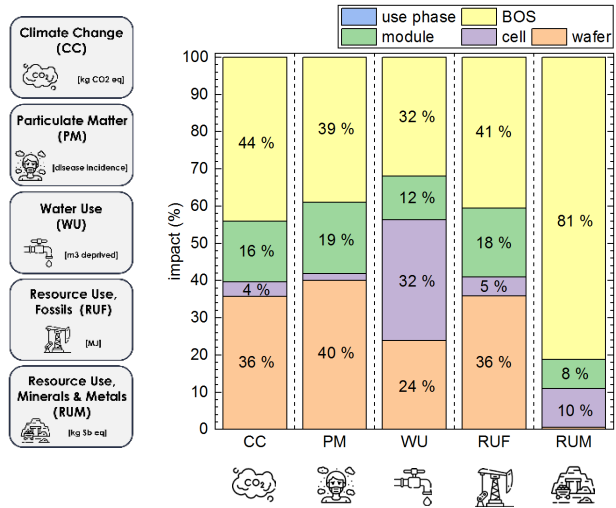


Figure 3: (left) Impact categories sensitive for PV system; (right) HJT standard 2022 impact.

Based on this study, CSEM proposed a roadmap to further reduce the carbon footprint of HJT by 34% (in the case of the kWp FU), namely: (i) Using European-made wafers (instead of Asian-made wafers); (ii) Removing two major CRM for HJT solar cell manufacturing by using indium-free Transparent Conductive Oxides (TCO) and silver-free metallization (in this study, copper plating). To achieve an even stronger footprint reduction, module processes must be upgraded by reducing the quantity of solar glass and removing the aluminum frame, to name a few.

In addition, carrying a sensitivity analysis of our results shows that a reduction of 9% of the HJT PV systems carbon footprint can be achieved either by: (i) reducing wafer thickness from 170 to 130 µm; (ii) increasing module efficiency from 21.75 to 24.5%; (iii) increasing PV systems' lifetime from 30 to 33 years.

Overall, LCA proved to be a valuable tool to assess the environmental benefits/impacts of a scenario compared to standard technology and gives insight on the impact of each building blocks of the PV system. Key recommendations for PV manufacturers were set to limit the environmental footprint of their product, and CSEM is orienting its clients in this direction. Furthermore, the implementation of LCA within the CSEM database and the use of costs considerations will help to achieve the sustainable development of PV to the TW-scale.

[1] Solar Power Europe & LUT, "100% Renewable Europe" (2020).

[2] Fraunhofer ISE & PSE GmbH, "Photovoltaics Report" (2021).

[3] LUT & Energy Watch Group, "Cost-efficient 1.5 K scenario" (2021).

[4] VDMA, "International Technology Roadmap for Photovoltaic" (2021).

Recent Developments of the Plastics Compounding Platform

H.-Y. Li, M. Roten, J. Escarré, T. Auderset, M. Despeisse

To cope with the demands of ongoing and future incoming projects, the compounding platform at CSEM has been expanded in the past years on its capacity for the development of customized polymeric materials used in PV modules. A number of material formulations developed on the platform have been transferred to industrial partners and are currently on the market or under the commercialization process. The materials from the platform also allow an easier root cause analysis of the degradation of the PV modules, in particular with novel cell/interconnection or module stack designs. The growing expertise at the compounding platform makes CSEM a unique R&D partner in the field of PV module technology.

A standard PV module mainly consists of a front cover, stringed cells and a back cover, bonded with two layers of polymeric adhesive film, commonly referred to as the encapsulant. Regarding the back cover, in 2021, over 60% of the modules are equipped with a multi-layered polymeric backsheets. In very recent years, the module industry has spread its R&D activities from the longstanding needs of trimming down the levelized cost of PV electricity by cost reduction and lifetime prolongation to improving the adaptability of PV modules into diverse application scenarios, e.g., BIPV (building integrated PV), VIPV (vehicle integrated PV), PIPV (product integrated PV), etc. To cater this evolving demand, the plastics compounding platform at CSEM focuses on the development of polymeric materials for PV modules, including encapsulants, backsheets, frontsheets and other functional polymeric layers.



Figure 1: CSEM compounding platform. A) lab compounding line; b) lab cast film line; c) pilot compounding line; d) pilot cast film line.

Recently, thanks to the success of a few technology transfers, CSEM has expanded the infrastructure available in the plastics compounding platform. Currently, the platform includes, in particular, the following equipments (see Figure 1):

- Dr.COLLIN TEACH-LINE twin-screw compounder ZK 25 x 24 L/D equipped with a single strand pelletizer (max. throughput: 4.0 kg/h).
- Dr.COLLIN Single-Screw cast film extrusion line 25 mm Φ x 25 D Type E 25E, capable of producing foils with width up to 18 cm wide (max. throughput: 10.0 kg/h).
- Nanjing KY pilot twin-screw compounding line equipped with underwater pelletizer (max. throughput: 20.0 kg/h).
- GWELL pilot cast film extrusion line equipped with two extruders (50/35, 45/35), capable of producing foils up to 3 layers with usable width up to 50 cm (max. throughput: 40.0 kg/h).
- Material analysis facility (e.g., DMDR, DSC, FTIR, Raman, UV-Vis-Nir). This is completed by multiple other tools (SEM, TEM, ...) within CSEM or available at partners.

- Accelerating lifetime testing facilities: climate chambers for damp heat, thermal cycling, humidity freeze, UV+ damp heat; UV chamber; Ovens; highly accelerated damp heat testing setup (high-pressure cooker test).

In addition, the platform has also built the infrastructure to develop wet coating formulations in the lab scale and has external partners for upscaling trials.

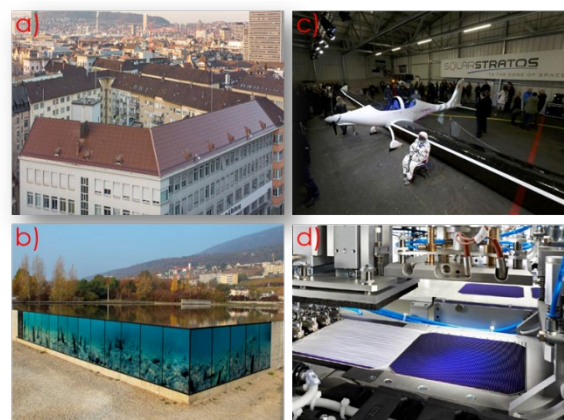


Figure 2: Examples of results from CSEM compounding platform.

The polymer compounding lab and expertise within the CSEM PV modules group is a unique asset which enables fast progress of R&D correlated to materials impact on performance, reliability, and/or aesthetics of PV modules, with for instance the following technologies demonstrated:

- A colouring interlayer (Figure 2a) has been developed to convert standard PV modules into coloured modules. CSEM is currently supporting Solaxess SA for its commercialization. Installations of modules with this technology have been realized. A specialty film (Figure 2b) has been developed to disguise the cells/interconnections in high-resolution image-enabled PV modules. The company Compàz has developed a few projects with this technology in Switzerland, Norway, and Italy.
- An adhesive film (Figure 2c) has been developed and qualified for the PV-integrated vehicles in stratosphere, like airplanes, balloons, drones, withstanding wider range thermal cycling.
- A carrier film for an interconnection technology (Figure 2d) has been developed. An encapsulant formulation for power-focused PV modules has been developed and transferred to an industrial partner. CSEM is currently supporting its commercialization.

The SIRIUS Project – Swiss Pilot Line for Aesthetic and Ultimate Power PV Modules

J. Zhao, J. Champliaud, N. Badel, L. Baume, L. Perla, A. Barrou, B. Paviet-Salomon, A. Faes, M. Despeisse, C. Ballif; L. Barraud*, B. Legradic*, R. Kramer*, T. Kössler*, L. Andreetta*, N. Holm*, W. Frammelsberger*, D. Baetzner*, D. Lachenal*

In the frame of the SIRIUS project (supported by the Swiss Federal Office of Energy), CSEM is supporting the transfer of its patented "tunnel-IBC" technology to semi-automated pilot production lines for back-contacted silicon heterojunction solar cells (at Meyer Burger Research in Hauterive) and the corresponding PV modules (at Meyer Burger Technology in Thun). This includes the development of suitable materials and encapsulation schemes for IBC modules, their reliability testing and failure-mode analysis, as well as the development of the next generation of highly bifacial tunnel-IBC devices.

Back-contacted amorphous/crystalline silicon heterojunction (HJT) solar cells demonstrated the highest power conversion efficiency (PCE) among single-junction, crystalline silicon-based solar cells, which, added to their superior aesthetic – owing to the absence of metal grid at the front – make them the perfect product for high power residential and mobile PV markets. With the support of several Swiss-funded projects in the last ten years, CSEM and Meyer Burger developed and patented a lean, mass production compatible process flow for such devices, the so-called "tunnel-IBC" technology, with independently certified PCE up to 25.4% on 200 cm² active area.

Within the SIRIUS project (2021-2024E), CSEM is supporting the industrialization of the tunnel-IBC technology. First, CSEM is developing the materials for monofacial tunnel-IBC modules with SmartWire interconnection to achieve long-term reliability. After hundreds of test modules manufacturing and developments, high reliability could be demonstrated achieving almost no degradation of modules after 1'500 thermal cycles instead of 200 cycles as required by the IEC norm, and after 8'000 hours damp heat instead of 1'000 hours as required by the IEC norm. These results demonstrated the ultimate reliability which can be achieved with selected materials and designs, achieving highest reliability observed in CSEM reliability testing unit.

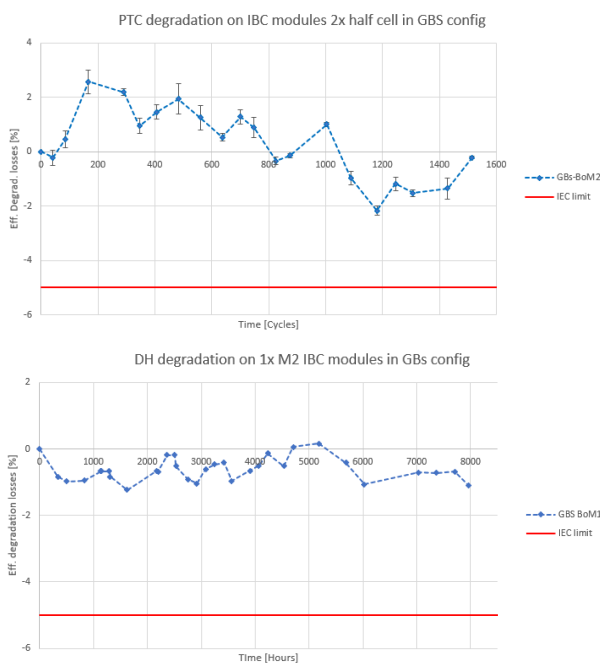


Figure 1: Results of accelerated aging on MB-CSEM IBC modules, (top): Thermal cycling results with <2% performance degradation after 7.5 times IEC norm testing, down: Damp heat results with <2% performance degradation after 8 times IEC norm testing.

Second, CSEM is working toward the technology demonstration of highly bifacial tunnel-IBC devices and their interconnection

scheme. A full 3D model of bifacial tunnel-IBC devices using the finite-difference time-domain method was established (see Figure 2) and was used to assess the opto-electrical losses that would occur in such devices. It resulted from our simulation that owing to the efficient lateral transport of charge carriers in the c-Si bulk, fill factors up to 85% are still achievable with bifacial tunnel-IBC devices in despite their lower metal coverage. Yet, transport losses rapidly scale up with increasing TCO sheet resistance, therefore a trade-off between the optical and the electrical properties of the TCO is required. In addition, the simulation tells that the major loss mechanism is the current crowding occurring at the TCO/metal interface, owing to the strongly reduced contact surface of this latter in the bifacial case. Specific contact resistances below 1 mΩ.cm² are required to keep the transport losses at an acceptable level. CSEM is currently testing various TCOs and metal pastes to solve this issue.

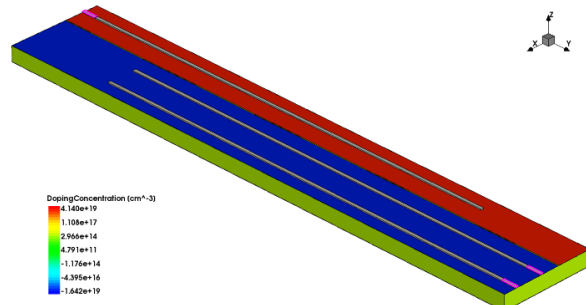


Figure 2: 3D simulation domain of a bifacial tunnel-IBC device.

Bifacial tunnel-IBC solar cells were then manufactured. Three devices with either single or double silver printing were integrated into one-cell mini-modules. The resulting bifaciality factors for each module IV parameter are given in Table 1. Importantly, for both groups, bifaciality over 80% has been measured for short-circuit current density (J_{sc}) and power conversion efficiency (PCE), which is a key factor to obtain additional output power from the rear side.

Table 1: Bifaciality factors of bifacial tunnel-IBC mini-modules.

| | J_{sc} | V_{oc} | FF | PCE |
|---------------------|----------|----------|------|-----|
| Single print | 82% | 99% | 102% | 83% |
| Double print | 80% | 99% | 102% | 81% |

As next steps, to improve the performance of bifacial tunnel-IBC devices, the contact resistance at the TCO/metal paste interface will be lowered by carefully engineering the former and testing novel materials for the latter. In addition, novel screen-printable resists with higher transparency will also be tested for higher J_{sc} bifaciality.

* Meyer Burger

Dynamic Photovoltaic Modules for Dual-land Usage

J. Levrat, D. Petri, D. Chudy, M. Despeisse, C. Ballif, G. Nardin*, M. Duchemin*, M. Ackermann*, L. Coulot*, B. Christ **, M. Baumann **

The local Swiss startup Insolight SA teamed up with CSEM and Agroscope to develop efficient and reliable dynamic solar panels for agrivoltaic market. The goal is to get the best compromise between agricultural and energy yields on the same land. In the frame of the InnoSuisse ATLAS project, Insolight and CSEM have optimized a novel type of solar panel, embedding a patented microtracking technology. Due to the built-in motorization and tracking algorithm, the system can either optimize solar production by focusing the direct light onto the solar cell segments or the crops production by focusing the light in between the cells. A pilot installation is currently operational in Conthey where the third project partner, Agroscope, is monitoring the crops growth by measuring the energy yield and also the fruit quality, the sap flow, the carbon assimilation, the chlorophyl content, fruit weight, the sugar content and the leaf size to demonstrate the benefits of the technology.

Agrivoltaics opens the perspective of new land for utility-scale photovoltaic installations, while at the same time fulfilling the protection needs of various crops. However, conventional photovoltaic panels have a limited use for agrivoltaics, as the shade generated by opaque modules can significantly degrade the agricultural yields. Spaced modules can increase the average irradiance, but at the cost of a lower Ground Covering Ratio and inhomogeneous irradiance patterns. In addition, PV installation with a fixed shading ratio is not ideal to adapt to seasonal changes and exceptional climatic events.

To circumvent these limitations, Insolight has developed with the support of CSEM translucent photovoltaic modules which circumvent the limitations of standard PV by enabling a tunable transmission of sunlight to the crops (Figure 1). The tunability is possible on a continuous range between the Electricity mode (E-mode – 15% transmission) and the Maximum Light Transmission mode (MLT-mode – 75% transmission).

The goal of the InnoSuisse ATLAS project, involving the technological startup Insolight, the agronomic center Agroscope and CSEM, is to optimize Insolight's agrivoltaic solution (Insolagrin), that includes the special solar dynamic modules embedding a microtracking system but also a static structure for protection of the crops, combined with sensors and a piloting algorithm to optimize crops growth throughout seasons. A set of micro-climatic sensors (temperature, Photosynthetically active Photon Flux Density (PPFD) provides feedback to the piloting to deliver the right Daily Light Integral (DLI) to the crops.

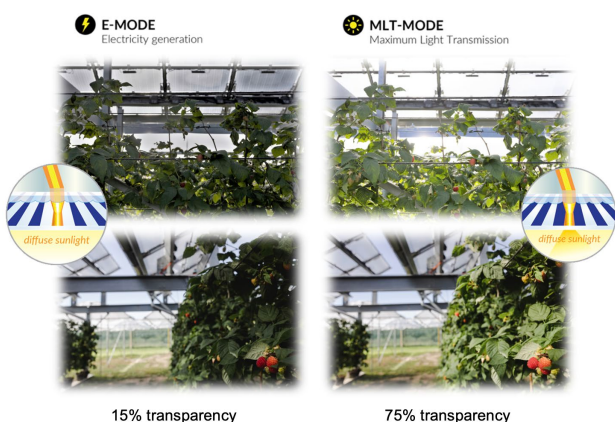


Figure 1: Example of adjustable sunlight transmission under modules developed during ATLAS project.

The solution is designed as a replacement of tunnel structures with a dual-use of the solar installation as an agricultural shading system. It delivers an optimal amount of light to the crops when the photosynthesis is the most efficient, while converting excess sunlight into electricity. Embedded in a static structure, the modules can provide a protection of the crops against climatic events while still enabling a dynamic adjustment of light transmission.

In this project, CSEM's role was to optimize the design of the PV modules for the special targeted conditions, i.e., the highest possible transmission for an optimum crops yield, the most performant bifacial modules with inhomogeneous irradiation on the rear side and the lowest possible weight to avoid reinforcement of the greenhouse. CSEM has also developed new metrology procedures for the power assessment of these dynamic non-conventional modules and assessed the reliability of the final solution. After a careful review of the failure modes, over 100 modules have been fabricated by selected external partner and measured at CSEM in view of field installation.

The first Insolagrin pilot installation covering 165 m² of agricultural land was built by Romande Energie at Agroscope in Conthey, Switzerland (Figure 2). This 18 kWp installation is connected to the grid. Raspberry and strawberry crops are grown under the installation and compared with control berries produced under plastic tunnels. During ATLAS project, the focus is to study the influence of piloting on the crop development and interpret these data for the optimization of the Insolagrin control algorithms. Key parameters linked to the agricultural production and plant physiology are monitored: yield, fruit quality, sap flow, carbon assimilation, and chlorophyl content.



Figure 2: Photograph of the Insolagrin pilot installation in Agroscope (Conthey).

* Insolight

** Agroscope

High-performance Large-area Organic Perovskite Devices for Lighting, Energy, and Pervasive Communications

X. Y. Chin, A. Walter, A. Paracchino, S.-J. Moon, Q. Jeangros

Taking advantage of the rapid development of metal halide perovskite optoelectronics, the EU H2020-funded project PeroCUBE (High-performance large area organic perovskite devices for lighting, energy, and pervasive communication) aims to demonstrate a light fidelity (LiFi) communication system using an emitter and a detector made with the same family of semiconductors, i.e., metal halide perovskites. Led by CSEM, a 14-partners strong consortium is developing perovskite-based photovoltaics (PV) and light-emitting diodes (LED) to create new opportunities for the lighting, energy harvesting and telecom industries in Europe.

PeroCUBE has the objective to exploit the wide compositional space of metal halide perovskite materials, notably 3D/2D heterostructures, and apply these materials and their combinations in novel light-emitting and energy-harvesting technologies. More specifically, the project aims to produce various perovskite-based prototypes for indoor lighting, portable electronics, and ultimately visual light communication through LiFi.

Part of the work done at CSEM is focusing on the development of single-junction perovskite solar cells. The aim is to use these devices as energy harvesters, notably for LiFi, in self-powered lamps or in other portable/wearable devices. Spin coating is used to produce solar cells with an active area up to 1 cm^2 , while meniscus coating methods are investigated to deposit the 500 nm-thick perovskite material uniformly on surfaces of around 100 cm^2 or more. Regarding the latter device geometry, perovskite mini modules produced with this approach reach an efficiency of close to 14% on such a substrate size.

Solar cells of different dimensions, from 1 mm^2 to 1 cm^2 , have been implemented as LiFi receivers to measure their bandwidth. Small-scale 1-mm^2 solar cells reach a bandwidth of close to 5 MHz, a record for this technology. This value drops with the active area of the device to reach less 100 kHz for 1 cm^2 devices due to capacitance losses.

In parallel to these solar cell research activities, CSEM is developing perovskite LEDs. These devices will be key components of the solar lamp prototype or the LiFi communication system envisioned in the project. Using materials and process parameters optimized by the University of Oxford, one of the project partner, CSEM is focusing on scaling up the dimensions of these LED devices. Figure 1 shows a functional green perovskite LED prototype with a 1-cm^2 active emission area developed by CSEM. The current-voltage-luminance characteristics show a low leakage current density ($<10^{-4}\text{ mA/cm}^2$) with a sharp turn-on voltage on the order of 3.6 V. The best performing LEDs have a maximum luminance of around 1000 cd/m^2 and maximum external quantum efficiency (EQE) of 6%. The performance of these green LEDs as LiFi emitter is now under investigation. The final aim will be to demonstrate high-efficiency red, green, and blue LEDs with an active area ranging from 1 cm^2 up to 100 cm^2 .

The next steps of the project will focus on improving the stability of perovskite green LEDs, notably by modifying the materials of the stack and by using advanced encapsulation strategies which are compatible with both rigid and flexible substrates. The development of thin-film deposition methods enabling the deposition of high-quality perovskite materials on large areas will also continue, with a first focus on green LED materials. Research efforts will then focus on scaling-up the two other colors, i.e., red and blue. Potential environmental and human

health hotspots induced by the industrial-scale implementation of these novel materials will be assessed quantitatively, with the aim of mitigating any detrimental impact as early as possible. Overall, PeroCUBE aims to deliver high-performance, yet low-cost photovoltaics, LED, and communication technologies, all produced with a minimal environmental impact and exhibiting a clear cost and performance benefit over existing technologies.

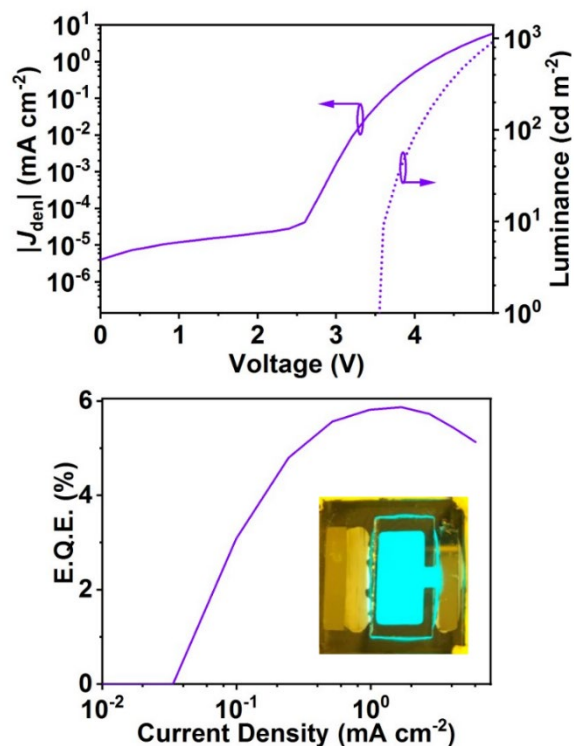


Figure 1: (top) Current-voltage-luminance characteristics of a green perovskite LED. (bottom) External quantum efficiency of perovskite green LED as a function of the applied current density. The inset shows the uniform electroluminescence from perovskite LEDs.

PeroCUBE is a collaboration between CSEM, Alpes Lasers (CH), Optiva Media (ES), Aura Light (IT), Vodafone Innovus, University of Patras, Eulambia, Noesis (GR), CNRS (FR), TU Wien (AT), Fraunhofer FEP (DE), TNO (NL), VTT (FI), and University of Oxford (GB), placed under the coordination of CSEM. The PeroCUBE project has received funding from the European Union's Horizon 2020 research and innovation program under Grant Agreement No. 861985.

High-efficiency 3-Terminal Perovskite/Silicon Tandems Based on Tunnel Junction IBC

L.-L. Senaud, J. Geissbühler, F. Sahli, M. Kikelj, G. Christmann, N. Badel, P. Wyss, C. Allebé, A. Descoeuilles, B. Kamino, A. Walter, A. Paracchino, X. Y. Chin, S.-J. Moon, Q. Jeangros, B. Paviet-Salomon, C. Ballif, D. Bätzner*, D. Lachenal*

This work represents a significant advancement in the field of 3-terminal tandem (3TT) perovskite/silicon devices, which do not need to be current matched, and hence can provide quasi-ideal energy output under any light spectrum. CSEM demonstrates the highest reported certified efficiency of 3TT device to-date, furthermore, achieved with a relatively large device size, including several mass production compatible features such as screen-printed metallization and the tunnel IBC concept. Additionally, we demonstrate that the 3TT architecture allows for the individual characterization of both sub-cells and for the investigation of the luminescent coupling by measuring directly the recycled current within the IBC bottom cell.

Monolithic two-terminal tandem (2TT) perovskite/silicon (PK/c-Si) solar cells have recently reached efficiencies exceeding 31%^[1], with a potential to go well beyond the usual learning curve of c-Si modules. However, due to the series connection of the sub-cells, the energy yield of such device is sensitive to the spectral balance of the incoming light^[2]. Three-terminal tandem (3TT) solar cells eliminate the current matching constraints present in 2TT devices while allowing for the independent operation of both sub-cells at their maximum power point.

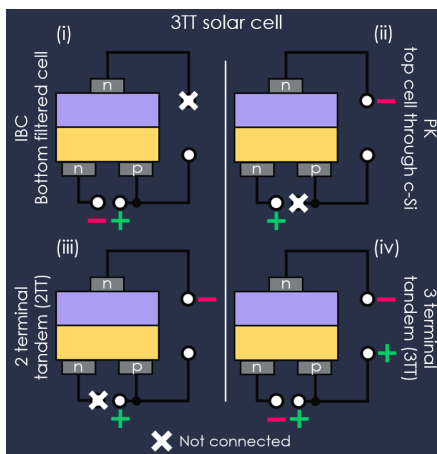


Figure 1: The different connection schemes of 3TT solar cells.

In this contribution, 3TT PK/c-Si solar cells based on tunnel junction heterojunction IBC are investigated. Notably, these devices feature an active area of 24.5 cm² as well as silver printed metallization at the front and rear sides of the cell. Thanks to the architecture of 3TT devices, it is possible to have access to four different connection schemes (see Figure 1): (i) IBC connection, (ii) PK through c-Si, (iii) 2TT configuration and (iv) 3TT configuration by connecting in parallel the IBC and the 2TT connection schemes. Thanks to these connection schemes, it is possible first to characterize the performance of both sub-cells independently, allowing us to study their impact on the efficiency of the 3TT device and second, to characterize the device either in 2TT or 3TT configurations. This demonstrates several interesting outcomes. First, by measuring the short circuit current (I_{sc}) inside the bottom cell while illuminating the top cell at half sun using LEDs at 450 nm for various applied voltages, it is possible to directly measure the luminescent coupling present between the PK and the IBC cells. Indeed, Figure 2.a shows the complete current-voltage curve presenting a maximal I_{sc} of 2.64 mA when the top cell is at open-circuit. Second, to measure the maximal efficiency in 3TT configuration, an efficiency mapping needs to be created as a function of both IBC and 2TT

voltages (Figure 2b). Here, the voltage of the IBC is fixed while the voltage of the 2TT is swept and the total efficiency is obtained by summing the power of the two sub-cells. The overall efficiency is then maximized for the best voltages combination, demonstrating here a high value of 29%. Finally, our best cell was certified in 2TT configuration. A world record efficiency of 29.56% for such a large area of 24.5 cm² is achieved (see Figure 2c). Our results clearly validate the proof of concept of such 3TT devices and are promising for both high efficiency energy scavengers and for the upscaling of tandem solar cells using a perovskite top cell.

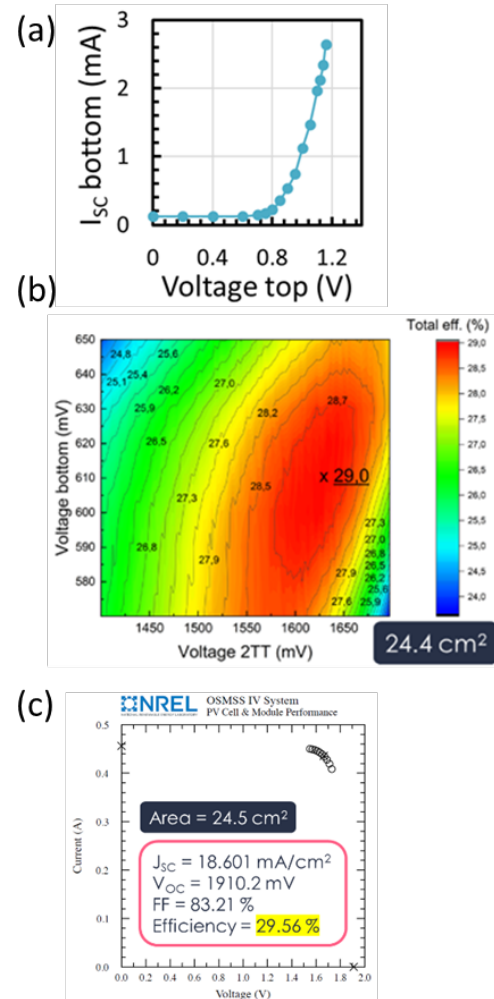


Figure 2: a) IBC short circuit current resulting from the luminescent coupling as a function of the PK voltage illuminated at half sun with LEDs at 450 nm, b) efficiency mapping as a function of the bottom and 2TT voltages, c) Parameters of our world record 3TT cell.

* Meyer Burger

^[1] <https://actu.epfl.ch/news/new-world-records-perovskite-on-silicon-tandem-sol/>

^[2] F. Gota, et al., 'Energy Yield Advantages of Three-Terminal Perovskite Silicon Tandem Photovoltaics', Joule 4, 2020.

Platform for Highly Efficient Industrial c-Si-based Solar Cells

A. Descoeuilles, C. Alleb  , N. Badel, J. Geissb  hler, A. Lachowicz, G. Nogay, L.-L. Senaud, P. Wyss, J. Zhao, C. Ballif, B. Paviet-Salomon

CSEM has set up a complete platform for the production and the characterization of high-efficiency crystalline silicon solar cells, featuring either low- or high-temperature passivating contacts. While the equipment and the developed processes are industry-relevant and compatible with large wafer sizes, this platform allows nevertheless for innovative and flexible R&D developments on all fabrication steps, aiming for high-conversion efficiencies at competitive costs. For the low-temperature approach (silicon heterojunction technology), several cell architectures can be produced ranging from standard both-side contacted cells (with >24% efficiency) to more advanced devices, such as interdigitated-back-contacted devices (>25%) and bottom cells for silicon/perovskite tandems (>29%). Concerning the high-temperature approach (TOPCon-like technology), the formation of the poly-Si layer by sputtering is deeply investigated, providing many advantages at the industrial level compared to existing solutions. A 22.8% PERT-like industrial solar cell featuring such a sputtered passivating contact at the back side has been realized, with a clear optimization path and potential for efficiencies of 25% and more. This unique platform allows CSEM to assess new processes and materials, and to support the development of reliable metallization and encapsulation schemes, which strongly impact field module performance.

In the context of the global energy transition, the need for efficient and affordable photovoltaics (PV) is nowadays more urging than ever. Crystalline silicon solar cells already largely dominate the PV market, but efficiency improvements are still required. The implementation of passivating contacts is the next major technology upgrade, which can be realized either with a low-temperature approach (silicon heterojunction technology, HJT) or with a high-temperature approach (TOPCon-like technology, or HTPC for high temperature passivating contacts). A complete, performant and flexible platform is installed at CSEM covering all aspects of production and characterization of such HJT and HTPC industrial solar cells (up to the M6 format), from as-cut wafers to finished devices (Figure 1). This technological platform allows CSEM conducting advanced R&D projects on specific processing steps, to develop new processes, materials and cell concepts, and also to provide services and small batch production for its customers.



Figure 1: Examples of clean room equipment dedicated to the production and characterization of high-efficiency crystalline silicon solar cells: chemical wet-bench for wafer texturing and cleaning (top), large-area PECVD-PVD cluster tool for various semiconductor thin film depositions (bottom), contacting unit for busbar-less solar cell electrical measurements (right).

CSEM, with its EPFL partner has been working on the HJT technology for 17 years. All process steps (wafer preparation by wet chemistry, depositions of silicon thin films and transparent conductive oxides by PECVD and PVD respectively, metallization by screen-printing) have been developed and optimized using a standard cell architecture with contacts on both sides, and efficiencies currently reach >24% on full-area 6-inch devices. Benefiting from these base processes, further developments have been performed recently on more advanced and efficient cell structures, namely interdigitated-back-contacted (IBC) cells and tailored bottom cells for

silicon/perovskite tandems. Increased efficiencies of >25% and >29% have been demonstrated on medium-size IBC and tandem devices (25 cm^2), respectively. The upscaling of the existing processes to full 6-inch format is currently under intense development for both cell architectures.

More recently, HTPC developments have been initiated at CSEM for a smooth upgrade of existing solar cell production lines with the addition of a single thin silicon layer deposition tool, enabling to boost cell efficiencies from ~23% to ~25%. Such HTPC cells compatible with a broad range of post-processing temperatures are also promising bottom cell candidates for silicon/perovskite tandem architecture and have enabled to reach efficiencies >28% at CSEM. The core element of HTPC is a thin layer of poly-silicon. At CSEM, this layer is advantageously deposited by sputtering, a high throughput technique, enabling to achieve the incorporation of phosphorous dopants, thanks either to a post-deposition (ex-situ) plasma-assisted process, either simply directly during the deposition process itself (in-situ) using a phosphorous-doped silicon target for the sputtering process. The optimization of the process parameters and of the target doping have enabled to reach very similar amount of phosphorus in the deposited silicon films with both methods (Figure 2), along with excellent values of passivation ($iV_{oc} \sim 730\text{ mV}$) and carrier extraction properties (contact resistivity $\sim 4\text{ m}\Omega\text{-cm}^2$).

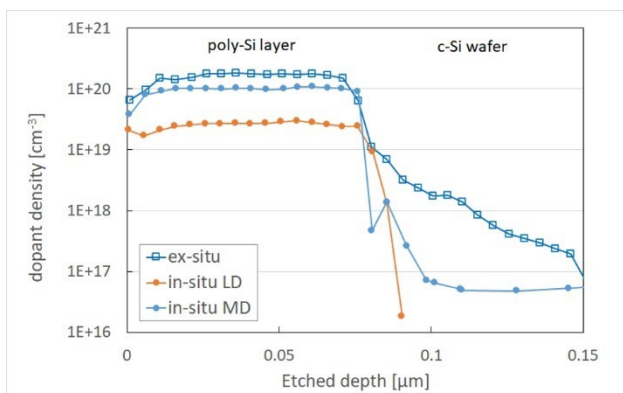


Figure 2: Concentration of active phosphorous dopants in the sputtered poly-Si layer and in the silicon wafer, for doping processes performed by ex-situ plasma-assisted and by in-situ doping with a lowly doped (LD) and a medium doped (MD) Si:P target (measured by ECV).

Lightweight Photovoltaic Modules for Vehicle Integration at CSEM

S. Prabhudesai, K. Nicolet, G. Cattaneo, J. Gerber, L. Jaques, J. Levrat, F. Mujovi, C. Charrière, M. Despeisse, A. Faes, J. Robin*, V. Leite*, J. Silva**

CSEM has developed in collaboration with Simoldes and CEiiA a first-of-its-kind unique light-weight module with a thick polymeric front sheet for vehicle-integrated applications. Due to the importance of an aerodynamic shape for the efficiency of the vehicle as well as aesthetic requirements from the car industry, CSEM has assessed the feasibility of integrating solar cells in a curved light-weight rigid impact-proof laminate. To allow for smooth integration in vehicle assembly lines, the stress tolerance of the module to different stresses induced in the assembly process have been simulated and experimentally validated.

Rapid growth of Electric Vehicle adoption and falling PV prices over the last decade, coupled with the recent surge in electricity and gas prices in Europe, has given a new boost to innovation in vehicle integrated photovoltaics (VIPV). PV modules integrated in vehicle roofs must be designed to match the requirements of the vehicle industry, such as superior aesthetics for a curved roof, crash resistance, compliance with automotive assembly lines, but the most important criteria being weight, to ensure the highest energy efficiency by minimizing the vehicle weight^[1].

The present work targets two key areas for the integration of lightweight PV modules in vehicles: The first one deals with the maximum stress that the solar cells can withstand before fracture, when encapsulated in a polymeric, lightweight, VIPV module. By replacing the glass-based front sheet with a lighter polymeric alternative, potentially a module weighing half the weight of a traditional glass-based module can be achieved. To ensure that such a module can withstand the heavy loads that may be generated during assembly of the vehicle and later in operation, a FEM based model has been developed.

A linear elastic FEM model was compared with a hyper-elastic FEM model to determine the value of applied load that would cause the tensile stress in the cell to reach the ultimate tensile stress of 200 MPa^[2], resulting in fracture. The model setup was replicated in the lab for validation (Figure 1).



Figure 1: Experimental setup for validation of FEM model on mechanical loading of VIPV module.

While the linear elastic model overestimated the stress on the cell under load (Figure 2), correction of material properties of the lightweight polymeric front sheet to a hyper-elastic material model yielded results in good agreement with experimental findings (Figure 3). A z-displacement comparison between simulated and experimental results was used for initial validation. The observation via electroluminescence imaging, of cell fracture occurring at the predicted failure load, was used as a conclusive final validation.

- Simoldes
- CEiiA

The second area of focus is the design consideration for a curved PV module. Different orientations and radii of curvature have been assessed to check the limit for cell bending before crack formation. Concave, convex and waveform shapes have been evaluated to not only help decide PV module lamination process but also provide feedback on this design constraint to the vehicle industry.

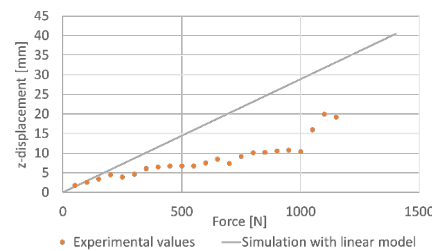


Figure 2: Overestimation of z-displacement of module centre point by Linear Elastic model.

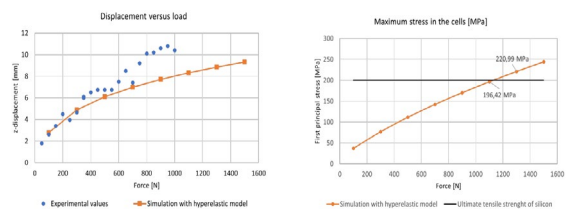


Figure 3: Hyper-elastic model showing a) Closer match of z-displacement between simulation and measurement, and b) accurate indication of failure point. Cell was found to be cracked at 1150 N.

Cell curvature test results indicate a lower stress build-up in convex shape integration than concave and wave shapes. The curved shape achieved using the mold and corresponding Electroluminescence imaging for different curvatures is seen in Figure 4a and Figure 4b, respectively.

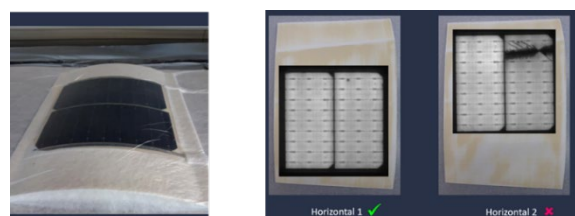


Figure 4: a) Encapsulated string + 3D sample in vacuum bag; b) electroluminescence imaging for curved pre-laminate testing at two different curvatures in horizontal string orientation.

This project has received funding from the SFOE under grant agreement No SI/502317-01.

[1] S. Prabhudesai, "Versatile Lightweight Photovoltaic Module Line at CSEM Using High Efficiency Crystalline Silicon Cells", 38th EUPVSEC, 6-10 September 2021.

[2] F. Kaule, W. Wang, S. Schoenfelder, Solar energy materials, vol. 120 (2014), pp. 441–447.

Solar-powered Smart Freight Container for Medicine Transportation

X. Bulliard, P. Duvoisin, C. Charrière, S. Prabhudesai, M. Despeisse, C. Ballif, M. Martin*, E. Seligman*

Local startup Swiss Airtainer SA teamed up with CSEM to develop smart, self-powered containers for shipping pharmaceutical drugs under temperature-controlled conditions. The containers, equipped with ultralight, custom-built solar panels developed by CSEM, keep medicines cold along the entire logistics chain, while full traceability prevents theft. The powering with solar energy was validated in real tests conditions and the firm plans to introduce its first containers on the market by end of 2022.

According to the World Health Organization, nearly 50% of vaccines lose efficacy in transit via air or sea largely due to cold chain break. The damage to medical drugs caused by temperature changes costs the pharmaceutical industry an estimated €35 billion a year. One third of the vaccines are losing their efficiency, due to temperature excursions and a further €200 billion a year is lost to theft and counterfeiting. These logistical failures are estimated to cause over 1 million human casualties and put the lives of additional patients at risk.

Swiss Airtainer is working with CSEM to tackle these issues with next-generation freight containers, which provide enhanced security and temperature control. The containers are sustainable as they are powered by a battery unit recharged by solar energy. CSEM designed unique solar panels for the containers, enabling them to operate independently, while allowing for real-time connectivity to continuously monitor the cold chain.

The number of cells, container surface coverage, expected production and consumption in different location and seasons were first evaluated by simulation. It appeared that a full coverage of the roof was enough to generate electricity for the normal usage. To address the other requirements, in terms of weight, custom-made panels based on a lightweight composite structure were designed. The composite stack was specifically tuned to resist to temperature and mechanical constraints. A structure with good dimensional stability and high resistance to impact was produced. The good resistance to impact was confirmed through hail test. For that kind of lightweight module, the weight can be reduced to less than 2 kg/m² and the thickness was only 1 mm. For comparison, conventional modules weight is around 16 kg/m² and five times thicker. When combined to the specialty composite of the container structure, this results in a total weight of 400 kg – versus 600 kg for regular containers.



Figure 1: Lightweight solar panels installed on the roof of the container.

After installation on the roof (Figure 1), the panels were connected to the battery units. The system then controlled the cooling unit. A fully equipped freight container was tested in Dubai in August 2021. Despite the intense sunlight and temperatures exceeding 48°C in the daytime and falling to 35°C

at night, the containers worked efficiently without any external power supply. The cold-chain technology was able to keep the containers at a steady 5°C with a tolerance of just ±0.1°C. The power generated by the solar panels during the day was enough to run the electronics and charge the battery. Then at night, the battery took over and powered the system until the charging could begin again.

In addition, each container has 16 sensors that send instantaneous alerts in case the container experiences temperature changes or sudden movement. This helps prevent theft and loss, as operators are notified if a container is opened unexpectedly or if the container's contents may have deteriorated. These sensors are as well powered by solar energy.

Current developments focus on the integration of other cell types, further weight reduction and the tuning of the color and design of the modules. This also involves additional work on special encapsulation technology. Figure 2 shows an example of recent developments.



Figure 2: Novel development of lightweight composite solar panels.

In summary, the self-solar-powered temperature-controlled container can be used to transport medicine with enhanced security and traceability with a major reduction in risk of cold chain break. The lightweight structure would cut the transportation-related carbon emissions by nearly 45%. These containers can be used to deliver drugs to airports that don't have the charging infrastructure that is usually required for current and conventional solutions. Market launch is scheduled for the end of this year.

This project has received funding from the ECSEL Joint Undertaking (JU) under grant agreement No 101007247 (ECS Energy). The JU receives support from the European Union's Horizon 2020 research and innovation program and Finland, Austria, Germany, Ireland, Iceland, Italy, Sweden, and Switzerland. CSEM and Swiss Airtainer thank them for their support.

* Swiss Airtainer

Reliable PV Solution for Stratospheric Applications

P. Duvoisin, X. Bulliard, H. Li, C. Charrière, S. Prabhudesai, G. Cattaneo, S. Pittet, M. Despeisse, C. Ballif, J. M Nicot*, D. Bausch*

CSEM has set up a versatile platform for the manufacturing of lightweight photovoltaic (PV) modules for applications to a wide range of domains, for example stratospheric applications. The lightweight PV solutions currently equip balloons for missions in the stratosphere piloted by the CNES. The missions of a few days to several months aim at studying meteorology or climate and the developed modules provide electricity for the scientific instrumentation. In addition to lightweight and high mechanical resistance, the PV modules have been specifically designed for functioning in the harsh stratospheric environment, under UV, ozone and temperature exposure.

CSEM and CNES are collaborating on the development of novel PV solutions to power the scientific instrumentation of balloons for missions in the stratosphere. For such missions, the requirements in terms of weight, mechanical properties and reliability are important and CSEM has developed unique PV solutions based on composite materials to satisfy these criteria. The use of composite materials allows the tailoring of mechanical properties by reinforcing the strength of the module in specific area, while preserving a high toughness, for a minimum weight. In contrast to typical glass-based PV modules which exhibit a weight superior to 15 kg/m^2 , the products developed can show a weight below 1 kg/m^2 . In these developments, the structure of the modules and its constituting elements (backsheet, frontsheet and encapsulants) were redesigned. In particular the composition of the encapsulant was formulated to withstand UV and ozone exposure in the stratosphere. The encapsulant is critical to protect the cells and maintain the whole integrity of the modules.

Two types of PV modules and solutions have been implemented for two different flight missions. In the mission Strato 2 (CNES), balloons are launched for typically 3 months around the equator to collect a wide range of data for a better understanding of meteorology and climate. For this mission, module with the composite-based architecture were directly fixed on the balloon basket, as shown on Figure 1a. The custom-made modules are dimensioned according to the room available on the basket.

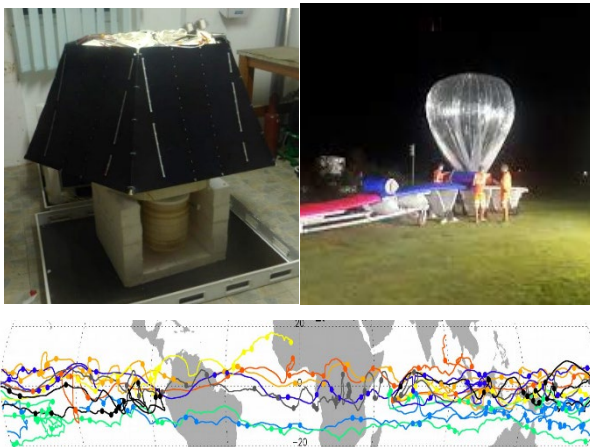


Figure 1: Pictures of the module placed on the basket of the balloon (a), the launching of the balloon (b) and the trajectory of the balloon for the mission Strato 2 (picture courtesy of CNES; copyright A. Herzog).

The functionality and reliability of the modules has been verified in a first validation mission of three months in 2020. A first scientific mission followed in 2021 and the next one is schedule

in 2023. Figure 1b shows the launching of the balloons and Figure 1c their trajectory during the validation mission.

In the project MEDOR (CNES), a larger electricity power is required, exceeding the power that could be generated by modules on the side of the basket. To circumvent this limitation, CNES and CSEM developed a solar store that hangs below the balloon. The store is folded during take-off or landing, and is deployed when the balloon reaches its cruising altitude. Figure 2 shows a picture of the store during deployment. The number of elements can be tuned and adapted to the power needed for a specific mission. Non-functional elements (without solar cell) are added for mechanical purpose and to avoid shadowing on the cells by the balloon. The solar modules of $1 \times 2 \text{ m}$ (3 on the pictures) are then added and electrically connected to the rest of the store. For this use case, the rigidity of the modules was critical to avoid buckling during deployment, while the toughness should be maintained in case of impact. The right balance between these mechanical properties could be achieved by controlling the composite stacking of the module. The whole system under the balloon was tested and validated in real conditions, in a first mission in Sweden in 2021.



Figure 2: Picture of solar store (partially shown) during deployment. The first mechanical elements are not equipped with solar cell, and the solar modules (3 on the picture) are then added to the store.

In summary, the lightweight PV modules, specifically designed for harsh stratospheric environment, have been validated in two different missions piloted by CNES. The technology finds direct applications in climate study and the knowledge gained can be used in a wide range of other applications.

* CNES, Toulouse, France

Graph-based Multi-site PV Forecasting Models

J. Simeunović, R. Carrillo, B. Schubnel, P.-J. Alet

Accurate photovoltaics forecasting is essential to integrate renewable energy sources into the power grid. CSEM has developed data-driven graph-based methods and compared them with commercial methods based on satellite images for forecasting PV production. CSEM's methods outperform the state of the art for horizons from one up to six hours ahead. Furthermore, CSEM developed a method that explicitly capture the differences in dynamics on different timescales. The results are easier to interpret, and their accuracy beats all other methods for forecasting horizons from four to six hours ahead.

Operating power systems with large amounts of renewables requires predicting photovoltaic (PV) power production with fine temporal and spatial resolution [1]. However, PV power production is dependent on weather conditions, especially cloud movement. State-of-the-art methods predict cloud dynamics using ground-based cameras, satellite images, and numerical weather predictions (NWP). The main problem with these approaches is their low temporal or spatial resolution, which poses a challenge for applications such as energy trading and grid congestion management.

To improve intra-day, multi-site PV forecasting, CSEM developed machine-learning methods which use the intuition that PV systems effectively provide a dense network of weather stations. The first model is a graph convolutional long-short-term memory network (GCLSTM). It consists of a graph convolution network and a recurrent neural network.

We have compared a GCLSTM model that relies solely on PV production and geographical data [2] with a commercial solution that uses weather models and cloud positions to forecast PV production. The commercial solution uses cloud positions from satellite images to propagate the movement of the clouds in the future. In addition, it uses online ground data (solar radiation or PV production) to correct the cloud-tracking forecasts.

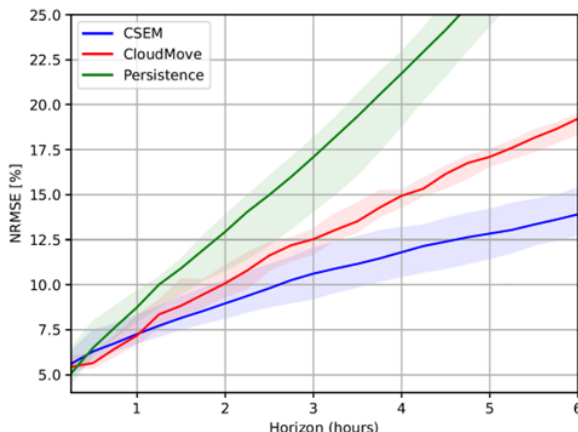


Figure 1: NRMSE evolution over the forecasting horizon of 6 hours ahead in steps of 15 minutes.

The results of the comparison between GCLSTM, cloud-tracking and the "smart persistence" model are shown on Figure 1. The comparison was made for the representative set of 18 locations and 21 days, which were selected to cover the range of possible

[1] R. E. Carrillo, P.-J. Alet, S. Müller, J. Remund, "A computationally light data-driven alternative to cloud-motion prediction for PV forecasting," in Proceedings of the World Conference on Photovoltaic Energy Conversion (WCPEC-8), Milan, Italy (2022).

[2] J. Simeunović, B. Schubnel, P.-J. Alet, R. E. Carrillo, "Spatio-Temporal Graph Neural Networks for Multi-Site PV Power

conditions in Switzerland (weather, terrain, distance to other instrumented sites, seasons). The data-driven model uses data from 304 PV stations scattered over Switzerland for both training and evaluation. Over the whole set, CSEM's data-driven technique yields a lower NRMSE than the commercial method for forecasting horizons above one hour.

Although, the GCLSTM is better than state-of-the-art methods, it includes both convolutional and recurrent neural networks, whose behavior is difficult to explain. Since PV power production is a physical phenomenon, models which can be interpreted from a physics perspective are more desirable. Therefore, CSEM introduced a temporal-spatial multi-windows graph attention network [3] (TSM-GAT) that can adapt to the dynamics of the problem, by learning different graphs over time. It consists of temporal attention and spatial attention with a multi-window mechanism, which captures the dynamics for different parts of the forecasting horizon. Thus, it is possible to interpret which PV stations have the most influence when making short-, medium- or long-term intra-day forecasts.

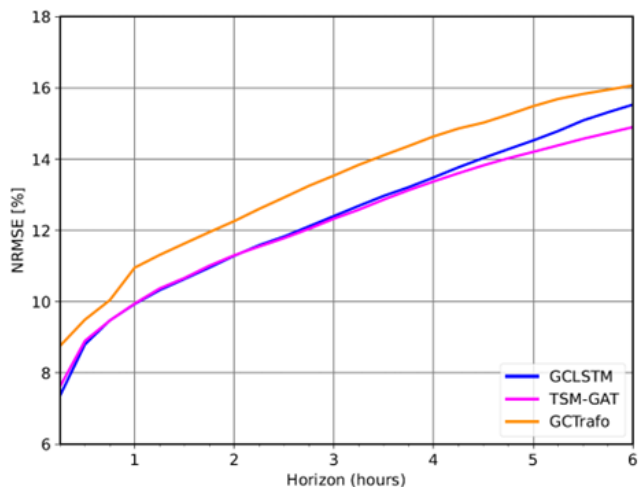


Figure 2: NRMSE for the Switzerland over the forecasting horizon of 6 hours ahead.

The comparison with different state-of-the-art models is shown in Figure 2. The results show that TSM-GAT is on par with GCLSTM [2]. Furthermore, the lower error slope and high accuracy in the fifth and sixth hour ahead prediction of the TSM-GAT could make it an attractive multi-site model for longer prediction horizons.

Forecasting," IEEE Transactions on Sustainable Energy 13(2), 1210–1220 (2022) [doi:10.1109/TSTE.2021.3125200].

[3] J. Simeunović, B. Schubnel, P.-J. Alet, R. E. Carrillo, P. Frossard, "Interpretable temporal-spatial graph attention network for multi-site PV power forecasting," Applied Energy 327, 120127 (2022) [doi:10.1016/j.apenergy.2022.120127].

Data-driven Flexibility Estimation of Buildings with Uncertainty Quantification

P. Scharnhorst, B. Schubnel, R. E. Carrillo, P.-J. Alet

Through increasing levels of renewable energy production, such as solar or wind, grid balancing is becoming increasingly difficult. Buildings are a promising source of consumption flexibility, which can be used to address the problem. CSEM has developed a novel set of algorithms to represent the building as a virtual battery, capable of storing and releasing energy. The model parameters of the virtual battery can be directly learned from measurement data, and uncertainty can be expressed via a user-defined parameter. The model was used to predict available consumption flexibility of a simulated building from the Energym® library with different levels of conservativeness. This approach be of high interest for aggregators and building managers to make the most of uncertain assets.

The intermittent behavior of solar or wind power production makes their widespread adoption a challenge for grid operators, who need to ensure a balance between power production and consumption. Demand response (DR) can enable the grid operators to achieve this balancing by adapting the consumption of end users to the available production [1]. With their potential to significantly change their consumption behavior in the short term, buildings are interesting candidates for providing this flexibility. To leverage the full capabilities of buildings for participation in this framework, an accurate estimation of their available consumption flexibility is needed. For this, detailed models, which are costly to obtain for each individual building and require expert knowledge to design, are usually used.

To reduce this modeling effort, CSEM has proposed a model of buildings in the form of a virtual battery, which tracks a numerical state variable that can be obtained from standard measurements of the building operation, like the indoor temperature and the specifications of the installed equipment. The capacity of the virtual battery, indicated through bounds on the state, incorporates knowledge about the operational constraints of the buildings' equipment and the thermal comfort of the occupants. In the model, three principal operating modes are encoded: receiving requests to increase consumption, receiving requests to decrease consumption, and nominal operation of the internal controller.

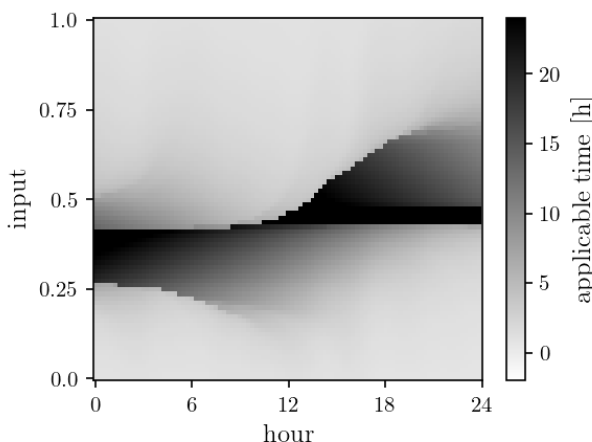


Figure 1: Availability times of different input levels (power fraction of the heat pump) depending on the time of the day.

[1] IEA (2022), Demand Response, IEA, Paris, <https://www.iea.org/reports/demand-response>

[2] D. Bertsimas, D. B. Brown, "Constructing Uncertainty Sets for Robust Linear Optimization." Operations Research 57 (6), 1483 (2009).

Having measurement data obtained in those three operating modes, the different parameters of the model can be learned. To incorporate uncertainty and account for the variance in the training data, risk measures [2] are used to specify different levels of conservativeness in the flexibility predictions, where the risk level can be chosen freely. This is done by describing the set of requests that lead with a given probability to no violation of the state bounds, and by reformulating it using a deterministic uncertainty set instead of the probabilistic constraints. For specific types of consumption requests, namely constant deviations from a baseline or constant absolute power levels, efficient methods for computing these uncertainty sets were developed. An example of a flexibility envelope describing the time a constant power level can be maintained, depending on the time of the day, is displayed in Figure 1.

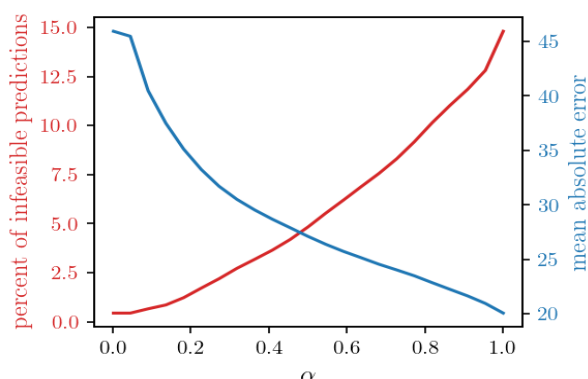


Figure 2: Trade-off between percentage of infeasible predictions and prediction accuracy, depending on the uncertainty parameter α .

The approach was tested on a building model from the simulation library Energym [3]. With three weeks of data from the month of January, the parameter identification was performed, and the predictions were evaluated during ten days under different weather conditions. Comparing the predictions for different choices of the uncertainty parameter α to the real available flexibility, a tradeoff between the number of infeasible predictions and the mean absolute error of the predicted available steps can be observed, as displayed in Figure 2. This tradeoff shows the decision to be made in choosing the uncertainty parameter, balancing the incentives for promising flexibility and penalties for not following consumption requests.

[3] P. Scharnhorst, B. Schubnel, C. Fernández Bandera, J. Salom, P. Taddeo, M. Boegli, T. Gorecki, Y. Stauffer, A. Peppas, C. Politi, "Energym: A Building Model Library for Controller Benchmarking", Appl. Sci. 11(8), 3518 (2021).

Automatic Quality Inspection of PV Modules Based on Minimal Set of Labelled Training Data

B. Schubnel, R. Langou, G. Cattaneo, P.-J. Alet

The IEA Net Zero by 2050 scenario implies that the annual deployment of photovoltaic capacity be multiplied by more than four from 2021 to 2030 [1]. To reach this goal and increase Europe's security of supply, several initiatives aim at bringing back all parts of the value chain to Europe [2]. CSEM is involved in research and innovation projects that seek to increase the automation and quality inspection in European production lines for solar cells and modules. In that context, CSEM has developed new algorithms for optical inspection of PV modules, which can be trained with as little as a few dozen labelled images and recognizes defects with a very high accuracy.

Alongside an increase in installed capacity from 160 GW (2021) to more than 600 GW of solar PV by 2030 [2], Europe aims at bringing back most parts of the solar manufacturing chain (polysilicon, wafers, cells, modules) to secure its access to power production technology. European manufacturing costs are still around 30% higher than their Asian counterparts [1] and high automation of the production lines together with the highest quality standards are necessary for the European solar industry to be competitive.

Optical inspection during the production of modules aims at detecting any bubbles, scratches, ribbon shifts, broken cells, or other defects that could have been made along the manufacturing line. Several constraints make the automation of this task challenging. The setup of the line setup can change from time to time. A given line can produce modules with different form factors and color. The lighting conditions and the visual background in the available location for optical inspection are often uncontrolled. Finally, the available set of labelled defects is often small and lacks representativeness. Indeed, the effort required to label data and segment defects makes standard deep-learning algorithms for vision-based anomaly detection out of reach for small or mid-size producers. This constraint is all the more severe that this labelling and segmentation must be done again each time the product or line changes.

To solve this challenge, CSEM has implemented a deep-learning solution that requires very few labelled images of modules and still shows very good performance for defect localization and module classification. Following recent advances in machine vision that used backbone classification and segmentation neural networks, which were pretrained on standard vision datasets, to extract relevant image features, the algorithmic chain (Figure 1) is capable of:

- detecting and extracting solar modules of different colors and shapes on very different backgrounds
- segmenting defects and labelling the modules as good or faulty. Further classes can be defined based on the shapes and characteristics of defects, and an additional classification layer can be implemented: either by applying rules on the defects in the segmentation map, or fully automatized using a CNN add-on on top of the backbone architecture
- making an in-depth analysis of ribbon shifts to spot anomalous ribbon alignment.

A web-based interface has been implemented for the users to interact with the algorithms and add potential labels.

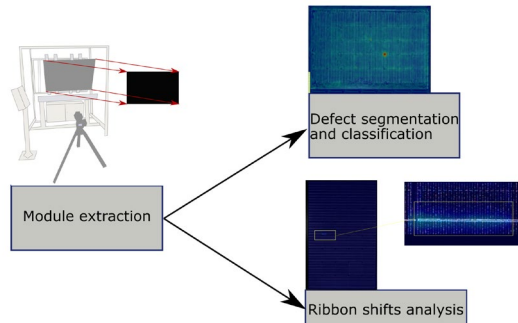


Figure 1: Algorithmic steps: module extraction via deep segmentation, defect segmentation and classification, and analysis of ribbon shift.

Thanks to the automated segmentation and extraction of the module from the original picture, the optical inspection can be installed at different locations on the production line and can also cope with setups where the position of the modules can change from picture to picture.

The algorithms have been tested directly on unfiltered data from a commercial production line. The segmentation toolchain could correctly localize the modules on the production line in 100% of the tested cases. Despite the training set being limited to a dozen of modules, with a few of them displaying small anomalies, the AUC (area under ROC curve) of the classifier reached 0.99 (1.0 is a perfect classifier) on the industrial test set of around 100 modules. The third step for the ribbon extraction also displayed an AUC of 0.99. Its diagnostics were confirmed on the few modules with ribbon shifts with a microscopic camera (Figure 2).

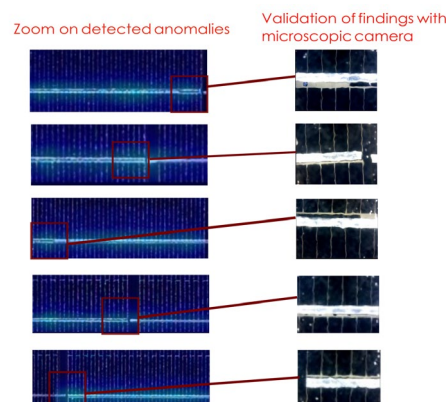


Figure 2: Detection and validation of ribbon shifts with microscopic camera.

[1] IEA, "Solar PV Global Supply Chains," International Energy Agency, Paris (2022).

[2] Directorate-General for Energy, "In focus: Solar energy – harnessing the power of the sun," European Commission, 13 September 2022, https://ec.europa.eu/info/news/focus-solar-energy-harnessing-power-sun-2022-sep-05_en

Battery SoX Balancing Based on zBMS Platform

C. Brivio, G. Thenaisie, N. Koch, E. Sanino, S. Bhoir, P. Iurilli, N. Koch, A. Hutter

Within the internal project ROBIN, we have developed algorithms, which improve the SoC balancing of battery cells and which allows a new concept of SoH balancing. Our validation tests proved that: (i) it is possible to rebalance unevenly unbalanced cells within minutes with 100% efficiency (standard passive balancing requires hours and will dissipate energy); (ii) it is possible to extend the lifetime of the battery pack of minimum 20% in 1st life application and minimum 35% in 2nd life applications (e.g., reused battery packs from 1st life).

The innovative zBMS^[1] battery management system, which is under development at CSEM (see Figure 1) is based on two radical innovations:

- Embedded Electrochemical Impedance Spectroscopy (EIS), which allows to understand dynamic and ageing phenomena occurring inside the battery cells and to build physics-based Electric Circuit Models (pECMs) to improve SoX estimation^[2] (e.g., State of Charge SoC, State of Health SoH, State of Safety SoS, etc.),
- Single-cell level control based on cell bypass, which enables improved SoX balancing strategies and safety based on hot swapping capability.

While the first innovation was proven to be feasible during Innosuisse project BATMAN, the SoX balancing strategies were evaluated during the internal CSEM ROBIN project. The developed algorithms leverage the zBMS bypass feature, where each and every battery cell can be either inserted in the string or bypassed, whereas one battery cell stays bypassed at all times.

The SoC balancing relies on the SoC estimation performed continuously (once per second) by the pECMs embedded into the zBMS CMS. At every iteration of the algorithm, the "worst" cell is identified as the cell with SoC furthest from the target SoC and the "target" cell is the cell with the SoC closest to the target and to which the "worst" must align. If the ΔSoC among the two is beyond a given threshold, the "buffer" cell is inserted for brief periods in place of the "worst" cell, as to reduce the unbalances.



Figure 1: zBMS prototype presented at the Battery Experts Forum in July 2022 with prismatic cells (LFP, 90Ah), featuring EIS and hot-swap.

The SoH balancing relies on the SoH estimation performed periodically (e.g., once per week) by the pECMs embedded into the zBMS Cell Management System (CMS). It is based on the concept of "buffer" cells, which is identified as the most aged cells at a specific point in time. The "buffer" cell stays out of the battery string for most of the time and it is only temporarily reinserted in place of other cells for other balancing purposes. By taking care

of the "buffer" cells it is possible to extend the lifetime of the battery pack.

SoC balancing have been tested directly on the zBMS prototype with different ΔSoC between the cells: 5%, 25% and 50%. In all tested scenarios, the SoC unbalances were corrected within minutes (15 minutes at best, 80 minutes at worst) and with no charge dissipation. If passive balancing was used, the same SoC unbalances correction would have required hours (24h in the worst case) and result in important energy losses on resistors.

SoH balancing algorithm have been tested on an emulated setup by cycling two cell-level setups (based on 12Ah Kokam NMC pouch cells) at 1C/1C continuous cycling rate. The results show that an advantage of ~20% in lifetime can be obtained in 1st life applications (e.g., automotive, 100% < SoH < 85%), while a more consistent improvement of ~35% can be obtained in 2nd life applications (e.g., stationary, SoH < 85%).

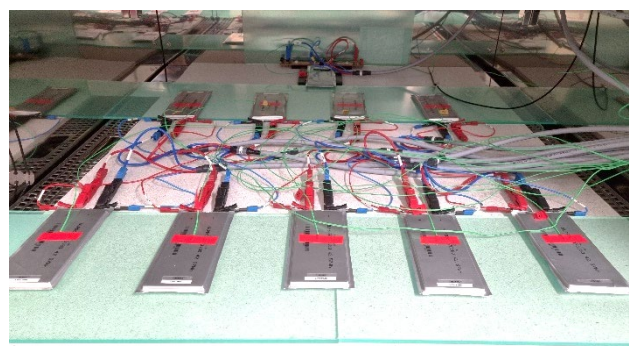


Figure 2: Emulated SoH balancing tests run in a controlled environment (BCS battery cycler + ACS thermostatic chamber).

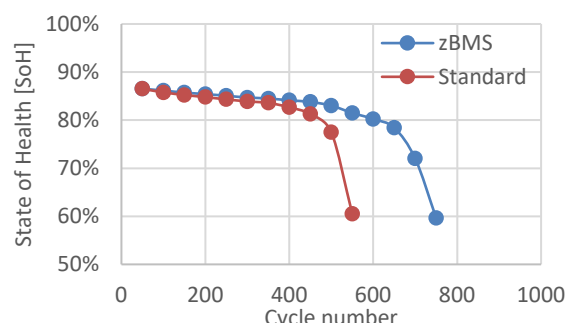


Figure 3: SoH balancing emulation tests results in case of 2nd life applications. Advantage of +35% lifetime has been measured.

In summary, we demonstrated that the innovative zBMS hardware and software architecture allows the realization of tangible advantages for SoX balancing. In a next step we intend to demonstrate advantages for safety improvements, e.g., a SoS algorithms avoiding thermal run-away.

[1] Patent EP21164505, "Battery system and battery management method, filing date 24.03.2021.

[2] P. Iurilli, EIS2MOD: a DRT-based modelling framework for li-ion cells, IEEE transactions on industry applications, 2021.

SoXery – an Online Tool to Evaluate Battery Ageing

S. Bhoir, C. Brivio, A. Hutter

An online tool to evaluate the aging in a battery, taking into account the anticipated usage conditions, was developed and made public. The tool bases on the expected power and temperature profile of the battery and on the cell chemistry to calculate the aging that the cell will undergo over a certain period. The output from the tool includes the calendar and cycle aging of the cell, the increase in the internal resistance of the cell as well as an unfulfillment map, which shows whether the cell was able to adhere to the usage profile or not. The tool is intended to be used as a first approximation by users who want to know the most appropriate cell chemistry given a usage profile, or for sizing their battery for a specific purpose.

Lithium-ion batteries are quite ubiquitous thanks to their high energy and power density. They are seen as one of the pillars of the energy transition. But one of the downsides of these batteries is that they undergo degradation with usage, i.e., they lose their ability to store a certain amount of energy or provide a certain amount of power. This is called capacity fade and power fade, respectively. It is of value to know the amount of degradation a battery will undergo since this can prevent electrical abuse such as over-charging/-discharging during usage, which is a cause of battery failures and fires. As part of the Open-Sesame project (IEA-EICES TASK 32 about modelling of energy storages for simulation/optimization of energy systems), CSEM was tasked with building an empirical battery aging model which can calculate the capacity and power fade in a cell, under a given set of usage conditions.

In this context, a stress-based empirical model was developed for NMC/LFP/LTO chemistries based on data from real experiments^[1] as well as data from literature. The model evaluated two aspects of the cell degradation:

- Calendar aging: This occurs when the cell is stored and not under use. It depends on the state of charge (SoC) and temperature at which the cell is stored.
- Cycle aging: This occurs while the cell is being used. Current rate (C-rate), depth of discharge (DoD), temperature and average SoC are all parameters that influence the amount of cycle aging.

Both these aspects result in state of health (SoH) decrease and state of resistance (SoR) increase in the cell. The model developed consists of relationships between these two aspects and their influencing parameters. Finally, this model is built in python such that it takes inputs such as the size of the battery, the battery chemistry and usage profile and outputs the battery degradation over the simulated period.

This python code is made available open-source as an online user-friendly tool at our CSEM server: tinyurl.com/soxery. The user must provide the profile parameters and battery parameters. The first profile parameter is the input profile in the .csv format. This file consists of power and temperature data for the cell at a certain time resolution. In addition to this, the user must also provide this time resolution and time horizon for the simulation. In the battery parameters, the user must provide the size of the battery pack, the cell chemistry and the minimum and maximum SoC allowed during the simulation. A user guide explaining these parameters in depth is also provided on the website.

The output of the simulation is displayed in two panels. The first panel displays KPIs such as SoH and SoR and the contributions

of calendar and cycle aging in each one of them. It also displays the total number of full equivalent cycles performed by the battery and maximum and minimum currents and temperatures imposed upon the battery. The second panel displays several graphs which depict the trend of certain parameters over the simulated period: SoH, SoR and SoC. For instance, Figure 1 shows the decrease in the SoH for a certain application profile.

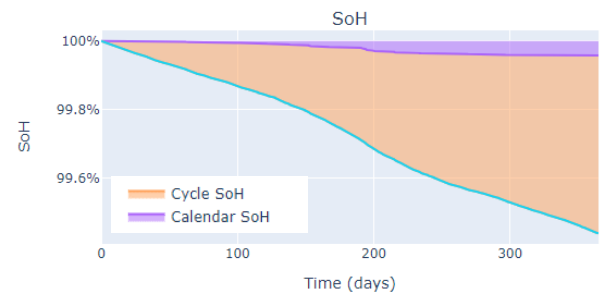


Figure 1: SoH decrease over usage.

A graph showing the input profile is also displayed so that the user may cross check if the input power profile has been applied as provided. Finally, an unfulfillment map is displayed. This map shows whether there were certain times during the simulation where the battery could not provide or absorb the power specified by the user. An example of such a map is shown in Figure 2.

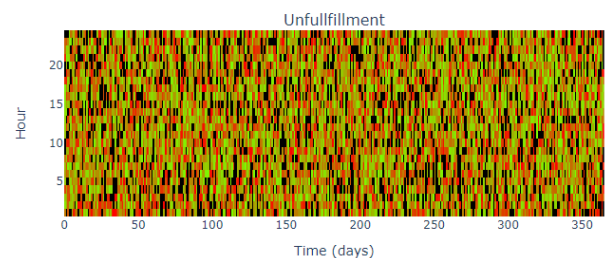


Figure 2: Unfulfillment map.

The green regions on the map show the instances when the battery SoC is away from the set maximum or minimum SoC while the red regions show the instances where it is not. The black regions depict the times where the input profile could not be followed. The amount of black in the map is an indication to the user that the battery sizing may need to be increased.

Based on this first release, CSEM is now investigating the possibilities to use the SoXery as a simulation toolbox to tune energy optimization framework. An example would be the use of SoXery into NRGMaestro™, the intelligent SW for district renewable energy management proposed by CSEM.

^[1] S. Bhoir, P. Calandro, C. Brivio, "Impact of V2G service provision on battery life," Journal of Energy Storage, p. 103178, 2021.

Results on Dendrite Detection for Li-metal Batteries

P. Iurilli, L. Luppi, C. Brivio, A. Hutter

Within the EU project HIDDEN, we investigated six non-invasive detection techniques to anticipate failures in Lithium Metal Batteries (LMBs) and to lay the basis for innovative self-healing mechanisms^[1]. The novel methodology is based on: (i) defining detection parameters to track the evolution of cell aging, (ii) defining a detection algorithm and applying it to cycling data, and (iii) validating the algorithm in its capability to detect failure. The main outcomes of the work include the characterization results of the tested LMBs under different cycling conditions, the detection techniques performance evaluation, and a sensitivity analysis to identify the most performing parameter and its activation threshold.

The application of Lithium Metal Batteries (LMBs) as secondary cells is still limited due to dendrite degradation mechanisms arising with cycling, where dendrite growth is responsible for safety risk and early cell failure. Studies to prevent and suppress dendritic growth using state-of-the-art materials are currently in development. CSEM analyzed impedance-based and voltage profile-based non-invasive techniques (Table 1) to track LMB degradation with specific detection parameters. The testing campaign was based on Li-NMC pouch cells (500 mAh capacity) produced within the HIDDEN project framework^[2].

Table 1. Overview of techniques and detection parameters.

| Characterization technique | Measurement protocol | Detection parameters |
|--|-------------------------------|---|
| Incremental Capacity (IC) | Full charge or Full discharge | 1) Peak position; 2) Peak intensity |
| Coulombic Efficiency (CE) | Full cycle | 1) CE value |
| Electrochemical Impedance Spectroscopy (EIS) | EIS | 1) Z_{arch} ; 2) Z_{max} ; 3) Z_{min} |
| Mid-Voltage | Full charge | 1) M-V |
| Cycle Time | Full cycle | 1) C-T |

Methodology

The developed methodology includes four steps, as shown in Figure 1:

- *Cell testing*: a specific testing protocol has been developed including (i) cell formation; (ii) diagnosis phases with capacity and EIS measurements and (iii) cycling phases with six different testing conditions (varying C-rate and Depth of Discharge (DoD)).
- *Detection parameter identification*: the parameters based on the techniques applied during cells' diagnosis listed in Table 1 and have been analysed with respect to capacity fade.
- *Thresholds setting*: specific values have been defined to trigger a self-healing action looking to the percentage increase of a given parameter.
- *Validation*: process to verify whether the warning signal resulting from exceeding a specific parameter threshold truly represents a condition preceding LMB degradation. It is based on two State of Health (SoH) checks: (i) SoH range, i.e., the cell must be in a given interval at trigger activation (e.g., 70%-90% as in Figure 2a) and (ii) SoH variation, i.e., the trigger activation should anticipate the SoH curve inflection point ("knee").



Figure 1. Schematic representation of developed methodology.

[1] P. Iurilli, L. Luppi, C. Brivio, Non-Invasive Detection of Lithium-Metal Battery Degradation. Energies 2022, 15, 6904.

Results and discussion

Three batches of LMBs have been tested with different protocol focus: different C-rates and 100% DoD, fixed C-rate and different DoD ranges. An example of detection results is given in Figure 2a, where triggering is highlighted in yellow: IC-based detection parameter anticipated the activation when the SoH was still higher than 90%. The impedance-based indicators trigger correctly in two cases out of three (Z_{max} and Z_{arch}), but too late in case of Z_{min} . Finally, both mid-voltage and cycle time parameters are activated in time respecting the validation criterium on the SoH. A sensitivity analysis was performed to compute the success rate of each detection technique. On average, the detection techniques successfully detected degradation in 60% of the cases and can be used to anticipate LMB failures and to lay the basis for self-healing mechanism activation.

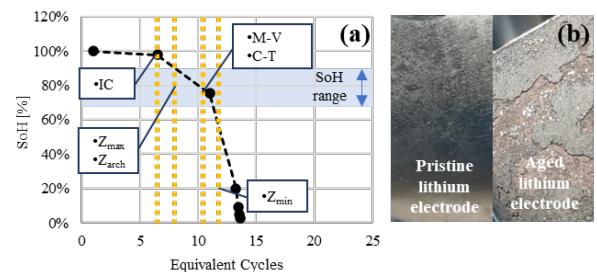


Figure 2: a) Detection results with triggering highlighted in yellow for cell ID29 cycled at C/20; 50% DoD. b) Post-mortem analyses.

Remarks and outlook

The results of this work can be analyzed at different levels:

- *Validity*: during the experimental phase, it was not possible to discriminate dendrite growth from dead lithium, the fast accumulation of Lithium, which was confirmed by post-mortem analysis (Figure 2b). All the tested cells reached their EoL due to cycling failure and not for short-circuit failure.
- *Replicability*: the obtained success rates depend on the experimental campaign performed due to the limited number of tested samples and to specificities of the tested cells (Li||NMC). The developed methodology can be replicated to other LMB, but different performance results should be expected.
- *Applicability*: the tested detection techniques can be implemented in embedded systems to sense degradation and trigger actions such as, for instance, self-healing methods, which is one of the possible routes to make LMB exploitable in real applications. Some techniques are easier than others, but in general all the non-invasive techniques proposed can be implemented in BMSs.

[2] The HIDDEN project is funded by European Union's Horizon 2020 research under Grant Agreement No. 957202.

Assessment of Hydrogen and Electric Buses for Public Transport in Switzerland

N. Koch, A. Hutter

As part of the Energy Strategy 2050, the Federal Council aims to replace diesel buses with alternative CO₂-neutral propulsion technologies. Commissioned by the Federal Office of Transport (FOT), CSEM conducted the study P-199 to assess the use of hydrogen technologies and battery electric buses for Swiss public transport. The study compared the performances of these buses for four different typical lines in the Fribourg public transport (TPF) network. The full report is available on the FOT website [1].

In Switzerland, about 6,000 public transport buses run on diesel fuel nationwide which represent an energy consumption of about 1.28 TWh/year. As part of the "Energy Strategy 2050 for Public Transport" program, the FOT has initiated a study to examine the potential of hydrogen in public transport and its performance compared to battery electric solutions [1]. The long-term objective being to bring to zero the CO₂ emission of public transportation.

Evaluated lines

To produce representative results, the assessment has been performed on 4 TPF lines using measurements acquired on buses in operation. The GPS traces are depicted in Figure 1.



Figure 1: GPS traces of evaluated TPF lines.

Lines 5 and 201 are urban lines with an average speed around 25 km/h, 3 stop (e.g., bus station, traffic light) per kilometer and a daily milage of 250 km. Lines 234 and 260 are rural lines with a higher average around 40 km/h, 1 stop per kilometer and a daily milage of 400 km. The average slope of the road is around 1% for lines 201 and 234 and up to 2% for lines 5 and 260.

Evaluated bus technologies

Using diesel bus (DB) as a baseline, hydrogen internal combustion engine bus (HICEB), fuel cell electric bus (FCEB) and battery electric bus (BEB) have been assessed. In HICEB, the energy released by the combustion of hydrogen mechanically drives the vehicle, while FCEB and BEB use electricity to supply their electric engine. The electricity is converted from hydrogen with a fuel cell in the case of the FCEB or straight from a battery for the BEB. The main characteristics of the different buses is presented in Table 1.

Table 1: Main characteristics of the different buses (*urban / rural lines).

| Parameter | Unit | DB | HICEB | FCEB | BEB |
|--------------|------|----------|----------|------|------|
| η_{t2w} | % | 33 / 40* | 36 / 43* | 44 | 73 |
| η_{w2t} | % | 0 | 0 | 73 | 73 |
| Weight | t | 12.6 | 12.6 | 14.6 | 14.4 |

The tank-to-wheel efficiency η_{t2w} , i.e., the proportion of energy that is effectively transferred to the wheel, is over 40% at full load for both the HICEB and the FCEB, taking into account all transmission losses. While an FCEB can exploit this efficiency over most of the engine speed range, the efficiency of a HICEB decreases at low speeds, which explains its lower average

efficiency. In contrast, a BEB achieves an efficiency of over 70%. The ability of electric engine buses (FCEB and BEB) to recover energy during braking is also considered with a similar efficiency (denominated η_{w2t} in the table).

Energy consumption

For every bus technology and line, the daily energy consumption is computed. The results obtained are presented in Table 2. These figures must be compared to the storage capacity of the different technologies. Figures depicted in *italic* show consumptions exceeding a typical storage capacity, while figures in **bold** exceed the max. capacity available in the market.

Table 2: Daily energy consumption.

| Line | DB [l] (kWh) | HICEB [kgH2] (kWh) | FCEB [kgH2] (kWh) | BEB [kWh] |
|------|-----------------|-----------------------|----------------------|--------------|
| 5 | 102 (990) | 27 (981) | 22 (726) | 499 |
| 201 | 97 (942) | 26 (858) | 21 (693) | 462 |
| 234 | 116 (1126) | 31 (1023) | 28 (924) | 596 |
| 260 | 112 (1088) | 30 (990) | 29 (957) | 663 |

Although hydrogen buses manage to compete with DB, BEB are reaching and exceeding the limits of storage capacity. The maximum vehicle weight being regulated, further increasing the battery capacity would result in a decrease of payload. Therefore, a BEB is not able to replace a DB as is (i.e., without adapting its operating schedule) while a hydrogen bus could. Even with the improvement of the batteries, it is unlikely that BEB will compete with the mileage of DB soon.

Conclusion and challenges

Although promising, the use of hydrogen in mobility applications suffer from several years of delay in terms of technology development and readiness compared to BEB. Indeed, BEB benefit from the growing electric passenger car market. This aspect is reflected in the acquisition cost of the FCEB which is currently around 40% higher than BEB. Moreover, the lower efficiency of FCEB and the currently high cost of hydrogen results in a higher overall energy consumption and a higher operating cost.

There is no one-size-fit-all solution. The selection must be carefully made according to the requirements of the lines. To ease this task, the evaluation procedure put in place by CSEM, which relies on recorded line data, can be made available to interested parties to help them decide whether a hydrogen or a battery electric bus is better suited for their network.

[1] <https://www.bav.admin.ch/bav/en/home/general-topics/research-and-innovation/research-and-innovation-programmes/energie-2050/project-results.html> - P-199.

ANNEXES

Publications

- [1] Annaheim, Simon; Braun, Fabian; Bernhard, Leah; Pfammatter, Amarim; Proen  a, Martin; Bonnier, Guillaume; Ferrario, Damien; Lemay, Mathieu; Rossi, Ren   M., "Proof-of-Concept Study for Reflectance Pulse Oximetry Using Optical-Fibre-Based Sensors", Current Directions in Biomedical Engineering, vol. 8, no. 2, 2022, pp. 121-124, doi:10.1515/cdbme-2022-1032

[2] Andreatta, Ga  lle Anne L  onie; Hendricks, Nicholas; Grivel, Aur  lie; Billod, Mathieu, "Grafted-to polymeric layers for highly adhesive electroless metal coatings on ultra-smooth 3D printed surfaces", ACS Appl. Electron. Mater. 2022, 4, 4, 1864-1874, 24 March 2022, doi:10.1021/acsaelm.2c00090

[3] Antognini, L.; Sthioul, C.; Dr  on, J.; Paratte, V.; T  rkay, D.; Senaud, L. -L.; Boccard, M., "Integration of thin n-type nc-si:H layers in the window-multilayer stack of heterojunction solar cells", Solar Energy Materials and Solar Cells, 248, December 2022, doi:10.1016/j.solmat.2022.111975

[4] Antonucci, Alessandra; Reggente, Melania; Roullier, Charlotte; Gillen, Alice J.; Schuergers, Nils; Zubkovs, Vitalijs; Lambert, Benjamin P.; Mouhib, Mohammed; Carata, Elisabetta; Dini, Luciana; Boghossian, Ardemis A., "Carbon nanotube uptake in cyanobacteria for near-infrared imaging and enhanced bioelectricity generation in living photovoltaics", Nature Nanotechnology, 17, 1111-1119 (2022), doi:10.1038/s41565-022-01198-x

[5] Blagojevic, Marjan; Dieudonn  , Anca; Kamecki, Louis; Kiziroglou, Michail; Krastev, Krassimir; Marty, David; Piguet, Damien; Spasic, Sasa; Wright, Steven; Yeatman, Eric, "Autonomous Electrical Current Monitoring System for Aircraft", IEEE Transactions on Aerospace and Electronic Systems, 2022, doi:10.1109/TAES.2022.3225253

[6] Buchwalder, S  bastien; Borzi, Aurelio; Diaz Leon, Juan J; Bourgeois, Florian; Nicolier, Cl  o; Nicolay, Sylvain; Neels, Antonia; Zywitzki, Olaf; Hogg, Andreas; Burger, Juergen, "Thermal Analysis of Parylene Thin Films for Barrier Layer Applications", Polymers 2022, 14, 3677, doi:202210.3390/polym14173677

[7] Caillat, Mary; Degott, Jean; Wuerzner, Arlene; Proen  a, Martin; Bonnier, Guillaume; Knebel, Jean-Fran  ois; Stoll, Chlo  ; Christen, Urvan; Durgnat, Virginie; Hofmann, Gregory; Burnier, Michel; Wuerzner, Gr  goire; Schoettker, Patrick, "Accuracy of blood pressure measurement across BMI categories using the OptiBPTM mobile application", Blood Pressure, vol. 31 (1), pp. 288-296, 2002, doi:10.1080/08037051.2022.2132214

[8] Cattin, J.; Petri, D.; Geissbuhler, J.; Despeisse, M.; Ballif, C.; Boccard, M., "Transferability of the light-soaking benefits on silicon heterojunction cells to module", IEEE Journal of Photovoltaics, 12(3), 662-668, December 2022, doi:10.1109/JPHOTOV.2021.3113861

[9] Ch  telat, Olivier; Rapin, Micha  l; Bonnal, Benjamin; Fivaz, Andr  ; Wacker, Josias; Sporrer, Benjamin, "Remotely Powered Two-Wire Cooperative Sensors for Biopotential Imaging Wearables", Sensors, vol. 22 (21), pp. 8219, 2002, doi:10.3390/s22218219

[10] Chin, Sanghoon; Denis, S  verine; Kundermann, Stefan; Brasch, Victor; Lecomte, Steve, "Digital OPLL-based distributed Brillouin sensing system in optical fibers", Optics Express, vol. 30, issue 11, pp. 18090-18097 (2022), 23 May 2022, doi:10.1364/OE.454067

[11] Degiorgis, Yan; Proen  a, Martin; Ghamri, Yassine; Hofmann, Gregory; Lemay, Mathieu; Schoettker, Patrick, "Photoplethysmography-Based Blood Pressure Monitoring Could Improve Patient Outcome during Anesthesia Induction", Journal of Personalized Medicine, vol. 12 (10), pp. 1571, 2002, doi:10.3390/jpm12101571

[12] Fairbrother, A.; Gnocchi, L.; Ballif, C.; Virtuani, A., "Corrosion testing of solar cells: Wear-out degradation behavior", Solar Energy Materials and Solar Cells, 248, December 2022, doi:10.1016/j.solmat.2022.111974

[13] Fairbrother, A.; Quest, H.;   zkalay, E.; W  chl, P.; Friesen, G.; Ballif, C.; Virtuani, A., "Long-term performance and shade detection in building integrated photovoltaic systems", Solar RRL, 6(5), October 2022, doi:10.1002/solr.202100583

[14] Frerichs, In  z; Adler, Andy; Zhanqi, Zhao; Haris, Kostas; Petmezias, Georgis; Cheimariotis, Aris; Lekka, Irini; Maglaveras, Nicos; Strodtthoff, Claas; Vogt, Barbara; Lasarow, Livia; Weiler, Norbert; Braun, Fabian; Proen  a, Martin; Rapin, Micha  l; Wacker, Josias; Lemay, Mathieu; Pessoa, Diego, "Respiratory Image Analysis", R. Paiva, P. de Carvalho, V. Kilintzis (Eds.), Wearable Sensing and Intelligent Data Analysis for Respiratory Management, Amsterdam (NE), Elsevier, May 2002

[15] Gay, Julien; Lachowicz, Agata; Blondiaux, Nicolas; Andreatta, Ga  lle Anne L  onie, "Selective Copper Electroplating on Patterned Self-Assembled Monolayers for Photovoltaic Applications", ACS Appl. Nano Mater. 2022, 5, 10, 15954-15961, doi:10.1021/acsanm.2c04291

- [16] Haug, F. -J.; Libraro, S.; Lehmann, M.; Morisset, A.; Ingenito, A.; Ballif, C., "Impact of rapid thermal processing on bulk and surface recombination mechanisms in FZ silicon with fired passivating contacts", *Solar Energy Materials and Solar Cells*, 238, May 2022, doi:10.1016/j.solmat.2022.111647
- [17] Heub, Sarah; Navaee, Fatemeh; Migliozi, Daniel; Ledroit, Diane; Boder-Pasche, Stéphanie; Goldowsky, Jonas; Vuille-dit-Bille, Emilie; Hofer, Joëlle; Gaiser, Carine; Revol, Vincent; Suter-Dick, Laura; Weder, Gilles, "Coplanar embedding of multiple 3D cell models in hydrogel towards high-throughput micro-histology", *Scientific Reports*, volume 12, Article number: 9991 (2022), doi:10.1038/s41598-022-13987-4
- [18] Hofmann, Gregory; Proença, Martin; Degott, Jean; Bonnier, Guillaume; Lemkaddem, Alia; Lemay, Mathieu; Schorer, Raoul; Christen, Urvan; Knebel, Jean-François; Schoettker, Patrick, "A novel smartphone app for blood pressure measurement: a proof-of-concept study against an arterial catheter", *Journal of Clinical Monitoring and Computing*, 37 (1), pp. 249-259, 2022, doi:10.1007/s10877-022-00886-2
- [19] Iurilli, P.; Brivio, C.; R. E. Carrillo, R. E.; Wood, V., "EIS2MOD: A DRT-based modelling framework for Li-ion cells," *IEEE Trans. on Ind. Applicat.*, vol. 58, no. 2, pp. 1429–1439, March 2022, doi:10.1109/TIA.2021.3134946
- [20] Iurilli, P.; Brivio, C.; R. E. Carrillo, R. E.; Wood, V., "Physics-Based SoH Estimation for Li-Ion Cells," *Batteries*, vol. 8, no. 11, Art. no. 11, November 2022, doi:10.3390/batteries8110204
- [21] Iurilli, P.; Brivio, C.; Wood, V., "Detection of Lithium-Ion Cells' Degradation through Deconvolution of Electrochemical Impedance Spectroscopy with Distribution of Relaxation Time," *Energy Technology*, vol. 10: 2200547, August 2022, doi:10.1002/ente.202200547
- [22] Iurilli, P.; L. Luppi, L.; Brivio, C., "Non-Invasive Detection of Lithium-Metal Battery Degradation," *Energies* 2022, 15(19), 6904, doi:10.3390/en15196904
- [23] Jacobs, D. A.; Wolff, C. M.; Chin, X. -Y.; Artuk, K.; Ballif, C.; Jeangros, Q., "Lateral ion migration accelerates degradation in halide perovskite devices", *Energy and Environmental Science*, 12, December 2022, doi:10.1039/d2ee02330j
- [24] Jafari, Safiye; Burr, Loïc; Migliorelli, Davide; Galve, Roger; Marco, M.-Pilar; Campbell, Katrina; Elliott, Chris; Suman, Michele; Sturla, Shana J.; Generelli, Silvia, "Smartphone-based magneto-immunosensor on carbon black modified screen-printed electrodes for point-of-need detection of aflatoxin B1 in cereals", *Analytica Chimica Acta*, Volume 1221, 15 August 2022, 340118, doi:10.1016/j.aca.2022.340118
- [25] Jokic, Petar; Azarkhish, Erfan; Bonetti, Andrea; Pons, Marc; Emery, Stephane; Benini, Luca, "A Construction Kit for Efficient Low Power Neural Network Accelerator Designs", *ACM Transactions on Embedded Computing Systems*, Volume 21, Issue 5, September 2022, Article No.: 56, pp 1–36, doi:10.1145/3520127
- [26] Kurth, Felix; Zinggeler, Marc; Schär, Sandra, "Printed Antifouling Electrodes for Biosensing Applications", *ACS Appl. Mater. Interfaces* 2022, 14, 51, 56578–56584, 13 December 2022, doi:10.1021/acsami.2c17557
- [27] Lehmann, M.; Desthieux, A.; Valle, N.; Morisset, A.; Wyss, P.; Eswara, S.; Haug, F. -J, "Bulk defects and hydrogenation kinetics in crystalline silicon solar cells with fired passivating contacts", *IEEE Journal of Photovoltaics*, 12(3), 711-721, April 2022, doi:10.1109/JPHOTOV.2022.3161871
- [28] Lütfolf, Fabian; Friebel, Florence; Kuznetsov, Ivan; Rudin, Benjamin; Emaury, Florian; Gallinet, Benjamin; Ferrini, Rolando; Basset, Guillaume; Resan, Bojan, "Wafer-scale replicated gratings for compressing ultrafast laser pulses at telecom wavelengths", *Optics Continuum*, 1(5), 1051-1059, 15 May 2022, doi:10.1364/OPTCON.456059
- [29] Marozau, Ivan; Unterhofer, Samuel; Berry, Martin; Aubry, Guillaume; Gonin, Pascal; Enquebecq, Richard; Dadras, Massoud; Sereda, Olha, "Reliability assessment of miniaturised electromechanical RF relays for space applications", *Microelectronics Reliability*, Vol 138, 114753, November 2022, doi:10.1016/j.microrel.2022.114753
- [30] Meyer, F.; Ingenito, A.; Diaz Leon, J. J.; Niquelle, X.; Allebé, C.; Nicolay, S.; Ballif, C., "Localisation of front side passivating contacts for direct metallisation of high-efficiency c-si solar cells", *Solar Energy Materials and Solar Cells*, 235, Januray 2022, doi:10.1016/j.solmat.2021.111455
- [31] Morisset, A.; Famprakis, T.; Haug, F.-J.; Ingenito, A.; Ballif, C.; Bannenberg, L. J., "In situ reflectometry and diffraction investigation of the multiscale structure of p-type polysilicon passivating contacts for c-si solar cells", *ACS Applied Materials and Interfaces*, 14(14), 16413-16423, March 2022, doi:10.1021/acsami.2c01225
- [32] Moroney, Niall; Del Bino, Leonardo; Zhang, Shuangyou; Woodley, Michael T. M.; Hill, Lewis; Wildi, Thibault; Wittwer, Valentin J.; Südmeyer, Thomas; Oppo, Gian-Luca; Vanner, Michael R.; Brasch, Victor; Herr, Tobias; Del'Haye, Pascal, "A Kerr polarization controller", *Nature Communications*, vol. 13 (1), pp. 398, 19 January 2022, doi:10.1038/s41467-021-27933-x

- [33] Moroney, Niall; Del Bino, Leonardo; Zhang, Shuangyou; Woodley, Michael T. M.; Hill, Lewis; Wildi, Thibault; Wittwer, Valentin J.; Südmeyer, Thomas; Oppo, Gian-Luca; Vanner, Michael R.; Brasch, Victor; Herr, Tobias; Del'Haye, Pascal, "A Kerr polarization controller", *Nature Communications*, vol. 13 (1), pp. 398, 2002, doi:10.1038/s41467-021-27933-x
- [34] Narduzzi, Simon; Favre, Dorvan; Nuria, Pazos; Dunbar, L. Andrea, "Deploying a Convolutional Neural Network on Edge MCU and Neuromorphic Hardware Platforms", Chapter 10, pp. 129-140, in *Industrial Artificial Intelligence Technologies and Applications* by River Publishers Series in Communications and Networking, June 2022, doi:10.13052/rp-9788770227902
- [35] Narduzzi, Simon; Mateu, Loreto; Jokic, Petar; Azarkhish, Erfan; Dunbar, L. Andrea, "Benchmarking Neuromorphic Computing for Inference", Chapter 1, pp. 1-20, in *Industrial Artificial Intelligence Technologies and Applications* by River Publishers Series in Communications and Networking, June 2022, doi:10.13052/rp-9788770227902
- [36] Secerovic, Amra; Ristaniemi, Aapo; Cui, Shangbin; Li, Zhen; Soubrier, Astrid; Alini, Mauro; Ferguson, Stephen J; Weder, Gilles; Heub, Sarah; Ledroit, Diane; Grad, Sibylle, "Toward the Next Generation of Spine Bioreactors: Validation of an Ex Vivo Intervertebral Disc Organ Model and Customized Specimen Holder for Multiaxial Loading", *ACS Biomater. Sci. Eng.* 2022, 8, 9, 3969–3976, August 2022, doi:10.1021/acsbiomaterials.2c00330
- [37] Senaud, L. -L.; Christmann, G.; Antognini, L.; Descoeuilles, A.; Geissbuhler, J.; Boccard, M.; Paviet-Salomon, B., "Bottom-up and top-down approaches for identifying and mitigating electrical losses in silicon heterojunction solar cells", *IEEE Journal of Photovoltaics*, 12(4), 906-914, July 2022, doi:10.1109/JPHOTOV.2022.3176983
- [38] Y. Sepehri, P. Pad, C. Kündig, P. Frossard, L. A. Dunbar, "Privacy-Preserving Image Acquisition for Neural Vision Systems," in *IEEE Transactions on Multimedia*, 2022, doi:10.1109/TMM.2022.3207018
- [39] Sideris, I., Crivelli, F. & Bambach, M., "GPyro: uncertainty-aware temperature predictions for additive manufacturing", *J Intell Manuf* (2022), 22 September 2022, doi:10.1007/s10845-022-02019-7
- [40] Tuomiranta, A.; Alet, P.-J.; Ballif, C.; Ghedira, H., "Calibration of ground surface albedo models", *Solar Energy*, 237, 239-252, May 2022, doi:10.1016/j.solener.2022.03.047
- [41] Tuomiranta, Arttu; Alet, Pierre-Jean; Ballif, Christophe; Ghedira, Hosni, "Calibration of ground surface albedo models", *Solar Energy*, Volume 237, Pages 239-252, 1 May 2022, doi:10.1016/j.solener.2022.03.047
- [42] Vischer, Annina S.; Rosania, Jana; Socrates, Thenral; Blaschke, Christina; Eckstein, Jens; Proust, Yara-Maria; Bonnier, Guillaume; Proen  a, Martin; Lemay, Mathieu; Burkard, Thilo, "Comparability of a Blood-Pressure-Monitoring Smartphone Application with Conventional Measurements—A Pilot Study", *Diagnostics*, vol. 12 (3), pp. 749, 13 February 2022, doi:10.3390/diagnostics12030749
- [43] Vuille-dit-Bille, Emilie; Deshmukh, Dhananjay V.; Connolly, Sinead; Heub, Sarah; Boder-Pasche, St  phanie; Dual, J  rg; Tibbitt, Mark. W.; Weder, Gilles, "Tools for manipulation and positioning of microtissues", *Lab Chip*, 2022, Advance Article, October 2022, doi:10.1039/D2LC00559J
- [44] Wacker, Josias; Bonnal, Benjamin; Braun, Fabian; Ch  telat, Olivier; Ferrario, Damien; Lemay, Mathieu; Rapin, Micha  l; Renevey, Philippe; Yilmaz, G  rkan, "Sensor technologies for mobile and wearable applications in mobile respiratory management", R. Paiva, P. de Carvalho, V. Klintzis (Eds.), *Wearable Sensing and Intelligent Data Analysis for Respiratory Management*, Amsterdam (NE), Elsevier, May 2002
- [45] Zubkovs, Vitalijs; Wang, Hanxuan; Schuergers, Nils; Weninger, Astrid; Glieder, Anton; Cattaneo, Stefano; Boghossian, Ardemis A., "Bioengineering a glucose oxidase nanosensor for near-infrared continuous glucose monitoring", *Nanoscale Advances*, 2022, 4 May 2022, doi:10.1039/d2na00092j

Proceedings

- [1] Antognini, L.; Senaud, L. -L.; Turkay, D.; Marthey, L.; Dr  on, J.; Paviet-Salomon, B.; Ballif, C., "Contact resistivity measurements and their applicability for accurate series resistance breakdown in heterojunction solar cell", Paper presented at the AIP Conference Proceedings 2487, August 2022, doi:10.1063/5.0090643
- [2] Askins, S.; Dominguez, C.; Nardin, G.; Ackermann, M.; Petri, D.; Despeisse, M.; Ant  n, I., "HIPERION: Scale-up of hybrid planar micro-tracking solar panels for rooftop compatible CPV", Paper presented at the AIP Conference Proceedings 2550, September 2022, doi:10.1063/5.0101843

- [3] Braun, Fabian; Bonnier, Guillaume; Rapin, Michaël; Yilmaz, Gürkan; Proust, Yara-Maria; Schneider, Sophie; Radan, Anda-Petronela; Strahm, Karin Maya; Surbek, Daniel; Lemay, Mathieu; Delgado-Gonzalo, Ricard, "Evaluation of a Wearable System for Fetal ECG Monitoring Using Cooperative Sensors", EMBC 2022, Glasgow, Scotland (UK), 11 July 2022, doi:10.1109/EMBC48229.2022.9871458
- [4] Chin, Sanghoon; Denis, Séverine; Jérôme, Van Zaen; Muntané, Enric; Amir, Khodabakhsh; Frans, Harren; Patrick, Bowen; Stephan, Schroder; Steve, Lecomte; Laurent, Balet, "Digital electronics platform-based supercontinuum light detection for mid-infrared trace gas sensing", CLEO: Applications and Technology 2022, 15 May 2022, paper AW4L.3, doi:10.1364/CLEO_AT.2022.AW4L.3
- [5] Chin, Sanghoon; Mitev, Valentin; Giraud, Eliane; Maulini, Richard; Hempel, Frank; Lang, Norbert; Wiese, Mathias; Zimmermann, Henrik; Boiko, Dmitri L., "Demonstration of mid-IR gas sensing with frequency-swept Fabry-Perot cavity quantum cascade laser", European Semiconductor Laser Workshop 2022 (ESLW 2022), Neuchâtel (Switzerland), 16 September 2022
- [6] Chin, Sanghoon; Mitev, Valentin; Giraud, Eliane; Maulini, Richard; Hempel, Frank; Lang, Norbert; Wiese, Mathias; Zimmermann, Henrik; Boiko, Dmitri L., "Utilization of a frequency-swept Fabry-Perot cavity quantum cascade laser for an innovative mid-IR spectrometer", CLEO 2022, San Jose, California (USA), 7 May 2022, paper AW4M.2, doi:10.1364/CLEO_AT.2022.AW4M.2
- [7] Diaz Leon, J. J.; Libraro, S.; Ingenito, A.; Alleb  , C.; H  bner, S.; Dippell, T.; Paviet-Salomon, B., "Sputtered polySi(n) passivating contacts compatible with direct metallization", Paper presented at the AIP Conference Proceedings 2709, November 2022, doi:10.1063/5.0126213
- [8] Jeanningros, Lo  c; Braun, Fabian; Van Zaen, J  r  me; Le Bloa, Mathieu; Porretta, Alessandra; Herrera, Claudia; Teres, Cheryl; Domenichini, Giulia; Carroz, Patrice; Graf, Denis; Pascale, Patrizio; Vesin, Jean-Marc; Thiran, Jean-Philippe; Pruvot, Etienne; Lemay, Mathieu, "Improving Photoplethysmography-Based Multiclass Cardiac Arrhythmia Detection via Pulse Wave Analysis", BMT 2022, Innsbruck (Austria), pp. 226, 30 September 2022, doi:10.1515/bmt-2022-2001
- [9] Jeanningros, Lo  c; Braun, Fabian; Zaen, J  r  me Van; Le Bloa, Mathieu; Porretta, Alessandra; Teres, Cheryl; Herrera, Claudia; Domenichini, Giulia; Carroz, Patrice; Graf, Denis; Pascale, Patrizio; Vesin, Jean-Marc; Thiran, Jean-Philippe; Pruvot, Etienne; Lemay, Mathieu, "Pulse Wave Analysis of Photoplethysmography Signals to Enhance Classification of Cardiac Arrhythmias", CinC 2022, Tampere (Finland), September 2022
- [10] Kiener, Lionel; Saudan, Herv  ; Cosandier, Florent; Perruchoud, G  rald; Pejchal, Vaclav; Rouvinet, Julien; Boudoire, Florent; Kalentics, Nikola, "Validation of compliant mechanisms made by metallic Additive Manufacturing", Advances in Optical and Mechanical Technologies for Telescopes and Instrumentation V, R. Geyl, R. Navarro (Eds.), Montr  al (Canada), pp. 30, 29 August 2022, doi:10.1117/12.2629199
- [11] Mitev, Valentin; Torcheboeuf, Nicolas; Krakowski, Michel; Resneau, Patrick; Larrue, Alexandre; Legoe, Pierre; Robert, Yannick; Vinet, Eric; Garcia, Michel; Parillaud, Olivier; Gerard, Bruno; Boiko, Dmitri L., "First Demonstration of Two-Photon Excitation Fluorescence Lifetime Measurements with Ultra-Short Pulse-on-Demand Light Emitter Utilizing Multiple Wide Quantum Wells", European Semiconductor Laser Workshop 2022 (ESLW 2022), Neuchâtel (Switzerland), 16 September 2022
- [12] Narduzzi, Simon; Bigdeli, Siavash. A; Liu, Shih-Chii; Dunbar, L. Andrea, "Optimizing the Consumption of Spiking Neural Networks with Activity Regularization", Proceedings of IEEE International Conference on Acoustics, Speech and Signal Processing (ICASSP), Singapore, May 2022, doi:10.1109/ICASSP43922.2022.9746375
- [13] Narduzzi, Simon; T  retken, Engin; Thiran, Jean-Philippe; Dunbar, L. Andrea, "Adaptation of MobileNetV2 for Face Detection on Ultra-Low Power Platform", IEEE Swiss Conference on Data Science (SDS) 2022, Lucerne, Switzerland. pp 1-6, June 2022, doi:10.1109/SDS54800.2022.00008
- [14] Paoletti, Samantha; Cattaneo, Stefano; Lecomte, Steve; Verjus, Christophe; Lemay, Mathieu; Volker, Andreas; Weder, Gilles; Revol, Vincent, "Advanced digital technologies in life sciences: Photonics and beyond", 2022, Zenodo, doi:10.5281/zenodo.7431821
- [15] Sainz Martinez, Cristina; Bach Cuadra, Meritxell; Jorge, Jo  o, "BigBrainMR: Development and in vivo validation of a multimodal digital phantom for Magnetic Resonance Imaging methods at 100 µm", BMT 2022, Innsbruck (Austria), pp. 381, 28 September 2022, doi:10.1515/bmt-2022-2001

- [16] Sainz Martinez, Cristina; Bach Cuadra, Meritxell; Jorge, João, "Framework and Validation of BigBrain-MR: A Novel Digital Phantom at 100µm Resolution for Ultrahigh Field MRI Methods Development", 13th Annual Scientific Symposium. Ultrahigh Field Magnetic Resonance: Clinical Needs, Research Promises and Technical Solutions, Berlin (Germany), pp. 66-70, 9 September 2022
- [17] Sainz Martinez, Cristina; Jorge, João; Bach Cuadra, Meritxell, "Development and in-vivo validation of BigBrain-MR: a multimodal computational phantom at 100µm", OHBM Annual Meeting, Glasgow, Scotland (UK), 20 June 2022
- [18] Saudan, Hervé; Kiener, Lionel; Novo, David; Cosandier, Florent; Perruchoud, Gérald; Lani, Sébastien; Hendricks, Nicholas; Boudoire, Florent; Schaffter, Virginien; Manoli, Chrysoula; Noël, Jérôme; Petagna, Paolo; Miler, Mickaël; Bilbeau, Damien; Henry, Mélanie, "Design & additive manufacturing of systems involving directly printed electrical wires and sensors", Proc. SPIE 12180, Space Telescopes and Instrumentation 2022: Optical, Infrared, and Millimeter Wave, 121805U (29 August 2022), doi:10.1117/12.2627775
- [19] Torcheboeuf, Nicolas; Mitev, Valentin; Balet, Laurent; Renevey, Philippe; Krakowski, Michel; Resneau, Patrick; Larrue, Alexandre; Legoe, Jean-Pierre; Robert, Yannick; Vinet, Eric; Garcia, Michel; Parillaud, Olivier; Gerard, Bruno; Boiko, Dmitri L., "Ultra-short pulse non-classical light emitters utilizing multiple wide quantum wells", CLEO 2022, San Jose, California (USA), 7 May 2022
- [20] Türetken, Engin; Saeedi, Sareh; Bigdeli, Siavash; Stadelmann, Patrick; Cantale, Nicolas; Lutnyk, Luis; Raubal, Martin; Dunbar, L. Andrea, "Real Time Eye Gaze Tracking for Human Machine Interaction in the Cockpit", Proc. SPIE 12019, AI and Optical Data Sciences III, 1201904, 2 March 2022, doi:10.1117/12.2607434
- [21] Yilmaz, Gurkan; Braun, Fabian; Adler, Andy; de Sousa, Antonio Moreira; Ferrario, Damien; Lemay, Mathieu; Chetelat, Olivier, "Split electrodes for electrical-conductivity-based tissue discrimination", EMBC 2022, Glasgow, Scotland (UK), 11 July 2022, doi:10.1109/EMBC48229.2022.9871552
- [22] Zanella, Frédéric; Schneider, Christian; Ceric, Luka; Basset, Guillaume, "Increasing the quantum efficiencies of advanced photonic imagers with microlens arrays", Precision Photonic Systems 22, Dornbirn, Austria, 13 December 2022, doi:10.5281/zenodo.7432809

Conferences and Workshops

- Balet, Laurent; Regamey, Yves-Julien; Ruffieux, David; Grassani, Davide; Boiko, Dmitri L.; Droz, Fabien; Lecomte, Steve, "Some of the Quantum Optics activities at CSEM", INMAQS 2022, Glasgow, Scotland (UK), 14 September 2022
- Boder-Pasche, Stéphanie, "Standardized and automated organoid workflows: from production to end-point analysis", Standardized and automated organoid workflows: from production to end-point analysis, 24 August 2022
- Boder-Pasche, Stéphanie, "Standardized Tools for Organoid on Plate", Biointerfaces International Zurich 2022, September 2022
- Boder-Pasche, Stéphanie; Sirugue, Pascaline; Heub, Sarah; Atakan, H. Baris; Goldowsky, Jonas; Ischer, Réal; Ledroit, Diane; Navaee, Fatemeh; Valentini, Thomas M.; Weder, Gilles, "Perfusion platform for bioengineered tissues", EUROoCS, 2022, Grenoble, July 2022
- Eichenberger, Martin; Basset, Guillaume, "Lightsafe: An interactive Security Technology for Banknotes and ID Documents", Optical and Digital Document Security 2022, Vienna (AT), 12 April 2022
- Fejzo, Aldo; Stergiou, Ioannis; Georg, Oravez; Markocic, Miha; Stefano, Cattaneo, "Point of Care measurement tools for biomonitoring", Kongress Graubünden forscht 2022, 21 September 2022

- Heinzelmann, Harry, "The Role of CSEM in Realising the Twin Green and Digital Transitions", Keynote at the EARTO Annual Conference 2022, Barcelona, Spain, 18 May 2022
- Karlen, Sylvain, "Hot vapor optical clock for chip-scale and high-performance space applications", 8th International Colloquium on Scientific and Fundamental Aspects of GNSS, Sofia (Bulgaria), 16 September 2022
- Kastanis, Iason, "There is something in the air", TechOutlook 2022, 28 March 2022
- Krähenbühl, Roger; Renggli, Martina; Mohrdiek, Stefan; Basset, Guillaume; Bundalo, Ivan-Lazar; Ghadimi, Amir, "Wafer-scale in-plane micro-optical interconnects for fiber arrays", ESTC 2022 Proceedings; ID027, 13 September 2022
- Luongo, Francesca; Netsch, Christoph; Valentin, Thomas; Goldowsky, Jonas; Kirschmann, Moritz; Van De Ville, Dimitri, "Improving the Classification of an unbalanced Spheroid", Personalized Health Technologies NEXUS ETH conference 2022 poster presentation, 7 June 2022
- Luongo, Francesca; Ntavelis, Evangelos; Kastanis, Iason; Schmid, Philipp A. E., "DeepFake for Life Sciences", PDA conference 2022 poster presentation, 16 May 2022

- Ntavelis, Evangelos; Shahbazi, Mohamad; Luongo, Francesca; Kastanis, Iason; Timofte, Radu; Danelljan, Martin; Van Gool, Luc, "Image Synthesis Applications", Ntavelis et al., Image Synthesis Applications, DataDays 2022, Zurich, 12 May 2022
- Offermans, Ton, "Phabulous – Fabrication technologies for free-form optics", EPIC TechWatch at ECOC, 21 September 2022
- Rouvinet, Julien; Cosandier, Florent, "Tripod Mechanism based on Flexible Joints produced by LPBF Additive Manufacturing", 1st International Conference on Advanced Manufacturing, (online only), 3 July 2022
- Ruffieux, David, "Timekeeping for efficient IoT radio scheduling", IEEE Symposium on VLSI Technology and Circuits conference, Honolulu, USA, 16 June 2022
- Russi, Mario, "Data Generation for Deep Learning", 7. F&E-Konferenz zu Industrie 4.0, Industrie 2025, 25 January 2022
- Russi, Mario, "Predictive Maintenance – Predictive Quality: Was alles in Anlagedaten steckt!", CSEM Next Alpnach, 5 December 2022
- Schmid, Philipp A. E., "AIWizard – Simplifying the evaluation and interpretation of Differential Scanning Calorimetry curves", CSEM Business Day, 3 November 2022
- Schmid, Philipp A. E., "Deep Learning für die Industrie: Oder – Wie kommen Fledermäuse in die Produktion?", AiCon 2022, Pfäffikon, 8 June 2022
- Schmid, Philipp A. E., "Deep Learning für die Industrie: Qualitätskontrolle, Prozessoptimierung und Predictive Maintenance", swissT.net Sektion 46 «Vision Systems», 15 June 2022
- Schmid, Philipp A. E., "Deepfake für die Industrie", Swiss Automation (Rapperswil), 23 August 2022
- Schmid, Philipp A. E., "Deepfake in the lab", Future Labs Live, Basel, 7 June 2022
- Schmid, Philipp A. E., "Deepfake und Fledermäuse in der Produktion", 9. Swiss Mechatronics Day (Zürich), 30 June 2022
- Schmid, Philipp A. E., "Gemtelligence – 100 Jahre Erfahrung in einer Software", 7. F&E-Konferenz zu Industrie 4.0, Industrie 2025, 25 January 2022
- Schmid, Philipp A. E., "Herausforderungen von Heute sind die Chancen von Morgen", 11. IHRUS-Fachtagung (Instandhaltung Rad und Schiene), 10 November 2022
- Schmid, Philipp A. E., "Ignite the spark of photonics application with the power of AI", Artificial Intelligence (AI) and Photonics: is it the golden goose? (Brugg AG), 4 July 2022
- Schmid, Philipp A. E., "KI und Experte - Friends or Foes?", Zuger Innovationstag 2022, 21 September 2022
- Schmid, Philipp A. E., "Ohne Sensoren keine Daten", SwissT.net Sektion 10 - Sensoren, 24 November 2022
- Schmid, Philipp A. E., "Predictive Quality", smart maintenance insights, 2 June 2022
- Schmid, Philipp A. E., "Process Innovation - AI for Industry", Takeda Global Manufacturing, 16 November 2022
- Schmid, Philipp A. E., "Robotics for advanced in vitro organ degeneration models for musculoskeletal research", 2022 PDA Robotics and Automation Conference, 16 May 2022
- Schmid, Philipp A. E., "Von Daten zum Nutzen", SDS2022 Pre-Conference - Smart Data zum Anfassen: Lösungen für die produzierende Industrie, 22 June 2022
- Schmid, Philipp A. E., "Von Qualitätskontrolle zu Predictive Maintenance – AI revolutioniert die Industrie", SGO-Leiterplattenseminar Uitikon (ZH), 29 September 2022
- Schmid, Philipp A. E.; Müller, Felix G.; Esteves, Emmanuel Esteves; Caspar, von Stülpnagel; Maddah, Suzy; Richerdt, Nicolas, "Without artificial intelligence, no digital transformation | Sans l'intelligence artificielle, pas de transformation digitale", BE 4.0 Industry 4.0 trade show hosted by Basel Area, 30 November 2022
- Schmid, Philipp A. E., "Data Driven Innovation - from Predictive Maintenance to Predictive Quality", AI+X Summit 2022, 14 October 2022
- Vorobyov, Alexander; Beyer, Christian; Nussbaum, Pascal; Schmid, David, "Chipless biodegradable tags, theoretical performance estimation", UkrMW-2022, 14 November 2022
- Vorobyov, Alexander; Unterhofer, Samuel; Sereda, Olha, "A new efficient production method of mm-wave components used in EFVS", 3AFTSAS, 14 September 2022
- Vorobyov, Oleksandr; Unterhofer, Samuel; Sereda, Olha, "A Cost-effective Production Method for High-precision MM-wave Waveguide Antennas and Components", UkrMW-2022, 14 November 2022
- Vuille-dit-Bille, Emilie; Bayat, Dara; Dubois, Marc-Alexandre; Overstolz, Thomas; Heub, Sarah; Sakar, Selman; Despont, Michel; Weder, Gilles, "Piezoelectric micromachined ultrasound transducers (PMUTs) for acoustic positioning of suspended microtissues", The Chemical and Biological Microsystems Society, Acoustofluidics 2022 Conference, Glasgow, United Kingdom, 118, 18 October 2022
- Wacker, Josias, "Electrodes in multi-sensor wearables", Electrodes for wearables - Introducing the sensors & the technology behind it, (online only), 12 January 2022
- Weder, Gilles, "Symposium on 3D Printing for Life Sciences", Tools for organoid-based biofabrication, 29 June 2022
- Zubkovs, Vitalijs; Leeners, Keno J.; Cattaneo, Stefano, "Handheld SWIR optical reader for monitoring carbon nanotube-based optical sensors", Biomedical Photonics Network, Book of Abstracts, Poster 15, 6 December 2022

Research Projects

| | |
|---|---|
| Botnar Research Center for Child Health (BRC) | COVENT – Improve ventilation safety by means of intra-tracheal pressure monitoring; a short-term and a long-term solution |
| Botnar Research Center for Child Health (BRC) | DAVINCI – Development and validation of a laminar flow test to detect COVID-19 immunity in saliva |
| Eurostars | AIRSWIM – Airborne instrument (LiDAR) for reliable shallow water imaging |
| Eurostars | COLIDE – Coherent lidar demonstration based on a novel swept laser engine in the beyond 2 µm wavelength range |
| Eurostars | DARE – Development of AI-supported remote patient monitoring solution |
| Eurostars | EXRIL – Frequency stabilized laser with compact low-cost fiber ferrule based optical reference |
| Eurostars | FITSILVER – Fitness and calorie tracking for the silver generation |
| Eurostars | IAP-CMM – Development and clinically test of a novel multimodal sensor system (hardware and algorithms) to continuously monitor in a noninvasive and straightforward way the intra-abdominal pressure (IAP) of intensive care patients (ICPs) |
| Eurostars | IMPULSE – Closed-loop control of blood pressure for people with spinal cord injury |
| Eurostars | LEVES – Mid-infrared system utilizing level-crossing chirp-spectroscopy in quantum cascade lasers |
| Eurostars | LONGLIGHT – Long lifetime 1.5 um modelocked lasers via improved gain glasses |
| Eurostars | POINT – Pulse oximetry garment for sleep apnea |
| Eurostars | SAFEUVC – Field-emission 210 nm light source for disinfection |
| Eurostars | SCREENBEAT – Screening and monitoring of cardiac arrhythmias and sleep apnea |
| Eurostars | SONATA – Multiple sclerosis patient management based on behavioural monitoring combined with AI transparency |
| Hans-Eggenberger-Stiftung | MAXIHE – Rack-mounted microresonator-based optical frequency comb for massively-parallel optical computing |
| Interreg | BECOM – Système de dépôt de multicouches minces et homogènes sur PCB et bio-capteurs |
| Interreg | METEOR – Revêtements fonctionnels hautes performances pour composants horlogers, diagnostics et pour l'instrumentation médicale |
| Interreg | NEODIAM – Développement de nouveaux outils de dépôt de diamant |
| Other | SMART-SOM – Pilot and demonstration of advanced silicon HJT cells and modules manufacturing |
| Other | STV4VDN – Smart thermostatic valve-based heating control for Neuchatel school building |
| SNI – Nanoargovia | META-DISPLAYS – Design and fabrication of metasurfaces for rollable displays |
| SNI – Nanoargovia | PEPS – Development of a printed electrochemical protein sensor |
| SNSF | AMORF – 3D printing of ductile amorphous metals |
| SNSF | CPAP-OBPM – Continuous remote monitoring in obstructive sleep apnea syndrome: effect of CPAP on blood pressure |
| SNSF | HEALTHYBABY – Monitoring the health of a fetus during labor using an AI |
| SNSF | NOBEL – Reinforcement learning for building controls |
| SNSF | PHASE_LOGIC – Phase logic networks for optimized computation |
| SNSF | AMELIZ – Advanced metallization strategies for heterojunction solar cells |

| | |
|---------------------------------------|---|
| SNSF | BLUVES – Development of nanophotonics based structures to generate blue and UV frequency comb for the calibration of spectrographs used in exoplanet search |
| SNSF | ENHEART – Exploring full content of optical signals to enhance cardiac arrhythmia screening |
| SNSF | PAPET – Protective, passivating & selective transport layers in perovskite/c-Si tandem solar cells |
| SNSF | SHAMAN – Shadow mask localization of thin films for back-contacted crystalline silicon solar cells & energy harvesters |
| SNSF / Ambizione | PUZZLE – Bridging gaps in the neuroimaging puzzle: advanced techniques for comprehensive mapping of brain anatomy and multi-scale network activity |
| SNSF / BRIDGE | CHIP-SEQ – Automated end-to-end microfluidic system for chromatin immunoprecipitation followed by sequencing |
| SNSF / BRIDGE | EMIL – Emotion in the loop, a step towards a comprehensive closed-loop deep brain stimulation in Parkinson's disease |
| SNSF / BRIDGE | ENABLE – Standardized integrated photonic nonlinear building blocks for lithium niobate on insulator |
| SNSF / BRIDGE | MAXIBRIDGE – Development of a microresonator-based optical frequency comb source |
| SNSF / BRIDGE | SUPERBATT – Polymeric superionic conductor enabled flexible high-energy-density battery |
| SNSF / BRIDGE | VIPS – Ultra-low power visual perception system |
| SNSF / BRIDGE | AOP-PLUGNPLAY – Implementation of adverse outcome pathway in a “plug & play” microfluidics system. Liver fibrosis as a proof of principle |
| SNSF / BRIDGE Discovery | FEMTOCHIP – Energy efficient optical frequency combs based on photonic integrated resonators and temporally structured pump light |
| SNSF / BRIDGE Discovery | GREENSPACK – Green smart packaging for perishable goods |
| SNSF / BRIDGE Discovery | LINIOS – Gas spectrometer based on lithium niobate on insulator photonics integrated circuit |
| SNSF / BRIDGE Discovery | OPOSSUM – Ultra-sensitive photonics accelerometers for next generation seismic sensor networks |
| SNSF / BRIDGE Discovery | SMARTROBOT – Towards intelligent sensor-enhanced robotic neurosurgery |
| SNSF / BRIDGE proof-of-concept | MB-SPOCK – Design, optimisation and manufacturing of the magnetic bearing and motor parts for a reaction wheel with low-level of exported vibrations |
| SNSF / COST | PEDALO – Positive energy district algorithms for load forecasting and optimal dispatch |
| SNSF / ERA-NET | TESLA – Transient electronics for sustainable digital agriculture |
| SNSF / ERA-NET | UTP4Q – A versatile quantum photonic IC platform through micro-transfer printing |
| SNSF / Sinergia | BIOREACT – In vitro organ degeneration models for musculo-skeletal research |
| Swiss Federal Office of Energy (SFOE) | ASSURED-PV – Assessing uncertainties and risks in photovoltaic plant performance and operation |
| Swiss Federal Office of Energy (SFOE) | COMET – Developement of copper metallization processes for current p-type and future n-type solar cells and modules |
| Swiss Federal Office of Energy (SFOE) | DELAPS – Demonstration of large-area passivating contact sputtering for high-efficiency solar cells |
| Swiss Federal Office of Energy (SFOE) | GIF – Greenhouse infrared filters |
| Swiss Federal Office of Energy (SFOE) | HALBION – Half bifacial back-contacted silicon heterojunction solar cells |

| | |
|---------------------------------------|--|
| Swiss Federal Office of Energy (SFOE) | HYSTIMATOR – Automated online hysteresis estimation for improved state estimation for LFP batteries |
| Swiss Federal Office of Energy (SFOE) | IEA-TASK13-2022 – Performance, operation & reliability of photovoltaic systems |
| Swiss Federal Office of Energy (SFOE) | IPRECISE – Industrial passivating contacts approaches for high efficiency c-Si Solar cells |
| Swiss Federal Office of Energy (SFOE) | LANTERN – Living labs interface for the energy transition |
| Swiss Federal Office of Energy (SFOE) | OPEN-SESAME – Modelling of energy storages for simulation/optimization of energy systems – open-source energy storage models |
| Swiss Federal Office of Energy (SFOE) | OPERA – Utilisation optimale de l'énergie renouvelable avec PAC pour les immeubles collectifs en rénovation |
| Swiss Federal Office of Energy (SFOE) | SIRIUS – Swiss pilot line for aesthetic and ultimate power PV modules |
| Swiss Federal Office of Energy (SFOE) | SOLARBODY-OFEN – Integration of photovoltaic element for automotive applications |
| Swiss Federal Office of Energy (SFOE) | SPET – High performance versatile components for electrification of future solar-powered aeronautical power train |

Innosuisse – Swiss Innovation Agency

| | | |
|------------------|----------------------|---|
| 59105.1 INNO-EE | ABAPOPS | AI-based analytics for performance optimisation of a portfolio of rooftop PV systems |
| 47005.1 IP-ICT | ADAPTIVESTORM | An ultra-energy-efficient AI chip for next-gen ICT applications |
| 52948.1 IP-EE | ADASTRA | A different approach for silicon-based tandem solar cells using perovskite on back-contacted devices with three-terminal wiring to go beyond 30% power conversion efficiency. |
| 48036.1 IP-ICT | ADRIOUS-LIDAR | Real-time autonomous navigation system for on-orbit servicing |
| 56367.1 IP-ICT | AIRO-PRINT | Adaptive system for automatic identification and marking of complex parts |
| 57735.1 INNO-ICT | AIRQUALITYDATA-STUDY | Data analytics for room cleaning detection and classification. |
| 49735.1 IP-LS | AIRVIMO | Airborne virus monitoring |
| 33572.1 IP-ENG | AMC | Process optimization for additive membrane care |
| 51090.1 IP-ENG | ASPIRE | Next generation SiC power electronics for e-mobility |
| 55307.1 IP-EE | ATLAS | Development of new generation agrivoltaic translucent module architecture based on silicon |
| 60399.1 INNO-LS | BREATH-BAG | Off-line collector for molecular breath analysis improving personalized medicine |
| 59372.1 INNO-EE | C7EM | Feasibility study of organic coatings based on cyclic carbonets on catode materials for Li-ion batteries |
| 61124.1 INNO-ENG | CAFE | Evaluation of Senbiosys compact and low-power CMOS photonic sensor for photoplethysmography |
| 43533.1 IP-ENG | CERANO | Development of barrier coatings onto anodized aluminium part for watch and medtech applications |

| | | |
|---------------------|-----------------------|---|
| 35221.1 IP-LS | CEREBRO | ASIC-enabled depth electrodes for neural recording and ablation |
| 44317.1 IP-EE | CHAMELEON | Development of advanced interconnection, solar cells, stringing, as well as colouring technologies and data analytics for mass production in 3S SolarPlus manufacturing line. |
| 57757.1 IP-ENG | CHAMLED | High-power femtosecond laser based chamfering system with free shape, sharp edge of TFT embedded substrates for mass production micro-LED display, next generation display. |
| FLAGSHIP PFFS-21-20 | CIRCUBAT | Swiss circular economy model for automotive lithium batteries |
| 50902.1 INNO-ENG | CM4QC-STUDY | Condition monitoring for quality control |
| 62228.1 IP-EE | COLORPOWER | New generation colored encapsulant foil solution for the manufacturing of next generationof colored photovoltaic modules for building integration, with focus on manufacturing costs, performance, aesthetics and reliability |
| 42657.1 IP-ICT | COSIMA | Cooperative sensors for electrographic imaging |
| 37705.1 IP-ENG | DALIE | Dry auto-localizing integrated electrodes |
| 61587.1 INNO-ENG | DEEP-FORREST | AI for area/volume calculation of wood piles using deeplearning based vision algorithms captured with a smartphone |
| 41190.1 IP-ICT | DEEPPROFILE | Aluminiumprofile in allen möglichen Dimensionen und Stückzahlen komplett digital mit Smartphone katalogisiert und identifiziert in der Pulverbeschichtungsproduktion |
| 60926.1 INNO-ENG | DEF-TAGGANT-READER-IS | New security taggant – reader device combination for security applications |
| 51719.1 IP-ENG | DENTIN | Adaptive endodontic instrument made of shape memory alloy |
| 56201.1 INNO-EE | DICHRO | Dichroic mirror optimization |
| 57765.1 IP-EE | DIGERATI | Dynamic graph machine learning for high resolution forecasting |
| 46776.1 IP-ICT | DRIVERCHECK2 | Intelligent vision system for driver monitoring coupled with steering command control system for improved road safety |
| 58209.1 INNO-EE | EASI-FC | Estimateurs pour accélérer l'adoption de solutions numériques dans le froid commercial |
| 51474.1 IP-ICT | E-BRAIN | Smart robust wireless control and management of heavy machines |
| 61130.1 INNO-ENG | EQUALITY | Fully automated quality control for europalets with 2D/3D Vision, robotics, and deep learning with data generation |
| 34950-1 | ERGO | Ultra-low power image sensor for IoT applications |
| 40657.1 IP-ENG | ESORTER | Vollautomatisches Sortieren von Sendungen bis 30kg stellt nach wie vor eine grosse Herausforderung dar. |
| 103.713 IP-LS | EXTRACE | Enabling single cell resolution analysis of cancer cells extracted from blood |
| 62984.1 INNO-EE | FALAFEL | Prototyping of new stack for translucent lightweight PV modules for AgriPV |
| 51355.1 IP-ENG | FATIGUE | Fabrication and testing of a silicon carbide pressure sensor for high temperatures. |
| 58359.1 INNO-LS | FEP-INT | Integration of an FEP membrane into a microfluidic chip for light-sheet microscopy |

| | | |
|------------------------------------|------------------|--|
| 43210.1 IP-ICT | FETA | Flexible low-power embedded time series signal accelerator |
| 44490.1 IP-ENG | FOCUS | Fibre-optic ultra-sensitive seismometer based on MEMS |
| 100.509 IP-ICT | FORKLIFT | Industry 4.0 – Teleoperations in a dynamic industrial environment |
| 101.441 IP-EE | FREESTILE | Development of new generation of photovoltaic tiles demonstrating cost effective manufacturing and high reliability |
| 41844.1 IP-ICT | GEMTELLIGENCE | Entwicklung von Software zur automatisierten Edelsteinanalyse |
| 55358.1 IP-ENG | HERACLES | Development of the next generation of wearables for athletes, that analyze biomarkers in the sweat during their workouts to provide insight into his/her metabolic activities during sport activities. |
| 43410.1 IP-ENG | HIHOLO | High-quality volume diffraction gratings for digital holography microscopy for enhanced resolution, acceptance angle, and field of view |
| 61312.1 IP-LS | HYGIE | Detection of respiratory infections in indoor spaces. |
| 41363.1 IP-LS | IMPLANT | Development of innovative customer-tailored composite multilayers in orthopedic- and trauma surgery |
| 53788.1 IP-ENG - Impulse CorePlate | IMPULSECOREPLATE | Development of a multiwell plate system for accurate 2D and 3D cell-based assays making use of groundbreaking, unique solutions that allow significant market opportunities to be seized. |
| 64456.1 INNO-LS | INSIGHT | Smart satellite roller screws technology |
| 58669.1 IP-LS | INSPIRING | Development of a device for in-mouth lactate monitoring for sports applications |
| 56816.1 IP-LS | LARVAESORTER | Development of a novel device capable of handling zebrafish larvae for high throughput |
| 52368.1 IP-ICT | LCAT | Smart asset tracking is key for operational efficiency and minimization of capital expenses. |
| 32970.1 IP-ENG | LEADME | Drug screening technology platform based on micro-LED and high-resolution MEA |
| 62814.1 IP-EE | LEARN-CEM | Self-learning energy manager |
| 43059.1 IP-ENG | LIFELUB | Development and implementation of a new lubrication technology |
| 64456.1 INNO-LS | LIRI | Liebert infection index (detect early respiratory infection risks in indoor spaces) |
| 51734.1 INNO-LS | LOPLUS | Machine learning powered light obscuration technology for improved robustness and particle classification |
| 50031.1 IP-ENG | LUPINE | High-resolution position sensor for space application |
| 61801.1 IP-ENG | M-CUBE | Development of a high-resolution magnetic field gradiometer. |
| 60238.1 INNO-ENG | MAGNAMI | Demonstration of an integrated NV-based magnetometer using the existing macQsiMAC prototype |
| 101.321.1 IP-ENG | MARIE | Automatized and electro mechanized syringe for animal health |
| 62573.1 INNO-ENG | MEMAJPRINT | Deposition of ion selective membranes (ISM) onto ion sensitive field effect transistors (ISFET) that are already industrially produced at Microsens |
| 64230.1 INNO-LS | METTLE | Mental stress evaluation with smartphone. |

| | | |
|------------------|------------------|--|
| 64456.1 INNO-LS | MITOPREP-STUDY | Concept study toward the automation of CellVie filtration process. |
| 60960.1 INNO-ENG | MOLTAL | Molten metal level sensor |
| 55022.1 IP-ICT | NAVIVIB | High-resolution space grade position navigation and timing GPS/GALILEO spaceborne receiver |
| 55896.1 INNO-ENG | NEODI | Industrialisation of boron-doped diamond electrode allowing sterilization of tape water for hand washing |
| 52886.1 IP-LS | NEON | Neonate monitoring – Add SpO2, BP and oHRM features to OxyPRem NIRS medical system |
| 55424.1 IP-LS | NEOS | The NeurOphthalmoscope – Early diagnosis of brain diseases |
| 61069.1 INNO-ENG | NICE | Nonlinear interferometer for f _{CEO} detection of 1550 nm Menhir Photonics lasers |
| 63681.1 INNO-LS | NIMP | Non-invasive microneedle patch for glucose monitoring |
| 56034.1 IP-LS | NIOXIS | Nitric oxide optical sensors for inflammation monitoring |
| 60518.1 INNO-LS | NOVOBIO | Injection-moulding of novel bioreactor for cell therapy manufacturing |
| 63050.1 INNO-EE | OPAL | Optimized PV panels for dichroic LCPV systems |
| 57515.1 IP-LS | ORGANEYEZER | High-throughput sorting of large and small organoids powered by deep learning for drug discovery, tissue engineering, and disease modeling |
| 58793.1 INNO-ENG | ORIL | Escapement with free impulse |
| 60042.1 IP-LS | ORTHO | Closing the gap in digital orthopedics |
| 64278.1 INNO-ENG | PANDA | Industrial level packaging of PICs light sources for datacom applications |
| 34473.1 IP-ENG | PANORAMA | Development of the new materials by multi-charge ion-implantation process |
| 61071.1 IP-LS | PERFORM | Biomimetic 3D tumor microenvironment on-chip for preclinical testing of cancer immunotherapies |
| 35477.1 IP-LS | PETE | Preeclampsia test at the point of care |
| 60157.1 INNO-EE | PIN7 | Evaluation of lightweight pv modules for agrivoltaics |
| 56325.1 INNO-ENG | PM4PREFEED-STUDY | Studie für Predictive Maintenance für Preform Feeder und andere Komponenten auf Infotech Maschinen |
| 56298.1 INNO-EE | POLLUTIONKEEPER | Water quality monitoring with multispectral imaging |
| 44145.1 IP-ICT | PROXIMITY | Capture system concept validation for in-orbit debris removal demonstration |
| 44098.1 IP-EE | PULSE | Polychromatic universal LED light source and IV extraction for novel solar cell architectures |
| 45216.1 IP-EE | PVBLIND | Photovoltaics technology on smart solar blind |
| 44587.1 IP-ENG | PYRAMID | High aspect ratio 3D pyramidal probes on CMOS MEA's for in vitro tissue model study |
| 60116.1 INNO-ENG | RAINBOW | Development of new types of surface structures on steel for decoration applications |

| | | |
|------------------|-------------------|---|
| 56972.1 IP-ENG | REACT | Development and implementation of a full pipeline for process optimization (offline, refinement & online) for generating gear grinding machines. |
| 40504.1 IP-ENG | REDULAS | Development of advanced femtosecond laser based ultra-precision manufacturing system for smart micro-LED display |
| 58612.1 INNO-ENG | RETONE | Feasibility study of a novel miniature optical microphone for next generation smart speakers |
| 101.798 IP-ENG | SANPRO | Predictive maintenance for wood sanding machines |
| 50339.1 IP-ENG | SAPHIR | Semi-transparent solar cells on watch saphir |
| 102.006 IP-EE | SELMA | Development of Li metal composite anodes for Li metal batteries |
| 61772.1 INNO-EE | SIPS | Smart illumination positioning system: feasibility study on automated position detection of lamp modules used for adaptive illumination of in-door plants |
| 57886.1 IP-ICT | SMARTLADLEGATE | Additive, real-time monitoring system to increase safety and efficiency for steel casting |
| 100.583 IP-ICT | SMARTRAIL | Maintenance, asset management and health indicator of rolling stock materials. |
| 43816.1 IP-ENG | SMARTSPRING | Intelligent spring that reduces machine downtime, prevents failures, and helps to design the optimum spring |
| 53212.1 IP-ICT | SMARTWASTE | Plug & play smart waste management |
| 35056.1 IP-ENG | SOMBRERO | Automatisierung der Auswertung thermoanalytischer Messkurven |
| 58504.1 IP-ENG | SPADLENS | Reliable development and characterization of SPAD sensors enhanced with thin and gap-less microlenses |
| 53012.1 IP-ICT | SPG-ROBOT | Development of a tool to automate floor processing tasks |
| 60055.1 INNO-LS | SPLAT | Depth measurement of bone laser-cuts. |
| 55059.1 IP-ENG | SUMIT | Development of a smart toilet add-on for urine monitoring with exchangeable printed biosensors |
| 50561.1 IP-LS | TESTMATE | A rapid self-test for sexually transmitted diseases that provides results in minutes, supported by digital health |
| 43052.1 IP-ENG | TURBOPREDICTIONS | Steigerung der Effizienz, der Verfügbarkeit und der Lebensdauer von Turbokompressoren aufgrund einer erweiterten Datenerhebung und -Analytik |
| 56068.1 INNO-LS | URINE-BAG-SENSORS | Technical concept for the development of a next generation urine biomarker measurement module |
| 46999.1 IP-ICT | VIVALDI | Quality control and high-accuracy tracking system for steel mills |
| 48014.1 IP-ENG | WATMON | Drinking water quality early indicator, base on refractive index change |

European Commission Projects

| | | |
|-------------------------------|------------|---|
| H2020 – CS2-CFP10 2019 | 3DGUIDE | Feasibility demonstration of 3D printing for a new efficient production method of mm-wave waveGUIDE antenna |
| H2020 - ATTRACT | AHEAD | Advanced heat exchange device |
| H2020 – INFRAINNOV-2019- 2020 | AIDAINNOVA | Advancement and innovation for detectors at accelerators |

| | | |
|-----------------------------------|---------------|---|
| H2020 – ECSEL | ANDANTE | AI for new devices and technologies at the edge |
| H2020 – ECSEL | APPLAUSE | Advanced optics, photonics and electronics packaging for multimodal sensing systems |
| H2020 – CS2 CFP08-2018 | AUDACITY | Compact powerful and reliable piezoelectric actuator for landing gear systems |
| H2020 – LC-SC3-RES-6 2018 | BE-SMART | Innovative building envelope for sustainable, modular, aesthetic, reliable and efficient construction |
| H2020 – FETOPEN | CFLOW | Coherent ultra-fast long wave infrared communications |
| H2020 – ECSEL 2019-1-IA | CHARM | Challenging environments tolerant smart systems for IoT and AI |
| HORIZON – CL4 2021 | CLUSTEC | Scalable continuous variable cluster state quantum technologies |
| H2020 – LC-SC3-EE-2019 | DOMOS | Operating system for smart services in buildings |
| HORIZON - EIC-2021 | ECLIPSE | ECL-based Infectious pathogen (bio)sensor |
| H2020 ICT-2020 | ELENA | European electro-optic and nonlinear PIC platform based on lithium niobate. |
| H2020 – NMBP-23-2020 | EMAPS-CARDIO | Electro-mechano-active polymer-based scaffolds for heart-on-chip |
| H2020 – ECSEL-2020-1-IA | Energy ECS | Smart and secure energy solutions for future mobility. |
| HORIZON – CL4 2022 | EROSS IOD | European robotic orbital support services in-orbit demonstration |
| H2020 – FETPROACT-2020 | EXPERIENCE | The “extended-personal reality”: augmented recording and transmission of virtual senses through artificial-intelligence |
| H2020 – ECSEL | Fit4Health | Cooperative sensors for health and sport monitoring |
| HORIZON – CL4 2021 | FLASH-COMP | Flawless and sustainable production of composite parts through a human centred digital approach |
| HORIZON – CL5 2021 | GENEX | New end-to-end digital framework for optimized manufacturing and maintenance of next generation aircraft composite structures |
| H2020 – SPACE 2018 | HEATPACK | New generation of high thermal efficiency components packages for space |
| H2020 – SC1-2019-Single-Stage-RTD | HEDIMED | Linking immune-mediated diseases to early exposures for innovative solutions |
| H2020 – MSCA-ITN-2019 | HIDDEN | Hunting invisibles: dark sectors, dark matter, and neutrinos |
| H2020 – LC-SC3-RES-15 2019 | HIGHLITE | High-performance low-cost modules with excellent environmental profiles for a competitive EU PV manufacturing industry |
| H2020 – LC-SC3-RES-15 2019 | HIPERION | Hybrid photovoltaics for efficiency record using integrated optical technology |
| H2020 – EEB 2017 | HYBUILD | Innovative compact hybrid electrical/thermal storage systems for low energy buildings |
| HORIZON – HLTH-2021 | INCHILDHEALTH | Identifying determinants for indoor air quality and their health impact in environments for children: measures to improve indoor air quality and reduce disease burdens |
| HORIZON CL4 2021 | LOLLIPOP | Lithium niobate empowered silicon nitride platform for fragmentation free operation in the visible and the NIR |
| H2020 – FETFLAG-2018-2020 | MACQSIMAL | Miniature hot atomic vapor cells-based quantum devices for sensing and metrology applications |

| | | |
|-----------------------------------|----------------|--|
| H2020 – NMBP-FOF-2018 | MANUELA | Additive manufacturing using metal pilot line |
| H2020 – ICT-2019-2 | MEDPHAB | Photonics solutions at pilot scale for accelerated medical device development |
| H2020 – ICT 2017 | MOLOKO | Multiplex photonic sensor for plasmonic-based detection of contaminants in milk |
| H2020 – ECSEL 2019-1-IA | MOORE4MEDICAL | Accelerate innovation in emerging medical devices with open technology platforms. |
| HORIZON - MSCA-2021 | Nano-ImmunoEra | Nanotechnology-enabled detection of clinically relevant antibodies for early cancer diagnosis and immunotherapy monitoring |
| H2020 – BG-2020-1 | NAUTILOS | New approach to underwater technologies for innovative, low-cost ocean observation |
| H2020 – LC-SC3 | NEON | Next-generation integrated energy services for citizen energy communities |
| H2020 – ECSEL | NEWLIFE | Devices and systems for baby and pregnant women monitoring |
| H2020 – SFS 2018 | NUTRISHIELD | Fact-based personalized nutrition for the young |
| H2020 – EIC-FTI-2018-2020 | OFFSHOREMUSTER | An integrated emergency response decision support system for enhancing workers' safety in offshore oil & gas operations |
| H2020 – NMBP-FOF 2018 | OLEDSOLAR | Innovative manufacturing processes and in-line monitoring techniques for the OLED and thin film and organic photovoltaic industries (CIGS and OPV) |
| H2020 – SC1-2019 Single-Stage-RTD | ORGANTRANS | Controlled organoids transplantation as enabler for regenerative medicine translation |
| HORIZON – CL4-2021 | PATTERN | Next generation ultra-high-speed microwave photonic integrated circuits using advance hybrid integration |
| HORIZON – CL5-2021 | PEPPERONI | Pilot line for European production of perovskite-silicon tandem modules on industrial scale |
| H2020 – NMBP-TR-IND-2019 | PEROCUBE | High-performance large area organic perovskite devices for lighting, energy, and pervasive communications |
| H2020 – ICT-2019-2 | PHABULOUS | Pilot-line providing highly advanced & robust manufacturing technology for optical free-form micro-structures |
| H2020 – FETFLAG 2018 | PHOG | Sub-poissonian photon gun by coherent diffusive photonics |
| H2020 – DT-2020-1 | PHOTONHUB | One-stop-shop open access to photonics innovation support for a Digital Europe |
| H2020 – EIC-FTI-2018-2020 | PHOTONSENS | A plug-and-play photonics-based biosensing platform for salmon pathogen detection |
| HORIZON – CL5-2021 | PILATUS | Digitalised pilot lines for silicon heterojunction tunnel interdigitated back contact solar cells and modules |
| H2020 – FETOPEN-2018-2019-2020-4 | RADIAL | Radiation source of light for picosecond laser pulse applications |
| H2020 – MSCA-RISE | RDC2MT | Research, demonstration, and commercialization of DC microgrid technologies |
| H2020 – LC-SC3-RES-4 2018 | RE-COGNITION | Renewable cogeneration and storage technologies integration for energy autonomous buildings |

| | | |
|-----------------------------------|-------------|--|
| HORIZON – CL4-2021 | RESILEX | Resilient enhancement for the silicon industry leveraging the European matrix. |
| H2020 – ICT 2018-2 | SARMENTI | Smart multisensor embedded and secure system for soil nutrient and gaseous emission monitoring |
| H2020 – SC1-2019 Single-Stage-RTD | SBR | Smart bone regeneration |
| HORIZON – CL5 2022 | SEAMLESS-PV | Development of advanced manufacturing equipment and processes aimed at the seamless integration of multifunctional PV solutions, enabling the deployment of IPV sectors |
| H2020 – SPACE 2018-2020 | SELECTOR | Surface mount technology (SMT) compatible electromechanical relay for compact redundancy ring |
| HORIZON – CL5 2021 | SIC4GRID | Next generation modular SiC-based advanced power electronics converters for enhanced renewables integration on the grid |
| H2020 – CS2-CFP10-2019-01 | SMARTWISE | Smart miniaturized and energy autonomous regional aircraft wireless sensor |
| HORIZON CL5 2021 | SOLID | Sustainable manufacturing and optimized materials and interfaces for lithium metal batteries with digital quality control. |
| H2020 – LC-BAT-2020-3 | SPARTACUS | Spatially resolved acoustic, mechanical, and ultrasonic sensing for smart batteries |
| HORIZON – CL4 2021 | SPRINTER | Low-cost and energy-efficient hybrid photonic integrated circuits for fiber-optic, free-space optical and mm-wave communication systems supporting time critical networking in industrial environments |
| H2020 – ECSEL | STORAGE | Embedded storage elements on next MCU generation ready for AI on the edge |
| H2020 – SPACE-2019 | SURPRISE | Super-resolved compressive instrument in the visible and medium infrared for earth observation applications |
| H2020 – CS2-CFP10 2019-01 | SWISSMODICS | Development of a sensor with wide spectrum sensitivity for monitoring of damage and defects in composite structures |
| H2020 – ICT-2020-2 | TRIAGE | Development of a smart, compact, and cost-effective optical air quality sensor network for the hyperspectral detection of all relevant atmospheric pollution gases |
| HORIZON – CL5 2021 | TRIUMPH | Triple junction solar modules based on perovskites and silicon for high performance, low-cost and small environmental footprint |
| H2020 – INFRAIA-2020-1 | VIPERLAB | Fully connected virtual and physical perovskite photovoltaics lab |
| H2020 – ICT 2018-2 | WELMO | Wearable electronics for effective lung monitoring |
| H2020 – ICT 2019-2 | ZEROAMP | Nanomechanical switch-based logic and non-volatile memory for robust ultra-low power circuits |

Space Projects

ESA Projects

| | |
|------------|---|
| A-CSAC | Advanced concept for chip-scale atomic clocks |
| AMICA | Flexure pivot for SPICA SAFARI in AM |
| ANGELE | Motion transformation compliant mechanism based on additive manufacturing |
| ANTICIPATE | 4D printing to construct a flexural pivot demonstrator for space applications |

| | |
|-----------------|--|
| ATOM | Manufacturing of the complex feature demonstrator for space application made of meta matrix composite (MMC) having the specific modulus > 30 GPa·cm ³ /g. |
| BIDTS | Benchmarking of integrated digitalisation technologies for application to new space projects and future ESA missions |
| CCM-MTG | Development and manufacture of corner cube mechanisms for MTG satellite |
| COLA | Exploitation of the potential of laser sheets and fast detectors to detect and identify the trajectory of particles in the mm-cm range in-situ |
| COMO | Coronavirus remote monitoring of outpatients with heart rate, breathing rate and skin temperature |
| COOLER | Compact opening louver |
| CRUSSADER | Capture system for servicing and debris removal. |
| DIVERSE | L-PBF process development, material design, characterization, and qualification |
| EDUROLE | Electrodynamic dust removal and cleaning of optical surfaces in lunar environments |
| ELISAMET | Laser metrology for the LISA mission |
| EUSO-B2 | Elegant breadboard lidar for extrem universe space observation – Phase B2 |
| EXPOSITION | Integrated flex pivot position sensor |
| FIFREDO | Fibered frequency doubler at 1560 nm |
| GC-CONNECT | Development of fluidic connections and packaging for gas chromatography chips |
| GERANIUM | Generative artificial intelligence for high performing inversion models |
| HELLENISE | Highly accelerated life test pilot supporting agile space engineering. |
| IMPROVE | Microvibration simulation and analysis tools |
| ISABELA | Development of a fine steering mirror breadboard |
| ISOL | Development of a high performance microvibration isolation system |
| LIDISOR2 | Development of an experimental optical ranging payload for future Galileo satellites |
| LINES | Lidar for infrastructure, natural risks, and environmental survey: space technology transfer programifac |
| LINGO | Flexible hinge design and analysis for the LISA optical assembly tracking mechanism development with OHB. |
| LPC | Low-power cathodes: development of field emitting cathodes arrays for space neutralisers |
| MACADAM | Magnetically levitated pump for space applications: requirements definition and commercial evaluation |
| MARBLE | Smart, reliable and cost-effective manufacturing, and fatigue verification of mission-critical structural items |
| MCC-X | Development of a miniaturized motor controller for space exploration |
| MDP-CHEF | Cost effective hermetically sealed chip fuses |
| OBSIDIAN | On-board system identification for uncertainty modelling & characterization |
| OSIP-VIB | Adaptive regulation for micro-vibration active-passive isolation systems |
| OSRC | Digital stabilisation electronics for lasers |
| PHOTAC-DERISK | Future atomic clock derisk |
| POWERSAIL | Disruptive PV power array technology to enable economic viability of SPS |
| R-MTS | Development and fabrication of robust miniature timing source (R-mTS) engineering models (EMs). These R-mTS EMs are double-resonance miniature atomic clocks. |
| RUBIK | Feasibility for urine Raman/SERS analysis for detecting bone changes due to exposure to reduced gravity and aging |
| SAMS | Development of a selective metallisation process that can be applied on 3D printed surfaces. |
| SLOTT | Straylight lidar verification tool, hardware pre-development |
| SMARTIES | Design, procurement and qualification testing of a Slip Ring assembly rotor based on additive manufacturing |
| SPACEDUSTBUSTER | Electrodynamic dust shield for lunar and martian missions |

| | |
|---------------|---|
| TRICYCLE | Technology review of high-performance gyroscopes |
| TRUMET-PDIODE | Characterization of photodiodes for the ESA's TRUTHS Mission |
| WALLIE | Development new time-of-flight detector |
| WAVEGUIDE | Development of waveguide switches based on friction-free mechanisms |

Industrial Property

Patent portfolio

In 2022, the CSEM filed on its name 17 patent applications related to new inventions (first filings). All these filings were regular applications (no provisional filings).

The patent portfolio was further enhanced by the extension to different countries of 13 patent applications based on previously filed inventions (7 cases of "filing under priority" and 6 cases of "entries into national/regional phase" from international applications).

Two additional patents were filed in the name of CSEM partners as a first filing for an invention developed in cooperation with CSEM inventors.

Collaboration with Research Institutes and Universities

| University | Institute | Professor | Field of collaboration |
|---|---|---------------------------|---|
| Adolphe Merkle Institut | Soft Matter Physics and Polymer Chemistry | U. Steiner, C. Weder | Bioinspired nanomaterials |
| Agroscope | Animal Production Systems and Animal Health | C. Ollagnier | Vital sign monitoring in livestock (pigs) |
| AIT Austrian Institute of Technology | Advanced Implant Solutions | L. Sajti | Magnetic inks |
| Alpen-Adria-Universität Klagenfurt, Austria | Digital Age Research Center | E. Andreeva | Cryptography & security |
| AO Research Institute Davos | Regenerative Orthopaedics | S. Grad, M. Stoddart | Biosensing and bioreactors |
| BFH, Bern University of Applied Sciences | Mikro- und Medizintechnik | G. Gruener | BinPicking & robotics |
| Cantonal Hospital St.Gallen | Lung Center | F. Baty, M. Bösch. | Unobtrusive assessment of sleep apnea using a wrist-worn device |
| CEA | Institut National de l'Énergie Solaire | D. Munoz | Silicon heterojunction & metallization |
| CHUV Lausanne | Department of Anesthesiology | P. Schoettker | Continuous blood pressure monitoring in patients undergoing induction of general anesthesia |
| CHUV Lausanne | Department of Nephrology and Hypertension | M. Pruijm, G. Wuerzner | Continuous blood pressure monitoring in dialyzed patients |
| CHUV Lausanne | Department of Nephrology and Hypertension | G. Wuerzner | Long-term blood pressure monitoring in patients with chronic hypertension |
| CHUV Lausanne | Head and Neck Surgery | S. Christian | Multispectral endoscopy for real time delineation in surger. |
| EMPA | Biomimetic Membranes & Textiles | R. Rossi, S. Annaheim | Unobtrusive assessment of sleep apnea using a wrist-worn device |
| EMPA | Cellulose & Wood Materials | G. Nyström | Chipless compostable sensor tags |
| EMPA | Laboratory for Thin Films and Photovoltaics | F. Fu | Perovskite based tandem cells |

| University | Institute | Professor | Field of collaboration |
|-------------------|---|------------------------------|--|
| EMPA | Swiss federal laboratories for materials science and technology | P. Hoffmann | Solid state lighting |
| EPF Lausanne | Computer Vision Laboratory | P. Fua | Reduced labelling machine learning |
| EPF Lausanne | Department Engineering Mechanics of Soft Interfaces | J. M. Kolinski | Smart interfaces/coatings |
| EPF Lausanne | DESL Distributed Electrical Systems Laboratory | M. Paolone | Predictive maintenance for batteries |
| EPF Lausanne | LA3 Automatic Control Laboratory | C. Jones | Automatic building model identification and optimized control |
| EPF Lausanne | Laboratory of Physics of Complex Matter | L. Forro | Nanomaterials |
| EPF Lausanne | LAP Processor Architecture Laboratory | P. lenne | Embedded systems |
| EPF Lausanne | LTS4 Signal Processing Laboratory | P. Frossard | Graph machine learning for power forecasting; Privacy preserving machine learning and hierarchical computing |
| EPF Lausanne | School of Computer and Communication Sciences | M. Payer | Embedded security |
| EPF Lausanne | STI IEM SCI-STI-AS | A. Skrjervic | Wireless power transfer |
| EPF Lausanne | TCL Telecommunications Circuits Laboratory | A. P. Burg | Ultra-low power design; Bias control |
| EPF Lausanne | Advanced NEMS Laboratory | G. Villanueva | Nanofabrication of devices made out lithium niobate on insulator |
| EPF Lausanne | Advanced Quantum Architecture Laboratory | E. Charbon | Micro-optics |
| EPF Lausanne | EPFL-ECAL Lab | N. Henchoz | Digital experience – Meditation study in collaboration with Ming Shan (Bullet's Taoist center) |
| EPF Lausanne | High Energy Physics Laboratory | O. Schneider | Micro-optics |
| EPF Lausanne | Instant-Lab | S. Henein | Vibrations damping for compliant mechanisms |
| EPF Lausanne | Institute of Bioengineering | B. Deplancke | Sequencing |
| EPF Lausanne | Laboratory of advanced semiconductors for photonics and electronics | N. Grandjean | Solid state lighting |
| EPF Lausanne | Laboratory of Nanobiotechnology | A. Boghossian | Biosensors |
| EPF Lausanne | LESO Solar Energy and Building Physics Laboratory | J.-L. Scartezzini | Human centric lighting |
| EPF Lausanne | LIPID Laboratory of Integrated Performance in Design | M. Andersen | Human centric lighting |
| EPF Lausanne | Microengineering | D. Briand, V. Subramanian | Printed electronics |

| University | Institute | Professor | Field of collaboration |
|---|---|------------------------------|---|
| EPF Lausanne | School of Engineering, Institute of Bioengineering | D. Van De Ville | Cuffless blood pressure estimation using raw photoplethysmography signal; Wearable heart rate measurement during daily life and sport |
| EPF Lausanne | ICLAB Integrated Circuits Laboratory | C. C. Enz | mm-wave radar transceiver design |
| EPF Lausanne | Photovoltaics & Thin-Film Electronics Laboratory | C. Ballif | Solar cells and modules |
| ETH Zürich | Computer Vision Laboratory | E. Konukoglu, L. van Gool | Machine learning |
| ETH Zürich | Data Analytics Lab | T. Hofmann | Machine learning |
| ETH Zürich | Department of Biosystems Science and Engineering | A. Hierlemann | Organoid sorting |
| ETH Zürich | Department of Chemistry and Applied Biosciences | M. Kovalenko | Fluorescence lifetime imaging |
| ETH Zürich | Department of Health Sciences and Technology | S. Sturla | Biosensing |
| ETH Zürich | Department of Information Technology and Electrical Engineering | M. F. Yanik | Neuroinformatics |
| ETH Zürich | Energy-Efficient Circuits and IoT Systems | T. Jang | Analog-to-digital converters |
| ETH Zürich | Institute for Electronics | V. Wood | State-of-health modeling for batteries |
| ETH Zürich | Institute of Energy and Process Engineering | M. Tibbitt | Acoustofluidics |
| ETH Zürich | Integrated Systems Laboratory | L. Benini | RISC-V, neural network |
| ETH Zürich | Mobile Health Systems Lab | W. Karlen | Development and evaluation of a slow wave sleep modulation framework including continuous blood pressure and glucose monitoring |
| ETH Zürich | Optical Nanomaterial Group | R. Grange | Integrated photonics for gas spectroscopy |
| FHGR, University of Applied Sciences of the Grisons | Departement Angewandte Zukunftstechnologien, Institut für Photonics und ICT IPI | U. Hauser-Ehninger | Solid state lighting |
| FHGR, University of Applied Sciences of the Grisons | Kompetenzzentrum für Datenanalyse, Visualisierung und Simulation | B. Studer, T. Leutenegger | Machine learning / photonics |
| FHNW, University of Applied Sciences Northwestern Switzerland | Institut für Nanotechnische Kunststoffanwendungen | M. Kristiansen | Micro and nano structuring |

| University | Institute | Professor | Field of collaboration |
|--|---|-------------------|---|
| FHNW, University of Applied Sciences Northwestern Switzerland | Institute for Chemistry and Bioanalytics | D. Meinel | Biosensing |
| FHNW, University of Applied Sciences Northwestern Switzerland | Institute of Chemistry and Bioanalytics | L. Suter-Dick | Biosensing and 3D in-vitro models |
| FHNW, University of Applied Sciences Northwestern Switzerland | Institute of Product and Production Engineering | B. Resan | Lasers |
| Fondazione Bruno Kessler | Integrated Radiation and Image Sensors | L. Gasparini | Time-of-flight lidar detectors |
| Geneva University Hospital | Paediatric Emergency Division | M. Rida Benissa | Diagnosis based on AI on chest sounds |
| Haute Ecole d'Ingénierie et de Gestion du Canton de Vaud (HEIG-VD) | Institut de recherche appliquée et développement | E. Messerli | FPGA programming and embedded processing |
| HE-ARC La-Chaux-de-Fonds | Engineering – Medical Devices | A. Kaempfer-Homsy | Biosensing |
| HSLU, Lucerne University of Applied Sciences | CC Electronics | E. Niederberger | Solid state lighting |
| HSLU, Lucerne University of Applied Sciences | Informatik | R. Meier | Cooperation in Smart Card Forum |
| HSLU, Lucerne University of Applied Sciences | Institut für Innovation und Technologiemanagement | C. Minonne | Machine learning (S. Rickli) |
| HSLU, Lucerne University of Applied Sciences | Institute of Electrical Engineering | T. Prud'homme | Vision, polarization camera; Calving detection in the barn with vision systems |
| Idiap Research Institute | Speech and Audio Processing | M. Magimai Doss | Detection of QRS landmark in ECG signals |
| Idiap Research Institute | Speech and Audio Processing | P. Motlicek | Modal a people monitoring system using multiple sensing modes (video, audio, ...) |
| Ifremer | Centre Méditerranée | J. Opderbecke | Bathymetric lidar |
| Imperial College of London, United Kingdom | Faculty of Engineering, Department of Electrical and Electronic Engineering | P. Mitcheson | Wireless power transfer |
| Imperial College of London, United Kingdom | Faculty of Engineering, Department of Electrical and Electronic Engineering | E. M. Yeatman | Energy harvesting for wireless sensor networks in aerospace applications; Smart materials |
| Institut für Kristallzüchtung, Berlin | Zentrum für Lasermaterialien | C. Kränkel | New laser crystals for high-power short pulse sources |

| University | Institute | Professor | Field of collaboration |
|--|---|---------------------------------------|--|
| IOB, Institute of Molecular and Clinical Ophthalmology Basel | Molecular Research Center | M. Renner | Retina organoid sorting |
| IOR, Istituto Ortopedico Rizzoli, Bologna, Italy | 2nd Orthopaedic and Traumatology Clinic | S. Zaffagnini | Clinical implantation and assessment |
| National Research Council of Italy | Institute of Applied Physics (IFAC) | V. Raimondi | Compressive sensing for space applications |
| National Technical University of Athens (NTUA) | School of Mechanical Engineering | I. Paraskevas | Systems identification methods |
| ONERA-France | Meudon Center | M.-C. Mérienne | Pressure sensitive painting |
| Politecnico di Torino, Italy | Electronics and Telecommunications | E. Magli | Compressive sensing for space applications |
| Robert-Bosch-Hospital | Clinical of Geriatric Rehabilitation | C. Becker | Fall prediction and detection |
| Sant'Anna School of Advanced Studies, Pisa | Institute of Communication, Information and Perception Technologies (TeCIP) | A. Bogoni | Photonics radar |
| SUPSI, University of Applied Sciences and Arts of Southern Switzerland | IDSIA Dalle Molle Institute for Artificial Intelligence | L. M. Gambardella | Machine learning |
| SUPSI, University of Applied Sciences and Arts of Southern Switzerland | PV Lab | M. Caccivio | Metrology |
| Swedish University of Agricultural Sciences | Biosystems and Technology | A. Herlin | Vital sign monitoring in livestock (pigs) in the framework of IoF2020 |
| Swiss TPH | Department of Medicine | D. Paris | Diagnostics |
| Università Campus Bio-Medico, Roma, Italy | Department of Orthopaedics and Trauma Surgery | V. Denaro | Clinical implantation and assessment |
| Université Bourgogne Franche-Comté | FEMTO-ST Institute & UTBM | F. Chérioux, V. Humblot, P. Briois | Smart coatings |
| Université Bourgogne Franche-Comté | Le2i Laboratory of Electronics, Information and Image | J. Dubois | Remote vital signal monitoring |
| University Hospital Basel | Research Center for Clinical Neuroimmunology and Neuroscience | Consultant Neurologist J. Lorscheider | Improving monitoring solutions for multiple sclerosis patients |
| University Hospital Inselspital Bern | Department ENT Surgery | M. Caversaccio | Image-guided micro-surgery for hearing aid implantation |
| University Hospital Inselspital Bern | Department of Cardiology and Clinical Research | E. Rexhaj | Clinical study on 24h ambulatory blood pressure monitoring in 70 hypertensive patients using wrist-located optical sensors |
| University Hospital Inselspital Bern | Department of Cardiology and Clinical Research | E. Rexhaj, S. Rimoldi | Clinical validation of a PAP sensor against non-invasive medical gold standard |

| University | Institute | Professor | Field of collaboration |
|---|---|--------------------------------|--|
| University Hospital Inselspital Bern | Department of Cardiovascular Surgery | D. Reineke | Clinical study on non-invasive blood pressure monitoring in 40 patients carrying a left ventricular assist device |
| University Hospital Inselspital Bern | Department of Intensive Care Medicine | J. Schefold, D. Reinecke | Validation of the extended AVA product with the non-invasive measure of the BP in reference to the medical gold standard and with a 40-patient cohort (pregnant women) |
| University Hospital Inselspital Bern | Lung Cancer Center | G. Kocher | Machine learning for efficient surgery |
| University Hospital Inselspital Bern | Universitätsklinik für Frauenheilkunde | A. Radan | Introduce AI and machine learning in cardiotocography (CTG) interpretation to improve clinical use; Wearable system for foetal ECG monitoring |
| University Hospital Inselspital Bern | Universitätsklinik für Frauenheilkunde | D. Surbek | AI-based decision support system for delivery & Fetal monitoring by transabdominal electrocardiogram recording: the ELAINE pilot project |
| University Hospital Inselspital Bern | Universitätsklinik für Neurologie, Schlaf-Wach-Epilepsie-Zentrum (SWEZ) | K. Schindler | Epilepsy detection and prediction |
| University Hospital Inselspital Bern | Universitätsklinik für Pneumologie | S. Ott | Unobtrusive assessment of sleep stages using a wrist-worn device |
| University Hospital of Basel | Cardiology | A. S. Vischer, T. Burkard | Accuracy of the RIVA digital blood pressure measurement App – a pilot study |
| University of Athens, Greece | Dept. of Informatics & Telecommunications | S. Hadjiefthymiades | Internet of things, location-based services, mobile and vehicular applications |
| University of Basel | Chemistry | E. Constable, C. Housecroft | Photochemistry |
| University of Basel | Psychiatry Hospital / Center for Chronobiology | C. Cajochen | Human centric lighting; Chronobiology |
| University of Bern | Quantum Optics Lab | A. Stefanov | Entangled photons for microscopy |
| University of Bern – ARTORG | Organs-on-Chip Technologies | O. Guenat | Biosensing |
| University of Essex, Colchester, United Kingdom | School of Computer Science and Electronic Engineering | L. Citi | Point-process and machine-learning-based neuro-muscular decoding/control algorithms |
| University of Geneva | Astronomy Department | F. Bouchy | Laser frequency combs for calibration of spectrographs |
| University of Geneva | School of Economics and Management | S. Engelke | Non-contact heart rate monitoring through vision system |
| University of Geneva | Sensors Group at Institut für Neuroinformatik, U | S.-C. Liu | Neuroinformatics |

| University | Institute | Professor | Field of collaboration |
|--|---|-------------------|---|
| University of Gothenburg, Sweden | Department of Orthopaedics | J. Wessberg | Sensory feedback |
| University of Lausanne | Department of Information Systems | K. Huguenin | Privacy and security in healthcare IoT systems |
| University of Ljubljana, Slovenia | Laboratory of Photovoltaics and Optoelectronics | Marko Topics | Device optical and electrical modelling |
| University of Neuchâtel | Complex Systems Group | V. Schiavoni | Security and data privacy in IoT systems; Usage of Trusted Execution Environments for cloud computation (IntelSGX) and IoT protocols (ARM's TrustZone) |
| University of Neuchâtel | Laboratoire Temps-Fréquence | G. Miletí | Atomic clocks |
| University of Pavia | Department of Chemistry | M. Pesavento | Chemical Sensor |
| University of Sherbrooke | Neonatology | E. Fortin-Pelerin | Evaluation of PAP measurement accuracy in sheep and neonatal human patients |
| University of Zurich | Institute of Neuroinformatics | T. Delbrück | On-chip convolutional neural network for visual scene processing |
| Vienna University | Department of Physical Chemistry | P. Lieberzeit | Chemical sensor |
| ZHAW, Zürich University of Applied Sciences | School of Engineering, Winterthur | R. Locher | Joint Innosuisse with Mettler-Toledo: Automatic evaluation of thermoanalytical curves (35056.1 IP-ENG) |

Teaching

| | Title of lecture | Context | Location |
|--|--|---|------------------------|
| S. Blanc | Innovation Management | Master Management, technologie et entrepreneuriat | University of Lausanne |
| S. Blanc | Tendances Transformationnelles | CAS en Management du changement | University of Lausanne |
| A. Corbaz | Systèmes d'exploitation (SYE) | Bachelor course | HEIG-VD |
| M. Despont | Packaging and hybridization, the valorization of MEMS technologies | Micro-534 Advanced MEMS 2022 (D. Briand) | EPF Lausanne |
| L. A. Dunbar | Digital Transformation | EMBA | EPF Lausanne |
| R. Krähenbühl | Nanotechnology and Industrialization | Information lecture | University of Basel |
| M. Lemay, P. Renevey, J. Jorge, M. Proença, F. Braun, G. Bonnier, R. Soltani, C. Aguet | Applied Biomedical Signal Processing | EPFL Course EE-512 | EPF Lausanne |
| N. Marjanovic, F. Zanella | Organic and Printed Electronics | Master course MICRO-505 | EPF Lausanne |
| B. Paviet-Salomon | Design of High Efficiency Solar Cells | Summer School Mont-Soleil | Neuchâtel |
| B. Paviet-Salomon | Silicon Heterojunction Solar Cells | SiliconPV tutorials | Online |
| R. Pugin | Micro/Nano-structured Functional Surfaces & Components | Highlights in Microtechnology – Summer School | EPF Lausanne |

| | <i>Title of lecture</i> | <i>Context</i> | <i>Location</i> |
|-------------|--|----------------|-------------------|
| D. Ruffieux | Radio Frequency Circuits Design Techniques | Master course | EPF Lausanne |
| G. Weder | Organ-on-chip and organoid technology for drug development | FSRM | Technopark Zürich |

Theses

PhD Degrees Awarded in 2022

| <i>Name</i> | <i>University</i> | <i>Title</i> |
|-----------------|-------------------|--|
| Iurilli, Pietro | ETH Zürich | State-of-health modeling for batteries |

CSEM Employees carrying out a PhD & PhD Funded by CSEM

| <i>Name</i> | <i>Professor / University</i> | <i>Theme / CSEM Unit</i> | <i>Start year</i> |
|--------------------------------|--------------------------------------|--|-------------------|
| Aguet, Clémentine | P. Frossard / EPF Lausanne | Generate realistic synthetic PPG data using Generative adversarial networks / Systems | 2019 |
| Ahmadi Najafabadi, Amir Mohsen | A. Skrivervik / EPF Lausanne | <i>Not defined yet</i> / Integrated & Wireless Systems | 2022 |
| Ayhan, Furkan | G. Villanueva / EPF Lausanne | LiNbO ₃ waveguide microfabrication for broadband optical frequency combs for astronomical spectrometers calibration light / Systems | 2020 |
| Bernard, Gaëtan | R. Logé / EPF Lausanne | Development of a production method of metal matrix composite for space applications using laser powder bed fusion / Micro&Nano Systems | 2020 |
| Bhoir, Shubham Sharad | M. Paolone / EPF Lausanne | Exploitation of electrochemical impedance spectroscopy for predictive maintenance for batteries / Sustainable Energy | 2021 |
| Biggio, Luca | T. Hofmann / ETH Zürich | Machine learning based domain adaptation and interpretability for time-series / Regional site - Alpnach | 2019 |
| Blum Roman | G. Miletí / University of Neuchâtel | Long-term frequency stability improvement of a 2-photon Rubidium clock / Systems | 2021 |
| Cerida Rengifo, Sammy | C. Enz / EPF Lausanne | Low-power and wide-tuning range frequency generation for FMCW radars in advanced CMOS technologies / Integrated & Wireless Systems | 2018 |
| Chang, Yaxing | L. Benini / ETH Zürich | Digital IC design for embedded machine learning / Integrated & Wireless Systems | 2022 |
| Del Giovane, Stefano | H. Altug / EPF Lausanne | New generation point of care sensing / Regional site - Landquart | 2021 |
| Dussouillez, Marion | C. Ballif / EPF Lausanne | Stability of perovskite solar cells / Sustainable Energy | 2019 |
| El-Zein, Yamane | K. Huguenin / University of Lausanne | Privacy-preserving data transmission and processing in digital health / Systems | 2019 |
| Gaudillière, Pierre Louis | D. Atienza / EPF Lausanne | Embedded machine learning for the controlling of PPG-based systems / Systems | 2021 |

| Name | Professor / University | Theme / CSEM Unit | Start year |
|---------------------------|--|--|------------|
| Ghorbanpoor, Mohsen | H. Wang / ETH Zürich | Not defined yet / Integrated & Wireless Systems | 2022 |
| Hefti, Olivia | C. Brès / EPF Lausanne | Periodic poling of lithium niobate on insulator photonics waveguide and its application / Systems | 2022 |
| Honzátko, David | P. Fua / EPF Lausanne | Defect detection using deep learning / Integrated & Wireless Systems | 2018 |
| Jeanningsros, Loïc | J.-P. Thiran / EPF Lausanne | Classification of cardiac arrhythmia based on PPG / Systems | 2020 |
| Klauser, Elias | A. Karimi / EPF Lausanne | Adaptive control of a high-performance active-passive hybrid micro-vibration isolation system for sensitive payloads / Systems | 2020 |
| Knuchel, Benoît | E. Oswald / AAU Klagenfurt | Embedded intrusion detection for the IoT / Integrated & Wireless Systems | 2022 |
| Lang, Guilain | M. Meboldt / ETH Zürich | Automatic generation of compliant mechanism designs / Systems | 2021 |
| Luongo, Francesca | E. Konukoglu / ETH Zürich | Generative methods for organoid data augmentation and generation / Regional site - Alpnach | 2022 |
| Miotello, Enrico | T. Jang / ETH Zürich | Advanced ADC design / Integrated & Wireless Systems | 2022 |
| Narduzzi, Simon | S.-C. Liu / ETH Zürich | Ultra-low-power resource algorithms for neuromorphic hardware / Integrated & Wireless Systems | 2020 |
| Ntavelis, Evangelos | L. van Gool / ETH Zürich | Multimodal learning & generation: Utilizing diverse inputs to generate & manipulate images / Regional site – Alpnach | 2019 |
| Sacchi, Nazareno | T. Jang / ETH Zürich | Not defined yet / Integrated & Wireless Systems | 2022 |
| Sainz Martinez, Cristina | M. Bach Cuadra / University of Lausanne & CHUV | MRI and EEG processing applied to human brain structure and function / Systems | 2020 |
| Sampaio Da Silva, Claudia | A. Hierlemann / ETH Zürich (Basel) | Automated platform for high throughput, deep learning-based sorting of 3D cell models / Regional site – Alpnach | 2021 |
| Scharnhorst, Paul | C. Jones / EPF Lausanne | Learning-based control for building and grid management / Sustainable Energy | 2019 |
| Sepehri, Yamin | P. Frossard / EPF Lausanne | Smart edge for hierarchical vision systems / Integrated & Wireless Systems | 2020 |
| Sideris, Iason | M. Bambach / ETH Zürich | Data-driven modeling for metal additive manufacturing process optimization / Regional site – Alpnach | 2021 |
| Simeunovic, Jelena | P. Frossard / EPF Lausanne | Network time series forecasting for smart grid application / Sustainable Energy | 2019 |
| Vuille-dit-Bille, Emilie | S. Sakar / EPF Lausanne | Acoustic manipulation of organoids / Micro&Nano Systems | 2021 |

Commissions and Committees

| | |
|--------------------|--|
| P.-J. Alet | EUPVSEC: scientific committee (member, topic organizer) European Commission, Innovation and Networks Executive Agency: expert European technology and innovation platform – photovoltaics (ETIP-PV): executive committee (member), steering committee (member), “Digital PV and grid” working group (leader) European technology and innovation platform – smart networks for the energy transition (ETIP-SNET): governing board (member) Intersolar Award (member of top jury) |
| G. Basset | Chairman of the conference, Product authentication & brand protection: becoming global and digital (Trustech 2021) |
| C. Beyer | Member of the board of Sensors.ch association |
| N. Blondiaux | Member of the council of the Academy of Engineering and Technology (AET) Member of the scientific committee of the EUSPEN 21st international conference & exhibition |
| F. Braun | Scientific Program Committee for BMT 2022 |
| C. Brivio | BEPA – Batteries Europe integrated working group member to WG6 Stationary Applications and Integration |
| S. Cattaneo | Expert for MSE Master Theses at OST Eastern Switzerland University of Applied Sciences Expert for W.A. de Vigier Foundation Innovation Coach for INOS Innovationsnetzwerk Ostschweiz |
| P. Dallemande | Secretary and Swiss representative of Technical Committee 5 "Information Technology Applications", International Federation for Information Processing (IFIP) |
| R. Delgado-Gonzalo | Expert Group in Digital Health in the Swiss Alliance for Data-Intensive Services |
| M. Despeisse | n-PV workshop committee, EUPVSEC topic organizer, SolarPower Europe. |
| M. Despont | Jury Member at the thesis of Thimothée Frei “Thermal management of components for high energy physics experiments and space applications” with Prof. V. Gass Member of the editorial board of Microelectronic Engineering Journal (Elsevier) Regional Program Chair of the 21st International Conference on Solid-State Sensors, Actuators and Microsystems (Transducers 2021) Vice-Chairman of the Swiss-MNT network |
| L. A. Dunbar | Academic co-Lead of Machine Learning Clinic in the Swiss Alliance for Data-Intensive Services Jury member of the BCN innovation prize Jury member of the Shapers Industry 4.0 prize Members of the subcommittee FA10 on Computer Vision and Human-Machine Interaction in Industrial and Factory Automation TinyML Swiss Committee |
| S. Emery | TinyML Swiss Committee |
| J. R. Farserotu | Member of the Technical Committee of the IEEE SOI-3D-Subthreshold (S3S) Conference |
| B. Gallinet | Chair and Research Co-ordinator The Hermes Partnership |
| E. Györvary | Member of scientific committee, International Workshop on Metallic Nano-Objects (MNO 2021) Member & CSEM representative of EARTO Working Group on Emerging Technologies for Healthcare Member & CSEM representative of EPOSS Association; Chair of WG Green ECS Member of Finnish Chamber of Commerce in Switzerland Member of the Board of European Organ-on-Chip Society (EUROoC); Chair of EUROoCS 2022 event session Member of the Core Team of Team Finland in Switzerland Member of the Extended Board of the Heterogeneous Technology Alliance (alliance federating the Fraunhofer (microelectronics), VTT, CEA-Tech, and CSEM) & leading the Health & AgriFood Platform Member of the Scientific & Organizing Committee of “Next Gen Organ-on-Chip & Organoids” event Member of the Steering Board of Innovation Group Digitalization at Swiss Food Research |

| | |
|------------------|--|
| H. Heinzemann | Expert, Austrian Research Promotion Agency FFG Expert, German Federal Ministry of Education and Research BMBF Member of the Board of the Heterogeneous Technology Alliance (HTA) Member of the Executive Board, EARTO Member of the Foundation Board, Switzerland Innovation Member of the Strategic Advisory Board "Produktion der Zukunft", Austrian Federal Ministry for Climate Action, Environment, Energy, Mobility, Innovation and Technology (BMK) Membre du Conseil d'Administration de Centredoc Program Committee, MNE 2022 Leuven Thesis expert for Bertrand Paviet-Salomon, CAS "Sustainable Development: Horizon 2030", U Geneva |
| M. Höchemer | SDS2022 Scientific Program Committee |
| A. Hutter | BEPA – Batteries Europe integrated working group member to WG5 Mobility Applications and Integration Commission des énergies et de l'eau de la ville de Neuchâtel Federal Office of Transport (FOT), Energy Strategy for Public Transport 2050 (ESPT 2050) programme, expert Innosuisse expert Vice-President iBAT Association (www.ibat.swiss) |
| A. Ingenito | BEPA – Batteries Europe integrated working group member to WG3 Advanced Materials and WG4 Cell Design and Manufacturing |
| C. Joder | Member of the Advisory Board of IAT (Center of Innovation for Assistive Technologies) at Swiss Paraplegic Center, Nottwil |
| R. Jose James | Chairman Swiss Chapter IEEE Electronic Packaging Society |
| C. Julia-Schmutz | Communication coordinator within the Heterogeneous Technology Alliance (HTA) CSEM Representative, BioAlps |
| H. F. Knapp | Board of Directors member for cluster initiative Toolpoint for Lab Science Jury member for the Innovationspreis of the Industrie- & Handelskammer Zentralschweiz Jury member for Zinno Ideenscheck Pre-jury member for Swiss Technology Award |
| G. Kotrotsios | Full Member of the Swiss Academy of Engineering Sciences SATW IDIAP, Member of the International Advisory Board Member of the Advisory Board of Kickstart Member of the Advisory Board of the NTN Innovation Booster Photonics Member of the Industrial Advisory Board of SATW |
| F. Kurth | Academic supervisor and external expert for PhD program at D-BSSE, ETH Zurich, Basel European Liquid Biopsy Society Member Expert for bachelor and master theses program at FHNW Muttenz Member of the technical program committee, International Conference on Miniaturized Systems for Chemistry and Life Sciences (mTAS) |
| M. Lemay | Board Member, Swiss Society for Biomedical Engineering Scientific Program Committee for BMT 2022 |
| N. Marjanovic | Member of the Organising Committee, Swiss ePrint 2022 |
| S. Mohrdiek | Member of Swissmem Fachgruppe Photonics Swissphotonics, Head of Swiss Photonic Packaging Laboratory (SPPL) |
| T. Offermans | Technical Coordinator of the PHABULOUS Pilot Line Association |
| S. Paoletti | Chair of the Swiss Symposium in Point of care diagnostics European Liquid Biopsy Society Member Executive Board member of biotechnet, Switzerland and co-lead of the IVD platform Member of the Bridge proposal evaluation panel |

| | |
|--------------------|--|
| A. Pauchard | CNCI Chambre Neuchâteloise du Commerce et de l'Industrie, Neuchâtel Conseil d'administration de Silatech SA Full Member of the Swiss Academy of Engineering Sciences SATW |
| E. Portuondo-Campa | Membre du Conseil d'Administration de Centredoc |
| R. Pugin | Member of the Expert Committee of the Association NTN Innovative Surfaces Member of the Omega Foundation Council Member of the Scientific Committee of the 4M Micro-Nano Manufacturing Association Member of the Scientific Committee of the World Congress on Micro and Nano Manufacturing |
| V. Revol | Chair of the Next Gen Organ-on-Chip & Organoids Symposium & Precision Liquid Handling Workshop Co-Founder and deputy head of the Digital Innovation Hub LifeHub.Swiss (www.lifehub.swiss) InnoSuisse expert |
| D. Ruffieux | Chair of the RF and mm-Wave Circuits Track of the International Technical Program Committee of the European Solid State Circuit Conference (ESSCIRC) |
| P. A. E. Schmid | Academic co-lead expert group ML-Clinic (ML in Industrial Practice) Swiss Alliance for Data-Intensive Services Accredited Coach for INOS Innovationsnetzwerk Ostschweiz CSEM Representative Swiss Mechatronics Cluster Founder and regional lead Digital Innovation Hub Robotics & Artificial Intelligence (www.raisehub.swiss) Industry 4.0 topic leader NTN Innovation Booster Databooster (www.databooster.ch) Member expert group Industry 4.0 SATW Steering committee PDA Robotics & Automation |
| D. Schmid | Point of entry INOS Innovationsnetzwerk Ostschweiz President of the Board KinderLab Landquart, Switzerland |
| P. Steiert | Advisory Board Member for Institute für Chemistry and Biological Chemistry at the ZHAW Advisory Council for cluster initiative Toolpoint for Lab Science Member of the Executive Board for Verein Nachhaltigkeitsnetzwerk Zentralschweiz Member of the Executive Board for Verein Startup Pilatus Member of the Executive Board of the PHABULOUS Pilot Line Association |
| A. Steinecker | Cluster manager "Production & Systems" at Technologie Forum Zug Coach for RIS Zentralschweiz CSEM contact for Smart Card Forum (René Meier, HSLU) CSEM Representative EPoSS and Member of Working Group Robotics CSEM Representative IVAM |
| A. Völker | IVAM: Fachgruppenleiter der Fachgruppe Photonik Member of Photonics21 Board of Stakeholders |
| G. Weder | Global Expert for GESDA Science Breakthrough Radar for organoids Member of the Board of European Organ-on-Chip Society (EUROoC) |

Prizes and Awards

- February 2022 CSEM Inventor Award has been given to Dr. Franz Xaver Pengg for a remarkable invention: an ultra-low-power transceiver, icyTRX, that can be integrated into Bluetooth chips, enabling greater miniaturization and a longer battery life for portable devices. (Neuchâtel, CH)
- March 2022 Arnaud Walter was rewarded with the SiliconPV 2022 Award for his presentation entitled "Perovskite/Silicon Tandems: First Realization with Rear Textured p-Type High-Temperature Passivating Contacts". (Konstanz, DE)
- March 2022 "Best Practice-Oriented Poster" goes to CSEM and Meteotest, for their work understanding the performance of data-driven and weather-based PV forecasting techniques. (Bern, CH)
- March 2022 Ewelina Obrzud, winner of the prestigious European Astronomical Society's MERAC Prize for her amazing work on new instrumental technologies. (Valencia, ES)
- October 2022 MATIS has won the Prix BCN Innovation 2022 with 150,000 Swiss francs. MATIS is a dynamic young CSEM start-up using multi-factor identification, including multispectral measurements and the latest AI techniques, to give a digital fingerprint to art works. (Neuchâtel, CH)
- November 2022 EPFL's Best 8% Thesis Distinction awarded to Laurie-Lou Senaud for her work on "Electrical Losses Mitigation In Silicon Heterojunction Solar Cells". (Lausanne, CH)
- December 2022 MATIS received a financial support from the Foundation for Technological Innovation (STI) of 100,000 Swiss francs.
- December 2022 Prix Durabilis 2022 UNIL-EPFL to Alexis Barrou for his work entitled "Life Cycle Analysis & Sustainable Technological Roadmap for Photovoltaic Panels". (Lausanne, CH)

ALLSCHWIL
Hegenheimermattweg 167A
4123 Allschwil

ALPNACH
Untere Gründlistrasse 1
CH-6055 Alpnach

BERN
Freiburgstrasse 2
CH-3008 Bern

LANDQUART
Bahnhofstrasse 1
CH-7302 Landquart

NEUCHÂTEL
Jaquet-Droz 1
CH-2002 Neuchâtel

ZÜRICH
Technoparkstrasse 1
CH-8005 Zürich



CONTACT
www.csem.ch
info@csem.ch
jobs@csem.ch